Analysis of flow and heat transfer inside different filter designs

ML Lekoko

orcid.org 0000-0002-6723-6048

Thesis accepted in fulfilment of the requirements for the degree *Doctor of Philosophy in Science with Applied Mathematics* at the North-West University

Promoter: Dr G Magalakwe

Graduation July 2023

23192267

Declaration

I declare that the thesis for the degree of Doctor of Philosophy at North-West University, Potchefstroom Campus, hereby submitted, has not previously been submitted by me for a degree at this or any other university, that this is my own work in design and execution and that all material contained herein has been duly acknowledged.

Acknowledgements

This research project would not have been possible without the assistance and encouragement of my supervisor, family, and friends. I want to thank the following individuals for their encouragement, motivation, and prayers throughout my PhD three-year journey.

Dr Gabriel Magalakwe, the research project advisor, for his invaluable guidance and assistance in ensuring this thesis was a huge success. He is my role model, an excellent researcher, and an inspiring academic. In addition, I would like to thank all pure and applied mathematics members of the postgraduate committee for their patience, understanding and support during the three years of efforts that went into this research project. Many thanks, Dr S.D. Oloniiju, for his valuable advice, discussions and suggestions when I encountered difficulties while working towards completing this research project.

My deepest and most tremendous gratitude goes to my beautiful parents, who have supported me throughout my academic journey. They have always been there for me, having faith in me and providing numerous opportunities for me to grow as a budding thinker. They have enriched this path; I could not have gotten this far without them. My lovely partner Lerato and my son Leago, thank you for your encouragement, and I must say that your presence in my life has helped me tremendously on this journey. Finally, I want to thank the CSIR-DST inter-bursary program for providing me with financial support during my studies. Opinions expressed and conclusions reached are solely those of the author and should not be attributed to the individuals mentioned above and entities.

Abstract

This research project's main purpose is to theoretically investigate internal flow, heat and mass transfer inside different filter designs. The efficiency of filtering methods used to reduce/remove particles deposited in a liquid varies greatly depending on the type of particles, the quality of filter media and filter design. As a result, it is ideal for engineers and scientists to design filters based on mathematical models (scientific evidence) that predict the dynamics of the filters to provide a better understanding of the flow, heat and mass transfer during the filtration process when designing filters. It is vital to have a design that yields optimal balance between the parameters that restrict the particles and allows desirable outflow and heat transfer. Pursuing to understand momentum variation, heat and mass transfer during the filtration process. The mathematical models presenting different filter designs under investigation will be formulated using continuity, momentum, concentration and energy conservation laws, along with physical laws representing forces that affect the process according to each filter design. The flow and heat transfer models under investigation are solved analytical and semi-analytical or numerical in cases where the model(s) could not be solved analytically. The obtained solutions of each model are then used to analyse flow, heat and mass transfer to understand the dynamics of each model and to highlight an optimal design amongst models considered in this research project. The study also aims to study the effects of various parameters in detail according to each filter design to have evidence-based findings that lead to optimal permeate production.

Keywords: Different filter designs; Flow and heat transfer; Analytical and numerical analysis; Steady/Unsteady filtration process; Magnetohydrodynamic fluid; Optimal permeates

Declaration of Publications

Details of contribution to publications that form part of this thesis.

Chapter 3

Lekoko, M.L., Oloniiju, S.D. and Magalakwe, G., 2022. Analysis of pressure and heat distribution in a dilating or contracting filter chamber with two outlets using multivariate spectral quasilinearization method. Heat Transfer, 51(2), pp.1543-1567.

Chapter 4

Lekoko, M.L., Oloniiju, S.D. and Magalakwe, G., 2022. Injection driven flow in a dilating or contracting filter chamber with parabolic left inlet velocity. International Journal of Non-Linear Mechanics, 142, p.103986.

Chapter 5

Lekoko, M.L., Oloniiju, S.D. and Magalakwe, G., 2022. Analysis of buoyancy driven flow inside a vertical filter chamber. Chaos, Solitons & Fractals, 161, p.112292.

Chapter 6

Lekoko, M.L., Oloniiju, S.D. and Magalakwe, G., Unsteady analysis of heat transfer and injection-driven flow in a vertical chamber, Under review at Heat and Mass transfer.

Chapter 7

Lekoko, M.L. and Magalakwe, G., Analytical and parametric analysis on MHD mixed convection flow in a porous filter chamber with chemical reaction and heat source/sink, submitted to Indian Journal of Physics.

Chapter 8

Lekoko, M.L. and Magalakwe, G., Closed-form solutions of injection driven flow and heat transfer inside an inclined horizontal filter chamber using Lie group method, under review at Journal of Heat Transfer.

Contents

List of Figures

List of Tables

Table of abbreviations

A table containing a list of abbreviations that will be used throughout text.

MHD	Magnetohydrodynamics
ODE	Ordinary Differential Equations
PDE	Partial Differential Equations

Chapter 1

Introduction

1.1 Literature Review

When processing liquids for human consumption, machinery, or industrial use, there are various important factors to consider. One of those factors is to improve the filtration process by removing particles that could cause injury or reduce the lifespan of machines/systems. The efficiency of filtering methods used to reduce/remove particles deposited in a liquid varies greatly depending on the type of particles, the quality of filter media and the filter design. As a result, it is important to investigate internal flow, heat and mass transfer to obtain research findings that play a critical role towards laying a good foundation that effectively allows designers to simulate the dynamics of the filter before the actual design.

Many industrial firms design a wide range of filters and are always searching for ways to improve their filter designs. Thus, it is of great benefit to such firms to have theoretical-based evidence that helps to achieve an optimal designs. Such filters are utilised in various applications such as clarification of beers, cleaning of gases, radioactive sludge treatment and purification of fluid; for more information about these applications, see [1–5]. Several studies have been carried out to understand better the impact of parameters resulting from flow dynamics and heat transfer during the filtration process [6–10].

The common challenges that different designs experiences are such that the use of materials such as porous medium and magnets to restrict particles from passing through the filter chamber might decrease the outflow (permeates). Also, the bigger pore size and weak magnetic strength allow fluid to move freely inside the chamber. On the other hand, to increase the pore size and use weaker magnetic strength allow unwanted particles to pass through the filter chamber. Therefore, it is vital to have a design that yields optimal balance between the pores and magnetic strength that restricts the particles and allows desirable outflow. Motivated by the studies in the literature and a guest to find an optimal balance between restricting particles while allowing desirable permeate outflow. The current research project seeks to further study the internal flow, heat and mass transfer during

filtration by investigating different filter designs. The research project aims to examine the effects of various parameters from these designs to have an evidence-based improved filter design.

Most realistic mathematical representations of flow, heat and mass transfer inside a filter chamber are modelled by a system of partial differential equations, which might be challenging to solve analytically. However, researchers have developed techniques to obtain numerical or semi-analytical solutions to solve systems that cannot be solved analytically. In numerous applications, it is well understood that ordinary differential equations are more accessible to solve computationally than partial differential equations. Thus, reducing the number of independent variables or, at the very least, reducing partial differential equations to ordinary differential equations is desirable. Researchers [11–17], have used traditional methods, such as the Lie group similarity transformation, to reduce differential equations to their simpler representations. The Lie group technique was used by various researchers to construct the invariant transformations that reduce the PDEs to ODEs which can be solved either numerically, semi-analytically or analytically, such as the works in [18–23]. In most of these studies, the focus was to demonstrate and explain the advantages of using the method to transform a system of equations into a simpler representation. Hence, the Lie group technique is proposed to transform governing equations from filter designs under investigation to lower dimensions without losing the generality of the problem.

Transforming the system of PDEs into a system of ODEs simplifies the system but does not imply that the transformed system can always be solved analytically. Thus semi-analytical methods and numerical techniques are proposed to solve systems representing designs under investigation that cannot be directly integrated. This research project will use the spectral-based quasi-linearisation method. The method is based on a generalised Newton–Raphson's linearisation of the system of non-linear partial differential equations. The linearised system is approximated in terms of the Lagrange polynomials on the Chebyshev–Gauss–Lobatto nodes. Several variations (schemes) of this method have been applied to heat and mass transfer problems in the literature [24–28].

In addition to numerical solutions, the research project uses the perturbation method to find semi-analytical solutions representing the dynamics of flow, heat and mass transfer phenomenon from one of the designs under investigation in this thesis. This ideal analytical method yields an approximation of the solutions since it allows one to use physical parameters affecting the dynamics of the problem under investigation as perturbation quantities when approximating the solutions using a series form. This method will enable one to integrate the equations resulting from equating powers of perturbation quantities analytically, unlike numerical techniques. The number of terms in the series representing the model solutions affects the accuracy of this method due to its series form. The method allows one to choose parameters as perturbation quantities that yield solutions that depend on those parameters. Also, this method linearise coupled system of equations as mentioned in the study by Modise and Magalakwe [29]. For more information, the reader is referred to work by Magalakwe et al. [16].

1.2 Parameters affecting filtering designs

There are useful dimensionless parameters in fluid dynamics to determine the flow and heat transfer characteristics. In this section, we discuss some of the important dimensionless parameters used in this study and their importance.

1.2.1 Permeation Reynolds number

Permeation Reynolds number, R_e, is defined as the ratio of a fluid's inertial to viscous forces. This parameter is defined as positive ($R_e > 0$) for fluid injection, negative ($R_e < 0$) for fluid suction and zero ($R_e = 0$) for no fluid injection or suction.

1.2.2 Wall/chamber dilation rate

When the filter chamber walls expand or contract, there is a change in the filter chamber height and this results in wall dilation rate, α. The wall dilation rate is zero ($\alpha = 0$) when the filter chamber volume stays the same, positive ($\alpha > 0$) when the filter chamber volume expand/increases and negative when the chamber volume contracts/decrease.

1.2.3 Stuart number/Magnetic parameter

The Stuart number, also known as the magnetic interaction parameter, is defined as the ratio of the electromagnetic to inertial forces of the fluid. Stuart number is relevant for the flow of electrically conducting fluids. The effect of this interaction leads to a force called the Lorentz force.

1.2.4 Thermal Grashof number

The Grashof number represents the ratio between the buoyancy force due to spatial variation in the fluid density (caused by temperature difference) to the restraining force due to the fluid's viscosity. Grashof number is a way to quantify the opposing forces.

1.2.5 Prandtl number

The Prandtl number is a ratio of momentum to thermal diffusivities. When the Prandtl number is smaller, that is, $P_r << 1$, the heat diffuses quickly compared to momentum (i.e. thermal diffusivity dominates). On the other hand, with a larger Prandtl number, $P_r >> 1$, the momentum diffusivity dominates. The Prandtl number controls the relative thickness of both momentum and thermal boundary layers.

1.2.6 Radiation parameter

The radiation parameter measures how the fluid emits or absorbs heat energy through electromagnetic waves. Positive radiation values mean that the fluid absorbs heat energy and emits energy for negative radiation values.

1.2.7 Joule heating parameter

The Joule heating parameter is the measure of how the electric current flows through an electrically conducting fluid that transfers electric energy to heat. Therefore, higher values of the Joule heating parameter decrease the transfer of electric energy due to higher resistance.

1.2.8 Internal heat source/sink parameter

The source/sink parameter defines the heat flux between the fluid and the surroundings. This parameter becomes a sink when the system loses energy to the surroundings and becomes a source when the system gains energy from the surrounding. The parameter is positive when it acts as the heat source to the system and negative when it acts as a heat sink.

1.2.9 Permeation parameter

The permeation parameter is the parameter that defines the ability of the fluid to permit through a porous medium. The permeation parameter is higher when fluid passes through the pores faster and lower when the fluid passes through the pores at a slower rate.

1.2.10 Richardson number

The Richardson number is the dimensionless parameter that expresses the ratio of the buoyancy effects to flow shear effects. It represents the importance of natural convection relative to the forced convection. When the Richardson number is less than 0.1, natural convection is negligible, greater than 10 means forced convection is negligible and mixed convection is when the Richards number ranges between 0.1 and 10.

1.2.11 Buoyancy ratio

It embodies the relative contribution of the species' buoyancy force to the thermal buoyancy force.

1.2.12 Schmidt number

The Schmidt number of a fluid is a dimensionless parameter defined as the ratio of momentum diffusivity (kinematic viscosity) and mass diffusivity. It characterises fluid flows with simultaneous momentum and mass diffusion convection processes.

1.3 Aims and Objectives

In this thesis, we describe flow and heat transfer models as well as a flow, heat and mass transfer model inside different filter chambers (designs) and compare these designs to highlight a filter design that performs optimally, thus producing more filtrates during the filtration process. Numerical, semi-analytical or analytical methods are used to obtain

solutions to equations representing filter designs under investigation. The obtained solutions are analysed to investigate how physical parameters arising from each design affect the system's momentum, temperature, concentration, skin friction, heat and mass transfer rate during operation. Also, we give clear advantages or disadvantages of the filters under investigation and compare them to achieve an evidence-based research conclusion that gives the design that yields optimal permeate production. This thesis's main aim is to theoretically investigate internal flow, heat and mass transfer inside different filter designs with the objective of understanding the dynamics of the designs better.

1.4 Thesis outline

This thesis is structured as follows:

- In chapter 2, we briefly introduce Lie's theory for differential equations. In particular, the chapter presents the algorithm to determine the Lie point symmetries of partial differential equations and invariant Lie transformation, which will be used throughout the thesis.

- Chapter 3 uses the multivariate spectral quasilinearisation method to find pressure and heat distribution in a dilating or contracting filter chamber with two outlets. Analyses of thermophysical parameters that drive outflow during the filtration process are provided through the graphs of the numerical solutions of the differential equations.

- In chapter 4, the solutions of the injection-driven flow in a dilating or contracting filter chamber with parabolic left inlet velocity are approximated using the spectral-based paired quasilinearisation technique. The parameters that affect momentum and heat transfer are studied to optimise the system's internal momentum and temperature.

- Chapter 5 uses the spectral quasilinearisation method to approximate the solutions of a buoyancy-driven flow inside a vertical filter chamber. Effects of physical forces that arise from the vertical filter design are investigated to indicate a combination of these parameters that yields the optimal permeate outflow.

- Chapter 6 uses a decoupled spectral-based linearisation technique to approximate the solutions of an unsteady injection-driven flow and heat transfer in a vertical chamber to advance the filtration process. To effectively have buoyancy-driven outflow, which utilises the gravitational force as permeate driving force, the parameters that arise from this design are analysed to have combinations of these parameters, which drive more permeates out of the filter chamber.

- In chapter 7, the perturbation method is used to analytically solve an MHD mixed convection flow in a porous filter chamber with a chemical reaction and heat source/sink. The parametric analysis of parameters leading to optimal outflow, mass and heat transfer is provided in this chapter.

- In chapter 8, closed-form solutions of an injection-driven flow and heat transfer inside an inclined horizontal filter chamber are obtained using the Lie point symmetry method. The obtained solutions are used to analyse the effects of parameters from the process dynamics to find combinations of parameters that yields maximum permeates outflow.

- In chapter 9, a comparison of filters under investigation is made to highlight the optimal design amongst all the designs in this research project.

Chapter 2

Preliminaries

This chapter presents the algorithm to determine the symmetries of PDEs, which will be used throughout this research project.

2.1 Introduction

Mathematical representations of real-life phenomena evolve in space and time, thus leading to partial differential equations. These equations representing real-life phenomena can be complex if not possible to solve analytically due to higher dimensions that differ from one phenomenon to another. The Norwegian mathematician Sophus Lie discovered a way to transform a system of such a higher dimension to a simpler one while preserving the original system's behaviour using Lie symmetry analysis more than a hundred years ago. Lie symmetry analysis provides a group of transforms that maps partial differential equations to ordinary differential equations without changing the dynamics of the phenomenon represented by partial differential equations. Due to the importance of the method (Lie symmetry analysis) to differential equations, several books have been written on this topic, see [23, 30–32] to mention a few. **The results and definitions below are from the books mentioned above, and we will not refer to them again**.

2.2 Local one-parameter Lie group

Let $x = (x^1, ..., x^n)$ be the independent variables with coordinates x^i and $u = (u^1, ..., u^m)$ be the dependent variables with coordinates u^α (n and m finite). Consider a change of the variables x and u involving a real parameter a:

$$T_a : \bar{x^i} = f^i(x, u, a), \ \bar{u^\alpha} = \phi^\alpha(x, u, a), \tag{2.1}$$

where a continuously ranges in value from a neighbourhood $\mathcal{D}' \subset \mathcal{D} \subset \mathbb{R}$ of $a = 0$, and f^i and ϕ^α are differentiable functions.

Definition 2.1. A set G of transformations (2.1) is called a *continuous one-parameter (local) Lie group of transformations* in the space of variables x and u if

(i) For T_a, $T_b \in G$ where $a, b \in \mathcal{D}' \subset \mathcal{D}$ then $T_b\, T_a = T_c \in G$, $c = \phi(a, b) \in \mathcal{D}$ (Closure)

(ii) $T_0 \in G$ if and only if $a = 0$ such that $T_0\, T_a = T_a\, T_0 = T_a$ (Identity)

(iii) For $T_a \in G$, $a \in \mathcal{D}' \subset \mathcal{D}$, $T_a^{-1} = T_{a^{-1}} \in G$, $a^{-1} \in \mathcal{D}$ such that $T_a\, T_{a^{-1}} = T_{a^{-1}}\, T_a = T_0$ (Inverse)

We note that the associativity property follows from (i). The group property (i) can be written as

$$\begin{aligned} \bar{\bar{x}}^i &\equiv f^i(\bar{x}, \bar{u}, b) = f^i(x, u, \phi(a, b)), \\ \bar{\bar{u}}^\alpha &\equiv \phi^\alpha(\bar{x}, \bar{u}, b) = \phi^\alpha(x, u, \phi(a, b)) \end{aligned} \tag{2.2}$$

and the function ϕ is called the *group composition law*. A group parameter a is called *canonical* if $\phi(a, b) = a + b$.

Theorem 2.1. For any $\phi(a, b)$, there exists the canonical parameter $\tilde{a}$ defined by

$$\tilde{a} = \int_0^a \frac{ds}{w(s)}, \text{ where } w(s) = \left.\frac{\partial\, \phi(s, b)}{\partial b}\right|_{b=0}.$$

2.3 Prolongation of point transformations and Group generator

The derivatives of u with respect to x are defined as

$$u_i^\alpha = D_i(u^\alpha), \quad u_{ij}^\alpha = D_j D_i(u_i), \cdots, \tag{2.3}$$

where

$$D_i = \frac{\partial}{\partial x^i} + u_i^\alpha \frac{\partial}{\partial u^\alpha} + u_{ij}^\alpha \frac{\partial}{\partial u_j^\alpha} + \cdots, \quad i = 1, ..., n \tag{2.4}$$

is the operator of total differentiation. The collection of all first derivatives u_i^α is denoted by $u_{(1)}$, i.e.,

$$u_{(1)} = \{u_i^\alpha\} \quad \alpha = 1, ..., m, \quad i = 1, ..., n.$$

Similarly

$$u_{(2)} = \{u_{ij}^\alpha\} \quad \alpha = 1, ..., m, \quad i, j = 1, ..., n$$

and $u_{(3)} = \{u_{ijk}^\alpha\}$ and likewise $u_{(4)}$ etc. Since $u_{ij}^\alpha = u_{ji}^\alpha$, $u_{(2)}$ contains only u_{ij}^α for $i \leq j$. In the same manner $u_{(3)}$ has only terms for $i \leq j \leq k$. There is natural ordering in $u_{(4)}$, $u_{(5)}$ $\cdots$.

In group analysis, all variables $x, u, u_{(1)} \cdots$ are considered functionally independent variables connected only by the differential relations (2.3). Thus the u_s^α are called differential variables [22].

We now consider a pth-order PDE(s), namely

$$E_\alpha(x, u, u_{(1)}, ..., u_{(p)}) = 0. \tag{2.5}$$

Prolonged or extended groups

If $z = (x, u)$, one-parameter group of transformations G is

$$\bar{x}^i = f^i(x, u, a), \quad f^i|_{a=0} = x^i,$$

$$\bar{u}^\alpha = \phi^\alpha(x, u, a), \quad \phi^\alpha|_{a=0} = u^\alpha. \tag{2.6}$$

According to Lie's theory, the construction of the symmetry group G is equivalent to the determination of the corresponding *infinitesimal transformations*:

$$\bar{x}^i \approx x^i + a\,\xi^i(x, u), \quad \bar{u}^\alpha \approx u^\alpha + a\,\eta^\alpha(x, u) \tag{2.7}$$

obtained from (2.1) by expanding the functions f^i and ϕ^α into Taylor series in a about $a = 0$ and also taking into account the initial conditions

$$f^i\big|_{a=0} = x^i, \quad \phi^\alpha|_{a=0} = u^\alpha.$$

Thus, we have

$$\xi^i(x, u) = \left.\frac{\partial f^i}{\partial a}\right|_{a=0}, \quad \eta^\alpha(x, u) = \left.\frac{\partial \phi^\alpha}{\partial a}\right|_{a=0}. \tag{2.8}$$

One can now introduce the *symbol* of the infinitesimal transformations by writing (2.7) as

$$\bar{x^i} \approx (1 + a\,X)x, \quad \bar{u^\alpha} \approx (1 + a\,X)u,$$

where

$$X = \xi^i(x, u)\frac{\partial}{\partial x^i} + \eta^\alpha(x, u)\frac{\partial}{\partial u^\alpha}. \tag{2.9}$$

This differential operator X is known as the infinitesimal operator or generator of the group G. If the group G is admitted by (2.5), we say that X is an *admitted operator* of (2.5) or X is an *infinitesimal symmetry* of equation (2.5).

We now see how the derivatives are transformed.

The D_i transforms as

$$D_i = D_i(f^j)\bar{D}_j, \tag{2.10}$$

where $\bar{D}_j$ is the total differentiations in transformed variables $\bar{x}^i$. So

$$\bar{u}^\alpha_i = \bar{D}_j(u^\alpha), \qquad \bar{u}^\alpha_{ij} = \bar{D}_j(\bar{u}^\alpha_i) = \bar{D}_i(\bar{u}^\alpha_j), \cdots.$$

Now let us apply (2.10) and (2.6)

$$\begin{aligned} D_i(\phi^\alpha) &= D_i(f^j)\bar{D}_j(\bar{u}^\alpha) \\ &= D_i(f^j)\bar{u}^\alpha_j. \end{aligned} \tag{2.11}$$

Thus

$$\left(\frac{\partial f^j}{\partial x^i}+u_i^\beta\frac{\partial f^j}{\partial u^\beta}\right)\bar{u}_j^\alpha=\frac{\partial\phi^\alpha}{\partial x^i}+u_i^\beta\frac{\partial\phi^\alpha}{\partial u^\beta}. \tag{2.12}$$

The quantities $\bar{u}_j^\alpha$ can be represented as functions of $x,u,u_{(i)}$, a for small a, ie., (2.12) is locally invertible:

$$\bar{u}_i^\alpha=\psi_i^\alpha(x,u,u_{(1)},a),\quad \psi^\alpha|_{a=0}=u_i^\alpha. \tag{2.13}$$

The transformations in $x,u,u_{(1)}$ space given by (2.6) and (2.13) form a one-parameter group (one can prove this but we do not consider the proof) called the first prolongation or just extension of the group G and denoted by $G^{[1]}$, the reader is referred to this book [22] for more details.

We let

$$\bar{u}_i^\alpha\approx u_i^\alpha+a\zeta_i^\alpha \tag{2.14}$$

be the infinitesimal transformation of the first derivatives so that the infinitesimal transformation of the group $G^{[1]}$ is (2.7) and (2.14).

Higher-order prolongations of G, viz. $G^{[2]}$, $G^{[3]}$ can be obtained by derivatives of (2.11).

Prolonged generators

Using (2.11) together with (2.7) and (2.14) we get

$$\begin{aligned}
D_i(f^j)(\bar{u}_j^\alpha) &= D_i(\phi^\alpha)\\
D_i(x^j+a\xi^j)(u_j^\alpha+a\zeta_j^\alpha) &= D_i(u^\alpha+a\eta^\alpha)\\
(\delta_i^j+aD_i\xi^j)(u_j^\alpha+a\zeta_j^\alpha) &= u_i^\alpha+aD_i\eta^\alpha\\
u_i^\alpha+a\zeta_i^\alpha+au_j^\alpha D_i\xi^j &= u_i^\alpha+aD_i\eta^\alpha\\
\zeta_i^\alpha &= D_i(\eta^\alpha)-u_j^\alpha D_i(\xi^j),\quad \text{(sum on } j).
\end{aligned} \tag{2.15}$$

This is called the first prolongation formula. Likewise, one can obtain the second prolongation, viz.,

$$\zeta_{ij}^\alpha = D_j(\eta_i^\alpha)-u_{ik}^\alpha D_j(\xi^k),\quad \text{(sum on } k). \tag{2.16}$$

By induction (recursively)

$$\zeta_{i_1,i_2,\ldots,i_p}^\alpha = D_{i_p}(\zeta_{i_1,i_2,\ldots,i_{p-1}}^\alpha)-u_{i_1,i_2,\ldots,i_{p-1}\,j}^\alpha D_{i_p}(\xi^j),\quad \text{(sum on } j). \tag{2.17}$$

The first and higher prolongations of the group G form a group denoted by $G^{[1]},\cdots,G^{[p]}$. The corresponding prolonged generators are

$$\begin{aligned}
X^{[1]} &= X+\zeta_i^\alpha\frac{\partial}{\partial u_i^\alpha}\quad \text{(sum on } i,\alpha),\\
&\cdot\\
&\cdot\\
&\cdot\\
X^{[p]} &= X^{[p-1]}+\zeta_{i_1,\ldots,i_p}^\alpha\frac{\partial}{\partial u_{i_1,\ldots,i_p}^\alpha}\quad p\geq 1,
\end{aligned}$$

where

$$X = \xi^i(x,u)\frac{\partial}{\partial x^i} + \eta^\alpha(x,u)\frac{\partial}{\partial u^\alpha}.$$

2.3.1 Prolongation of (1+1)-dimensional PDE

Consider a second-order PDE

$$E(t,x,u,u_t,u_x,u_{tt},u_{xx},u_{tx}) = 0, \tag{2.18}$$

where t and x are two independent variables and u is a dependent variable. Let

$$X = \tau(t,x,u)\frac{\partial}{\partial t} + \xi(t,x,u)\frac{\partial}{\partial x} + \eta(t,x,u)\frac{\partial}{\partial u}, \tag{2.19}$$

be the infinitesimal generator of the one-parameter group G of transformation (2.1). The *first prolongation* of the operator X is denoted by $X^{[1]}$ and is given by

$$X^{[1]} = X + \zeta_1(t,x,u,u_t,u_x)\frac{\partial}{\partial u_t} + \zeta_2(t,x,u,u_t,u_x)\frac{\partial}{\partial u_x}$$

where

$$\begin{aligned}
\zeta_1 &= D_t(\eta) - u_t D_t(\tau) - u_x D_t(\xi), \\
\zeta_2 &= D_x(\eta) - u_t D_x(\tau) - u_x D_x(\xi)
\end{aligned}$$

and the total derivatives D_t and D_x are given by

$$D_t = \frac{\partial}{\partial t} + u_t\frac{\partial}{\partial u} + u_{tx}\frac{\partial}{\partial u_x} + u_{tt}\frac{\partial}{\partial u_t} + \cdots, \tag{2.20}$$

$$D_x = \frac{\partial}{\partial x} + u_x\frac{\partial}{\partial u} + u_{xx}\frac{\partial}{\partial u_x} + u_{tx}\frac{\partial}{\partial u_t} + \cdots. \tag{2.21}$$

Likewise, the the second prolongation of X is given by

$$X^{[2]} = X + \zeta_1\frac{\partial}{\partial u_t} + \zeta_2\frac{\partial}{\partial u_x} + \zeta_{11}\frac{\partial}{\partial u_{tt}} + \zeta_{12}\frac{\partial}{\partial u_{tx}} + \zeta_{22}\frac{\partial}{\partial u_{xx}}. \tag{2.22}$$

where

$$\begin{aligned}
\zeta_{11} &= D_t(\zeta_1) - u_{tt} D_t(\tau) - u_{tx} D_t(\xi), \\
\zeta_{12} &= D_x(\zeta_1) - u_{tt} D_x(\tau) - u_{tx} D_x(\xi), \\
\zeta_{22} &= D_x(\zeta_2) - u_{tx} D_x(\tau) - u_{xx} D_x(\xi).
\end{aligned}$$

Applying the definitions of D_t and D_x given above, we obtain

$$\begin{aligned}
\zeta_1 &= \eta_t + u_t\eta_u - u_t\tau_t - u_t^2\tau_u - u_x\xi_t - u_tu_x\xi_u. && (2.23)\\
\zeta_2 &= \eta_x + u_x\eta_u - u_t\tau_x - u_tu_x\tau_u - u_x\xi_x - u_x^2\xi_u. && (2.24)\\
\zeta_{11} &= \eta_{tt} + 2u_t\eta_{tu} + u_{tt}\eta_u + (u_t)^2\eta_{uu} - 2u_{tt}\tau_t - u_t\tau_{tt} - 2(u_t)^2\tau_{tu}\\
&\quad -3u_tu_{tt}\tau_u - (u_t)^3\tau_{uu} - 2u_{tx}\xi_t - u_x\xi_{tt} - 2u_tu_x\xi_{tu} - (u_t)^2u_x\xi_{uu}\\
&\quad -(u_xu_{tt} + 2u_tu_{tx})\xi_u. && (2.25)\\
\zeta_{12} &= \eta_{tx} + u_x\eta_{tu} + u_t\eta_{xu} + u_{tx}\eta_u + u_tu_x\eta_{uu} - u_{tx}(\tau_t + \xi_x) - u_t\tau_{tx} - u_{tt}\tau_x\\
&\quad -u_tu_x(\tau_{tu} + \xi_{xu}) - u_t^2\tau_{xu} - (2u_tu_{tx} + u_xu_{tt})\tau_u - (u_t)^2u_x\tau_{uu} - u_x\xi_{tx}\\
&\quad -u_{xx}\xi_t - (u_x)^2\xi_{tu} - (2u_xu_{tx} + u_tu_{xx})\xi_u - u_t(u_x)^2\xi_{uu}. && (2.26)\\
\zeta_{22} &= \eta_{xx} + 2u_x\eta_{xu} + u_{xx}\eta_u + (u_x)^2\eta_{uu} - 2u_{xx}\xi_x - u_x\xi_{xx} - 2(u_x)^2\xi_{xu}\\
&\quad -3u_xu_{xx}\xi_u - (u_x)^3\xi_{uu} - 2u_{tx}\tau_x - u_t\tau_{xx}\\
&\quad -2u_tu_x\tau_{xu} - (u_tu_{xx} + 2u_xu_{tx})\tau_u - u_t(u_x)^2\tau_{uu}. && (2.27)
\end{aligned}$$

2.4 Group admitted by a PDE

Definition 2.2. The vector field

$$X = \xi^i(x,u)\frac{\partial}{\partial x^i} + \eta^\alpha(x,u)\frac{\partial}{\partial u^\alpha}, \tag{2.28}$$

is a *point symmetry* of the pth-order PDE (2.5), if

$$X^{[p]}(E_\alpha) = 0 \tag{2.29}$$

whenever $E_\alpha = 0$. This can also be written as

$$X^{[p]}\, E_\alpha\Big|_{E_\alpha=0} = 0, \tag{2.30}$$

where the symbol $|_{E_\alpha=0}$ means evaluated on the equation $E_\alpha = 0$.

Definition 2.3. Equation (2.29) is called the *determining equation* of (2.5) because it determines all the infinitesimal symmetries of (2.5).

Definition 2.4 (Symmetry group)**.** A one-parameter group G of transformations (2.1) is called a symmetry group of equation (2.5) if (2.5) is form-invariant (has the same form) in the new variables $\bar{x}$ and $\bar{u}$, i.e.,

$$E_\alpha(\bar{x}, \bar{u}, \bar{u_{(1)}}, \cdots, \bar{u_{(p)}}) = 0, \tag{2.31}$$

where the function E_α is the same as in equation (2.5).

2.5 Group invariants

Definition 2.5. A function $F(x,u)$ is called an *invariant of the group of transformation* (2.1) if

$$F(\bar{x},\bar{u}) \equiv F(f^i(x,u,a),\, \phi^\alpha(x,u,a)) = F(x,u), \tag{2.32}$$

identically in x, u and a.

Theorem 2.2 (Infinitesimal criterion of invariance)**.** A necessary and sufficient condition for a function $F(x,u)$ to be an invariant is that

$$X\,F \equiv \xi^i(x,u)\frac{\partial F}{\partial x^i} + \eta^\alpha(x,u)\frac{\partial F}{\partial u^\alpha} = 0\,. \tag{2.33}$$

It follows from the above theorem that every one-parameter group of point transformations (2.1) has $n-1$ functionally independent invariants, which can be taken to be the left-hand side of any first integrals

$$J_1(x,u) = c_1, \cdots, J_{n-1}(x,u) = c_n$$

of the characteristic equations

$$\frac{dx^1}{\xi^1(x,u)} = \cdots = \frac{dx^n}{\xi^n(x,u)} = \frac{du^1}{\eta^1(x,u)} = \cdots = \frac{du^n}{\eta^n(x,u)}.$$

Theorem 2.3. If the infinitesimal transformation (2.7) or its symbol X is given, then the corresponding one-parameter group G is obtained by solving the Lie equations

$$\frac{d\bar{x^i}}{da} = \xi^i(\bar{x},\bar{u}), \quad \frac{d\bar{u^\alpha}}{da} = \eta^\alpha(\bar{x},\bar{u}) \tag{2.34}$$

subject to the initial conditions

$$\bar{x^i}\big|_{a=0} = x, \quad \bar{u^\alpha}\big|_{a=0} = u\,.$$

2.6 Lie algebras

Let us consider two operators X_1 and X_2 defined by

$$X_1 \;=\; \tau_1(t,x,u)\frac{\partial}{\partial t} + \xi_1(t,x,u)\frac{\partial}{\partial x} + \eta_1(t,x,u)\frac{\partial}{\partial u},$$

and

$$X_2 \;=\; \tau_2(t,x,u)\frac{\partial}{\partial t} + \xi_2(t,x,u)\frac{\partial}{\partial x} + \eta_2(t,x,u)\frac{\partial}{\partial u}.$$

Definition 2.6 (Commutator)**.** The *commutator* of X_1 and X_2, written as $[X_1,X_2]$, is defined by $[X_1,X_2] = X_1(X_2) - X_2(X_1)$.

Definition 2.7 (Lie algebra)**.** A Lie algebra is a vector space L of operators with the following property : For all $X_1, X_2 \in L$, the commutator $[X_1,X_2] \in L$.

The dimension of a Lie algebra is the dimension of the vector space L.

Theorem 2.4. The set of all solutions of any determining equation forms a Lie algebra.

2.7 Conclusion

This chapter gave some basic definitions and results of the Lie symmetry analysis of PDEs. These included the algorithm in determining the Lie point symmetries.

Chapter 3

Analysis of pressure and heat distribution in a dilating or contracting filter chamber with two outlets using multivariate spectral quasilinearization method

The development of efficient filters is an essential part of industrial machinery design, specifically to increase the lifespan of a machine. In the filter chamber design considered in this chapter, magnetic material is placed along the horizontal surface of the filter chamber. The inside of the filter chamber is layered with porous material to restrict the outflow of unwanted particles. This chapter aims to investigate the flow, pressure and heat distribution in a dilating or contracting filter chamber with two outlets driven by injection through a permeable surface. The proposed model of the fluid dynamics within the filter chamber follows the conservation equations in the form of partial differential equations. The model equations are further reduced to a steady case through Lie's symmetry group of transformation. They are then solved using a multivariate spectral based quasilinearization method on the Chebyshev-Gauss-Lobatto nodes. Insights and analyses of the thermophysical parameters that drive optimal outflow during filtration process are provided through the graphs of the numerical solutions of the differential equations. We find, among other results, that expansion of the filter chamber leads to an overall decrease in internal pressure and an increase in heat distribution inside the filter chamber. The results also show that shrinking the filter chamber increases the internal momentum inside the filter, which leads to more outflow of filtrates.

NOMENCLATURE

c_p - Specific heat, $J/kg\,K$
g - Gravitational acceleration, m/s^2
$\dot{h}$ - Wall dilation rate, m/s
H_0 - Magnetic field strength N/mA
k - permeability of porous medium m^2
$\bar{P}$ - Pressure, Nm^{-2}
s - Kinematic viscosity, m^2/s
V_w - Axial velocity at the wall, m/s
$\bar{u}$ - Axial velocity, m/s
$\bar{v}$ - Normal velocity, m/s
t - Time, s
$\bar{x}$ - Axial coordinate, m
$\bar{y}$ - Normal coordinate, m
T - Temperature of the fluid, K
T_w - Temperature at wall, K
T_h - Fluid temperature at a certain height, K
t - Dimensionless time
x - Dimensionless axial coordinate
y - Dimensionless normal coordinate
u - Dimensionless axial velocity
v - Dimensionless normal velocity
P - Dimensionless pressure
G_r - Grashoff number
N - Stuart number
R_e - Permeation Reynolds number
R - Dimensionless porosity variable
J - Dimensionless Joule heating parameter
P_r - Prandtl number

Greek symbols

ρ - Density, kg/m^3
$\bar{\Psi}$ - Stream function, m^2/s
σ - Electrical conductivity of fluid, S/m
μ - Magnetic permeability, H/m
Ψ - Dimensionless stream function
α - Dimensionless wall dilation rate
ϕ - Porosity
θ - Dimensionless temperature function
λ - Thermal diffusion
β - Thermal expansion

Subscripts

w - Wall condition
h - Chamber height

3.1 Introduction

There are numerous essential aspects to consider when treating liquids for human, machinery, and industrial usage. One element is to improve the filtering process by eliminating particles that might cause injury or shorten the lifespan of machines/systems. The efficiency of filtering methods in reducing/removing particles deposited in a liquid varies significantly on the kind of particles and the type and quality of the filter media or system. As a result, for engineers to create efficient filters, it is preferable to develop a mathematical model that predicts the dynamics of the filter and helps to understand the effect of the system parameters.

Studies have been conducted to understand better the impact of factors derived from flow dynamics through a porous medium in filtering applications. Several analytical, approximate analytical and numerical approaches have been utilized to solve the governing nonlinear equations to predict and determine the actual flow behaviour. Fallah et al. [6] created a mass balance particle transport equation that takes filtering into account. The authors gave the steady-state transport equation and the solution for particle suspension flow with a constant filter coefficient.

Chellam and Wiesner [7] investigated a single-phase slip flow across permeable porous media. The authors in [7] used the finite difference methods to solve the momentum transfer problem numerically. The results show that the variation from an average flow was minimal enough to ignore the effects of walls. They also reported that fluid slip reduces the impact of boundaries even further, suggesting that viscous shear pressure is limited to smaller areas. Zuo-jin [8] investigated a model of non-Newtonian fluid filtration characteristics in a porous medium with the pressure gradient expressed in terms of filtration velocity. The cross-diagonal decomposition ZG technique was used to solve the governing equations defining the flow dynamics. The analysis shows that in the event of a specified production rate, the power index substantially influences the pressure distribution in the near-wall region.

Uchida and Aoki [9] investigated the transfer of biological fluids through expanding or contracting channels. The authors computed the exact solution of the Navier-Stokes equation for unsteady flow in a semi-infinite contracting or expanding circular conduit. When the pipe dilates, the study reported that fluid flow next to the wall is significantly delayed and reverses at Reynolds numbers over a threshold range. The studies [10, 33] examined the flow of fluid through an expanding channel with porous walls using numerical and analytical methods. They further investigated the effect of permeability and expansion ratio on both the velocity and pressure distribution. Using the Liouville-Green transformation, Jankowski and Majdalani [34] found an analytical solution for laminar flow in a porous channel with high wall suction and a weakly oscillatory pressure. The study shows that when suction is increased or viscosity is reduced, the acoustic boundary layer declines, similar to the Stokes layer over rigid walls.

Zhou and Majdalani [35] used the finite difference approach and asymptotic methodology to analyze the mean flow for slab rocket motors for small perturbations parameters. It was observed that the accuracy of the analytical solution diminishes for small Reynolds number and large wall regression ratio. Also, it was found that increasing the Reynolds number reverses the flow speed and increases energy consumption in the flow. Majdalani and Zhou [36] conducted a comparable investigation for medium to large injection and suction driven through the channel flow with expanding or contracting walls. The authors used perturbations in the crossflow Reynolds number and solved the equations using asymptotical and numerical methods. The results found that for non-expanding channels, the suction profile approaches a linear shape. Ali et al. [37] studied the heat and mass transfer in a nanofluid flowing in a channel with contracting/expanding walls. The authors found the analytical solutions using the homotopy analysis method and compared their results with numerical ones to ensure accuracy. Also, it was found that velocity at the centre of the channel is higher when the wall expands than when it contracts.

Using the homotopy perturbation method, Akinshilo [38] studied the flow and heat transfer in a nanofluid conveyed through an expanding or contracting porous channel under a uniform magnetic field. Their finding indicates that increasing the Hartmann parameter increases the overall wall drag and the Nusselt number. Robinson [39] conducted a numerical study to confirm the existence of multiple solutions for laminar incompressible steady flow in a parallel plate porous channel with uniform suction at both walls.

Zaturska et al. [40] conducted a study on the theoretical treatment of the flow of a viscous incompressible fluid that is driven along a channel by steady uniform suction through porous parallel rigid walls. Studies [41, 42] reported multiple solutions to the problem of laminar flow through a permeable channel for both injection or suction. Majdalani et al. [43] studied two-dimensional viscous flow between slowly expanding or contracting obstacles with low permeability using the traditional perturbation technique. Their findings found that when the rate of contraction is increased and either the rate of expansion or permeation is lowered, the pressure drop along the plane of symmetry rises.

Mekheimer and Abo-Elkhair [44] investigated the natural flow in expanding or contracting blood vessels using Lie group analysis and perturbation method to obtain analytical solutions. The authors found that for ample volume space, the average pressure decreases, while for less space, the pressure variation increases. Dinarvand et al. [45] used homotopy analysis and perturbation methods to solve Berman's model of two-dimensional viscous flow in porous channels with wall suction or injection. They concluded that the homotopy perturbation method solution is invalid for large values of the Reynolds number, a flaw previously identified in other perturbation approaches.

The current chapter extends the work done in Magalakwe et al. [16] by investigating the effect of the pressure and the temperature variation during the filtration process in a filter chamber with two outlets to optimize outflow. This chapter aims to redesign the filter and give scientific evidence of the flow, pressure variation, and heat distribution that lead

to optimal filtration of the modified filter design. Closed-form solutions with a significant number of terms and conditional solutions can be too complicated for engineers to interpret in reality [46]. It is for this reason, we have chosen to use a spectral based quasilinearization method. The method is premised on a generalized Newton-Raphson's linearization of the system of nonlinear partial differential equations. The linearized system is approximated in terms of the Lagrange polynomials on the Chebyshev-Gauss-Lobatto nodes. Several variations of this method have been applied to heat and mass transfer problems in the literature. One of which is the study by Majeed et al. [47]. A Chebyshev spectral Newton iterative method was used to study the effects of partial surface slip and heat flux on heat transfer dynamics in a non-Newtonian Casson fluid moving due to a stretching cylinder. The equations describing the heat transfer and hydromagnetic Hiemenz flow of micropolar fluid streaming over an impermeable nonlinear dilating/contracting sheet were discretized using a Chebyshev based Newton iterative scheme in the study by Mahmood et al. [48]. Ghaffari et al. [49] used a spectral-based iterative technique to analyze the dynamics of a non-orthogonal time-dependent Hiemenz flow of the Walter B fluid moving towards a non-uniformly heated surface. Additional studies in which spectral-based linearization methods have been applied to understand the dynamics of heat and mass transfer problems include, but are not limited to, studies such as [24–28]. In each of these studies, the technique was reported to be accurate.

3.2 Mathematical Model

We consider an electrically conducting viscous incompressible fluid flow inside a filter channel bounded by two weak permeable surfaces, which allows fluid injection through the walls with constant velocity V_w perpendicular to the surface. The chamber is opened on both sides, which serve as outlets for the liquid outflow. The surfaces are maintained at constant temperature T_w to lower fluid density, making particles move faster, increasing the fluid kinetic energy and causing fluid flow inside the channel. To remove unwanted particles, the design of the filter is such that magnets, porous surfaces and medium are integrated into the system to restrict the outflow of unwanted particles, thus leading to the effect of the following forces on the system:

- From Darcy's law, the surface force due to porosity is given by

$$\mathbf{F^1} = F_x^1\mathbf{i} + F_y^1\mathbf{j} = -\frac{s\phi}{k}u\mathbf{i} - \frac{s\phi}{k}v\mathbf{j}.$$

- From Lorenz's law of electromagnetism and Archimedes' principle, the body forces are

$$\mathbf{F^2} = F_x^2\mathbf{i} = -\sigma\mu^2 H_0^2 u\mathbf{i}, \quad \text{and} \quad \mathbf{F^3} = F_y^3\mathbf{j} = g\rho\beta(T - T_w)\mathbf{j},$$

  respectively. The work done by $\mathbf{F^2}$ result in the Joule heating, which is the only energy source term according to the filter design in Magalakwe et al. [16]. For a more detailed derivation of these forces, the reader is referred to Tenreiro et al. [50].

The continuity, momentum and energy conservation equations for the filtration model are [16, 37, 50]:

$$\frac{\partial \bar{u}}{\partial \bar{x}} + \frac{\partial \bar{v}}{\partial \bar{y}} = 0, \tag{3.1}$$

$$\frac{\partial \bar{u}}{\partial t} + \bar{u}\frac{\partial \bar{u}}{\partial \bar{x}} + \bar{v}\frac{\partial \bar{u}}{\partial \bar{y}} + \frac{1}{\rho}\frac{\partial \bar{P}}{\partial \bar{x}} - s\left[\frac{\partial^2 \bar{u}}{\partial \bar{x}^2} + \frac{\partial^2 \bar{u}}{\partial \bar{y}^2}\right] + \frac{s\phi}{k}\bar{u} + \frac{\sigma\mu^2 H_0^2}{\rho}\bar{u} = 0, \tag{3.2}$$

$$\frac{\partial \bar{v}}{\partial t} + \bar{u}\frac{\partial \bar{v}}{\partial \bar{x}} + \bar{v}\frac{\partial \bar{v}}{\partial \bar{y}} + \frac{1}{\rho}\frac{\partial \bar{P}}{\partial \bar{y}} - s\left[\frac{\partial^2 \bar{v}}{\partial \bar{x}^2} + \frac{\partial^2 \bar{v}}{\partial \bar{y}^2}\right] + \frac{s\phi}{k}\bar{v} - g\beta(T - T_w) = 0, \tag{3.3}$$

$$\frac{\partial T}{\partial t} + \bar{u}\frac{\partial T}{\partial \bar{x}} + \bar{v}\frac{\partial T}{\partial \bar{y}} - \lambda\left[\frac{\partial^2 T}{\partial \bar{x}^2} + \frac{\partial^2 T}{\partial \bar{y}^2}\right] - \frac{\sigma\mu^2 H_0^2}{\rho c_p}\bar{u}^2 = 0. \tag{3.4}$$

Here, $\bar{u}$ and $\bar{v}$ are respectively the axial and normal components of the fluid's velocity, T is the temperature, ρ is the density of the fluid, $\bar{P}$ is the pressure distribution in the chamber, s is the kinematic viscosity of the liquid, g is the gravitational acceleration, β is thermal expansion, λ is the thermal diffusivity, t is time, ϕ is the porosity, k is the permeability of the porous medium, σ is the electrical conductivity of the fluid, μ is magnetic permeability, H_0 is the magnetic field strength, and c_p is the specific heat.

The boundary conditions are:

$$\begin{aligned}
&\text{(i)} && \bar{u}(\bar{x}, h(t), t) = 0, \quad \bar{v}(\bar{x}, h(t), t) = -V_w, \quad T(\bar{x}, h(t), t) = T_w, \\
&\text{(ii)} && \frac{\partial \bar{u}(\bar{x}, 0, t)}{\partial \bar{y}} = 0, \quad \bar{v}(\bar{x}, 0, t) = 0, \quad \frac{\partial T(\bar{x}, 0, t)}{\partial \bar{y}} = 0, \\
&\text{(iii)} && \frac{\partial \bar{u}(0, \bar{y}, t)}{\partial \bar{x}} = 0.
\end{aligned} \tag{3.5}$$

We define the pressure Poisson equation by applying the continuity equation (3.1) and summing the derivative of Equation (3.2) with respect to x and the derivative of Equation (3.3) with respect to y, which yields:

$$\left[\frac{\partial^2 \bar{P}}{\partial x^2} + \frac{\partial^2 \bar{P}}{\partial y^2}\right] - 2\rho\left[\frac{\partial \bar{u}}{\partial x}\frac{\partial \bar{v}}{\partial y} - \frac{\partial \bar{u}}{\partial y}\frac{\partial \bar{v}}{\partial x}\right] + \sigma\mu^2 H_0^2\frac{\partial \bar{u}}{\partial x} - g\beta\rho\frac{\partial T}{\partial y} = 0. \tag{3.6}$$

The above equation (3.6) is solved subject to the following boundary conditions:

$$\begin{aligned}
&\text{(i)} && \bar{P}(\bar{x}, h(t), t) = P_w, \\
&\text{(ii)} && \frac{\partial \bar{P}(\bar{x}, 0, t)}{\partial \bar{y}} = 0, \\
&\text{(iii)} && \bar{P}(0, \bar{y}, t) = 0.
\end{aligned} \tag{3.7}$$

We introduce the following non-dimensional quantities given below

$$
\begin{aligned}
&u=\frac{\bar{u}}{V_w}, \quad v=\frac{\bar{v}}{V_w}, \quad x=\frac{\bar{x}}{h(t)}, \quad y=\frac{\bar{y}}{h(t)}, \quad \Psi=\frac{\bar{\Psi}}{hV_w}, \quad P=\frac{\bar{P}}{\rho V_w^2}, \quad R_e=\frac{hV_w}{s},\\
&\bar{t}=\frac{tV_w}{h}, \quad \alpha=\frac{h\dot{h}}{s}, \quad N=\frac{\sigma h\mu^2H^2}{\rho V_w}, \quad \frac{1}{R}=\frac{s\phi h}{kV_w}, \quad G_r=\frac{g\beta h^3(T_w-T_h)}{s^2},\\
&\theta=\frac{T-T_h}{T_w-T_h}, \quad J=\frac{\sigma H_0^2hV_w}{\rho c_p(T_w-T_h)}, \quad P_r=\frac{s}{\lambda},
\end{aligned}
\tag{3.8}
$$

which after being substituted into Equations (3.2) to (3.4) and (3.6) yield the following dimensionless system:

$$
\frac{\partial u}{\partial t}+u\frac{\partial u}{\partial x}+v\frac{\partial u}{\partial y}+\frac{\partial P}{\partial x}-{R_e}^{-1}\left[\alpha y\frac{\partial u}{\partial y}+\frac{\partial^2u}{\partial x^2}+\frac{\partial^2u}{\partial y^2}\right]+R^{-1}u+Nu=0, \tag{3.9}
$$

$$
\frac{\partial v}{\partial t}+u\frac{\partial v}{\partial x}+v\frac{\partial v}{\partial y}+\frac{\partial P}{\partial y}-{R_e}^{-1}\left[\alpha y\frac{\partial v}{\partial y}+\frac{\partial^2v}{\partial x^2}+\frac{\partial^2v}{\partial y^2}\right]+R^{-1}v-G_r\theta=0, \tag{3.10}
$$

$$
\frac{\partial^2P}{\partial x^2}+\frac{\partial^2P}{\partial y^2}-2\left[\frac{\partial u}{\partial x}\frac{\partial v}{\partial y}-\frac{\partial u}{\partial y}\frac{\partial v}{\partial x}\right]+N\frac{\partial u}{\partial x}-\frac{G_r}{R_e^2}\frac{\partial\theta}{\partial y}=0, \tag{3.11}
$$

$$
\frac{\partial\theta}{\partial t}+u\frac{\partial\theta}{\partial x}+v\frac{\partial\theta}{\partial y}-P_r^{-1}R_e^{-1}\left[\frac{\partial^2\theta}{\partial x^2}+\frac{\partial^2\theta}{\partial y^2}\right]-J\bar{u}^2=0. \tag{3.12}
$$

Similarly, the boundary conditions (3.5) and (3.7) become

$$
\begin{aligned}
&\text{(i)} \quad u(x,1,t)=0, \quad v(x,1,t)=-1, \quad P(x,1,t)=1, \quad \theta(x,1,t)=1,\\
&\text{(ii)} \quad \frac{\partial u(x,0,t)}{\partial y}=0, \quad v(x,0,t)=0, \quad \frac{\partial P(x,0,t)}{\partial y}=0, \quad \frac{\partial\theta(x,0,t)}{\partial y}=0,\\
&\text{(iii)} \quad \frac{\partial u(x,y,t)}{\partial x}=0, \quad P=0, \quad \text{at } x=0.
\end{aligned}
\tag{3.13}
$$

3.2.1 Lie group analysis

With the help of Maple, we found that the dimensionless eqs. (3.9) to (3.12) admit the following six Lie point symmetries:

$$
X_1=\frac{\partial}{\partial t}, \quad X_2=\frac{\partial}{\partial x}, \quad X_3=\frac{\partial}{\partial\theta}+yG_r\frac{\partial}{\partial P}, \quad X_4=F_2(t)\frac{\partial}{\partial P}.
$$

Lie symmetries X_1 and X_2 are the only generators that leave the system and the boundary conditions invariant. It follows from the translation symmetry, X_1, that the system of eqs. (3.9) to (3.12) reduces to the following steady state system of equations:

$$u\frac{\partial u}{\partial x}+v\frac{\partial u}{\partial y}+\frac{\partial P}{\partial x}-{R_e}^{-1}\left[\alpha y\frac{\partial u}{\partial y}+\frac{\partial^2 u}{\partial x^2}+\frac{\partial^2 u}{\partial y^2}\right]+R^{-1}u+Nu=0, \tag{3.14a}$$

$$u\frac{\partial v}{\partial x}+v\frac{\partial v}{\partial y}+\frac{\partial P}{\partial y}-{R_e}^{-1}\left[\alpha y\frac{\partial v}{\partial y}+\frac{\partial^2 v}{\partial x^2}+\frac{\partial^2 v}{\partial y^2}\right]+R^{-1}v-G_r\theta=0, \tag{3.14b}$$

$$\frac{\partial^2 P}{\partial x^2}+\frac{\partial^2 P}{\partial y^2}-2\left[\frac{\partial u}{\partial x}\frac{\partial v}{\partial y}-\frac{\partial u}{\partial y}\frac{\partial v}{\partial x}\right]+N\frac{\partial u}{\partial x}-\frac{G_r}{R_e^2}\frac{\partial \theta}{\partial y}=0, \tag{3.14c}$$

$$u\frac{\partial \theta}{\partial x}+v\frac{\partial \theta}{\partial y}-P_r^{-1}R_e^{-1}\left[\frac{\partial^2 \theta}{\partial x^2}+\frac{\partial^2 \theta}{\partial y^2}\right]-Ju^2=0. \tag{3.14d}$$

Similarly, boundary conditions (3.13) become

$$\begin{aligned}
&\text{(i)} \quad u(x,1)=0, \quad v(x,1)=-1, \quad P(x,1)=1, \quad \theta(x,1)=1,\\
&\text{(ii)} \quad \frac{\partial u(x,0)}{\partial y}=0, \quad v(x,0)=0, \quad \frac{\partial P(x,0)}{\partial y}=0 \quad \frac{\partial \theta(x,0)}{\partial y}=0,\\
&\text{(iii)} \quad \frac{\partial u(0,y)}{\partial x}=0, \quad P(0,y)=0.
\end{aligned} \tag{3.15}$$

3.3 Method of Solution

We use a spectral-based iterative method to discretize the partial differential equations describing the internal dynamics of fluid flow inside the filter chamber. The general idea is, first, to linearize the system of differential equations. In this section, we use the method proposed by Bellman and Kalaba [51] to linearize the system starting with a reasonable initial guess of the solutions, which is then used to solve the linearized system until the solutions converge. The grid points are defined as the Chebyshev-Gauss-Lobatto points:

$$\tilde{x}_i|_{i=0}^{N_x}=\cos\left(\frac{i\pi}{N_x}\right); \quad \tilde{x}(x)=\frac{2}{L}\left[x-\frac{L}{2}\right]; \quad x\in[0,L], \tag{3.16a}$$

$$\tilde{y}_j|_{j=0}^{N_y}=\cos\left(\frac{y\pi}{N_y}\right); \quad \tilde{y}(y)=2\left[y-\frac{1}{2}\right]; \; y\in[0,1], \tag{3.16b}$$

where N_x and N_y represent the number of grid points in x and y respectively. The next step is to assume that the solutions are in the form of the Lagrange interpolating polynomials, which in general, for a function, $\vartheta(x,y)$, is written in the form:

$$\vartheta(x,y)\approx\Theta(x,y)=\sum_{p=0}^{N_x}\sum_{q=0}^{N_y}\Theta(x_p,y_q)L_p(x)L_q(y), \tag{3.17}$$

where $L_p(x)$ are the Lagrange polynomials:

$$L_p(x) = \prod_{\substack{p=0 \\ p\neq i}}^{N_x} \frac{x - x_p}{x_i - x_p}; \quad \text{with} \quad L_p(x_i) = \delta_{pi} = \begin{cases} 1 & p = i \\ 0 & p \neq i. \end{cases} \tag{3.18}$$

Similarly, $L_q(y)$ is defined as:

$$L_q(y) = \prod_{\substack{q=0 \\ q\neq j}}^{N_y} \frac{y - y_q}{y_j - y_q}; \quad \text{with} \quad L_q(y_j) = \delta_{qj} = \begin{cases} 1 & q = j \\ 0 & q \neq j. \end{cases} \tag{3.19}$$

The approximation of the partial derivative of $\vartheta(x, y)$ with respect to x is defined at the collocation points $(\tilde{x}_i, \tilde{y}_j)$ as

$$\frac{\partial \vartheta}{\partial x}(\tilde{x}_i, \tilde{y}_j) \approx \sum_{p=0}^{N_x} \sum_{q=0}^{N_y} \Theta(x, y) \frac{dL_p}{dx}(\tilde{x}_i) L_q(\tilde{y}_j) = \sum_{p=0}^{N_x} \Theta(x_p, y_j) \frac{dL_p}{dx}(\tilde{x}_i) = \overset{x}{\mathbf{D}} \boldsymbol{\Theta}_j = \frac{2}{L} \overset{\tilde{x}}{\mathbf{D}} \boldsymbol{\Theta}_j;$$
$$j = 0, 1, \ldots, N_y, \tag{3.20}$$

where $\overset{\tilde{x}}{\mathbf{D}} = \frac{L}{2} \overset{x}{\mathbf{D}}$ is the standard Chebyshev differentiation matrix of size $(N_x + 1)$ by $(N_x + 1)$ [see [27, 52]]. The factor $\frac{L}{2}$ comes from transformation of the truncated semi-infinite physical domain of the model to the computational domain. The vector $\boldsymbol{\Theta}_j$ is defined as

$$\boldsymbol{\Theta}_j = [\vartheta(x_0, y_j), \vartheta(x_1, y_j), \ldots, \vartheta(x_{N_x}, y_j)]'; \; j = 0, \ldots, N_y. \tag{3.21}$$

Here, $(\prime)$ denotes the transpose of the matrix. Higher order derivatives are obtained by matrix multiplication or by taking corresponding power of the differentiation matrix. In similar manner, the approximation of the partial derivatives with respect to y is defined as

$$\frac{\partial \vartheta}{\partial y}(\tilde{x}_i, \tilde{y}_j) = \sum_{q=0}^{N_y} \Theta(x_i, y_q) \frac{dL_q}{dy}(\tilde{y}_j) = \sum_{q=0}^{N_y} \overset{y}{\mathbf{D}}_{j,q} \boldsymbol{\Theta}_q = \sum_{q=0}^{N_y} 2\overset{\tilde{y}}{\mathbf{D}}_{j,q} \boldsymbol{\Theta}_q. \tag{3.22}$$

In Equation (3.22), $\overset{\tilde{y}}{\mathbf{D}}_{j,q}$ are entries of the standard Chebyshev differentiation matrix of size $(N_y + 1)$ by $(N_y + 1)$.

To solve Equation (3.14), we first linearize the system using the quasilinearization method. The linearization method is based on the generalization of the Newton–Raphson method to

differential equations. The linearization technique is constructed by taking the linear terms of the Taylor expansion about an initial guess of the solutions of the differential equations so that the difference in the solutions between two successive iterations is assumed to be small. Therefore, using the quasilinearization method, and for two consecutive iterations (s) and $(s+1)$, we have the following system of linearized equations

$$-R_e^{-1}u_{xx}^{s+1} + a_{u_x}^s u_x^{s+1} + a_u^s u^{s+1} - R_e^{-1}u_{yy}^{s+1} + a_{u_y}^s u_y^{s+1} + a_v^s v^{s+1} + P_x^{s+1} = R_u^s, \quad (3.23a)$$

$$b_u^s u^{s+1} - R_e^{-1}v_{xx}^{s+1} + b_{v_x}^s v_x^{s+1} + b_v^s v^{s+1} - R_e^{-1}v_{yy}^{s+1} + b_{v_y}^s v_y^{s+1} + P_y^{s+1} - G_r\theta^{s+1} = R_v^s, \quad (3.23b)$$

$$c_{u_x}^s u_x^{s+1} + c_{u_y}^s u_y^{s+1} + c_{v_x}^s v_x^{s+1} + c_{v_y}^s v_y^{s+1} + P_{xx}^{s+1} + P_{yy}^{s+1} - G_r R_e^{-2}\theta_y^{s+1} = R_P^s, \quad (3.23c)$$

$$d_u^s u^{s+1} + d_v^s v^{s+1} - P_r^{-1}R_e^{-1}\theta_{xx}^{s+1} + d_{\theta_x}^s \theta_x^{s+1} - P_r^{-1}R_e^{-1}\theta_{yy}^{s+1} + d_{\theta_y}^s \theta_y^{s+1} = R_\theta^s, \quad (3.23d)$$

where

$$\begin{aligned}
&a_{u_x}^s = u^s, \quad a_u^s = u_x^s + R^{-1} + N, \quad a_{u_y}^s = v^s - \alpha y R_e^{-1}, \quad a_v^s = u_y^s,\\
&b_u^s = v_x^s, \quad b_{v_x}^s = u^s, \quad b_v^s = v_y^s + R^{-1}, \quad b_{v_y}^s = v^s - \alpha y R_e^{-1},\\
&c_{u_x}^s = 2v_y^s + N, \quad c_{u_y}^s = -2v_x^s, \quad c_{v_x}^s = -2u_y^s, \quad c_{v_y}^s = 2u_x^s,\\
&d_u^s = \theta_x^s + 2Ju^s, \quad d_v^s = \theta_y^s, \quad d_{\theta_x}^s = u^s, \quad d_{\theta_y}^s = v^s,
\end{aligned}$$

and

$$\begin{aligned}
R_u^s &= u^s u_x^s + v^s u_y^s, \qquad & R_v^s &= v^s v_y^s + u^s v_x^s,\\
R_P^s &= 2u_x^s v_y^s - 2v_x^s u_y^s, \qquad & R_\theta^s &= u^s\theta_x^s + v^s\theta_y^s + Ju^{2s}.
\end{aligned}$$

The system of linearized equations (3.23) are approximated on the collocation points defined in Equation (3.16) and in terms of the Lagrange interpolating polynomials so that, we have

$$\left[-\frac{1}{R_e}\overset{x}{\mathbf{D}}^2+\mathbf{a}^{\mathbf{s}}_{\mathbf{u_x}}\overset{x}{\mathbf{D}}+\mathbf{a}^{\mathbf{s}}_{\mathbf{u}}\mathbf{I}\right]\mathbf{U}_j^{s+1}-\sum_{q=0}^{N_y}\left[\frac{1}{R_e}\overset{y}{\mathbf{D}}^2-\mathbf{a}^{\mathbf{s}}_{\mathbf{u_y}}\overset{y}{\mathbf{D}}\right]\mathbf{U}_q^{s+1}+\left[\mathbf{a}^{\mathbf{s}}_{\mathbf{v}}\mathbf{I}\right]\mathbf{V}_j^{s+1}+\left[\overset{x}{\mathbf{D}}\right]\mathbf{P}_j^{s+1}=\mathbf{R}_u^s, \tag{3.24a}$$

$$\left[\mathbf{b}^{\mathbf{s}}_{\mathbf{u}}\mathbf{I}\right]\mathbf{U}_j^{s+1}-\left[\frac{1}{R_e}\overset{x}{\mathbf{D}}^2-\mathbf{b}^{\mathbf{s}}_{\mathbf{v_x}}\overset{x}{\mathbf{D}}-\mathbf{b}^{\mathbf{s}}_{\mathbf{v}}\mathbf{I}\right]\mathbf{V}_j^{s+1}-\sum_{q=0}^{N_y}\left[\frac{1}{R_e}\overset{y}{\mathbf{D}}^2-\mathbf{b}^{\mathbf{s}}_{\mathbf{v_y}}\overset{y}{\mathbf{D}}\right]\mathbf{V}_q^{s+1}$$
$$+\sum_{q=0}^{N_y}\left[\overset{y}{\mathbf{D}}\right]\mathbf{P}_q^{s+1}-\left[G_r\mathbf{I}\right]\mathbf{\Theta}_j^{s+1}=\mathbf{R}_v^s, \tag{3.24b}$$

$$\left[\mathbf{c}^{\mathbf{s}}_{\mathbf{u_x}}\overset{x}{\mathbf{D}}\right]\mathbf{U}_j^{s+1}+\sum_{q=0}^{N_y}\left[\mathbf{c}^{\mathbf{s}}_{\mathbf{u_y}}\overset{y}{\mathbf{D}}\right]\mathbf{U}_q^{s+1}+\left[\mathbf{c}^{\mathbf{s}}_{\mathbf{v_x}}\overset{x}{\mathbf{D}}\right]\mathbf{V}_j^{s+1}+\sum_{q=0}^{N_y}\left[\mathbf{c}^{\mathbf{s}}_{\mathbf{v_y}}\overset{y}{\mathbf{D}}\right]\mathbf{V}_q^{s+1}+\left[\overset{x}{\mathbf{D}}^2\right]\mathbf{P}_j^{s+1}$$
$$+\sum_{q=0}^{N_y}\left[\overset{y}{\mathbf{D}}^2\right]\mathbf{P}_q^{s+1}-\sum_{q=0}^{N_y}\left[\frac{G_r}{R_e^2}\overset{y}{\mathbf{D}}\right]\mathbf{\Theta}_q^{s+1}=\mathbf{R}_P^s, \tag{3.24c}$$

$$\left[\mathbf{d}^{\mathbf{s}}_{\mathbf{u}}\mathbf{I}\right]\mathbf{U}_j^{s+1}+\left[\mathbf{d}^{\mathbf{s}}_{\mathbf{v}}\mathbf{I}\right]\mathbf{V}_j^{s+1}-\left[\frac{1}{P_rR_e}\overset{x}{\mathbf{D}}^2-\mathbf{d}^{\mathbf{s}}_{\theta_\mathbf{x}}\overset{x}{\mathbf{D}}\right]\mathbf{\Theta}_j^{s+1}-\sum_{q=0}^{N_y}\left[\frac{1}{P_rR_e}\overset{y}{\mathbf{D}}^2-\mathbf{d}^{\mathbf{s}}_{\theta_\mathbf{y}}\overset{y}{\mathbf{D}}\right]\mathbf{\Theta}_q^{s+1}=\mathbf{R}_\theta^s, \tag{3.24d}$$

where $j=0,1,2,\ldots,N_y$ and $\mathbf{I}$ is the identity matrix of size (N_x+1) by (N_x+1).

The axial and normal components velocity, pressure distribution and temperature in the filter chamber were obtained using the numerical scheme described in Equation (3.24). Unless otherwise stated in the figures or discussion in 3.4, we used the following parameter values to compute the numerical solutions: $P_r=0.6, R_e=2, \alpha=1, G_r=0.6, J=0.3, N=0.5, R=0.1$. Based on the filter design, the choice of $P_r<1$ is to study momentum diffusivity, $R_e=2$ due to weak injection, $\alpha=1$ since the chamber slowly expands, $G_r=0.6$ to minimize the instability at the bottom wall, $J=0.3$ is to reduced fluid bulk resistance, $N=0.5$ to minimize drag force effects at the walls, $R=0.1$ due to weak injection which lead to low permeation. The residual errors of the axial and normal components of the conservation of linear momentum equations, pressure Poisson equation and the energy conservation equation were calculated and presented in Figure 3.1. The errors presented in Figure 3.1a were obtained using $N_x=30, N_y=10$, while Figure 3.1b were computed using $N_x=60, N_y=20$. The residual errors converge on the fourth iteration in both cases, and there is no improvement in the numerical accuracy of the solutions with any further iterations. These figures demonstrate the accuracy and rapid convergence of the numerical scheme employed in solving the system of equations (3.14).

3.4 Results and discussion

This section presents graphical representations of the axial velocity, normal velocity, pressure, and temperature distribution inside the filter chamber. These figures were analyzed to find the parameters that produce the optimal filtrates. The analysis is carried out to

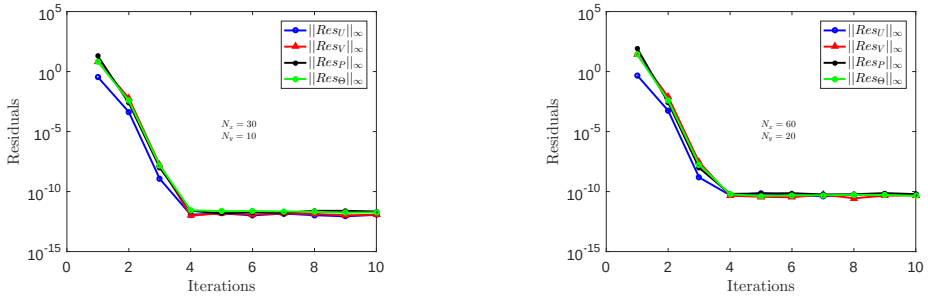

(a) (b)

Figure 3.1: Residual errors of the axial and normal velocities, temperature and pressure distribution in the filter chamber.

investigate the effects of the injection rate of the fluid, R_e, dilation rate of the chamber walls, α, the porosity of the media, R, magnetic field interaction with the fluid, N, buoyancy force, G_r, momentum-thermal diffusivity ratio, P_r, and heat sink, J. Our choice of the range of parameter values used in this study solely depends on the flow we want inside the filter chamber. We choose $P_r < 1$ to investigate the effects of dominant momentum diffusivity on the flow velocity, pressure and temperature distribution. Our preference for $R_e > 0$ is to show the constant injection of fluid into the filter chamber. The values $-1 \leq \alpha \leq 1$ were preferred to investigate how a change in the volume space of the filter chamber affects the outflow. Negative values of α indicate the contraction of the filter chamber, while positive values of α indicate expansion of the filter chamber. The values of the medium porosity, R, were intentionally chosen to be small values to keep the pore size small enough to minimize the outflow of contaminants. The high values of the magnetic field strength, N, were chosen to make the magnetic field strong enough to remove magnetic particles before entering the filter chamber. We choose the value of $G_r < 1$ because we want to maintain the laminar nature of the fluid. However, our analysis also investigates the effects of dominant buoyancy force on the flow profiles. The parameter values used in this study were chosen based on a similar filter design studied in Lekoko et al. [16].

3.4.1 Effects of the injection rate of the fluid

Figure 3.2a shows the effects of Reynolds number (R_e) on the axial velocity when the filter channel expands ($\alpha > 0$). From the figure, it can be seen that when more fluid is injected into the filter channel (increase R_e), the axial velocity decreases towards the filter channel walls and increase towards the middle of the channel at $y = 0$. This increase towards the centre of the channel is because the viscous force is less dominant inside the channel for more injection and filter channel volume. Furthermore, at both channel outlets, it can be noted that the axial velocity profile has an anti-symmetric behaviour. The fluid bulk on the left half of the channel moves towards the filter chamber's left opening, hence the negative axial velocity. In contrast, the fluid bulk in the right half of the filter channel moves towards the chamber's right outlet, resulting in positive axial velocity. The axial velocity is zero at $x = \frac{L}{2}$ due to stagnation point flow in the middle of the filter chamber.

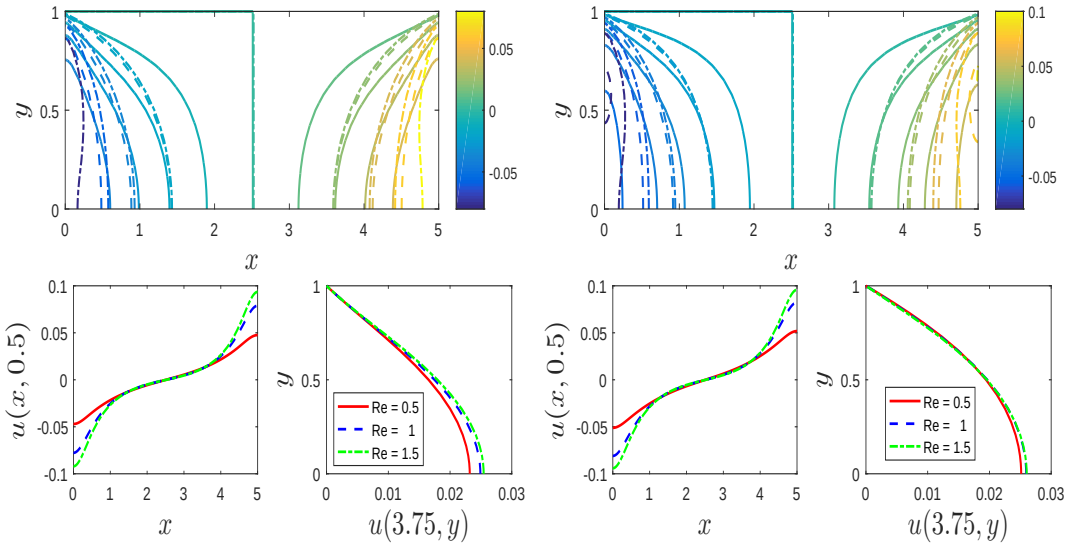

(a) Expansion ($\alpha > 0$) (b) Contraction ($\alpha < 0$)

Figure 3.2: The effects of fluid injection rate R_e on the momentum in the normal direction when the filter chamber (a) expands ($\alpha > 0$) and (b) contracts ($\alpha < 0$).

Figure 3.2b shows that decreasing filter channel volume ($\alpha < 0$) while injecting more fluid into the filter channel, the fluid moves faster in the centre of the channel than when the chamber dilates ($\alpha > 0$). The viscous force is more dominant near the channel walls than in the centre when the fluid injection is more, and the chamber contracts. Hence, the axial velocity increases in the center of the chamber and decreases towards the channel walls.

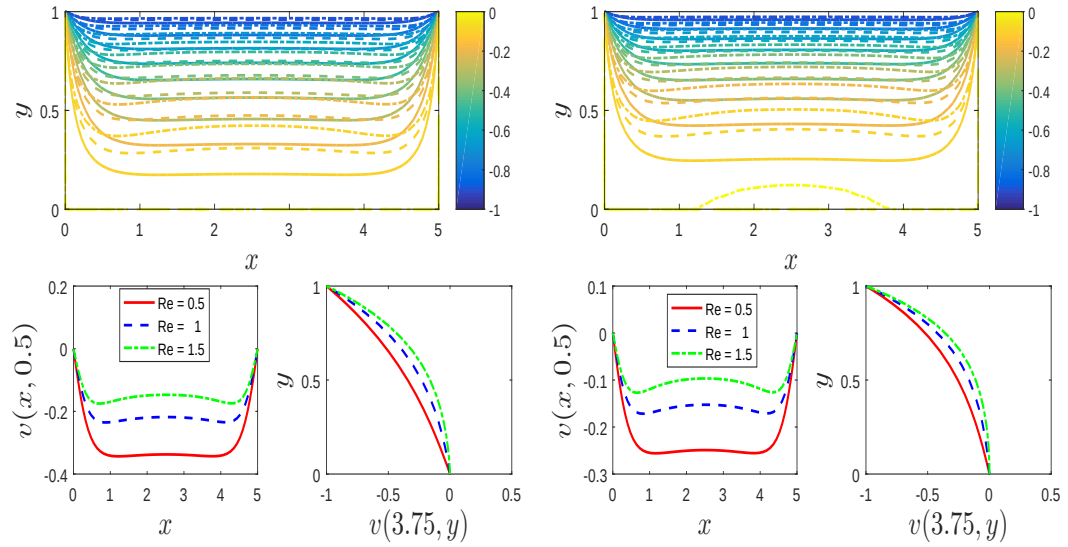

(a) Expansion ($\alpha > 0$) (b) Contraction ($\alpha < 0$)

Figure 3.3: Influence of the injection rate R_e on the normal component velocity when the filter chamber (a) expands ($\alpha > 0$) and (b) contracts ($\alpha < 0$).

Figure 3.3 shows the effect of fluid injection rate on the normal component velocity when

the filter channel is dilated and contracted. From Figure 3.3a, it can be seen that increasing fluid injection is directly proportional to the normal velocity. More fluid injection into the chamber increases the normal component velocity when the filter channel is expanded ($\alpha > 0$). The normal velocity decreases from the upper wall to the centre of the filter channel for either less or more fluid injection while the increasing filter chamber volume ($\alpha > 0$). When the channel contracts ($\alpha < 0$) while injecting more fluid into the chamber, as shown in Figure 3.3b, the magnitude of the normal component velocity is less than the velocity when the filter channel expands ($\alpha > 0$). This phenomenon happens because the inertia force is more dominant than the viscous force in a small control volume. Thus, the fluid particles move faster and freely in the middle of the filter chamber without creating too much internal friction, hence the increase in the normal component velocity of the fluid.

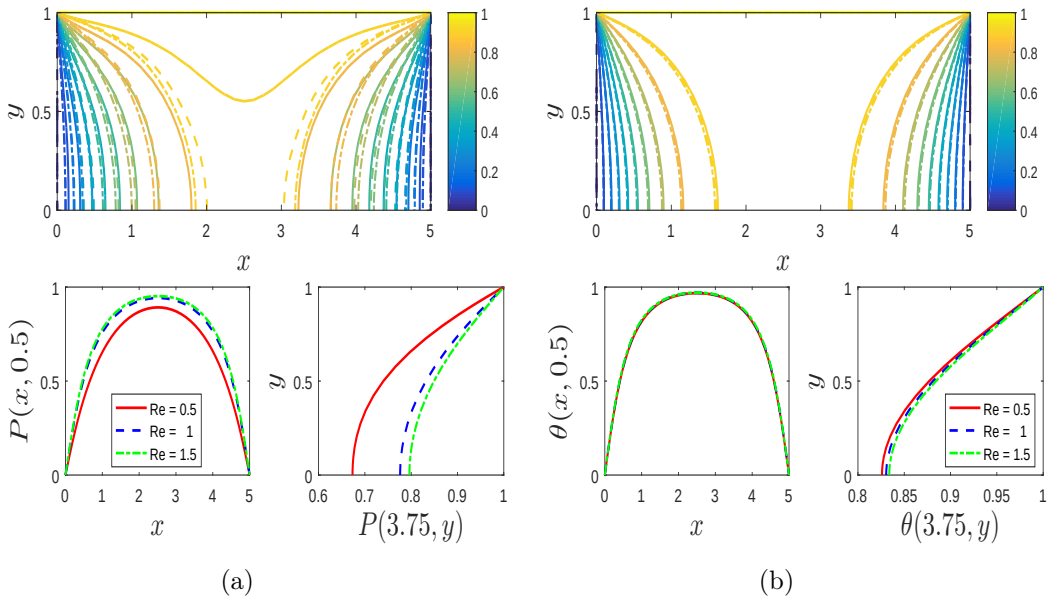

Figure 3.4: Pressure and temperature distribution in the filter chamber when the injection rate is varied.

Figure 3.4a shows the effect of Reynolds number (R_e) on the pressure distribution for filter channel expansion. We remark here that there is an increase in pressure in the normal and axial directions when more fluid is injected into the filter channel. However, when less fluid is injected into the chamber, small R_e, there is less pressure distribution. This less pressure is because there is less fluid in the filter chamber, which allows free movement of fluid particles, thus creating low internal energy and less pressure distribution. On the other hand, the effects of Reynolds number on the temperature distribution is shown in Figure 3.4b. It can be seen that more fluid injection into the filter chamber increases the temperature distribution in the filter chamber. This increase is because inertia force becomes more dominant, and fluid particles begin to cluster together due to more fluid injection, thus creating high internal energy, which results in more temperature distribution than when less fluid is injected.

3.4.2 Effects of the chamber dilation rate

Figure 3.5 describes the effects of the chamber dilation rate on the velocity in the axial and normal directions. Figure 3.5a shows that when the chamber contracts, the axial velocity is more due to work done by the walls of the channel, which leads to an increase in internal flow momentum. The increase in internal momentum will push the fluid bulk towards the outlets, thus increasing the axial velocity. On the other hand, when the chamber expands, the axial velocity decreases while the normal component velocity increases. This increase in velocity is because the additional space created by expansion allows more flow in the normal direction while reducing flow in the axial direction to allow the fluid to occupy the extra volume space created by the expansion of the filter chamber.

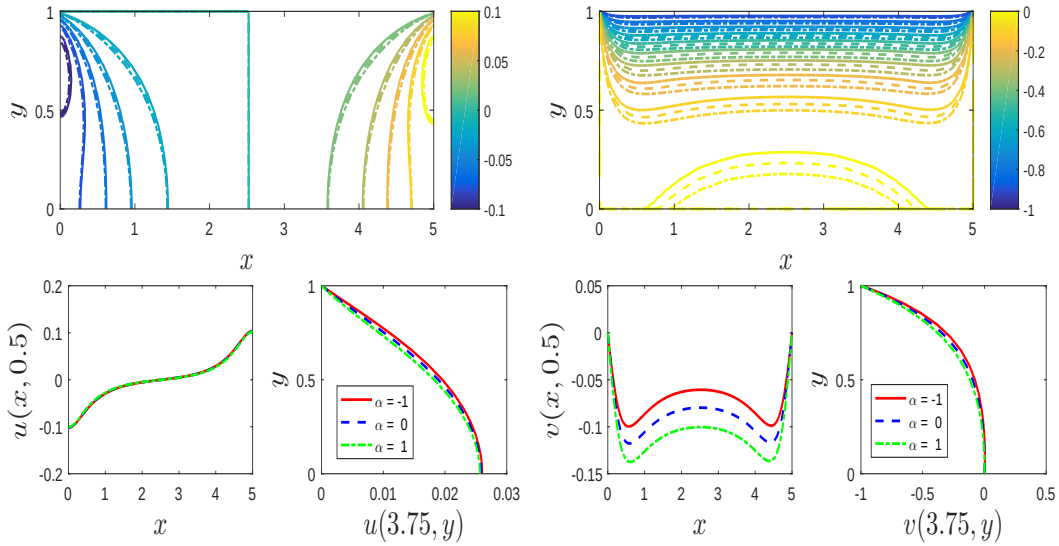

Figure 3.5: Effects of the filter chamber dilation rate on the velocity in the axial and normal direction.

Figure 3.6 shows the effects of expanding ($\alpha > 0$) and contracting ($\alpha < 0$) the chamber on the pressure and temperature distribution. Figure 3.6a depicts that when the filter chamber contracts, there is less area for the fluid particles to occupy, leading to more pressure distribution across the chamber. The figure also shows that the more the chamber expands, the less pressure inside the chamber. This dynamic is expected as physical law dictates that pressure distribution is inversely proportional to the area occupied by fluid particles. Figure 3.6b shows that when the filter chamber expands while fluid is being injected into the chamber, the temperature distribution becomes higher than when the chamber contracts. This increase in temperature is because fluid particles move freely when the chamber expands, leading to more temperature. However, when the chamber contracts, particles are crowded together, making it difficult for the fluid particles to move, producing less internal energy.

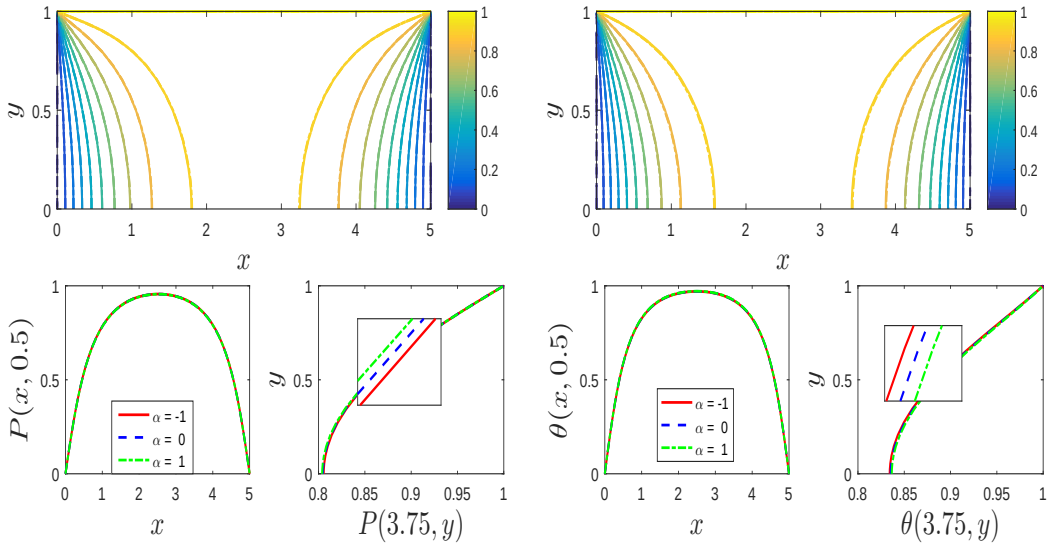

(a) (b)

Figure 3.6: Effects of the variation of the filter chamber dilation rate on the pressure distribution and temperature in the filter chamber.

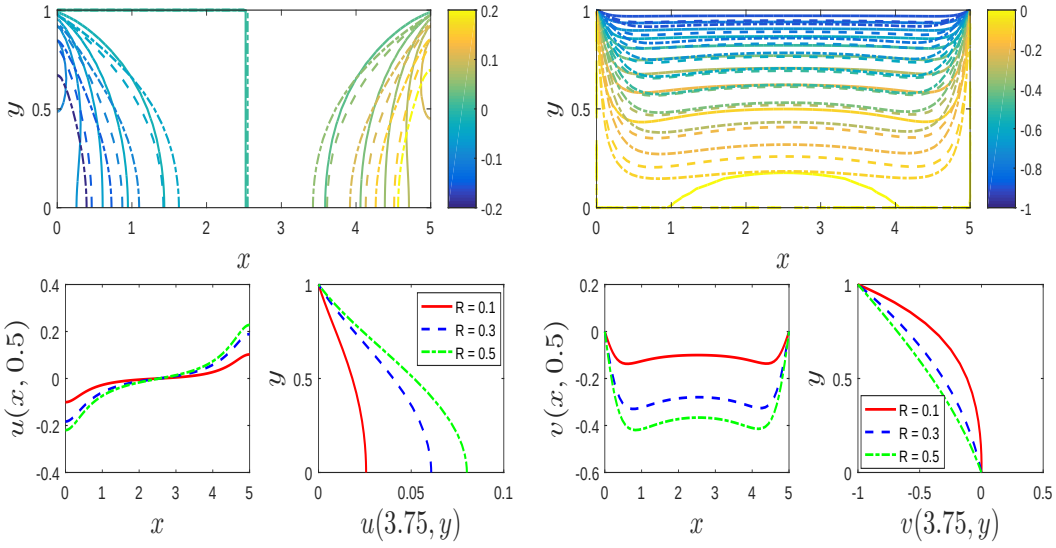

(a) (b)

Figure 3.7: Effects of the porosity of the medium on the axial and normal components velocity.

3.4.3 Effects of the media porosity

In Figure 3.7, we show the effect of porosity (R) on the internal velocities. Figure 3.7a shows that when more fluid particles are injected inside the filter chamber, flow speed increases in the axial direction when the pore size increases. This increase in flow speed is due to the ability of particles to move freely when the pore size increases. Figure 3.7b shows that the velocity in the normal direction decreases. This behaviour is because more

particles flow in the axial direction as soon as the pore size increases.

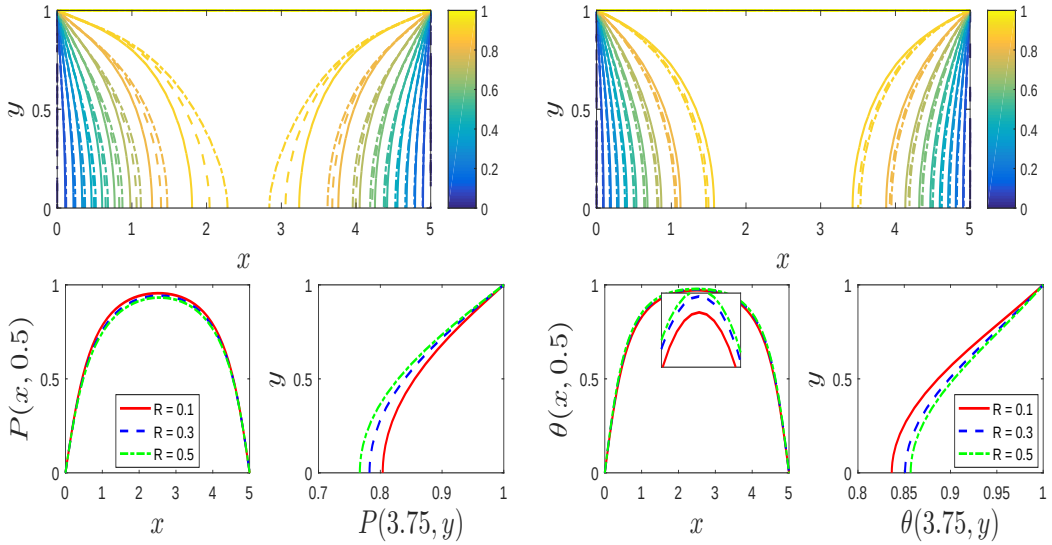

(a) (b)

Figure 3.8: Pressure and temperature distribution for different values of the porosity parameter.

Figure 3.8 shows the effects of porosity (R) on the pressure and temperature distribution. It can be seen from Figure 3.8a that the internal pressure decreases with an increase in the pore size because work done by the filter medium decreases, thus creating less internal stress. Additionally, the pressure distribution along the length of the chamber reduces as the fluid stream towards the outlets. This decrease is a result of the pressure variation becoming atmospheric pressure at the outlets of the channel. Figure 3.8b shows that the temperature decreases along the chamber height since fluid particles close to the channel walls absorb more temperature compare to fluid particles far from the walls. Temperature increases more with increased pore size because free movement of particles leads to more internal energy due to work done by the movement of particles.

3.4.4 Effects of magnetic field strength

The effects of the magnetic field parameter on the velocity in the axial and normal directions are shown in Figure 3.9. The axial velocity decreases as the magnetic field gets stronger Figure 3.9a. This decrease is because the magnet creates a Lorenz force that opposes the motion of the fluid particles, thus slowing down the fluid flow. Along the normal direction, the magnetic field parameter has minimal effect on the normal velocity since the Lorenz force affects the flow only in the direction of the outflows as seen in Figure 3.9b. The momentum in the normal direction decreases more towards the outlets since injected particles freely flow in the axial direction towards the outlets.

Figure 3.10 shows the effect of the magnetic field parameter on the pressure and temperature distribution inside the chamber. Figure 3.10a shows that in the normal direction, pressure increases as the magnetic field gets stronger. This pressure increase results from

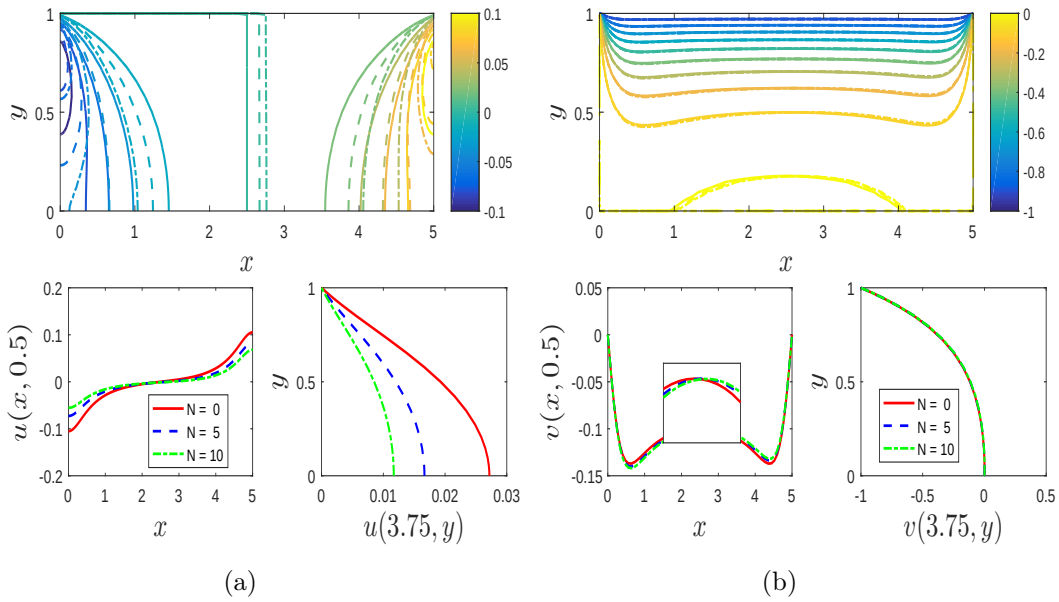

(a) (b)

Figure 3.9: Axial and normal components velocity profiles for different values of the magnetic field parameter.

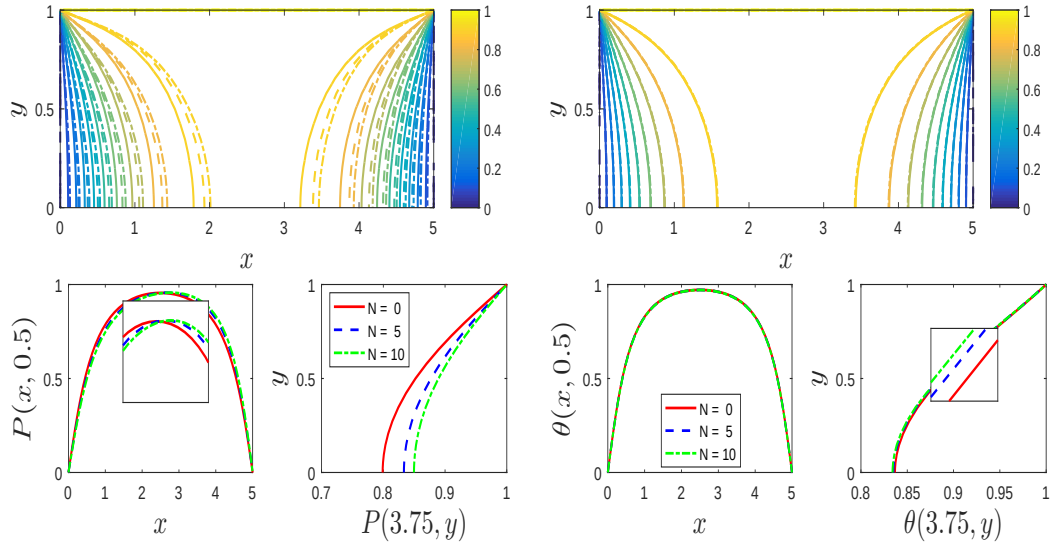

(a) (b)

Figure 3.10: Effects of variation of the magnetic field parameter on pressure and temperature distribution in the filter chamber.

work done by the magnet, which creates clustering of the fluid particles, thus creating more pressure in the filter channel. However, on the other hand, Figure 3.10b shows that temperature distribution decreases as the magnetic field becomes stronger. This decrease in temperature is because fluid particles are clustered and invariably creates lesser internal energy than when fluid particles are not clustered.

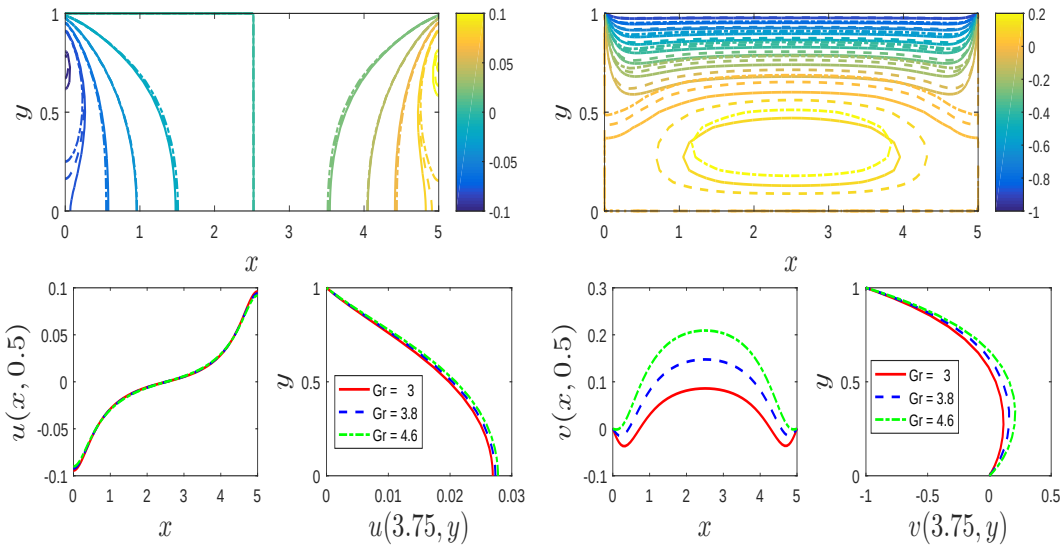

(a) (b)

Figure 3.11: Effects of buoyancy force on the velocity in the axial and normal components for high Grashof numbers.

3.4.5 Effects of buoyancy force

The effects of a high Grashof number on the velocity in the axial and normal directions are shown in Figure 3.11. From both Figures 3.11a and 3.11b, the Grashof number increases the velocity in axial and normal components because the buoyancy force is more dominant, making the fluid less dense, thus allowing easy flow of the fluid particles.

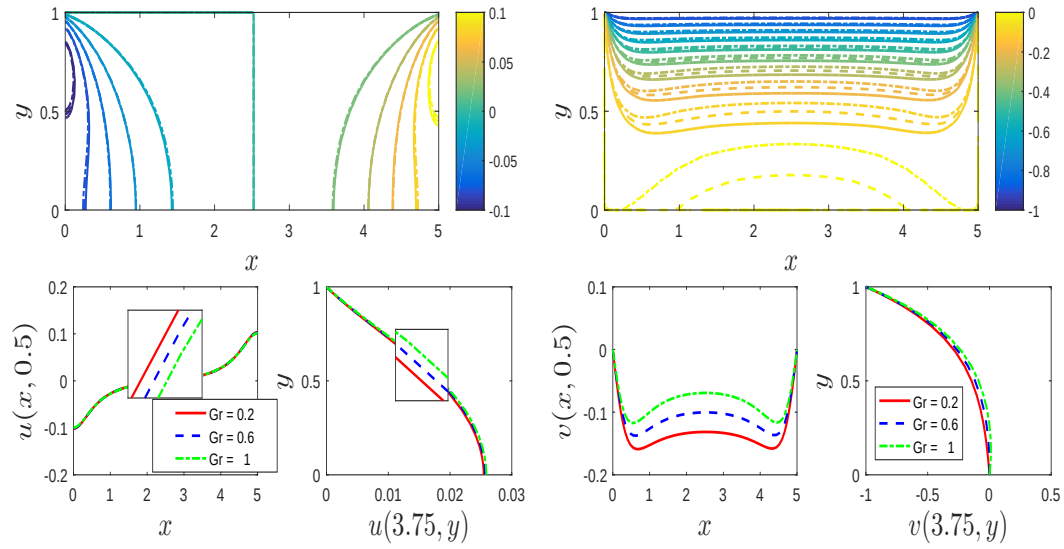

(a) (b)

Figure 3.12: Effects of buoyancy force on the velocity in the axial and normal directions for low Grashof numbers.

The effects of $G_r < 1$, which indicate the case when viscous force dominates the buoy-

ancy force on the axial and normal velocities, are depicted in Figure 3.12. From both Figures 3.12a and 3.12b, we see that increase in the Grashof number leads to a decrease in the magnitude of the axial velocity. The figure also shows that the increased value of the Grashof number increases the magnitude of the velocity along the normal direction. This behaviour is because the viscous force is more dominant, which impedes the movement of fluid particles, thus decreasing the momentum of the fluid particles as they move towards the outlets of the chamber.

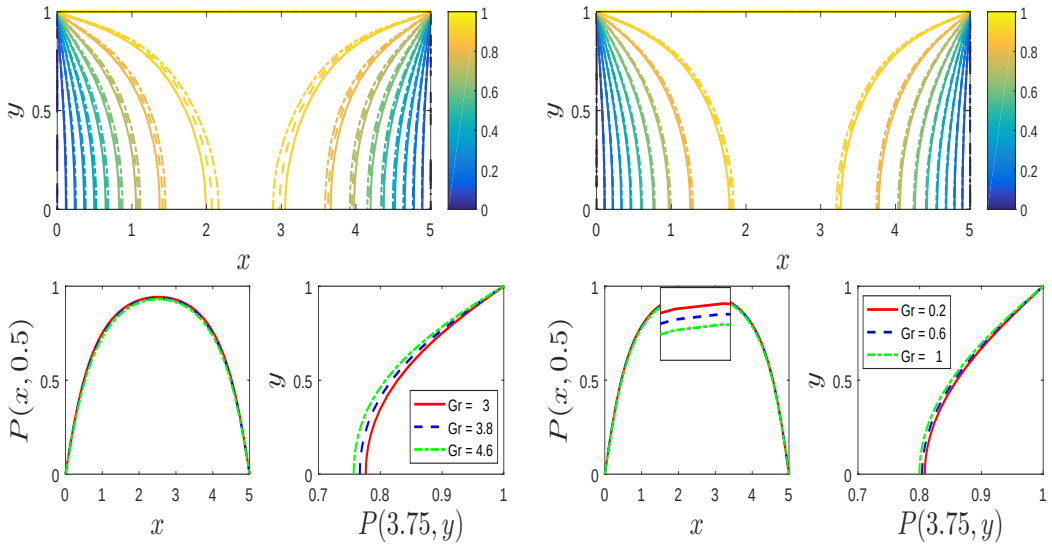

(a) (b)

Figure 3.13: Effects of buoyancy force on total internal pressure in the filter chamber for (a) high and (b) low Grashof numbers.

The effects of $G_r \geq 1$ and $G_r \leq 1$ on the internal pressure distribution are shown in Figure 3.13. According to Figure 3.13a and Figure 3.13b, the system generates more internal pressure when $G_r \leq 1$ compared to when $G_r \geq 1$. The dominant effects of viscous force cause this relatively high internal pressure when Grashof number is low.

The effects of $G_r \geq 1$ and $G_r \leq 1$ on the internal temperature are shown in Figure 3.14. From both Figure 3.14a and Figure 3.14b, it can be seen that the internal temperature is more for low Grashof number. When the Grashof number is low, the high internal temperature is caused by the dominant effect of viscous force, resulting in less energy loss due to heat sink (Joule heating).

3.4.6 Effects of momentum-thermal diffusivity ratio

The effects of the Prandtl number on the velocity in the axial and normal components are shown in Figure 3.15. The figure shows the minimal impact of the Prandtl number on momentum in the axial and normal directions. This minimal effect results from more conduction instead of convection within the chamber, in which thermal diffusion dominates momentum diffusion.

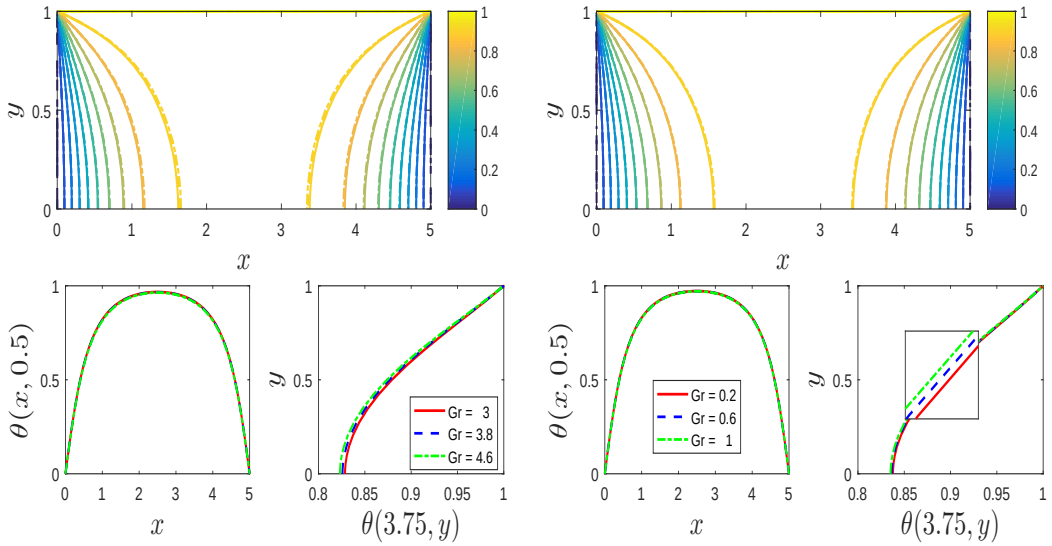

Figure 3.14: Effects of buoyancy force on the temperature distribution in the filter chamber for (a) high and (b) low Grashof numbers.

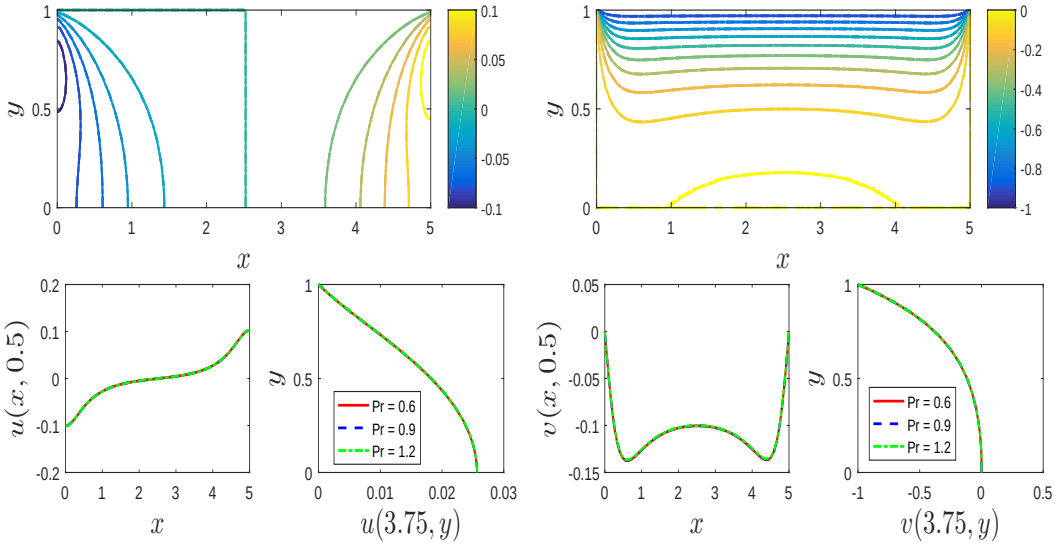

Figure 3.15: Axial and normal components velocity profiles for different values of the Prandtl number.

The effects of the Prandtl number on the pressure and temperature are shown in Figure 3.16. Figure 3.16a indicates that there is minimal pressure variation due to dominant thermal diffusivity. Figure 3.16b shows that increasing the Prandtl number increases the internal temperature variation because dominant thermal diffusivity allows fluid to absorb more energy caused by heat conduction.

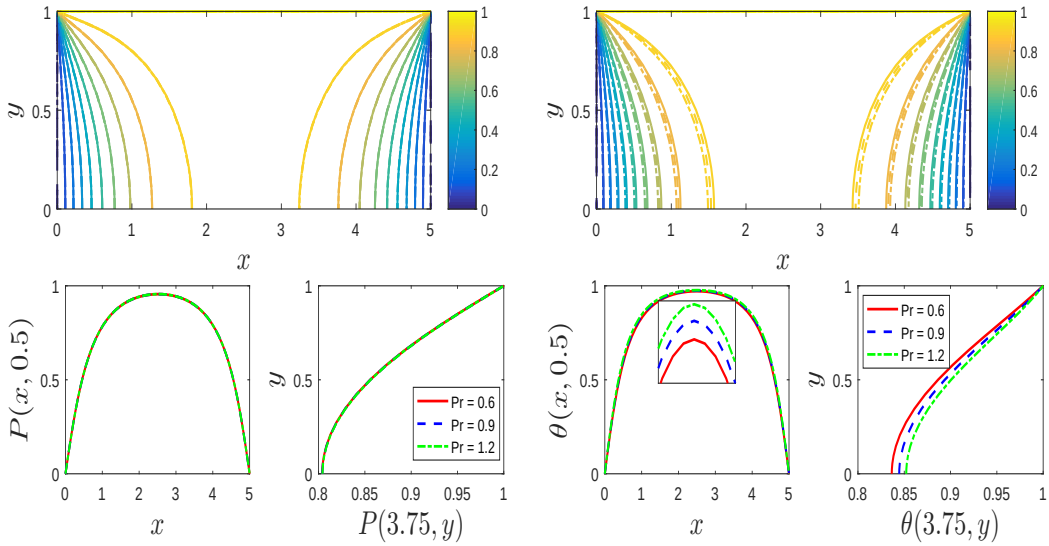

(a) (b)

Figure 3.16: Total internal pressure variation and temperature distribution in the filter chamber for different values of the Prandtl number.

3.4.7 Effects of heat sink

The effects of the Joule heating parameter on the pressure and temperature are shown in Figure 3.17. Figure 3.17a shows that the internal pressure increases as the Joule heating parameter decreases. This pressure increase is because, for less Joule heating or heat sink, Lorenz force is minimal, leading to higher internal pressure due to the free flow of fluid particles. In Figure 3.17b, we can see that the internal temperature decrease with an increase in the heat sink parameter. This decrease in temperature is because the system loses kinetic energy, which reduces internal temperature distribution.

3.4.8 Effects of R_e, α, N, R on wall friction coefficient

The effects of fluid injection, wall dilation rate, magnetic field strength and the medium porosity on the skin friction profiles are shown in Figure 3.18. The asymmetric nature of the skin friction coefficient is due to the consideration of two outlets for the filter chamber. This asymmetric nature means that the average overall drag at the filter chamber walls is approximately equal to zero. The skin friction coefficient is zero everywhere except near the chamber's outlets, where of course, the coefficient is non-zero and asymmetric. However, we observe that more fluid injection, contraction of the filter chamber, increase in the medium pore size and decrease in the magnetic field strength increase the magnitude of the skin friction coefficients near the outlets of the filter chamber.

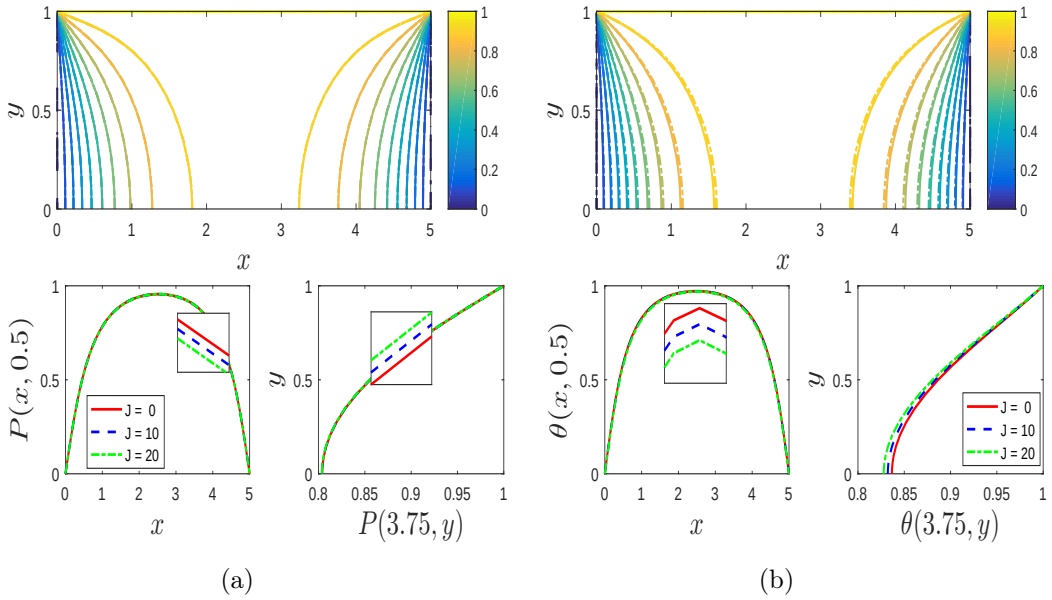

(a) (b)

Figure 3.17: Effects of heat sink on pressure variation and temperature distribution inside the filter chamber.

3.5 Conclusion

This chapter used a multivariate spectral quasilinearization method to study the internal flow, pressure and heat distribution of an electrically conducting fluid in a filter chamber bounded by two weak permeable surfaces. The channel is configured to have two openings on the axial axis two ends, which serve as outlets for the filtered fluid. The equations describing the configuration follow the fundamental conservation of mass, linear momentum and energy. The translation symmetry is used to reduce the system of partial differential equations by one independent variable. The pressure distribution in the chamber is described using the pressure Poisson equation, which is obtained from the continuity and momentum conservation equations. We analyzed the influence of fluid injection, wall dilation rate, the porosity of the chamber, magnetic field interaction, buoyancy force and heat sink on the flow speed, pressure and temperature distribution. The results show that:

1. However, less fluid injection into the chamber allows free streaming of fluid particles, resulting in less internal pressure. On the other hand, more injection into the chamber creates high internal energy, which results in an overall increase in internal temperature distribution.

2. The contraction of the chamber leads to an increase in internal momentum, which pushes the fluid particles towards the openings on both ends of the filter chamber, thus increasing the axial velocity. However, when the filter chamber expands, the momentum in the normal direction increases because the extra volume created by expansion needs to be occupied by fluid particles, resulting in a decrease in the axial velocity. Additionally, as expected, the pressure distribution is inversely proportional to the chamber dilation.

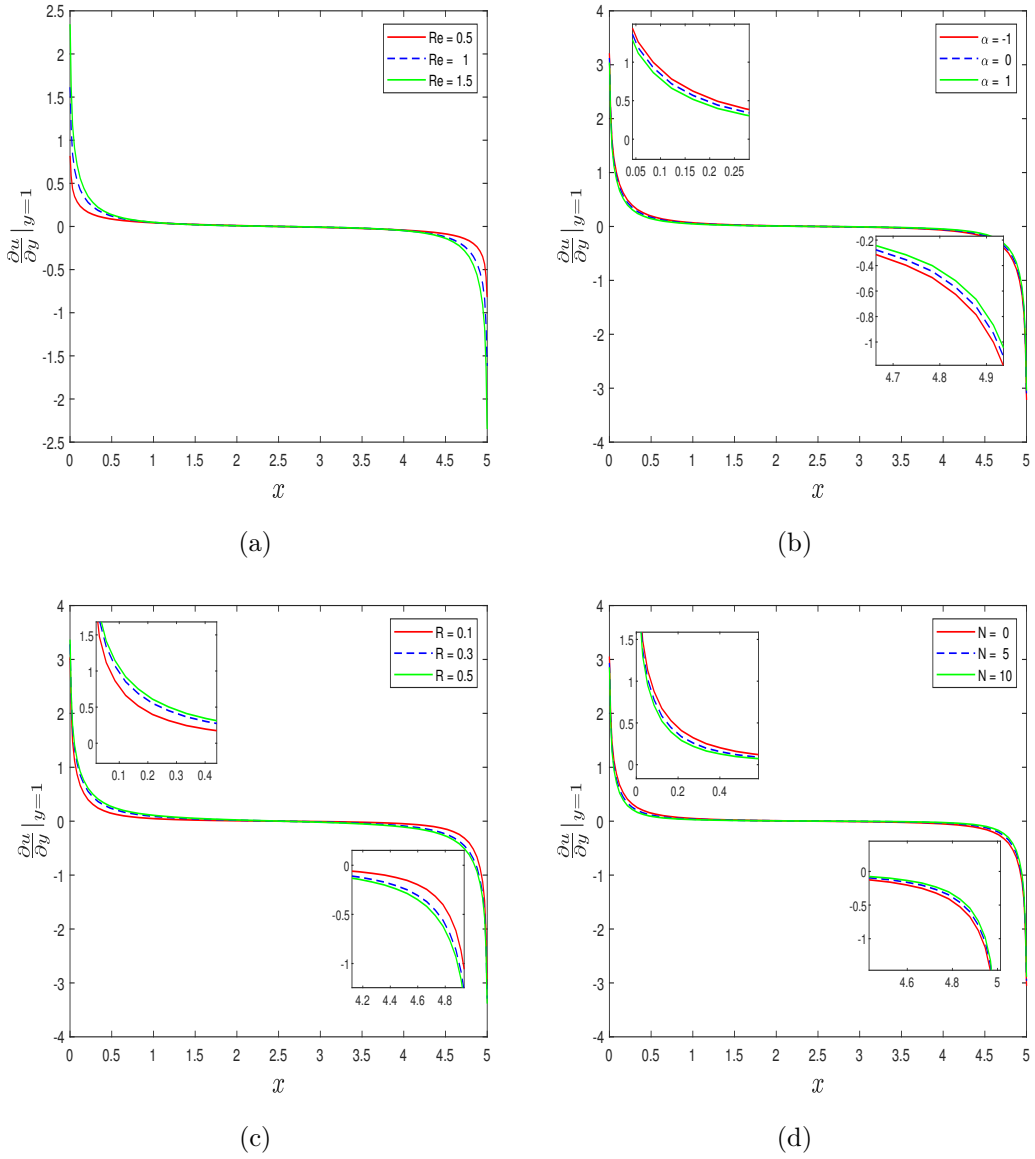

Figure 3.18: Effects of fluid injection, chamber wall dilation rate, medium porosity and magnetic field strength on the drag coefficient at the walls of the filter chamber.

3. Increasing the size of the pores results in more flow towards the outlets of the chamber, leading to an increase in the normal component velocity. The increase in pore size also reduces the axial momentum and decreases the total internal pressure variation.

4. Magnetic field interaction increases pressure variation in the chamber. On the other hand, it decreases temperature distribution because less internal energy is created when there is a strong magnetic field.

5. Although increasing magnetic field strength is ideal for optimal performance of the filter by minimizing the injection of unwanted particles into the filter chamber, it brings drag towards the filter chamber outlets, decreasing outflow velocity.

Chapter 4

Injection driven flow in a dilating or contracting filter chamber with parabolic left inlet velocity

Filter design is an essential aspect of the development of industrial machines. This chapter investigates and analyses an injection-driven flow in a dilating or contracting filter chamber with weak permeable walls. The design is such that an opening allows influx into the filter channel with parabolic velocity and another opening that serves as an outlet for the filtrates. The model follows the mass conservation, incompressible Navier-Stokes and the energy conservation equations. The study seeks steady-state operation to understand a stable filtration process. The solutions of the dependent variables are then approximated using the spectral-based paired quasilinearization technique. We found, among other results, that in the region where the flow is developing due to the inflow velocity, the axial flow when the chamber compresses is greater than the velocity when the filter chamber expands.

NOMENCLATURE

c_p - specific heat, $J/kg\,K$
g - acceleration due to gravity, m/s^2
G_r - Grashoff number
$\dot{h}$ - filter wall dilation or contraction rate, m/s
H_0 - magnetic field strength, N/mA
J - Joule heating parameter
k - porous medium permeability, m^2
N - Stuart number
P - non-dimensional pressure variation
$\bar{P}$ - pressure variation, Nm^{-2}
P_r - Prandtl number
R_e - permeation Reynolds number
R - permeability parameter
s - mass diffusivity, m^2/s
t - non-dimensional time
$\bar{t}$ - time, s
T - temperature of the fluid, K
T_w - temperature at wall, K
$\bar{u}$ - axial velocity, m/s
u - non-dimensional axial velocity
U_{in} - axial inflow velocity
V_w - normal velocity at the wall, m/s
$\bar{v}$ - normal velocity, m/s
v - non-dimensional normal velocity
$\bar{x}$ - axial coordinate, m
x - non-dimensional axial coordinate
$\bar{y}$ - normal coordinate, m
y - non-dimensional normal coordinate

Greek symbols

α - wall dilation or contraction rate
β - heat expansion
θ - non-dimensional temperature
λ - heat diffusion
μ - magnetic field permeability, H/m
ρ - fluid density, kg/m^3
σ - fluid electrical conductivity, S/m
ϕ - porosity
$\bar{\Psi}$ - dimensional stream function, m^2/s
Ψ - non-dimensional stream function

Subscripts

w - filter wall
h - filter height
in - inflow

4.1 Introduction

There are various essential factors to consider when designing a piece of machinery for industrial usage. To have the best design that optimally services the industrial needs is critical but can be challenging to achieve. Significant scientific findings need to be considered when developing and building industrial machinery, primarily from the theoretical understanding and analysis of the machine or the process it will be applied. Various research aims to highlight scientific evidence that aid engineers to have an effective manufacturing process of the machines and to improve subsequent designs. One such important design is the filter chamber used in several industrial fluid flow machines.

The investigation of heat and mass transfer dynamics has led to scientific studies that have helped engineers develop effective filters for industrial use. Finding and analysing the solutions of mathematical models that describe various flow, heat and mass transfer problems has been an area of scientific interest, particularly for researchers and engineers keen on understanding the dynamics of different filtration processes to find a filter that achieves the optimal filtration.

The analysis in the current chapter is based on filter design with parabolic left inlet fluid injection. It highlights significant findings that will provide engineers with better knowledge of essential aspects of a filter chamber in achieving optimal design. In this chapter, an analysis is carried out to study the magnetohydrodynamic flow of fluid streaming in the horizontal direction in a filter chamber bounded by two semi-permeable plates. Injection through the semi-permeable parallel plates and axial fluid infusion through the left opening of the filter chamber is investigated, and the fluid is assumed to leave the filter chamber through the right opening of the filter. The inflow velocity profile at the filter chamber's left opening is considered to be fully developed upon entering the filter chamber and taken to be parabolic. The magnetic field interaction at the chamber walls results in a change in the parabolic profile of the flow as the fluid streams horizontally through the filter chamber. So far, a variety of experimental and analytical investigations have been done to investigate the magnetohydrodynamic and heat transfer properties of liquid metal flows in a duct and those with free surfaces exposed to MHD forces [53–55].

A numerical investigation for the entrance problem of convective MHD channel flow inside parallel plates was carried out by Yang and Yu [56]. The authors considered both cases of constant heat flow and wall temperature. In the absence of free convection, their findings show that the entrance length velocity is inversely proportional to M^2, the magnetic field parameter, for large Hartmann numbers, as predicted by Shercliff [57]. Also, they found out that when the dissipations are significantly enough, the fluid temperature initially is lower than at the walls but eventually exceeds it. Nigam and Singh [58] studied the heat transfer in a laminar flow inside parallel plates under the influence of a magnetic field. For the heat transfer problems related to Hartmann's velocity profile for forced flow inside two infinite parallel plates, the authors obtained the conservation of energy equation solutions. They found, among other results, that ionic conductivity reduces the mixed mean temperature

at any point between the plates while increasing the local Nusselt number.

Analytical methods were used by Alpher [59] and Back [60] for various values of the Hartmann number by taking axial heat conduction and constant wall temperature into account for thermally developing flow under the Hartmann velocity profile and constant thermal properties. Eraslan and Eraslan [61] studied a general mathematical model of magnetohydrodynamic thermal entrance regions in a parallel plate channel. They took into account uniform wall temperatures, Hall effects, axial conduction, Joule heating and viscous dissipation. They concluded that Hall currents significantly impact the thermal problem and that axial heat conduction cannot be ignored for low Peclet numbers. Bhat and Mittal [62] investigated forced convective heat transfer in a fully developed laminar flow of magnetohydrodynamic fluid subjected to Hall and ion slip currents. Javeri [63] used the variational Galerkin–Kantorowich technique to evaluate the thermal entrance solution, taking into account the third kind (convective) boundary conditions at the walls. They found that the Biot number substantially affects the local Nusselt number.

Analytic solutions of partial differential equations can be challenging to find, and even when found, they can be hard to interpret due to the inclusion of special functions or integrals [46]. Because of this, a spectral-based paired quasilinearization will be chosen to solve the system of partial differential equations that describe the model being investigated in this study. The spectral paired quasilinearization method decouples the system into linearized pairs. The resulting linearized pairs are then solved using the spectral collocation approach. The spectral collocation method follows from approximating the velocity, temperature and pressure profiles as a linear combination of the Lagrange polynomials evaluated on the Chebyshev-Gauss-Lobatto nodes [26, 64, 65].

4.2 Model Formulation

The chapter analyses an incompressible viscous fluid flowing inside a filter chamber layered with a porous medium. The chamber walls are bounded by semi-permeable surfaces, allowing fluid particles into the filter chamber through the walls. Fluid particles are also injected into the filter chamber through the left opening, while the right orifice serves as an outlet for the filtrates. We assumed that fluid injection into the filter chamber through the filter walls is at a constant velocity, V_w. In contrast, the velocity of the fully developed injection through the left inlet assumes a parabolic nature, $\bar{U}_{in}$. The chamber walls are kept at constant temperature T_w to make the fluid less dense. This reduction in the fluid density increases the speed and kinetic energy of the fluid, thus causing the fluid injected through the semi-permeable walls to move inside the filter chamber. The model of the filter chamber is such that a constant magnetic field with strength, H_0, permeable walls with permeability, k, and porous medium with porosity, ϕ, are consolidated to regulate the outflux of unwanted particles. It is for this reason that we consider the following forces to act on the system:

i. The surface force due to porosity which is given, from the Darcy law, as

$$\mathbf{F^1} = F_x^1\mathbf{i} + F_y^1\mathbf{j} = -\frac{s\phi}{k}u\mathbf{i} - \frac{s\phi}{k}v\mathbf{j}. \tag{4.1}$$

ii. The body forces obtained from the Lorenz electromagnetism law and Archimedes principle are given, respectively, as

$$\mathbf{F^2} = F_x^2\mathbf{i} = -\sigma\mu^2 H_0^2 u\mathbf{i}, \quad \text{and} \quad \mathbf{F^3} = F_y^3\mathbf{j} = g\rho\beta(T - T_w)\mathbf{j}. \tag{4.2}$$

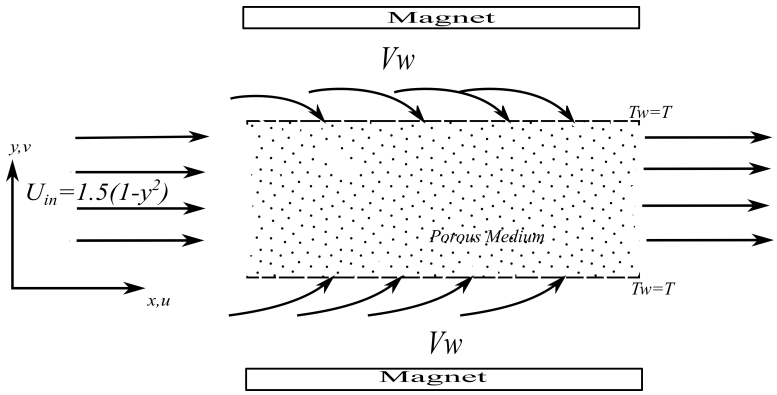

Figure 4.1: Geometrical configuration of the filter chamber

We refer readers to Magalakwe et al. [16] and Tenreiro et al. [50] for a detailed derivation of these forces. See Figure 4.1 for the geometrical configuration of the filter chamber. Upon considering the forces mentioned above and assumptions, the equation describing the pressure distribution, conservation of mass, conservation of linear momentum and conservation of energy in the filter chamber are given, respectively, as [16]:

$$\left.\begin{aligned}
&\frac{\partial^2\bar{P}}{\partial\bar{x}^2} + \frac{\partial^2\bar{P}}{\partial\bar{y}^2} = -\sigma\mu^2 H_0^2\frac{\partial\bar{u}}{\partial\bar{x}} + g\beta\rho\frac{\partial T}{\partial\bar{y}} + 2\rho\left[\frac{\partial\bar{u}}{\partial\bar{x}}\frac{\partial\bar{v}}{\partial\bar{y}} - \frac{\partial\bar{u}}{\partial\bar{y}}\frac{\partial\bar{v}}{\partial\bar{x}}\right],\\
&\frac{\partial\bar{u}}{\partial\bar{x}} + \frac{\partial\bar{v}}{\partial\bar{y}} = 0,\\
&\frac{1}{\rho}\frac{\partial\bar{P}}{\partial\bar{x}} + \frac{\partial\bar{u}}{\partial\bar{t}} + \bar{u}\frac{\partial\bar{u}}{\partial\bar{x}} + \bar{v}\frac{\partial\bar{u}}{\partial\bar{y}} = s\left[\frac{\partial^2\bar{u}}{\partial\bar{x}^2} - \frac{\partial^2\bar{u}}{\partial\bar{y}^2}\right] - \frac{s\phi}{k}\bar{u} - \frac{\sigma\mu^2 H_0^2}{\rho}\bar{u},\\
&\frac{1}{\rho}\frac{\partial\bar{P}}{\partial\bar{y}} + \frac{\partial\bar{v}}{\partial\bar{t}} + \bar{u}\frac{\partial\bar{v}}{\partial\bar{x}} + \bar{v}\frac{\partial\bar{v}}{\partial\bar{y}} = s\left[\frac{\partial^2\bar{v}}{\partial\bar{x}^2} + \frac{\partial^2\bar{v}}{\partial\bar{y}^2}\right] - \frac{s\phi}{k}\bar{v} + g\beta(T - T_w),\\
&\frac{\partial T}{\partial\bar{t}} + \bar{u}\frac{\partial T}{\partial\bar{x}} + \bar{v}\frac{\partial T}{\partial\bar{y}} = \lambda\left[\frac{\partial^2 T}{\partial\bar{x}^2} + \frac{\partial^2 T}{\partial\bar{y}^2}\right] + \frac{\sigma\mu^2 H_0^2}{\rho c_p}\bar{u}^2 = 0.
\end{aligned}\right\} \tag{4.3}$$

In the system of equations (4.3), $\bar{t}$ is time, $\bar{P}$ is the pressure distribution inside the filter chamber, $\bar{u}$ is the fluid velocity in the axial direction ($\bar{x}$), $\bar{v}$ is the fluid velocity in the normal direction ($\bar{y}$), T is the temperature distribution in the filter chamber, ρ is the fluid density, s is the fluid kinematic viscosity, g is the acceleration due to gravity, β is fluid thermal expansion, λ is the thermal diffusivity of the fluid, ϕ is the porosity of the porous medium, k is the permeability of the porous medium, σ is the fluid electrical conductivity,

μ is magnetic permeability, H_0 is the constant strength of the magnetic field, and c_p is the specific heat. The flow in the filter chamber is set up subject to the following conditions:

$$\left.\begin{aligned}
&\text{at } \bar{y}=h(\bar{t}),\ \bar{P}(\bar{x},\bar{y},\bar{t})=P_w,\ \bar{u}(\bar{x},\bar{y},\bar{t})=0,\ \bar{v}(\bar{x},\bar{y},\bar{t})=-V_w,\ T(\bar{x},\bar{y},\bar{t})=T_w,\\
&\text{at } \bar{y}=0,\ \bar{P}_{\bar{y}}(\bar{x},\bar{y},\bar{t})=0,\ \bar{u}_{\bar{y}}(\bar{x},\bar{y},\bar{t})=0,\ \bar{v}(\bar{x},\bar{y},\bar{t})=0,\ T_{\bar{y}}(\bar{x},\bar{y},\bar{t})=0,\\
&\text{at } \bar{x}=0,\ \bar{P}(\bar{x},\bar{y},\bar{t})=0,\ \bar{u}(\bar{x},\bar{y},\bar{t})=\bar{U}_{in},\ \bar{v}(\bar{x},\bar{y},\bar{t})=0,\ T(\bar{x},\bar{y},\bar{t})=0.
\end{aligned}\right\} \tag{4.4}$$

The non-dimensional system of equations:

$$\left.\begin{aligned}
&\frac{\partial^2 P}{\partial x^2}+\frac{\partial^2 P}{\partial y^2}=-N\frac{\partial u}{\partial x}+\frac{G_r}{R_e^2}\frac{\partial \theta}{\partial y}+2\left[\frac{\partial u}{\partial x}\frac{\partial v}{\partial y}-\frac{\partial u}{\partial y}\frac{\partial v}{\partial x}\right],\\
&\frac{\partial P}{\partial x}+\frac{\partial u}{\partial t}+u\frac{\partial u}{\partial x}+v\frac{\partial u}{\partial y}=\frac{1}{R_e}\left[\alpha y\frac{\partial u}{\partial y}+\frac{\partial^2 u}{\partial x^2}+\frac{\partial^2 u}{\partial y^2}\right]-\frac{1}{R}u-Nu,\\
&\frac{\partial P}{\partial y}+\frac{\partial v}{\partial t}+u\frac{\partial v}{\partial x}+v\frac{\partial v}{\partial y}=\frac{1}{R_e}\left[\alpha y\frac{\partial v}{\partial y}+\frac{\partial^2 v}{\partial x^2}+\frac{\partial^2 v}{\partial y^2}\right]-\frac{1}{R}v+G_r\theta,\\
&\frac{\partial \theta}{\partial t}+u\frac{\partial \theta}{\partial x}+v\frac{\partial \theta}{\partial y}=\frac{1}{P_r R_e}\left[\frac{\partial^2 \theta}{\partial x^2}+\frac{\partial^2 \theta}{\partial y^2}\right]+J\bar{u}^2
\end{aligned}\right\} \tag{4.5}$$

is obtained following the introduction of the dimensionless quantities below:

$$\left.\begin{aligned}
&u=\frac{\bar{u}}{V_w},\quad \Psi=\frac{\bar{\Psi}}{hV_w},\quad \alpha=\frac{h\dot{h}}{s},\quad \theta=\frac{T-T_h}{T_w-T_h},\quad G_r=\frac{g\beta h^3(T_w-T_h)}{s^2}\\
&v=\frac{\bar{v}}{V_w},\quad t=\frac{\bar{t}V_w}{h},\quad P=\frac{\bar{P}}{\rho V_w^2},\quad N=\frac{\sigma h\mu^2 H_0^2}{\rho V_w},\quad J=\frac{\sigma H_0^2 h V_w}{\rho c_p(T_w-T_h)},\\
&x=\frac{\bar{x}}{h(t)},\quad y=\frac{\bar{y}}{h(t)},\quad R_e=\frac{hV_w}{s},\quad R=\frac{kV_w}{s\phi h},\quad P_r=\frac{s}{\lambda}.
\end{aligned}\right\} \tag{4.6}$$

The boundary conditions (4.4) correspondingly become

$$\left.\begin{aligned}
&\text{at } y=1,\ P(x,y,t)=1,\ u(x,y,t)=0,\ v(x,y,t)=-1,\ \theta(x,y,t)=1,\\
&\text{at } y=0,\ P_y(x,y,t)=0,\ u_y(x,y,t)=0,\ v(x,y,t)=0,\ \theta_y(x,y,t)=0,\\
&\text{at } x=0,\ P(x,y,t)=0,\ u(x,y,t)=U_{in},\ v(x,y,t)=0,\ \theta(x,y,t)=0.
\end{aligned}\right\} \tag{4.7}$$

Symmetry transformation shows that the system is reduced to a steady-state regime which leads to a stable filtration process with the following conservation equations

$$\left.\begin{aligned}
&\frac{\partial^2 P}{\partial x^2}+\frac{\partial^2 P}{\partial y^2}=-N\frac{\partial u}{\partial x}+\frac{G_r}{R_e^2}\frac{\partial \theta}{\partial y}+2\left[\frac{\partial u}{\partial x}\frac{\partial v}{\partial y}-\frac{\partial u}{\partial y}\frac{\partial v}{\partial x}\right],\\
&\frac{\partial P}{\partial x}+u\frac{\partial u}{\partial x}+v\frac{\partial u}{\partial y}=\frac{1}{R_e}\left[\alpha y\frac{\partial u}{\partial y}+\frac{\partial^2 u}{\partial x^2}+\frac{\partial^2 u}{\partial y^2}\right]-\frac{1}{R}u-Nu,\\
&\frac{\partial P}{\partial y}+u\frac{\partial v}{\partial x}+v\frac{\partial v}{\partial y}=\frac{1}{R_e}\left[\alpha y\frac{\partial v}{\partial y}+\frac{\partial^2 v}{\partial x^2}+\frac{\partial^2 v}{\partial y^2}\right]-\frac{1}{R}v+G_r\theta,\\
&u\frac{\partial \theta}{\partial x}+v\frac{\partial \theta}{\partial y}=\frac{1}{P_r R_e}\left[\frac{\partial^2 \theta}{\partial x^2}+\frac{\partial^2 \theta}{\partial y^2}\right]+Ju^2.
\end{aligned}\right\} \tag{4.8}$$

Similarly the boundary conditions (4.7) take the form

$$\left.\begin{aligned}
&\text{at } y=1,\ P(x,y)=1,\ u(x,y)=0,\ v(x,y)=-1,\ \theta(x,y)=1,\\
&\text{at } y=0,\ P_y(x,y)=0,\ u_y(x,y)=0,\ v(x,y)=0,\ \theta_y(x,y)=0,\\
&\text{at } x=0,\ P(x,y)=0,\ u(x,y)=U_{in},\ v(x,y)=0,\ \theta(x,y)=0.
\end{aligned}\right\} \tag{4.9}$$

4.3 Method of Solution

This section describes the implementation of the solution method, namely, the paired quasilinearization method (PQLM), used in solving the system of two-dimensional partial differential equations. The technique is premised on linearizing the equations using a generalized Taylor expansion and using spectral collocation. The linearization is based on the method of Bellman and Kalaba [51], and the paired quasilinearization is based on the studies in [64–66]. Paired quasilinearization decouples the system into pairs and minimizes the computational cost required in inverting and solving the full matrix system. This chapter considers the pairs of the momentum conservation equations and the pairs of the pressure distribution and energy conservation equations. To solve the system of equations (4.8), we begin by applying the quasilinearization to the momentum conservation equations so that we have

$$\begin{aligned}
&-Re^{-1}u^{r+1}+u^{r}u_{x}^{r+1}+\left[u_{x}^{r}+R^{-1}+N\right]u^{r+1}-Re^{-1}u_{yy}^{r+1}+\left[v^{r}-\alpha yRe^{-1}\right]u_{y}^{r+1}+\left[u_{y}^{r}\right]v^{r+1}\\
&\qquad=u^{r}u_{x}^{r}+v^{r}u_{y}^{r}-P_{x}^{r}, \qquad (4.10)\\
&v_{x}^{r}u^{r+1}-Re^{-1}v_{xx}^{r+1}+u^{r}v_{x}^{r+1}+\left[v_{y}^{r}+R^{-1}\right]v^{r+1}-Re^{-1}v_{yy}^{r+1}+\left[v^{r}-\alpha yRe^{-1}\right]v_{y}^{r+1}\\
&\qquad=v^{r}v_{y}^{r}+u^{r}v_{x}^{r}-P_{y}^{r}+Gr\theta^{r}, \qquad (4.11)
\end{aligned}$$

where $r, r+1$ are two successive iterations. The updated solutions of the axial and normal velocities and their derivatives are then used in the second pairs so that we have the following linearized pairs

$$P_{xx}^{r+1}+P_{yy}^{r+1}-GrRe^{-2}\theta_{y}^{r+1}=2\left[u_{x}^{r+1}v_{y}^{r+1}-u_{y}^{r+1}v_{x}^{r+1}\right]-Nu^{r+1}, \tag{4.12}$$

$$-(PrRe)^{-1}\theta_{xx}^{r+1}+\left[u^{r+1}\right]\theta_{x}^{r+1}-(PrRe)^{-1}\theta_{yy}^{r+1}+\left[v^{r+1}\right]\theta_{y}^{r+1}=Ju^{2^{r+1}}. \tag{4.13}$$

The linearized pairs are solved in terms of a $(M_x+1)\times(M_y+1)$ multivariate Lagrange polynomials of the form:

$$a(x,y)\approx\sum_{m=0}^{N_x}\sum_{n=0}^{N_y}A(x_m,y_n)L_m(x)L_n(y)\quad s.t.\quad a=\{u,v,P,\theta\}, \tag{4.14}$$

on the Chebyshev-Gauss-Lobatto points:

$$\hat{x}_i = -\cos\left(\frac{i\pi}{M_x}\right), \quad \hat{y}_j = -\cos\left(\frac{j\pi}{M_y}\right), \quad j = 0, \ldots, M_y,\ i = 0, \ldots, M_x, \tag{4.15}$$

which are transformed into the physical domain using the following affine mappings:

$$\hat{x}(x) = \frac{2}{L}\left(x - \frac{L}{2}\right), \quad x \in [0, L], \tag{4.16a}$$

$$\hat{y}(y) = 2\left(y - \frac{1}{2}\right), \quad y \in [0, 1]. \tag{4.16b}$$

We define the Lagrange polynomials in x and y as:

$$L_m(x) = \prod_{\substack{m=0 \\ m \neq i}}^{M_x} \frac{x - x_m}{x_i - x_m}; \quad \text{such that} \quad L_m(x_i) = \delta_{mi} = \begin{cases} 1 & m = i \\ 0 & m \neq i, \end{cases} \tag{4.17}$$

and

$$L_n(y) = \prod_{\substack{n=0 \\ n \neq j}}^{M_y} \frac{y - y_n}{y_j - y_n}; \quad \text{such that} \quad L_n(y_j) = \delta_{nj} = \begin{cases} 1 & n = j \\ 0 & n \neq j, \end{cases} \tag{4.18}$$

respectively. Approximation of the derivatives of $a(x, y)$ with respect to the variables x and y are respectively defined on the points $(\hat{x}_i, \hat{(y)}_j)$ as

$$\frac{\partial a}{\partial x}(x, y) \approx \sum_{m=0}^{M_x} \sum_{n=0}^{M_y} A(x, y) \frac{dL_m}{dx}(\hat{x}_i) L_n(\hat{y}_j) = \sum_{m=0}^{M_x} A(x_m, y_j) \frac{dL_m}{dx}(\hat{x}_i) = \mathbf{D}^{(1,0)} \mathbf{A}_j = \frac{2}{L} \hat{\mathbf{D}}^{(1,0)} \mathbf{A}_j,$$
$$j = 0, \ldots, M_y, \tag{4.19}$$

and

$$\frac{\partial a}{\partial y}(x, y) \approx \sum_{n=0}^{M_y} A(x_i, y_n) \frac{dL_n}{dy}(\hat{y}_j) = \sum_{n=0}^{M_y} \mathbf{D}^{(0,1)} \mathbf{A}_n = 2 \sum_{n=0}^{M_y} \hat{\mathbf{D}}^{(0,1)} \mathbf{A}_n. \tag{4.20}$$

We note here that the differentiation matrices $\hat{\mathbf{D}}^{(1,0)}$ and $\hat{\mathbf{D}}^{(0,1)}$ are the standard Chebyshev differentiation matrices in x and y respectively [52]. These matrices are scaled to map the computational domain to the physical domain using the transformation defined

in Equation (4.16). Higher-order derivatives in both variables are obtained by taking corresponding powers of the matrices. In this study, we define the second-order derivatives with respect to x and y as $\hat{\mathbf{D}}^{(2,0)}$ and $\hat{\mathbf{D}}^{(0,2)}$ respectively, which are scaled accordingly using the factors $\left(\frac{2}{L}\right)^2$ and 4. See references [24, 26, 27] for more details on the spectral collocation approach. We now apply collocation to the linearized pairs so that we have the following numerical scheme:

$$\left[-Re^{-1}\mathbf{D}^{(2,0)} + \mathbf{U}^r\mathbf{D}^{(1,0)} + (\mathbf{U}^r + R^{-1} + N)\right]\mathbf{U}_j^{r+1} - \sum_{n=0}^{M_y}\Big[Re^{-1}\mathbf{D}^{(0,2)} - (\mathbf{V}_x^r - \alpha y_n Re^{-1})\mathbf{D}^{(0,1)}\Big]\mathbf{U}_n^{r+1} + \left[\mathbf{U}_y^r\right]\mathbf{V}_j^{r+1} = \mathbf{U}^r\mathbf{U}_x^r + \mathbf{V}^r\mathbf{U}_y^r - \mathbf{P}_x^r, \tag{4.21a}$$

$$[\mathbf{V}_x^r]\,\mathbf{U}_j^{r+1} - \left[Re^{-1}\mathbf{D}^{(2,0)} - \mathbf{U}^r\mathbf{D}^{(1,0)} - (\mathbf{V}_y^s + R^{-1})\right]\mathbf{V}_j^{r+1} - \sum_{n=0}^{M_y}\Big[Re^{-1}\mathbf{D}^{(0,2)} - (\mathbf{V}^r - \alpha y_n Re^{-1})\mathbf{D}^{(0,1)}\Big]\mathbf{V}_n^{r+1} = \mathbf{V}^r\mathbf{V}_y^r + \mathbf{U}^r\mathbf{V}_x^r - \mathbf{P}_y^r + Gr\boldsymbol{\Theta}^r, \tag{4.21b}$$

$$\mathbf{D}^{(2,0)}\mathbf{P}_j^{r+1} + \sum_{n=0}^{M_y}\mathbf{D}^{(0,2)}\mathbf{P}_n^{r+1} - \sum_{n=0}^{M_y}GrRe^{-2}\mathbf{D}^{(0,2)}\boldsymbol{\Theta}_n^{r+1} = 2(\mathbf{U}_x^{s+1}\mathbf{V}_y^{r+1} - \mathbf{U}_y^{r+1}\mathbf{V}_x^{r+1}) - N\mathbf{U}^{r+1}, \tag{4.21c}$$

$$\left[-(PrRe)^{-1}\mathbf{D}^{(2,0)} + \mathbf{U}^{r+1}\mathbf{D}^{(1,0)}\right]\boldsymbol{\Theta}_j^{r+1} - \sum_{n=0}^{M_y}\left[(PrRe)^{-1}\mathbf{D}^{(0,2)} - \mathbf{V}^{r+1}\mathbf{D}^{(0,1)}\right]\boldsymbol{\Theta}_n^{r+1} = J\mathbf{U}^{r+1}, \tag{4.21d}$$

and the following boundary conditions:

$$\left.\begin{aligned} &\mathbf{U}^{r+1}(x_i, y_{M_y}) = 0, \quad \sum_{m=0}^{M_y}\mathbf{D}_{0,m}^{(0,1)}\mathbf{U}^{r+1}(x_i, y_m) = 0, \quad \mathbf{U}^{r+1}(x_0, y_j) = U_{in}, \\ &\mathbf{V}^{r+1}(x_i, y_{M_y}) = -1, \quad \mathbf{V}^{r+1}(x_i, y_0) = 0, \quad \mathbf{V}^{r+1}(x_0, y_j) = 0, \end{aligned}\right\} \tag{4.22}$$

$$\left.\begin{aligned} &\mathbf{P}^{r+1}(x_i, y_{M_y}) = 1, \quad \sum_{m=0}^{M_y}\mathbf{D}_{0,m}^{(0,1)}\mathbf{P}^{r+1}(x_i, y_m) = 0, \quad \mathbf{P}^{r+1}(x_0, y_j) = 0, \\ &\boldsymbol{\Theta}^{r+1}(x_i, y_{M_y}) = 1, \quad \sum_{m=0}^{M_y}\mathbf{D}_{0,m}^{(0,1)}\boldsymbol{\Theta}^{r+1}(x_i, y_m) = 0, \quad \boldsymbol{\Theta}^{r+1}(x_0, y_j) = 0. \end{aligned}\right\} \tag{4.23}$$

4.4 Results and discussion

This section analyses the effects of injection and dilation rates, buoyancy force, permeability, heat sink, magnetic field interaction and momentum-thermal diffusivity ratio on the axial and normal flow velocities, pressure variation and heat distribution inside the filter chamber. Unless varied in the figures presented in this section, the following values are used in the parametric analysis of the aforementioned flow properties:

Algorithm 1 Evaluation of the numerical solutions of the axial velocity, normal velocity, pressure and temperature using the PQLM.

1: define the number of grid points in x and y
2: define the differentiation matrices according to Ref. [52]
3: map the computational domain $[-1,1]^2$ to $[0,L]\times[0,1]$
4: scale the differentiation matrices
5: choose initial guess $\mathbf{U}^0, \mathbf{V}^0, \mathbf{P}^0, \boldsymbol{\Theta}^0$ for the solutions
6: **for** $r = 0, 1, 2, \ldots,$ **do**
7: define linear equations (4.21a) and (4.21b)
8: impose boundary conditions (4.22)
9: solve the system for $\mathbf{U}$ and $\mathbf{V}$
10: update $\mathbf{U}, \mathbf{V}$ and their derivatives
11: define linear pairs (4.21c) and (4.21d)
12: impose boundary conditions (4.23)
13: solve the linear system for $\mathbf{P}$ and $\boldsymbol{\Theta}$
14: update $\mathbf{P}, \boldsymbol{\Theta}$ and their derivatives
15: calculate the residuals
16: **if** all $\|\text{residuals}\|_\infty < 10^{-7}$ **then**
17: accuracy is achieved, **end for**
18: **else**
19: **repeat** *steps 7 to 15*

$Re = 2, \alpha = 1, R = 0.1, N = 0.5, Gr = 0.6, Pr = 0.6, J = 0.3$. The parameter values used in this study were chosen based on the filter design we envisage and to enable us to make a direct comparison with the design in Lekoko et al. [67].

4.4.1 Effects of wall contraction and expansion, α, on the velocity, pressure and temperature.

Figure 4.2 shows that when the filter chamber compresses, the magnitude of the axial velocity at the region close to the filter chamber's left inlet before the fluid becomes fully developed is greater than the velocity of the fluid when the filter chamber expands. These dynamics result from the movement of fluid particles in the normal direction to occupy the space created by the expansion of the filter chamber, and compression of the filter leads to increased out-flux of fluid particles. Beyond a critical point (at $x \approx 0.75$), when the flow is past the entrance length, the axial flow rate remains constant along the length of the chamber because, at this point, the fluid is fully developed. The sudden compression of the filter chamber creates a region where fluid particles close to the chamber walls move faster than the fluid particles when the walls dilate. Figure 4.2a shows that when the chamber compresses, fluid particles close to the channel wall become excited and decelerate faster in the entrance length region. In contrast, the fluid particles near the walls decelerate slower when the filter chamber dilates. However, towards the outlet of the filter, the fluid particles move faster when the filter chamber contracts compared to when the chamber expands, as seen in Figure 4.3. This behaviour towards the outlet of the filter chamber is similar

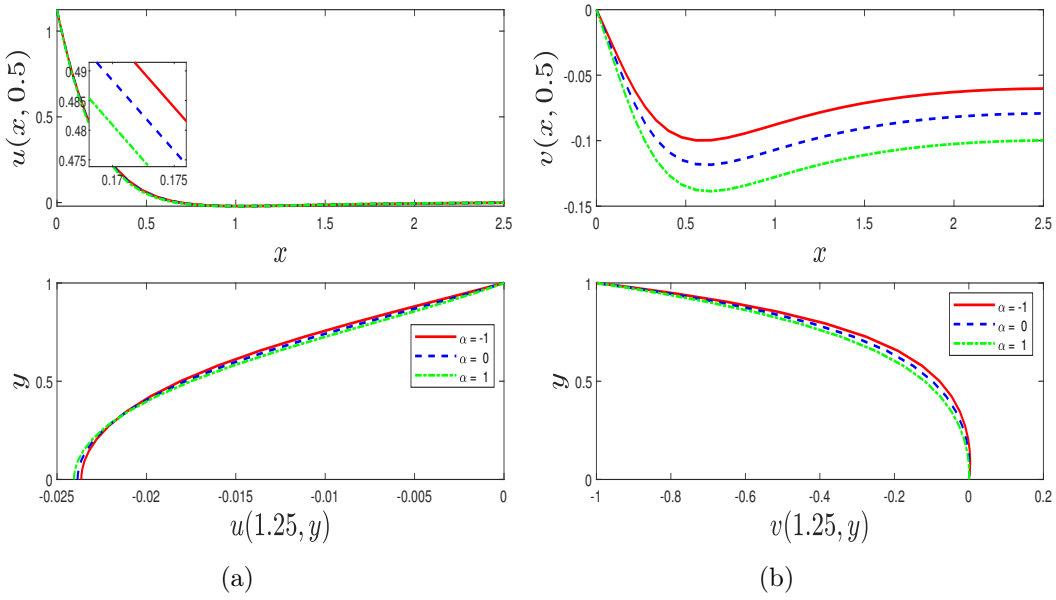

Figure 4.2: Dependency of wall dilation rate, α, on the axial and normal velocities of the fluid.

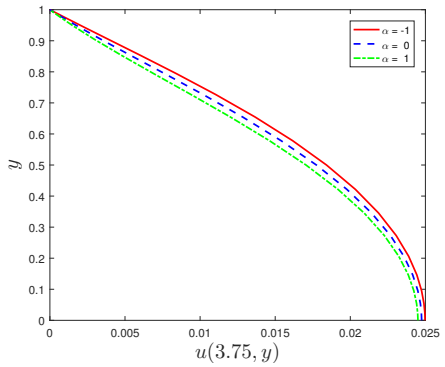

Figure 4.3: Effect of the wall dilation rate on the axial velocity after the fluid is fully developed.

to what was observed in Lekoko et al. [67]. Close to the centre of the chamber, around $y \approx 0$, there is a transition in the behaviour of the fluid particles. In this region, the fluid decelerates faster when the filter chamber expands. The internal temperature increases when the chamber volume space increases since the work done by the system increase when particles move freely due to additional space created by expansion. The internal pressure in both directions increases due to work done by the walls during contraction. This behaviour attests to the inverse proportionality of pressure distribution and the area occupied by the fluid particles. The contraction of the filter chamber causes fluid particles to cluster, thus amplifying internal pressure. However, when the filter chamber expands, more space is created inside the filter chamber for fluid particles to move freely, thus diminishing the pressure distribution inside the filter chamber.

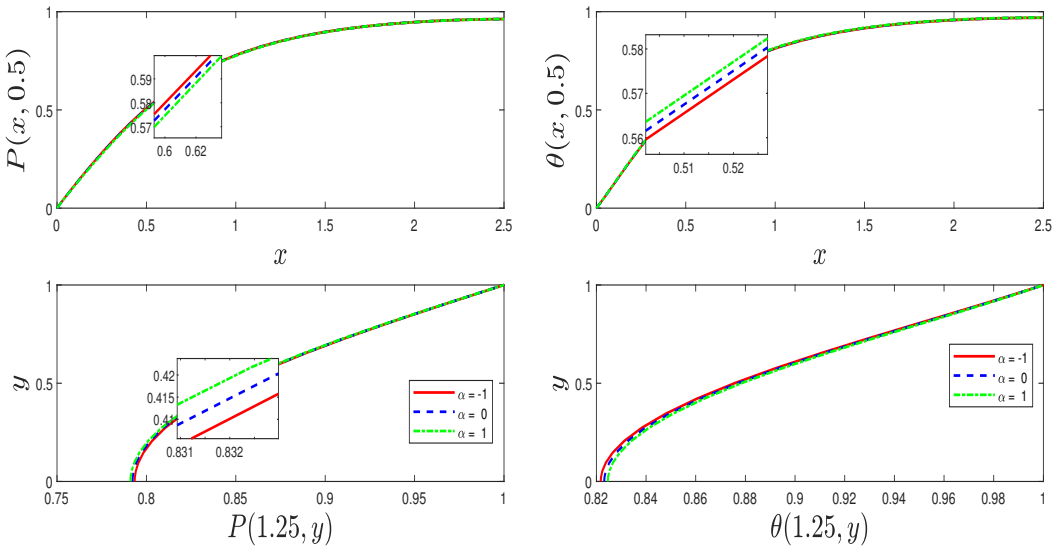

(a) (b)

Figure 4.4: Effects of α on pressure variation and temperature distribution in the chamber.

4.4.2 Effects of injection rate, Re, on the velocity, pressure and temperature.

As the fluid enters the filter chamber with velocity, $U_{in} = 1.5(1 - y^2)$, it travels a certain distance through the filter chamber before it becomes fully developed. According to Figure 4.5a, the fluid enters the filter at higher axial velocity due to the momentum of the fluid before entering the chamber but decreases as it moves inside the filter when more fluid is injected through the permeable walls. This decrease in flow velocity is due to the increase in internal drag when more fluid particles are injected into the chamber, increasing the viscous force created by the filter walls. When the system allows more fluid injection through the permeable walls, it causes a reverse flow that is more dominant than the flow across the filter chamber's length, thus reducing the axial momentum. On the other hand, the normal-component flow rate increases when fluid injection increases because the system experience more work done by fluid injection through the permeable walls. Since the momentum is directly proportional to velocity, the increase in the normal component velocity increases the momentum along the height of the filter chamber. Therefore, increasing the flow in the normal direction as depicted by Figure 4.5b.

Due to more thermal diffusion happening at the walls compared to the centre of the filter chamber, the internal temperature is high at the walls and less in the centre of the filter chamber as shown in Figure 4.6. At the filter's left entry region, the internal temperature is higher for less fluid injection since fluid particles move freely, thus increasing the kinetic energy and velocity. However, when more fluid is injected into the filter chamber, fluid particles are clustered at the region close to the inlet, thus resulting in less free movement of fluid particles and, consequently, less internal kinetic energy. Once the fluid particles reach a critical point, kinetic energy is proportional to the fluid injection rate. The internal pressure, in both directions, increases with an increase in fluid injection because more

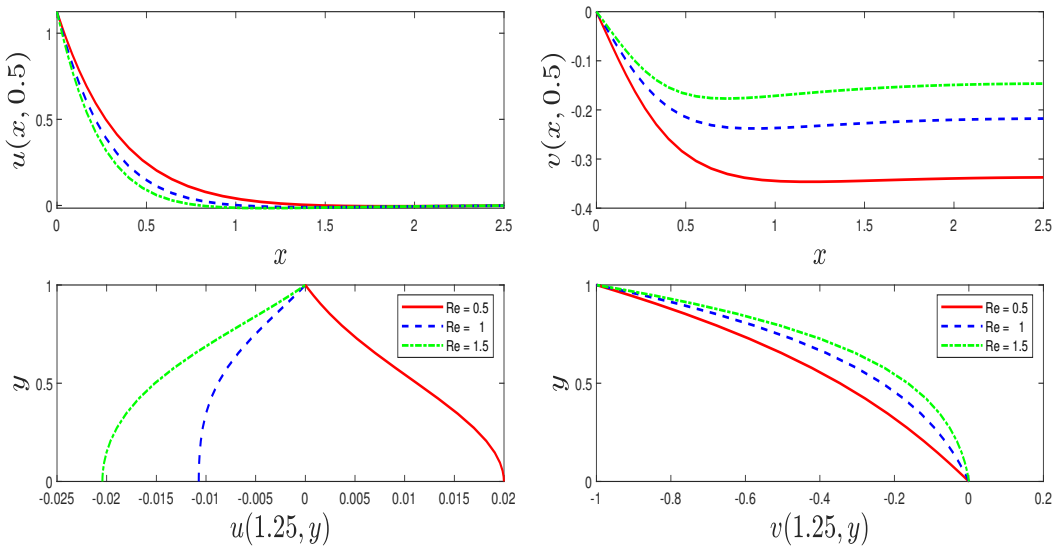

(a) (b)

Figure 4.5: Effects of fluid injection rate on the axial and normal velocities of the fluid.

internal mass leads to more pressure distribution inside the filter chamber.

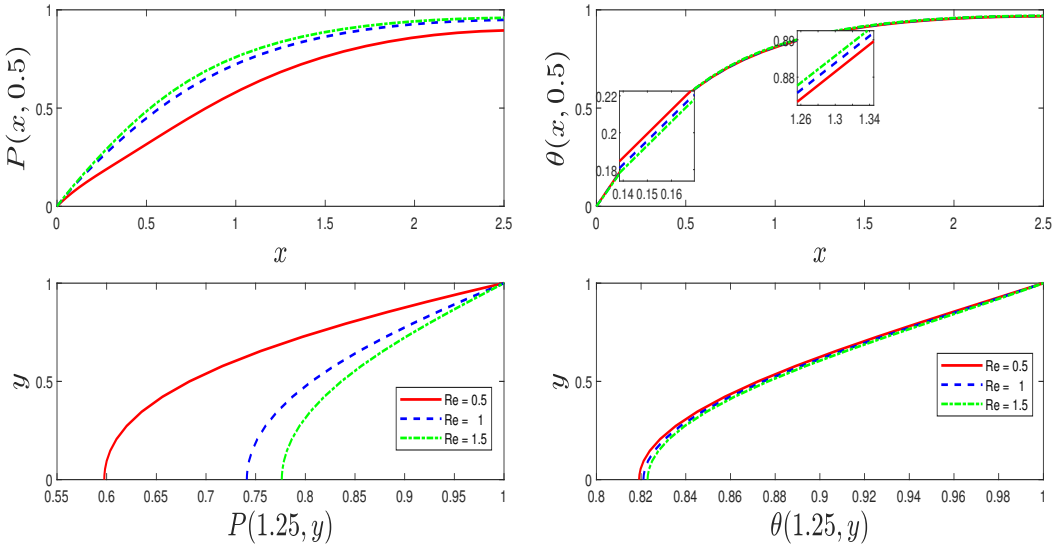

(a) (b)

Figure 4.6: Parametric dependency of the pressure variation and temperature distribution in the chamber on fluid injection rate.

4.4.3 Effects of the permeability parameter, R, on the velocity, pressure and temperature

Figure 4.7 shows that the fluid axial velocity increase as the permeability parameter increases in the entrance length region. However, the dynamics become reversed as soon as the fluid becomes fully developed. As the fluid becomes fully developed, the permeability parameter decreases the axial component velocity. The more the medium permeates, the

more fluid particles become free and occupy the available space in the porous medium. The normal velocity component increases with an increase in porous medium permeation. An increase in permeability leads to increased linear momentum along the x inside the filter chamber, increasing the fluid velocity magnitude, since small pore size do more work on the fluid particles compared to bigger pores. The internal pressure variation in the axial and normal direction decreases when the medium permeability increases (Figure 4.8). The decrease in pressure is due to a reduction in the work done inside the filter chamber because the internal stress in the filter chamber dwindles. The smaller the permeability, the more work the porous material does, creating more pressure distribution in the filter chamber. When the flow becomes fully developed, increased permeation rate amplifies the temperature distribution inside the chamber because the movement of fluid particles resulting from high permeation leads to increased kinetic energy. However, a high permeation rate diminishes energy within the entrance region length, thus decreasing temperature at the entrance region.

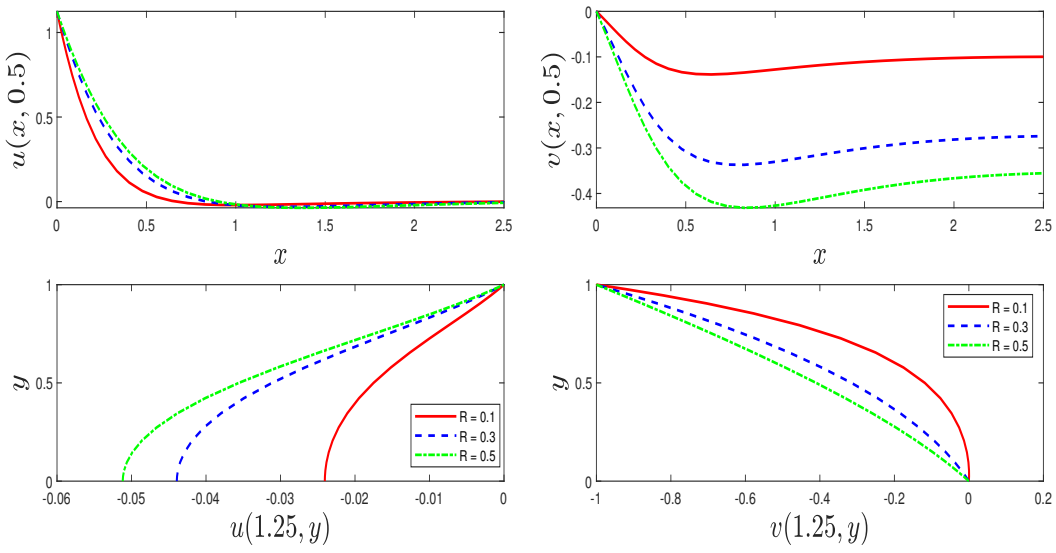

(a) (b)

Figure 4.7: Effects of permeability of the medium on the axial and normal velocities of the fluid.

4.4.4 Effects of magnetic field strength, N, on the flow rates, pressure and temperature distribution.

Figure 4.9 shows that increasing the strength of the magnetic field diminishes both the axial and normal components flow rates. This behaviour is because reinforcing the magnetic field binds fluid particles together, thus creating a drag force that opposes outflow and decreases momentum in both directions. Beyond the entrance length region, the influence of the magnetic field on the flow in the axial direction becomes minimal. However, the magnetic field affects the flow rate in the normal direction because the magnets are placed to act transversely to the axial axis. The effect of the magnetic field parameter on the internal pressure distribution is shown in Figure 4.10, and it can be seen that the pres-

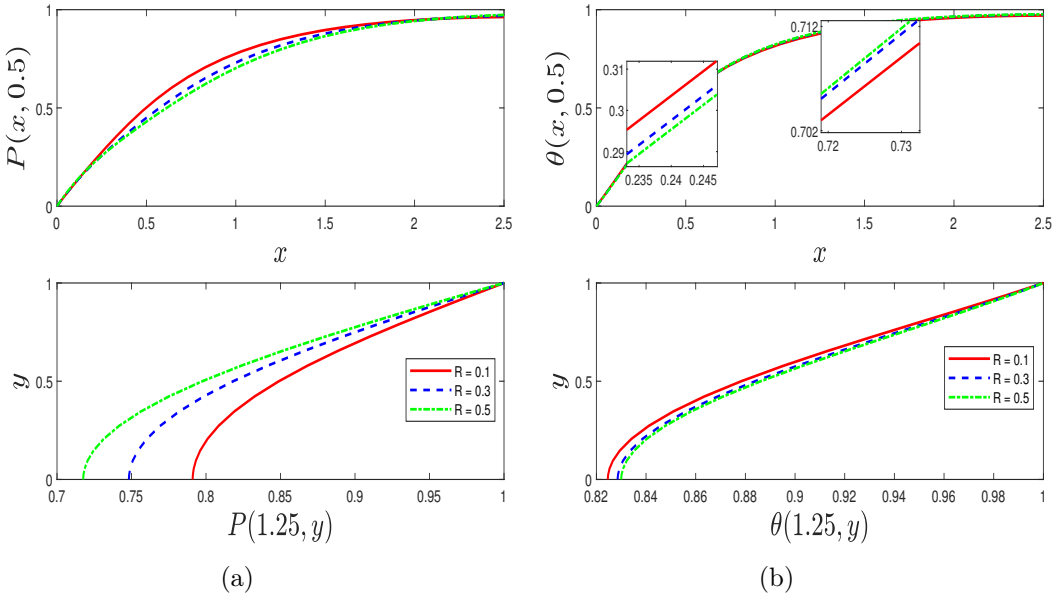

(a) (b)

Figure 4.8: Effects of permeability on pressure variation and temperature distribution inside the chamber.

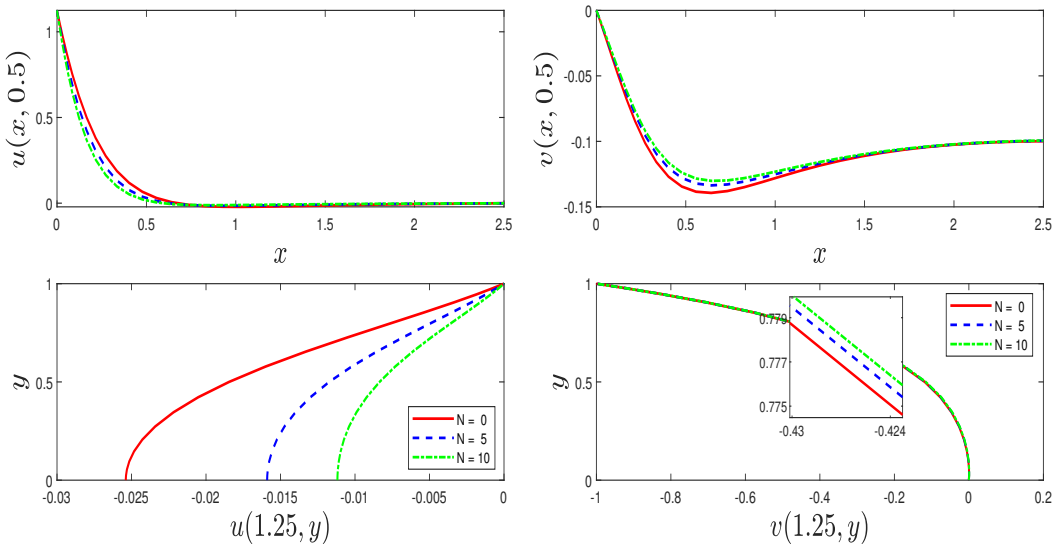

(a) (b)

Figure 4.9: Effects of magnetic field strength on the fluid flow rates.

sure distribution increases in both directions as the magnetic field is strengthened. The pressure increase due to the amplification of the magnetic field is because the work done by the magnetic field moves fluid particles towards the walls of the filter chamber. The temperature distribution in the filter chamber intensifies with an increase in the magnetic field parameter towards $y = 0$ because the magnetic force creates more clusters of fluid particles, thus creating more internal energy.

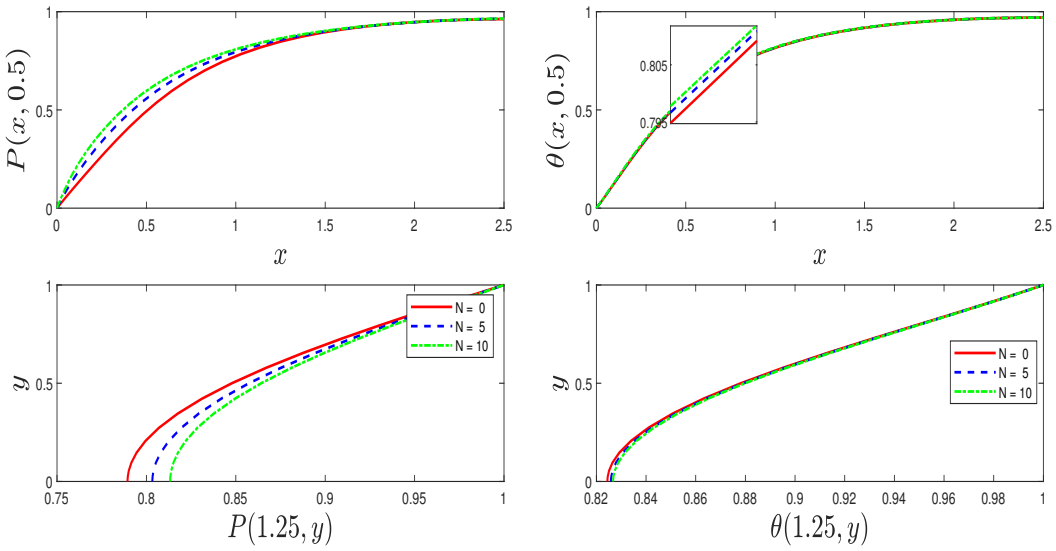

(a) (b)

Figure 4.10: Effects of magnetic field strength on pressure variation and temperature distribution in the chamber.

4.4.5 Effects of Grashof number Gr (buoyancy force), on the flow rates, pressure and temperature distribution

Figure 4.11 shows that increasing the buoyancy force parameter enhances the velocity in the axial direction. This dynamic is caused by more buoyancy force resulting in less density, thus leading to easy streaming of fluid particles. In contrast, the velocity in the normal component diminishes as the buoyancy force is enhanced since less dense particles move slower due to their weight acting downward.

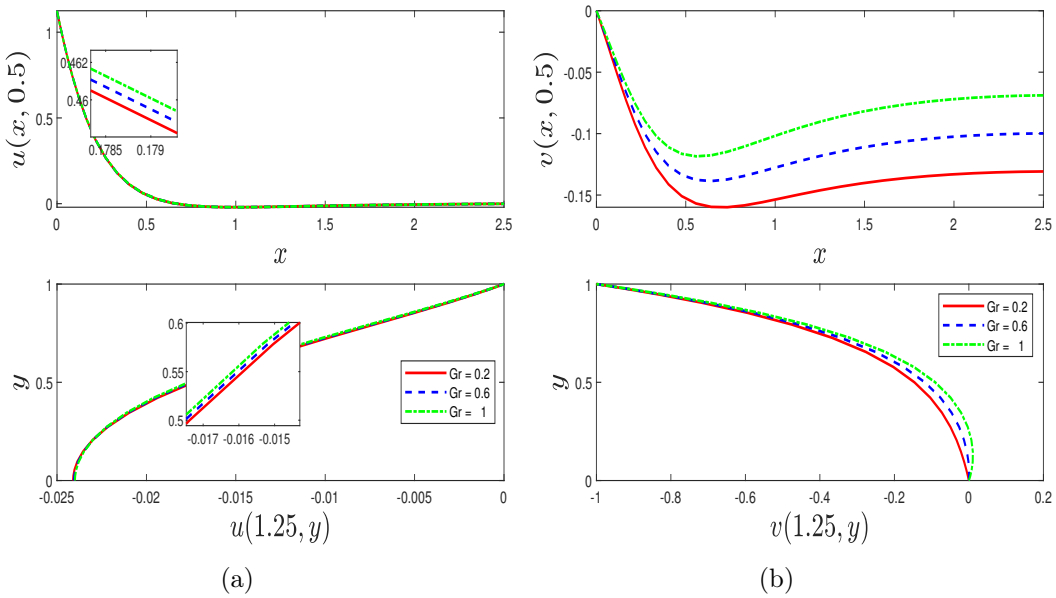

(a) (b)

Figure 4.11: Effects of buoyancy force on the velocities in the axial and normal components.

As portrayed by Figure 4.12, enhanced buoyancy force diminishes the internal pressure distribution in the filter chamber because the higher buoyancy effect implies that the fluid is less dense. Consequently, less work is done by the fluid particles inside the filter chamber. Thus, creating less internal pressure. Similar dynamics are observed in the temperature distribution since less work inside the filter chamber creates less internal energy.

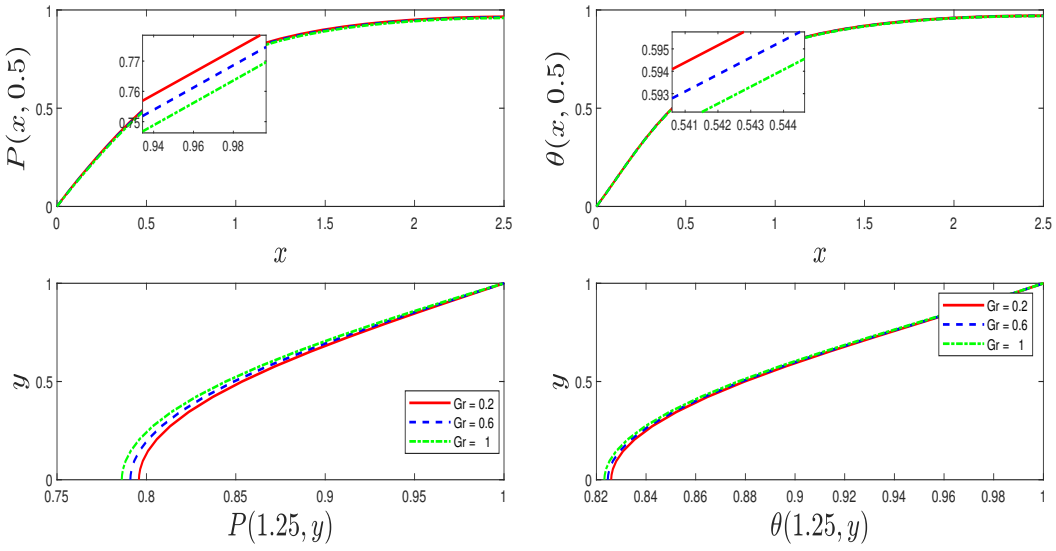

(a) (b)

Figure 4.12: Influence of buoyancy force on the pressure variation and temperature distribution inside the filter chamber.

4.4.6 Effects of momentum-thermal diffusivity ratio, Pr

The momentum-thermal diffusivity ratio has a minimal effect on the velocity of the fluid and the pressure distribution inside the filter chamber. Figure 4.13 shows that when the fluid is fully developed, increasing the Prandtl number increases the internal temperature distribution because enhancing the momentum-thermal diffusivity ratio increases the momentum diffusivity inside the filter chamber. This increase in momentum diffusivity creates resistance to the flow of the fluid, thus creating more internal energy and consequently increasing the temperature distribution in the filter chamber. Whereas, at the entrance length region, increased momentum-thermal diffusivity ratio diminishes the temperature in the region. This behaviour is because momentum diffusivity is less dominant in the entrance length region due to fluid inflow through the inlet.

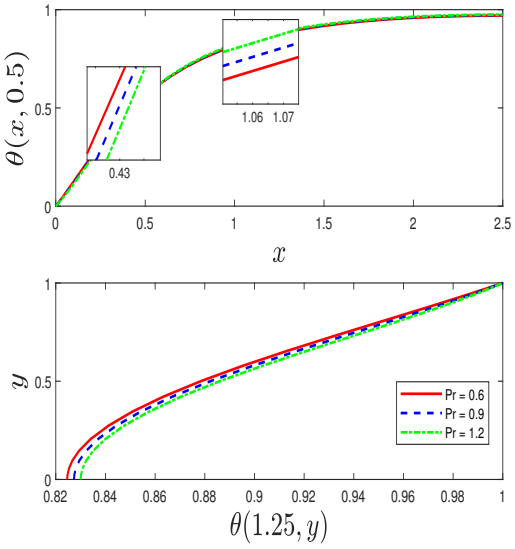

Figure 4.13: Effects of momentum-thermal diffusivity ratio on the temperature distribution inside the filter chamber.

4.4.7 Effects of heat sink, J

When Joule heating increases, as shown in Figure 4.14b, fluid temperature decreases; this is due to fluid particles finding it difficult to move due to the effect of the magnetic force. The increase in Joule heating reduces kinetic energy, and as a result, diminishes the temperature distribution in the filter chamber. Figure 4.14a shows that pressure distribution decreases with an increase in the heat sink parameter. This dynamic is due to Lorenz force becoming minimal for small Joule heating or heat sink, resulting in higher internal pressure caused by the free movement of fluid particles for small values of Joule heating parameter.

4.4.8 Impact of wall dilation, fluid injection, porous medium permeability and magnetic field strength on the overall wall drag

The wall drag in the current filter design is unlike the asymmetric behaviour of the wall drag observed in a filter chamber with two outlets studied by Lekoko et al. [67]. As portrayed by Figure 4.15, since there is an inflow U_{in} at the left inlet, there is higher shear stress at the walls of the filter chamber in the entrance length region compared to the wall shear stress at the outlet. Additionally, wall shear stress at the outlet is lesser than wall drag at the inlet because the fluid particles in the entrance length region have more velocity than particles at the outlet. Fluid particles in the fully developed region experience less wall shear stress, almost zero, than particles at the inlet and outlet. The wall drag increases in magnitude as the wall dilation rate decreases, as seen in Figure 4.15a. When the filter chamber contracts, particles are clustered at the chamber's walls, creating more frictional force as they move along the walls of the filter; in contrast, a less frictional force is generated at the walls when the filter expands because fluid particles move at a lesser speed. There is more frictional force at the chamber's walls for less fluid injection because more fluid particles injection pushes the particles away from the walls into the centre of

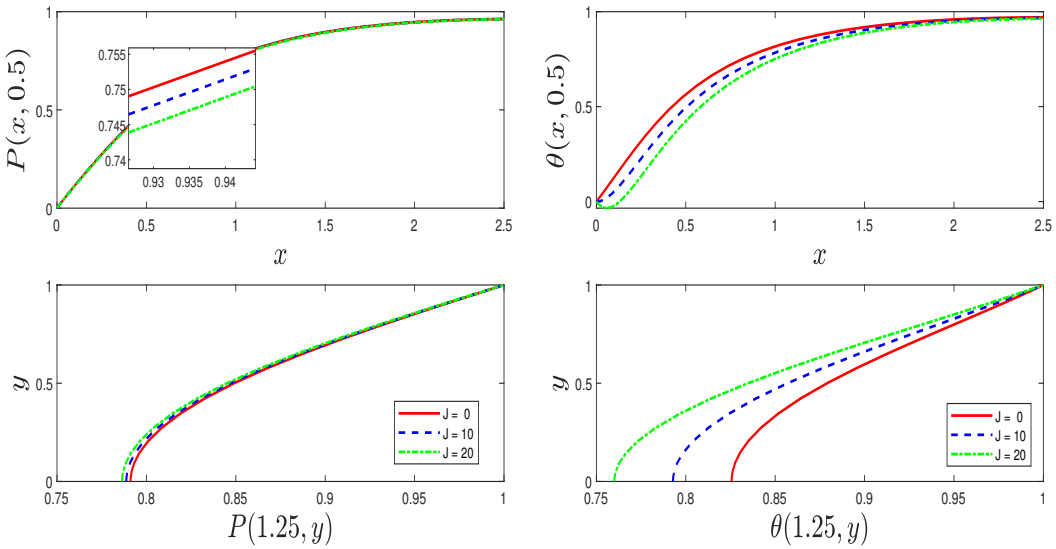

(a) (b)

Figure 4.14: Effects of heat sink on pressure variation and temperature distribution inside the filter chamber.

the filter chamber. Therefore, there is less wall shear stress at the entrance length region when more fluid is injected into the filter chamber. However, an opposite behaviour is observed at the outlet because the fluid is fully developed, and the effect of the injection is minimal. The higher the permeation, the higher the frictional force exerted by the filter's wall because more permeation increases the flow rate. Although, in the fully developed region, the porous medium is well-saturated, and fluid particles move at a slower rate, thus creating less wall drag for higher permeability. Increased magnetic field strength creates less wall drag because the more potent the magnetic field, the less the velocity of the fluid due to the resistance created by magnetic flux. This resistance consequently creates a less frictional force at the filter chamber walls.

4.5 Conclusion

This chapter investigated an injection-driven flow in a dilating or contracting filter chamber bounded by two semi-permeable walls. Fluid particles entered the filter chamber with a parabolic velocity through an opening on the left end of the axial axis. The filter chamber is constructed to have an orifice on the right end of the axial axis, serving as the solitary outlet for the filtered fluid particles. The governing equations described by the Navier-Stokes, continuity and energy conservation equations were reduced to a steady state equations using Lie point symmetry method and solved using the spectral-based paired quasilinearization method. Analysis of the influence of parameters such as injection rate, permeability, wall dilation or contraction rate, magnetic flux strength on the flow rates, pressure variation, temperature distribution and wall drag were carried out. Among other results, we found that:

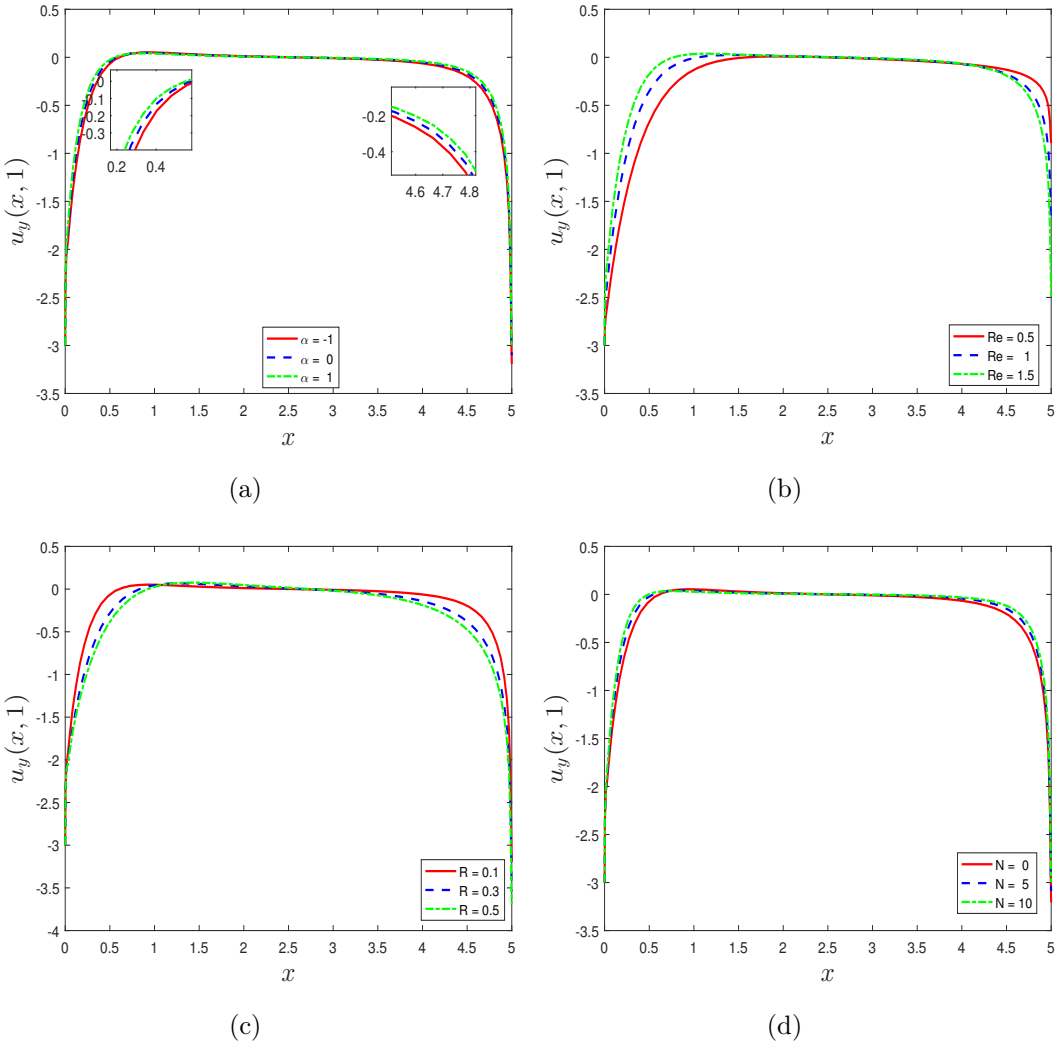

Figure 4.15: Effects of wall dilation, fluid injection, media permeability and magnetic field strength on the wall drag.

1. When the filter chamber contracts, fluid particles close to the filter's walls in the entrance length region decelerate faster, and consequently, a high opposing frictional force at the wall. Further, the contraction of the filter chamber amplifies the pressure variation inside the filter.

2. To avoid the occurrence of a reverse flow in the filter chamber, it is essential to keep the injection rate minimal because more fluid injection creates a region of reverse flow. Fluid particles exert a relatively high temperature in the entrance region for less fluid injection. Pressure variation inside the chamber increases as more fluid is injected into the filter chamber.

3. In the region where the fluid is fully developed, the magnetic field has minimal influence on the fluid flow rates. However, amplifying the magnetic field increases the pressure variation and temperature distribution inside the filter chamber while creating less friction at the filter walls.

Chapter 5

Analysis of buoyancy driven flow inside a vertical filter chamber

Designs based on scientific evidence play an essential role when engineering machinery. This chapter seeks an alternative way of filtering particles using a permeable surface. The filter is designed so that the effects of heat from a permeable bottom wall create a force that drives permeates out of the filter chamber. The model follows the mass conservation, incompressible Navier-Stokes and the energy conservation equations. Effects of parameters arising from flow dynamics and heat distribution are studied to better understand the theory behind the filtrations process. Graphical representations of skin friction and Nusselt number inside the filter chamber are plotted against filtration dynamics parameters. We found that more permeates are produced when the internal energy is low since the system loses internal temperature when less dense fluid, which possesses heat, is withdrawn from the chamber. In addition, the chamber volume increase permeates outflow since it enhances the pulling effects of the buoyancy force. It is found that increasing the Richardson number ehnances the buoyancy forces and viscous effects; thus, decreasing permeates outflow velocity and eventually reduces wall drag coefficient. The wall drag coefficients on the left and right vertical walls have extrema towards the bottom of the filter chamber, in the region, $0 < y < 2\%H$.

NOMENCLATURE

c_p - specific heat, $J/kg\,K$

g - acceleration due to gravity, m/s^2

H - height of the filter chamber, m

L - length of the filter chamber, m

U_L - constant velocity exerted by the left wall, m/s

U_R - constant velocity exerted by the right wall, m/s

f_x - body forces in the axial direction, Nm^{-2}

f_y - body forces in the axial direction, Nm^{-2}

Φ - heat source or sink

κ - thermal conductivity, W/mK

q_r - radiative heat flux

ν - kinematic viscosity

V_w - suction velocity at the wall, m/s

u - axial velocity, m/s

v - normal velocity, m/s

T - temperature of the fluid, K

x - axial coordinate, m

y - normal coordinate, m

P - total pressure of the system, m

u^* - non-dimensional axial velocity

v^* - non-dimensional normal velocity

θ - non-dimensional temperature

x^* - non-dimensional axial coordinate

y^* - non-dimensional normal coordinate

κ_r - mean absorption coefficient, m

σ_r - Stefan-Boltzmann constant, m

ρ - fluid density, kg/m^3

δ - filter chamber volume ratio

λ - internal heat generation parameter

R_i - Richardson number

R_e - Reynolds number

P_r - Prandtl number

R - radiation parameter

U - work done by the vertical walls

C_f - skin friction coefficient

N_u - Nusselt number

Subscripts

w - filter wall

5.1 Introduction

Scientific findings provide engineers and scientists with theoretical knowledge to improve the efficiency of filter designs that separate particles from liquid arising from warming dense material. When filtering, one of the most challenging issues is transferring heat at the desired rate to maintain the quality of the final product (filtrates). Overall, optimizing filtrate production by controlling forces affecting the flow without overworking the filter system can be a complicated issue to address when designing the filter system. To find ways on how to handle such issues when designing filters, it is ideal to start with the theoretical foundation and analyse the flow and heat transfer behaviour for better, if not perfect, designs. One of the essential areas of theoretical studies and design is controlling the flow and heat at the desired rate. Hence, a lot of work has been done on flow and heat transfer using different mathematical tools to obtain solutions that give scientific evidence that can be used to improve such designs.

Sa et al. [68] conducted the study of incompressible flow and heat transfer. Their study validated the Boussinesq approximation in an incompressible flow with slight temperature variation. The mathematical formulation was validated using the INS3D (Incompressible Navier-Stokes Solve) code for numerical results. Their results have shown that the Boussinesq approximation could predict flow behaviour accurately for both free, mixed and forced convection problems. The viscous incompressible fluid driven by buoyancy in an open-ended rectangular cavity with permeable surfaces was examined by Hossain et al. [69]. The effects of buoyancy force variation and the permeability of the surfaces were the centre of attention in their study. The authors numerically solved the governing boundary layer equations representing the flow and heat transfer using the upwind finite-difference method combined with successive over-relaxation iteration techniques. Their findings show that the fluid temperature near the upper surface of the cavity is enhanced due to buoyancy force.

Recently, Dizjeh and Brinkerhoff [70] investigated the buoyancy-driven flow stability in a channel between an isothermal heated vertical and adiabatic vertical walls. The authors proposed the finite difference method to solve the derived stability equation. Their findings show that the bottom flow resembles a boundary layer with an irrotational core velocity close to the adiabatic wall, which is strongly affected by the Grashof number and aspect ratio. The application of the buoyancy-driven flow inside refrigerated cabinets and freezers was studied by Hermes et al. [71] using the CFD model. The authors evaluated the program performance by comparing it with the numerical solutions of classical cavity flows driven by buoyancy found in the literature. Abin Rejeesh et al. [72] investigated mixed convection flow caused by buoyancy, which is generated due to a non-uniformly heated wall moving uniformly using the finite difference scheme. Their findings show that the temperature inside the cavity undergoes non-monotonic changes in the mixed convection region. However, in the forced convection regime, when the Richardson number $R_i << 1$, the temperature in the central region of the cavity remains constant.

Moallemi and Jang [73] studied the effect of the Prandtl number on the flow and heat transfer process of mixed convection in a bottom wall heated and side walls insulated lid-driven square cavity numerically. They discovered that buoyancy effects are more prominent for higher Prandtl numbers. Basak et al. [74] examined a mixed convection lid-driven flow in a square cavity with the bottom wall heated uniformly and non-uniformly, respectively. In contrast, the two vertical walls are maintained at constant cold temperature, and the top insulated wall moves with uniform velocity. The findings depict that the natural or forced convection is based on both the parameters $R_i\left(=\frac{G_r}{R_e^2}\right)$ and P_r. The network method was used to solve fluid flow and heat transport in porous media by Cánovas et al. [75]. The study found that the method can be used without any mathematical manipulations besides what the program needs. The analysis of the stable filtration process inside a horizontal chamber was done by Magalakwe et al. [16]. The study found that to have a well-behaved flow; there should be a good balance between the fluid injection into the filter chamber and buoyancy effects. The dominant effects of buoyancy were found to bring instability to the chamber wall. A lot of studies have been done to learn more about mixed convection flow in different geometry, which arises from channels bounded by different boundaries, such as the works by [76–82].

This chapter is motivated by the filtration process to improve techniques for removing unwanted solid materials from the fluid. The chapter also, seeks to investigate further the filtration process in Magalakwe et al. [16] by redesigning a filter such that buoyancy force acts in the direction of permeates outflow instead of pulling the flow towards the chamber walls. Hence, the current filter design is such that it filters solid from the liquid at the bottom permeable plate. The bottom plate is kept at a constant temperature to make the fluid less dense and allow outflow driven by buoyancy force in the direction of gravity. The bottom wall is permeable, allowing only liquid to flow through it while restricting solid particles from remaining inside the chamber. After some time, the solid particles are expected to pile up, forming a filter cake due to restrictions caused by the permeable wall; hence flushing the system is ideal for free liquid movement.

Even though the filter cake has its advantage, which is enhancing the effects of the filter medium, it makes filtrates cleaner. However, this decreases outflow. The current design is such that the system flushes out restricted particles before this decrease in discharge happens, thus ignoring the influence of filter cake during the process. The flow starts when the dense fluid melts so that the work done by the vertical walls and the buoyancy effects are enough to drive flow out of the filter chamber. The chapter's goal is to investigate a mathematical model representing the current flow and heat transfer. After that, solve the model using the spectral method to provide a theoretical fluid flow analysis of how different parameters affecting the flow can be controlled to optimize the filtrates (outflow) and fluid temperature. Furthermore, the study will provide a physical interpretation of the results to understand the flow velocity and temperature variation inside a vertical filter chamber during the filtration process.

The current chapter is concerned with the theoretical analysis of the buoyancy-driven flow

and heat transfer in a vertical filter chamber. The chapter seeks to understand the dynamics that arise when the heated bottom wall heats fluid inside the filter chamber, such as Richardson number, Reynolds number, radiation parameter, chamber volume, heat generation and Prandtl number. The partial differential equations describing the flow and heat transfer in the proposed filter chamber are solved using a spectral-based linearization technique. Detailed documentation of this procedure, particularly for multivariate differential equations, can be found in Motsa et al. [27] and Lekoko et al. [67]. The technique has been established to be accurate, efficient and convergent. See study Acharya [83] where the method was used to analyze heat and mass transfer problems.

5.2 Model Formulation

A steady incompressible fluid flow and heat transfer in the x-y plane is considered, as shown in the figure below

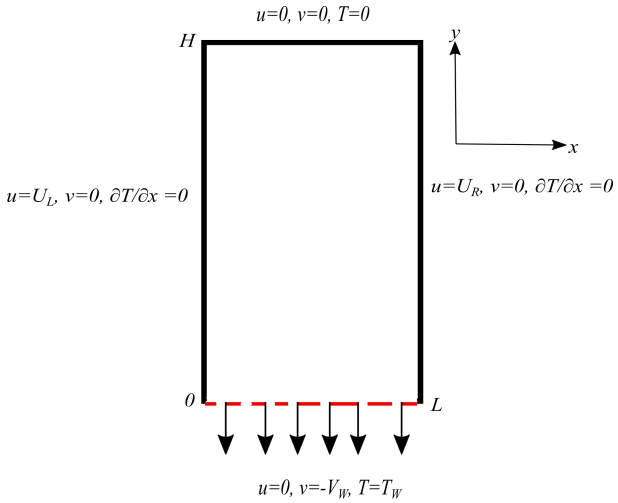

Figure 5.1: Flow and heat transfer schematic representation.

Thus, the conservation mass, momentum, and energy are as follows [84, 85]:

$$\left.\begin{aligned}
&\frac{\partial u}{\partial x}+\frac{\partial v}{\partial y}=0,\\
&\frac{1}{\rho}\frac{\partial P}{\partial x}+u\frac{\partial u}{\partial x}+v\frac{\partial u}{\partial y}=\nu\left[\frac{\partial^2 u}{\partial x^2}+\frac{\partial^2 u}{\partial y^2}\right]+f_x,\\
&\frac{1}{\rho}\frac{\partial P}{\partial y}+u\frac{\partial v}{\partial x}+v\frac{\partial v}{\partial y}=\nu\left[\frac{\partial^2 v}{\partial x^2}+\frac{\partial^2 v}{\partial y^2}\right]+f_y,\\
&u\frac{\partial T}{\partial x}+v\frac{\partial T}{\partial y}=\frac{\kappa}{\rho c_p}\left[\frac{\partial^2 T}{\partial x^2}+\frac{\partial^2 T}{\partial y^2}\right]+\frac{1}{\rho c_p}\Phi,
\end{aligned}\right\} \tag{5.1}$$

since the flow is laminar and the filter chamber walls are smooth, no work is done by neighbouring fluid layers due to the effect of shear forces, which is converted into heat. As a result, energy production through viscous dissipation is neglected in the energy equation.

5.2.1 Momentum equations

There are no external body forces (i.e. $f_x = 0$) in the axial direction since vertical walls exert constant pressure and velocity during operation. Thus, the system is such that there is no axial momentum variation. Also, since the constant temperature (T_w) is applied at the bottom chamber wall, temperature variation within the fluid bulk results in a body force that pulls fluid particles downwards. This results in a thermal convection flow driven by buoyancy forces. As a result, the gravitational acceleration is the only meaningful body force thus, internal pressure remains constant. Thus, system momentum is given by

$$u\frac{\partial v}{\partial x} + v\frac{\partial v}{\partial y} = \nu\left[\frac{\partial^2 v}{\partial x^2} + \frac{\partial^2 v}{\partial y^2}\right] + f_y. \tag{5.2}$$

Variations in density indicate that the fluid is compressible as opposed to incompressible. Because the fluid under discussion is incompressible and the flow is driven by buoyancy, we can use the *Boussinesq approximation*, in which density fluctuations are assumed to be negligible except for the gravity term [86, 87]. Thermal convection occurs as a result of density variation, which can be described in terms of temperature at constant pressure as follows:

$$\rho_w - \rho = \rho\beta(T - T_w), \quad (at\, constant\, P) \tag{5.3}$$

where β is the thermal expansion coefficient. Because buoyancy force resists gravitational acceleration, the net external force, which is the difference between two forces in the y direction, becomes:

$$f_y = g(\rho_w - \rho). \tag{5.4}$$

Substitution of equation (5.3) into equation (5.4), gives

$$f_y = g\rho\beta(T - T_w). \tag{5.5}$$

Using the above result in (5.2) yields

$$u\frac{\partial v}{\partial x} + v\frac{\partial v}{\partial y} = \nu\left[\frac{\partial^2 v}{\partial x^2} + \frac{\partial^2 v}{\partial y^2}\right] + g\rho\beta(T - T_w). \tag{5.6}$$

5.2.2 Energy Equation

The current design is such that there is heat conduction due to wall temperature and fluid radiates energy. Thus the conventional energy equation which accounts for the effect of radiative transfer flux ($\bigtriangledown q_r$), heat flux due to conduction is given by $\frac{\kappa}{\rho c_p}\left[\frac{\partial^2 T}{\partial x^2} + \frac{\partial^2 T}{\partial y^2}\right]$ and interaction of fluid particles which give rise to internal heat energy (Q_0) is given by

$$u\frac{\partial T}{\partial x} + v\frac{\partial T}{\partial y} = \frac{1}{\rho c_p}\left[\kappa\frac{\partial^2 T}{\partial x^2} + \kappa\frac{\partial^2 T}{\partial y^2} + \frac{\partial q_r}{\partial y}\right] + \frac{1}{\rho c_p}Q_0. \tag{5.7}$$

Since radiative heat flux is normal to bottom plate heated with constant temperature and flow is 2-dimensional, the radiative heat flux only changes with respect to y. Utilizing the

usual *Rosseland approximation* of radiative heat flux term q_r as described by Bardos et al. [88] to represent the radiative heat flux in terms of temperature, we define q_r as

$$q_r = \frac{-4\sigma_r}{3k_r}\frac{\partial T^4}{\partial y}, \tag{5.8}$$

where T^4 can be expressed as a linear combination of temperature by using Taylor series expansion about T since the temperature variation inside the filter is assumed to be sufficiently small. Thus,

$$T^4 \approxeq 4T_h^3 T - 3T_h^4, \tag{5.9}$$

after neglecting higher order terms beyond the first degree in $(T - T_h)$. By substituting equation (5.9) into equation (5.8), we get

$$q_r = \frac{-4\sigma_r}{3k_r}\frac{\partial}{\partial y}(4T_h^3 T - 3T_h^4). \tag{5.10}$$

Differentiating equation (5.10) with respect to y and using the obtained results into the energy equation (5.7), yields the energy equation inside the vertical filter chamber as

$$u\frac{\partial T}{\partial x} + v\frac{\partial T}{\partial y} = \frac{\kappa}{\rho c_p}\left[\frac{\partial^2 T}{\partial x^2} + \frac{\partial^2 T}{\partial y^2}\right] - \frac{16\sigma_r T_h^3}{3\rho c_p k_r}\frac{\partial^2 T}{\partial y^2} + \frac{1}{\rho c_p}Q_0. \tag{5.11}$$

5.2.3 Boundary conditions

The mathematical model describing the flow and heat transfer is complete once the boundary conditions are stated.

- At the top wall $(y = H)$: there is no suction or injection and movement of the filter chamber wall in both the axial and normal direction, thus $u(x, H) = 0,\ v(x, H) = 0$. This is due to no-slip condition at the top since the fluid layers close to the top wall approximate the axial and normal velocity of the wall (i.e zero velocity). Also, the temperature of the wall is taken to be zero, thus $T(x, H) = 0$.

- At the vertical walls $(x = 0,\ x = L)$: the design is such that the work done by walls moves the fluid with constant axial velocities, namely left velocity (U_L) and right velocity (U_R), respectively. Since fluid layers close to the wall approximate the velocity generated by the wall due to work done by the wall, therefore $u(0, y) = U_L$ and $u(L, y) = U_R$. The vertical walls are not moving in the y direction, the velocity in the y direction due to no-slip condition are given by $v(0, y) = 0$ and $v(L, y) = 0$. In addition, the walls are thermodynamically adiabatic, meaning no heat flux can enter or leave the walls; therefore $\left.\frac{\partial T}{\partial x}\right|_{x=0,L} = 0$ on the vertical walls

- At the bottom wall $(y = 0)$: the wall is at rest, so the no-slip condition yields $u(x, 0) = 0$. The normal velocity is given by $v(x, 0) = -V_w$, since permeates exit the chamber downwards through the permeable wall. The negative sign denotes the downwards outflow of permeates. The fluid inside the filter chamber is heated from the bottom with constant temperature $T(x, 0) = T_w$ to melt the dense fluid.

Based on the presumptions which arise from the filter design, the system of equations describing the flow and heat transfer inside a filter chamber is given by

$$\left.\begin{aligned}
&\frac{\partial u}{\partial x}+\frac{\partial v}{\partial y}=0,\\
&u\frac{\partial v}{\partial x}+v\frac{\partial v}{\partial y}=\nu\left[\frac{\partial^2 v}{\partial x^2}+\frac{\partial^2 v}{\partial y^2}\right]+g\rho\beta(T-T_h),\\
&u\frac{\partial T}{\partial x}+v\frac{\partial T}{\partial y}=\frac{\kappa}{\rho c_p}\left[\frac{\partial^2 T}{\partial x^2}+\frac{\partial^2 T}{\partial y^2}\right]-\frac{16\sigma_r T_h^3}{3\rho c_p k_r}\frac{\partial^2 T}{\partial y^2}+\frac{Q_0}{\rho c_p}(T-T_h).
\end{aligned}\right\} \tag{5.12}$$

Subject to the following boundary conditions:

$$\left.\begin{aligned}
&\text{at } y=0,\ u(x,0)=0,\ v(x,0)=-V_w,\ \theta(x,0)=T_w,\\
&\text{at } y=H,\ u(x,H)=0,\ v(x,H)=0,\ \theta(x,H)=0,\\
&\text{at } x=0,\ u(0,y)=U_L,\ v(0,y)=0,\ \theta_x(0,y)=0,\\
&\text{at } x=L,\ u(L,y)=U_R,\ v(L,y)=0,\ \theta_x(L,y)=0.
\end{aligned}\right\} \tag{5.13}$$

5.2.4 Dimensional analysis

To understand the influence of physical quantities on the flow and heat transfer inside the vertical filter chamber, we introduce the dimensionless quantities below [89]:

$$\left.\begin{aligned}
&U=\frac{u}{V_w},\quad v^*=\frac{v}{V_w},\quad x^*=\frac{x}{L},\quad y^*=\frac{y}{H},\quad \theta=\frac{T-T_h}{T_w-T_h},\quad \delta=\frac{L}{H}\\
&R_i=\frac{g\beta L(T_w-T_h)}{V_w^2},\quad R_e=\frac{LV_w}{\nu},\quad \lambda=\frac{Lq_0}{\rho c_p V_w},\quad P_r=\frac{\rho c_p\nu}{\kappa},\quad R=\frac{4\sigma_r T_h^3}{3\kappa_r\kappa}.
\end{aligned}\right\} \tag{5.14}$$

According to the current filter design, the velocity U is given by U_R-U_L which is the net work done by vertical walls. Thus, the coupled system of equations representing the current case study is as follows:

$$\left.\begin{aligned}
&U\frac{\partial v^*}{\partial x^*}+\delta v^*\frac{\partial v^*}{\partial y^*}-\frac{1}{R_e}\left[\frac{\partial^2 v^*}{\partial x^{*2}}+\delta^2\frac{\partial^2 v^*}{\partial y^{*2}}\right]-R_i\theta=0,\\
&U\frac{\partial \theta}{\partial x^*}+\delta v^*\frac{\partial \theta}{\partial y^*}-\frac{\delta^2}{P_r R_e}\left[1+4R\right]\frac{\partial^2\theta}{\partial y^{*2}}-\lambda\theta=0.
\end{aligned}\right\} \tag{5.15}$$

The boundary conditions takes the following dimensionless form:

$$\left.\begin{aligned}
&\text{at } y^*=0,\ v^*(x^*,0)=-1,\ \theta(x^*,0)=1,\\
&\text{at } y^*=H,\ v^*(x^*,H)=0,\ \theta(x^*,H)=0,\\
&\text{at } x^*=0,\ v^*(0,y^*)=0,\ \theta_x(0,y^*)=0,\\
&\text{at } x^*=L,\ v^*(L,y^*)=0,\ \theta_x(L,y^*)=0.
\end{aligned}\right\} \tag{5.16}$$

The dimensionless wall drag at the left and right vertical walls are defined as follow:

$$C_f\Big|_{x^*=0,L}=\frac{2}{R_e}\frac{\partial v^*}{\partial y^*}\bigg|_{x^*=0,L}, \tag{5.17}$$

where $C_f\big|_{x^*=0}$ corresponds to the wall drag at the left vertical wall while $C_f\big|_{x^*=L}$ corresponds to the drag at the right vertical wall. The heat flux rate, that is the Nusselt number is defined as

$$Nus = -\delta(1+4R)\frac{\partial\theta}{\partial y^*}\bigg|_{y^*=0}. \tag{5.18}$$

5.3 Solution method

Dropping the asterisk for clarity, we proceed to solve the coupled system of equation

$$\left.\begin{aligned} U\frac{\partial v}{\partial x} + \delta v\frac{\partial v}{\partial y} - \frac{1}{R_e}\left[\frac{\partial^2 v}{\partial x^2} + \delta^2\frac{\partial^2 v}{\partial y^2}\right] - R_i\theta = 0, \\ U\frac{\partial \theta}{\partial x} + \delta v\frac{\partial \theta}{\partial y} - \frac{\delta^2}{P_r R_e}\left[1+4R\right]\frac{\partial^2 \theta}{\partial y^2} - \lambda\theta = 0, \end{aligned}\right\} \tag{5.19}$$

through the quasilinearization method introduced by Bellman and Kalaba [90]. Approximate solutions were sought in terms of the Lagrange interpolating polynomials collocated on the transformed Chebyshev-Gauss-Lobatto nodes:

$$\{x_i, y_j\} = \{L, H\}\left[-\cos\frac{\pi\{i,j\}}{\{N_x, N_y\}}\right], \qquad \begin{smallmatrix} i=0,1,2,\ldots,N_x; \\ j=0,1,2,\ldots,N_y. \end{smallmatrix} \tag{5.20}$$

Here, N_x and N_y are, respectively, the number of collocation points in the x and y domains. See studies such as Motsa et al. [27, 91] and Lekoko et al. [67] for the development of a pseudo-spectral quasilinearization scheme for partial differential equations. This procedure has been sufficiently documented in the literature and established to be computationally efficient, convergent and computationally accurate for multivariate differential equations [92]. System of eq. (5.19) is transformed into a coupled discrete form and solved iteratively for a fixed number of iterations. The spectral-based linearized form of system of eq. (5.19) is obtained as

$$\left.\begin{aligned} &\Big[-\frac{1}{Re}\mathsf{D}^2 + U\mathsf{D} + diag[\delta V_{y\{j,r\}}]\Big]V_{\{j,r+1\}} - \sum_{m=0}^{N_y}\Big[\frac{\delta^2}{Re}\mathcal{D}^2_{j,m} \\ &\qquad - diag[\delta V_{y\{j,r\}}]\mathcal{D}_{j,m}\Big]V_{\{m,r+1\}} - Ri\Theta_{\{j,r+1\}} = \delta V_{\{j,r\}}V_{y\{j,r\}} \\ &\Big[diag[\delta\Theta_{y\{j,r\}}]\Big]V_{\{j,r+1\}} + \Big[U\mathsf{D} - \lambda\Big]\Theta_{\{j,r+1\}} - \sum_{m=0}^{N_y}\Big[\frac{\delta^2(1+4R)}{PrRe}\mathcal{D}^2_{j,m} \\ &\qquad - diag[\delta V_{\{j,r\}}]\mathcal{D}_{j,m}\Big]\Theta_{\{m,r+1\}} = \delta V_{\{j,r\}}\Theta_{y\{j,r\}}. \end{aligned}\right\} \tag{5.21}$$

In the above system of linearized discrete systems, D and $\mathcal{D}$ are, respectively, the scaled differentiation matrices for the x and y variables based on the affine transformation $[-1,1]^2 \mapsto [0,L]\times[0,H]$. The differentiation matrix is defined in Trefethen [93]. Higher order derivatives are obtained by taking corresponding powers of the matrices. r and $r+1$ are two successive iterations. V and Θ are numerical values of v and θ, both of size $(N_x+1)\times(N_y+1)$.

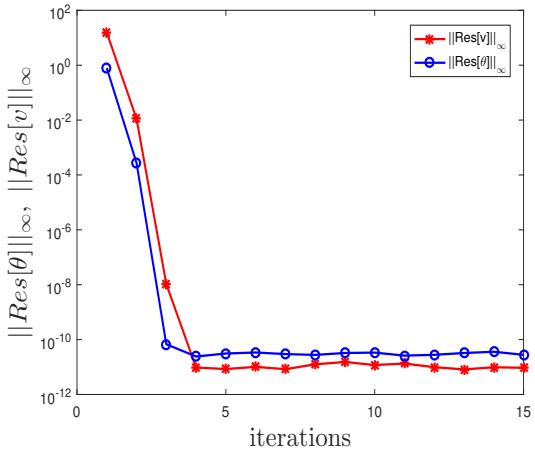

Figure 5.2: Convergence of the infinity norm of the residual error functions of the discrete iterative scheme.

Figure 5.2 portrays the infinity norm of the residual error functions plotted after every iteration. The figure shows that the numerical scheme for the equations studied herein converges after the fourth iteration and the solutions are accurate. The numerical solutions used in the following analysis are obtained after the tenth iteration.

5.4 Results and discussion

The influence of parameters that arise from the dynamics of flow and heat transfer during filtration, such as vertical walls, Richardson number, Reynolds number, radiation parameter, chamber volume, heat generation and Prandtl number are presented in this section. The following values of parameter in the dynamics of filtration process are used: $U = 2, R_i = 1, Re = 1, R = 1, \delta = 0.5, \lambda = 0.4, Pr = 0.7$, unless varied in figures discussed in this section.

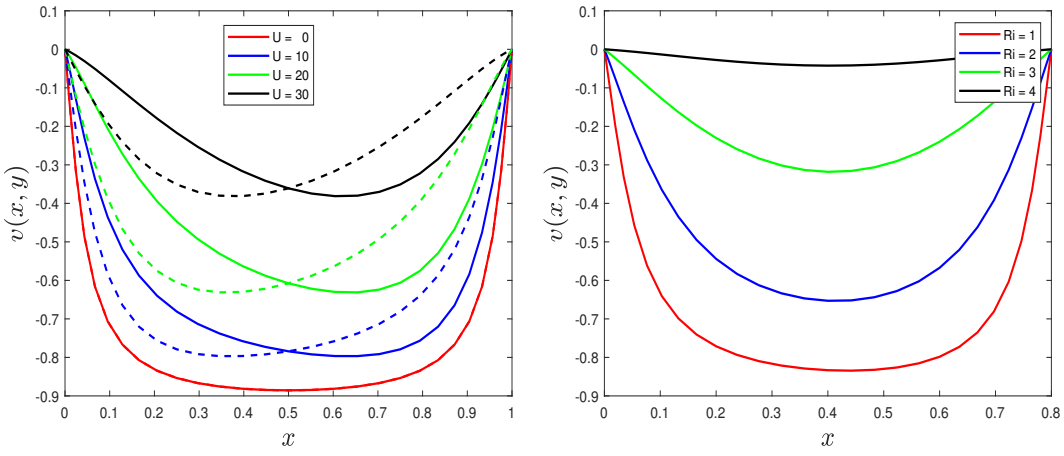

(a) (b)

Figure 5.3: Effect of: (5.3a) U (dotted lines represent same magnitude of U in the negative direction) and (5.3b) R_i on the permeates outflow.

Figure 5.3 indicates that the decrease in work done by the chamber walls (U) and Richardson parameter (R_i) increase the outflow velocity. Also, Figure 5.3a shows that there is more flow in the direction of the net work done by the chamber walls. The increase in axial flow inside the chamber decreases fluid outflow speed because the internal work done moves fluid particles in the axial direction and decreases fluid movement in the permeate direction. This behaviour agrees with the symmetric nature of the flow velocity in Magalakwe et al. [16] when there is no work done by the wall. Also, Figure 5.3b shows that the increase in R_i leads to an increase in buoyancy which reduces flow velocity inside the filter chamber due to minor addition of energy; this is in good agreement with the flow studied in Celik et al. [81] and Momanyi et al. [82]. This decrease in outflow velocity is caused by high-temperature variation when most of the fluid bulk is highly dense. This decrease in the outflow of the fluid bulk is because highly-dense bulk is heavier to move. The influence of both the work done by the walls and R_i have minimal effects on the fluid temperature.

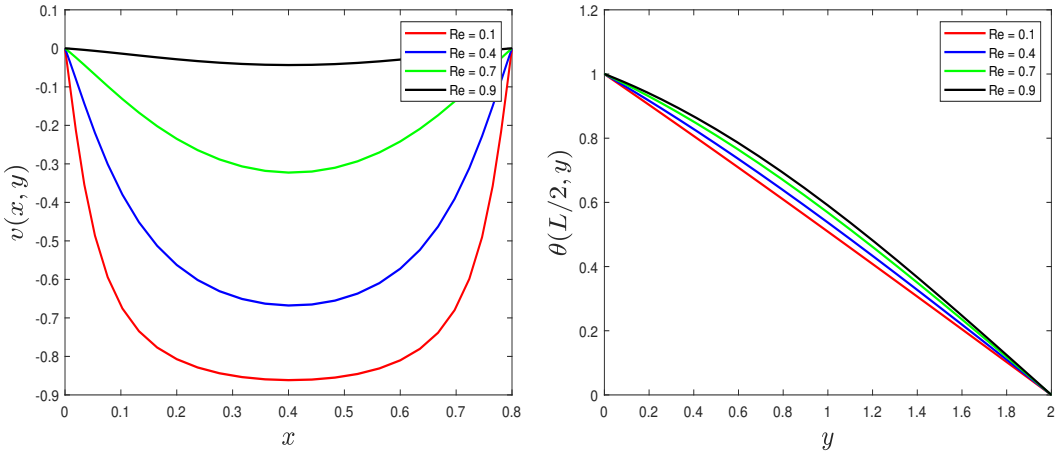

(a) (b)

Figure 5.4: Effect of R_e on the: (5.4a) permeates outflow and (5.4b) temperature distribution inside the filter chamber.

Figures 5.4a and 5.5a, respectively, show that the increase in Reynolds number (R_e) and thermal radiation (R) decrease the fluid outflow. The decrease in the outflow velocity when R_e increases is due to more fluid mass inside the filter chamber such that the movement of fluid particles is deterred. On the other hand, an increase in thermal radiation, R, results in a loss of internal energy in the form of radiation. Figure 5.4b shows that an increase in R_e increases fluid temperature. This behaviour is because the increase in R_e enhances the work done inside the filter chamber, amplifying internal energy. This influence of Reynolds number on velocity and temperature variation inside a vertical chamber agrees with theoretical results of Bded et al. [94]. The temperature decreases, as shown in Figure 5.5b, since the system loses temperature when less dense fluid, which possesses heat, is sucked out of the chamber. Modise and Magalakwe [29] reported similar observations. The flow behaviour and heat distribution inside the vertical chamber when radiation varies agree with the finding in Miyagawa et al. [95].

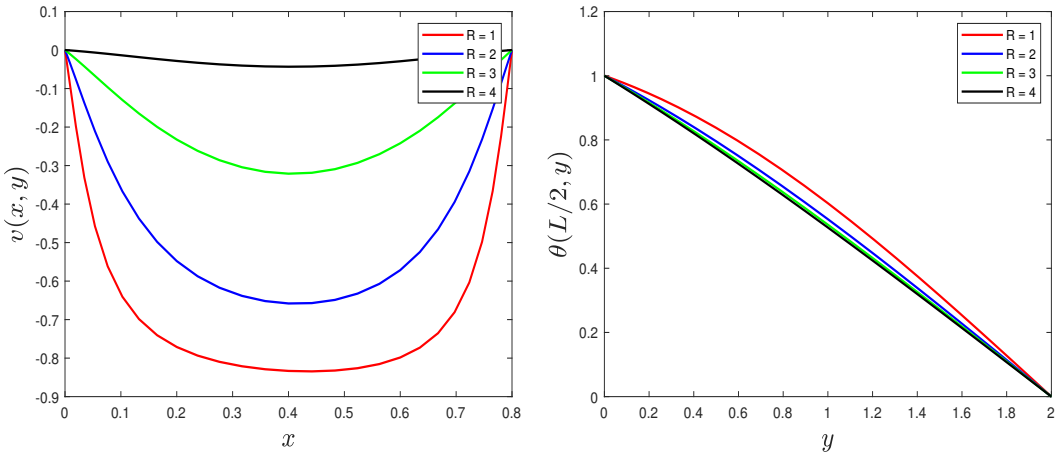

(a) (b)

Figure 5.5: Effect of R on the: (5.5a) permeates flow and (5.5b) internal temperature in the filter chamber.

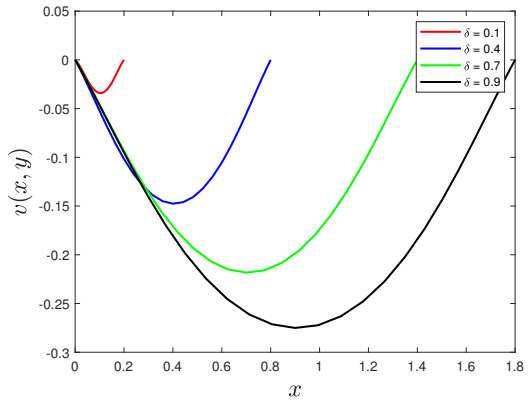

Figure 5.6: Effect of δ on the permeates outflow.

According to Figure 5.6, it is evident that the increase in chamber volume increases the outflow. This increase in flow is due to the rise in the ability of particles to move freely when the chamber space grows. In addition, the chamber volume increases the permeates outflow because it enhances the pulling effects of the buoyancy force. The velocity behaviour when the volume increases agree with the findings in Magalakwe et al. [16].

According to Figures 5.7a and 5.8a, it can be observed that increasing the Prandtl number (P_r) and heat generation (λ) decreases the fluid outflow velocity. The increase in P_r and λ also increase fluid temperature as depicted by Figures 5.7b and 5.8b. This behaviour arises because a decrease in Prandtl number and internal heat generation increases momentum and decreases heat distribution, respectively. Physically, the presence of an additional internal heat generation in the form of a heat source generally raises the temperature of the system, as depicted in Figure 5.8b. Also, for fluids with small P_r, exploring the high thermal conductivities, heat diffusion from the bottom wall takes place faster than fluids with higher P_r. It can be noted that when P_r is low, heat diffuses fast, making

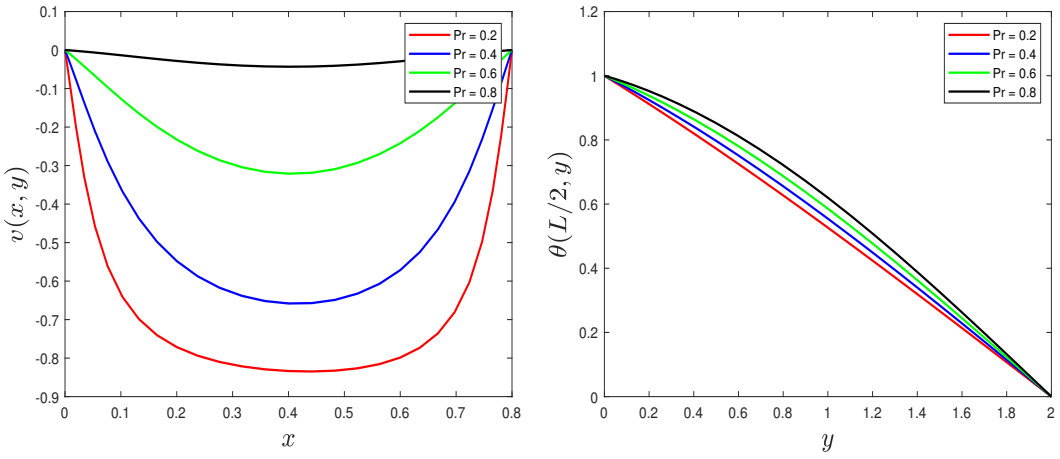

(a) (b)

Figure 5.7: Effect of P_r on the: (5.7a) permeates outflow and 5.7b temperature field inside the filter chamber.

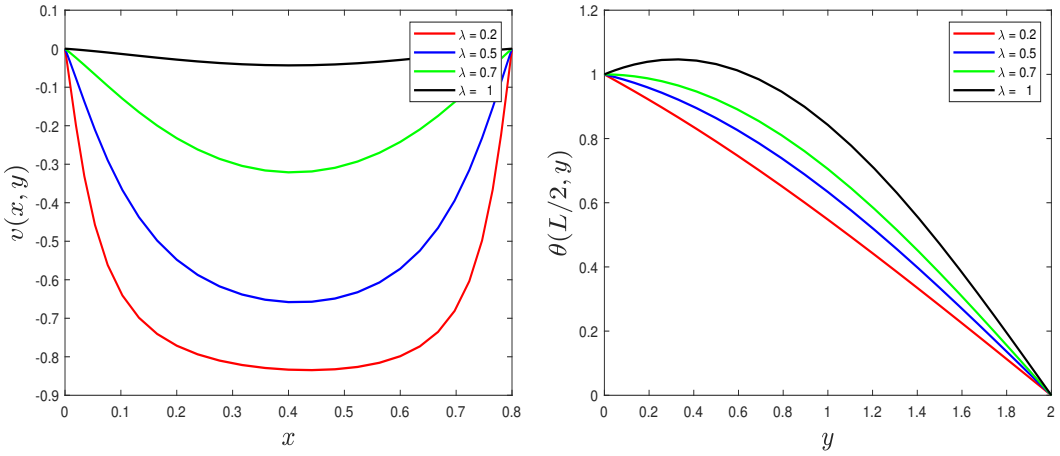

(a) (b)

Figure 5.8: Effect of λ on the permeates flow 5.8a and temperature fields 5.8b inside the filter chamber.

particles less dense, and because of suction from the porous bottom wall, the internal temperature decreases, as shown in Figure 5.7b. Thus, permeates outflow increases while internal temperature decreases as Prandtl number and internal heat generation decrease. The decrease in temperature when permeates outflow increases is because fluid particles the posses energy (heated) are sucked out of the filter chamber. Thus, the more internal temperature is removed from the filter chamber, decreasing internal energy. This behaviour agrees with the studies in Modise and Magalakwe [29].

We remark here that the system uses more energy to produce filtrates fast when it loses internal temperature in the form of suctioned dense particles, thus increasing outflow velocity (permeates).

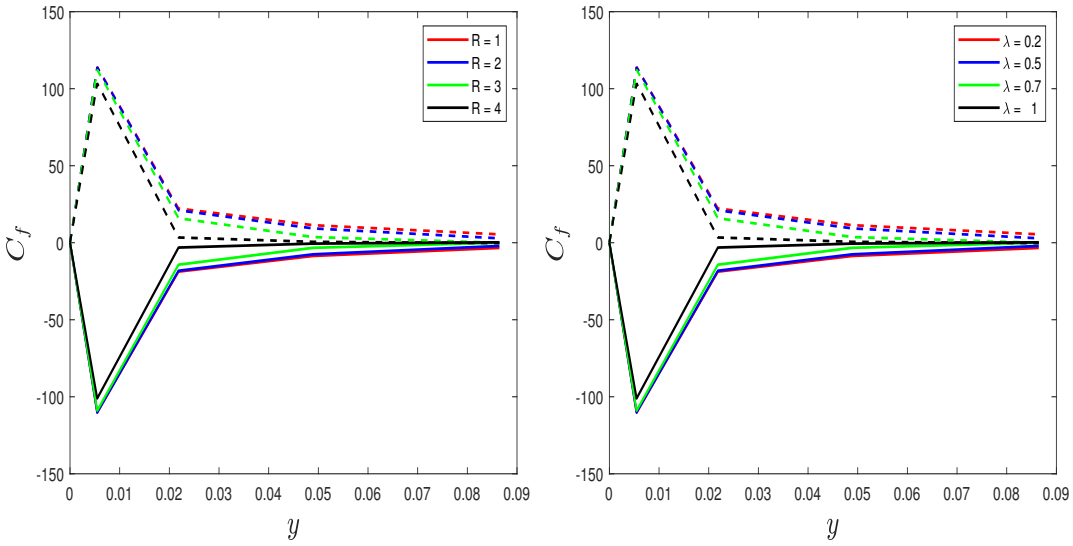

(a) (b)

Figure 5.9: Variation of skin friction coefficients on the left vertical wall (solid lines) and right vertical wall (dashed lines) against radiation parameter (5.9a) and heat generation parameter (5.9b).

Figure 5.9 indicates that the skin friction is minimal when fluid particles are close to the heated bottom wall. This minimal effect is because the wall's temperature decreases the viscosity of the fluid layer near the bottom wall, thus allowing free movement of the fluid. The skin friction on the left and the right walls increases slightly far from the bottom wall and decreases towards zero after that region. The slight increase in skin friction is caused by the clustering of particles towards the bottom wall as they are filtered out of the chamber before particles lose viscous effect due to the impact of wall temperature. A similar dynamic is observed when the influence of other parameters is considered. It is also clear from the figure that the increase in both radiation and internal generation decreases skin friction. This decrease in skin friction is caused by the rise in temperature when heat generation increases. Also, the hot fluid radiates more when the high internal temperature decreases fluid flow resistance.

Figure 5.10 shows a decrease in Reynolds number, and an increase in the filter chamber volume increases the skin friction coefficient. The increase in the value of the vertical wall drag coefficients when Reynolds number decreases is because viscous force is more dominant than inertia force. On the other hand, enlarging the filter volume increases internal fluid particles, thus enhancing wall friction.

Figure 5.11 shows that the wall drag coefficient decreases when both Richardson and Prandtl numbers increase. This decrease is caused by high-temperature variation that results when most fluid bulk is dense, thus reducing fluid movement. Also, increasing the Prandtl number decreases momentum diffusivity, thus enhancing friction.

Figure 5.12 shows that, on the one hand, the left vertical wall drag becomes more when

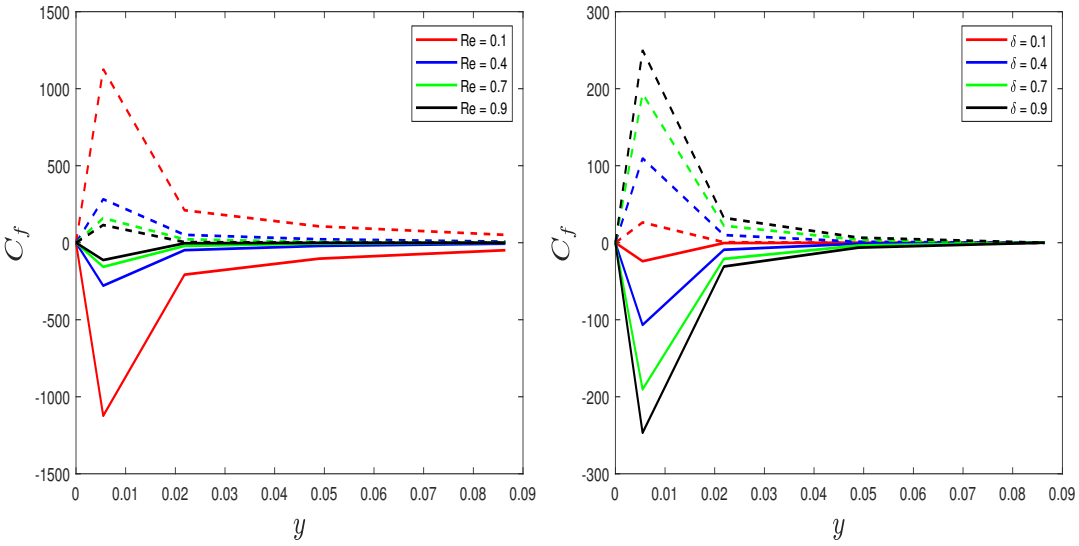

(a) (b)

Figure 5.10: Variation of skin friction coefficient on the left vertical wall (solid lines) and right vertical wall (dashed lines) against Reynolds number (5.10a) and filter volume ratio (5.10b).

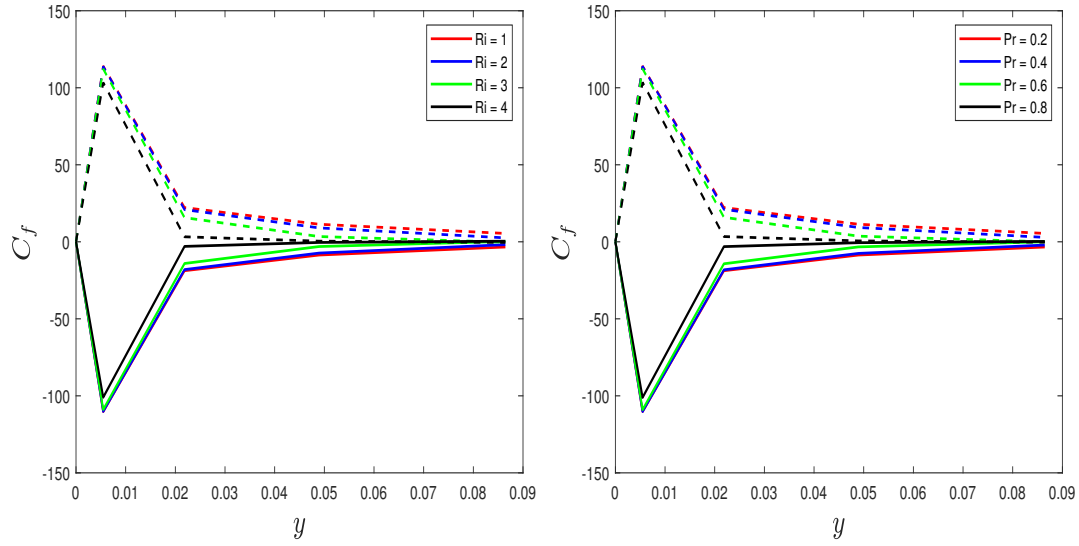

(a) (b)

Figure 5.11: Variation of skin friction coefficient on the left vertical wall (solid lines) and right vertical wall (dashed lines) against Richardson number (5.11a) and Prandtl number (5.11b).

work done by the walls is less. The right vertical wall friction fluctuates since particles move from the left wall towards the right wall. This fluctuation creates a random movement of particles at the right vertical wall.

We remark that the wall drag coefficients on the left and right vertical walls have extrema

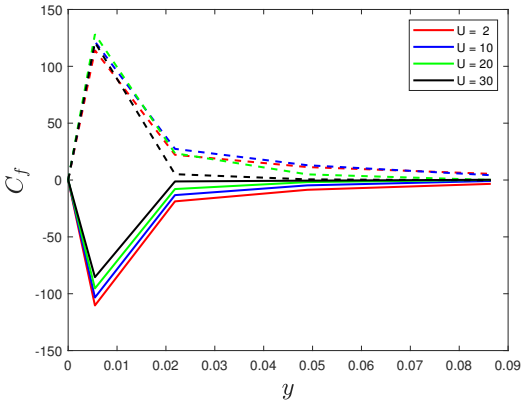

Figure 5.12: Variation of skin friction coefficient through the left vertical wall (solid lines) and right vertical wall (dashed lines) against net work done by the walls.

towards the bottom of the filter chamber, in the region, $0 < y < 2\%H$.

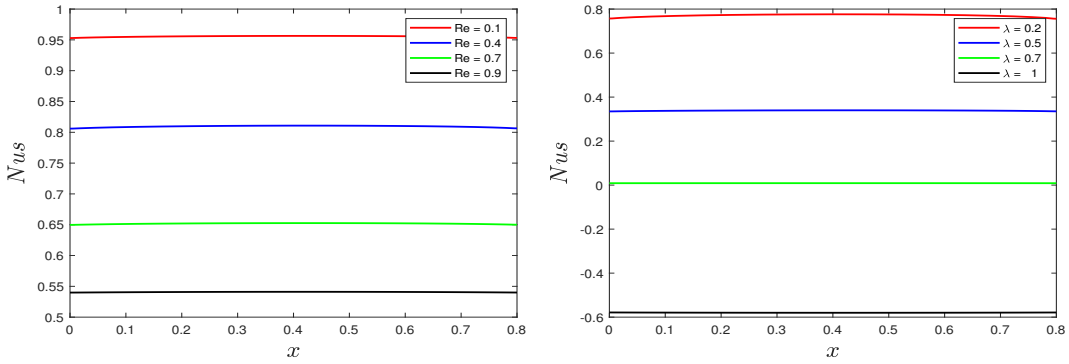

(a) (b)

Figure 5.13: Variation of Nusselt number at the heated bottom wall with (5.13a) Reynolds number and (5.13b) heat generation.

Figure 5.13 indicates that the increase in both the Reynolds number and heat generation parameter leads to a decrease in the Nusselt number. Since there is more viscous shear for small R_e, fluid particles are clustered together, and there is more heat flux. Similarly, when there is less heat generation, fluid particles find it difficult to interact, resulting in less movement of particles. Thus, heat flux increases since particles cluster longer when they move slowly.

Figure 5.14 indicates that the increase in both chamber volume and radiation increases heat flux. This increase in heat flux arises from high conduction when fluid radiates more, as well as the fact that when the volume increases, the fluid bulk increases the ability of heat transfer, thus increasing heat flux.

Figure 5.15 shows that the decrease in the Prandtl numbers increases heat flux. This increase in heat flux arises because less Prandtl number leads to more thermal diffusion.

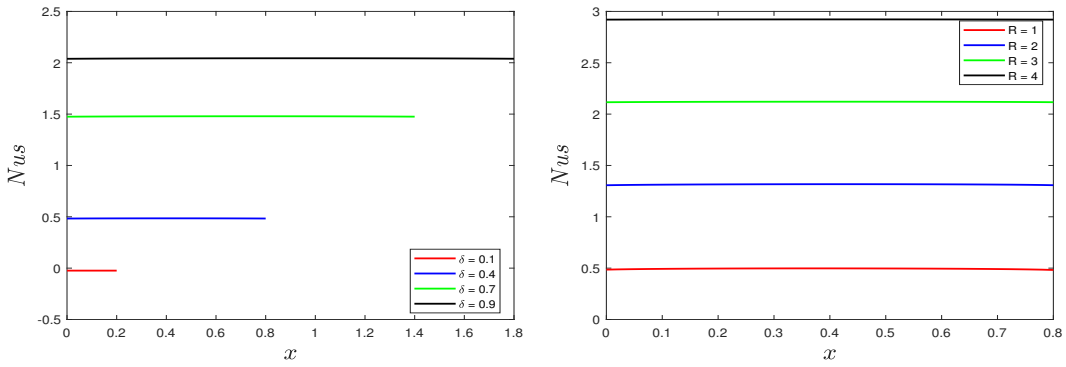

(a) (b)

Figure 5.14: Variation of Nusselt number at the heated bottom wall with (5.14a) filter volume ratio and (5.14b) radiation parameter.

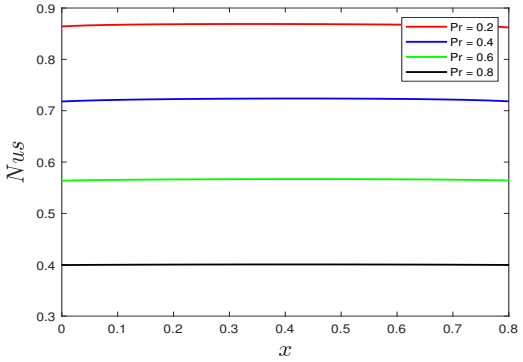

Figure 5.15: Variation of Nusselt number at the heated bottom wall with the Prandtl number.

We remark that the heat flux coefficient at the heated bottom wall is almost uniform for all the parameters because the filter's base is heated at a constant temperature.

5.5 Validation

The study in this chapter seeks to improve the filtration process by redesigning the filter studied in Magalakwe et al. [16]. The filter under investigation is designed, so that buoyancy force acts in the permeate outflow direction, thus increasing permeates production. The buoyancy force acts in the direction of gravity; hence it increases the velocity along the y-axis when internal temperature decreases the fluid density. This physical law agrees with the findings obtained in this study.

The results obtained in the current case study agree with other related filtration process studies; see studies, such as Lekoko et al. [67] and Lekoko et al. [96]. The results showed that the outflow velocity of the current study, which is in the normal direction, correlates with the normal velocity obtained in the filter designs studied by [67, 96]. Also, permeates outflow in the current study increases with a decrease in the Richardson number, $\left(\frac{G_r}{R_e^2}\right)$

since the normal velocity acts in the direction of buoyancy force. Due to the nature of the porous heated wall at the bottom of the filter chamber, the well-known effects of some parameters on both momentum and temperature tend affect the system oppositely because gravity and suction act in the outflow direction, hence they do negative work on the internal flow and heat distribution.

5.6 Conclusion

This chapter presented the theoretical understanding of the dynamics of steady-state filtration operation in a vertical filter chamber when the bottom wall is exposed to constant heat. The spectral quasilinearization method was used to approximate the solutions of the differential model. The study has led to the following conclusions:

i. The vertical walls of the filter chamber must exert the same work, that is, no axial movement, to produce the optimal permeate during the filtration process. This zero work done by the vertical walls also brings a vital symmetric nature to the outflow velocity, maintaining a well-balanced outflow.

ii. During the operation, delaying transition (from laminar to turbulent) is required to increase permeates velocity. It is ideal to operate the filter at a lower Reynolds number value to delay the transition.

iii. It is crucial to have a low temperature to increase permeates outflow. So the filter uses less energy when the Reynolds number is low but produce permeates with high speed. This operation saves energy but speeds up the flow during production.

iv. The increase in the radiation parameter is not ideal when the operation aims to maximize the outflow velocity because it reduces permeates outflow. It is suitable if the process saves energy since radiation conserves internal energy.

v Allowing fluid particles to move freely is ideal since this increases the permeates outflow; hence increasing the filter chamber volume is required for more permeates production.

vi. During filtration, small values of radiation parameter, Reynolds number, Richardson number and Prandtl number, and significant volume are needed to decrease friction.

vii. During filtration, small thermal radiation, high Reynolds, Richardson, Prandtl and heat generation numbers are needed to make the fluid bulk less dense, thus increasing the free movement out of the chamber.

viii. To have more permeates outflow, the internal density needs to be minimal, such that the ability to move dense fluid towards the bottom wall diminishes since more dense fluid moves slower than the less dense fluid. Hence buoyancy needs to be minimal during operation to allow free movement of particles at the bottom.

Chapter 6

Numerical analysis of unsteady injection driven flow and heat transfer in a vertical chamber: Filtration

The transition between steady and unsteady state regimes plays a vital role during filtration. This chapter considers a theoretical investigation of the advancement into an unsteady state regime of flow and heat transfer dynamics in a vertical chamber. The chapter examines the effects of time-dependent inflow velocity on the internal flow and energy dynamics. Graphical representations of the time evolution of the flow speed, pressure and temperature are analysed. Also, the impacts of flow and heat parameters on the skin friction, Nusselt number and average vertical wall pressure are studied. The results indicate that as time evolves, permeate production increases because speed, internal work, and pressure intensify with time. In addition, to aid internal flow, high injection rate, suction rate, Richardson number and Stuart number are ideal during operation because these parameters minimise the overall friction of the filter chamber's walls.

NOMENCLATURE

c_p - heat capacity, $J/kg\,K$
g - gravitational acceleration, m/s^2
G_r - Grashof number
$\dot{h}$ - contraction/expansion rate, m/s
B_0 - magnetic strength, N/mA
J - resistive heating parameter
S_t - magnetic parameter
P - dimensionless pressure
P^* - pressure, Nm^{-2}
P_r - Prandtl number
R_e - Reynolds number
R_d - permeability parameter
R_i - Richardson number
ν - mass diffusivity, m^2/s
t^* - dimensionless time
t - time, s
T - fluid temperature, K
T_w - wall temperature, K
u - velocity along the axial, m/s
u^* - dimensionless axial velocity
U_{in} - inflow velocity along the axial m/s
V_{out} - permeates outflow velocity m/s
v - velocity along the normal, m/s
v^* - dimensionless velocity along the normal
x - horizontal coordinate, m
x^* - dimensionless horizontal coordinate
y - vertical coordinate, m
y^* - dimensionless vertical coordinate
$5L$ - chamber height, m
L - chamber length, m
N_{u_r} - Nusselt number on the right wall
N_{u_t} - Nusselt number at the top wall
C_f - skin friction
P_A - average pressure Nm^{-2}

Greek symbols

β - expansion due to heat
θ - dimensionless temperature
λ - diffusion due to heat
μ - magnetic field strength permeability, H/m
ρ - density of the fluid, kg/m^3
σ - electrical conductivity, S/m

Subscripts

w - filter surface wall
h - chamber height
in - inflow
out - outflow

6.1 Introduction

Viscous fluid flow inside the channel caused by buoyant thermal forces occurs in various natural and mixed convection situations. Experimental and theoretical researchers have made significant efforts to advance the importance of viscous fluids inside various channels, evident by the many experimental and theoretical studies of such flows. According to the review by Oztop et al. [97], several studies have been conducted to better understand the mixed convection phenomena inside closed ducts due to the importance of such flows in industries. These flows have industrial and practical applications in combustion process, solar collector designs, aircraft cabins ventilation, solar buildings, thermal storage system, heat exchangers, filtration process, electronic components cooling, fuel cell, to name a few [98–111].

The present chapter draws our attention to a filtration process because of its importance in various manufacturing processes. Removing contaminants from viscous fluids can be challenging unless external forces are applied to the fluid particles to enable flow within the filter medium. Two of the most important factors to consider are fluid viscosity and the thermal property of the fluid or the filter chamber. Thermal effects are essential to make the fluid particles less viscous and enable easy flow through the filter medium. Appropriate fluid temperature and viscosity are critical to producing quality permeate and protecting the system from damages during operation. Thus, an evidence-based understanding of the theoretical analysis of flow and heat flux dynamics inside filters is essential when designing an effective filter.

Several studies have analysed thermally driven flows in different shapes and different thermal boundary conditions. Motivated by plane glass production, Moallemi and Jang [73] examined heat transfer and flow inside a square closed domain whose flow is produced by shear forces caused by the buoyancy and movement of the upper wall. The authors found that buoyancy effects in the square closed domainq increase when the Prandtl number increase. The influence of shear and buoyancy inside an enclosure domain exposed to heat at the bottom with the other sides kept at room temperature was investigated by Onyejekwe [112] using the finite difference method. Their study discovered that the so-called core flow is sensitive to boundary conditions and mechanical wall motion. To comprehend the process of solar pond heat extraction, Cha and Jaluria [113, 114] conducted a numerical investigation of mixed flow convection inside a horizontal cavity with an inlet on the left and outlet on the right. The study reported that the velocity was highly influenced by the mixed convection parameter $\frac{G_r}{R_e^2}$.

Jha et al. [115] analysed the impacts of injection/suction and transverse magnetic field on a steady free convection vertical flow inside a microchannel. The study considered heat jump and velocity slip at the surfaces and derived analytical solutions of the velocity, heat, skin friction, volume flow and heat transfer rates. It is clear from the study that a decrease in the ratio of ambient wall temperature difference enhances the effects of suction/injection fluid velocity slip and fluid temperature jump. The convection buoyancy-

driven flow in a 2D cavity was investigated by Garandet et al. [116]. The authors proposed an analytical approach to solving the magnetohydrodynamics model and then examined how transverse magnetic fields affect the flow. It is found in the study that everywhere in the cavity, the velocity gradient is constant except where the effects of viscosity are significant. Chen and Weng [117] investigated a fully developed free convection flow inside a vertical microchannel with an opening on one side and asymmetric wall heat. The authors found that the influence of fluid wall interaction with rarefaction decreases heat transfer while increasing volume flow rate. Jha et al. [118] advanced the study of Chen and Weng [117] by analysing the effects of injection/suction on a steady laminar flow. The authors found that velocity increases while heat transfer decreases when injection/suction occurs on the surfaces. They also found that this behaviour is due to the channel's velocity and heat decline. Sheikholeslami et al. [119] outlined a numerical simulation of an MHD natural convection heat transfer in an L-shape inclined enclosure filled with nanofluid.

Much attention has been paid to understanding thermally-driven flow in rectangular enclosures. The need to quantify the relative contribution of mixed convection to heat transfer between two vertical walls and optimise axial outflow out of a rectangular filter studied in [16, 67, 120] drove the motivation of the current study. The literature above shows that none of these studies has dealt with buoyancy's negative effects during the filtration process. That is, the case in which buoyancy pulls the flow towards the horizontal walls and creates a drag force opposing axial permeates flow. Hence, the current design is such that the fluid permits out of the bottom permeable plate to allow buoyancy force to act in the outflow direction. This chapter seeks to extend the work in [16, 67, 96, 120] by redesigning the filter chamber in such a way that buoyancy force becomes one of the forces which drive permeates out of the filter chamber instead of creating internal drag during the filtration process.

Closed-form solutions of partial differential equations representing viscous flow inside various channels can be difficult to obtain, and even when obtained, they can be challenging to analyse due to integrals and special function [121, 122]. Due to this challenge, we use a decoupled spectral-based linearisation technique to find the numerical solutions of the differential equations representing the case study under investigation. The spectral collocation scheme follows from approximating the dependent variables as a finite sum of the Lagrange polynomials evaluated on the Chebyshev-Gauss-Lobatto nodes [27, 65, 123].

6.2 Model Formulation

Figure 6.1 shows the filter design of the case study under investigation. The current theoretical study explores transient flow and heat transfer properties of the viscous fluid inside the filter driven by a variable injection from the left porous wall influenced by magnetic force. According to the filter design, we introduce the constant magnetic field on the left side of the filter as a first line of defence to restrict magnetic contaminants from entering the filter chamber. The top and right walls are heated at uniform temperatures to decrease the effect of viscous force. The injection on the left wall and suction at the

bottom varies over time; thus, momentum variation is in the x and y directions during the filtration process.

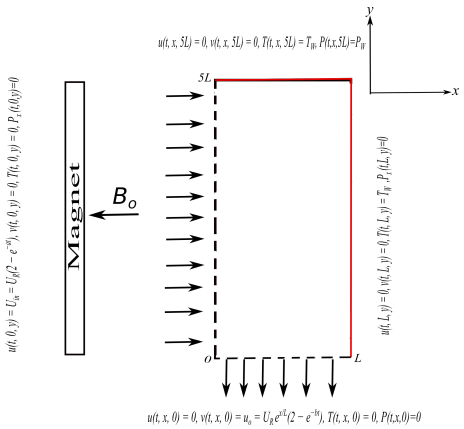

Figure 6.1: Geometrical view of the flow design

The general mass, momentum and energy conservation of the case study is given by:

$$\left.\begin{aligned} &\nabla \cdot \mathbf{u} = 0, \\ &\frac{\partial \mathbf{u}}{\partial t} + \mathbf{u} \cdot \nabla \mathbf{u} = -\frac{1}{\rho}\nabla p + \nu \nabla^2 \mathbf{u} + \mathbf{F}, \\ &\frac{\partial T}{\partial t} + \mathbf{u} \cdot \nabla T = \frac{1}{\rho c_p}\left[k\nabla^2 T + \nabla \mathbf{q_r}\right] + Q, \end{aligned}\right\} \tag{6.1}$$

where $\mathbf{u} = u\mathbf{i} + v\mathbf{j}$ is the velocity vector containing the components u and v along the x and y directions, $\mathbf{F}$ is the net force vector resulting from the filter design and flow behaviour, $\mathbf{q_r}$ is the net radiative heat flux, and Q is the source/sink caused by the effects of the magnetic field known as Joule heating.

According to the current filter design, the forces that affect internal momentum are buoyancy force ($\mathbf{F^B}$) due to thermal effects from the walls and the Lorentz force ($\mathbf{F^L}$) caused by impact of the magnetic strength, which is written as follows:

$$\mathbf{F} = \mathbf{F^B} + \mathbf{F^L}. \tag{6.2}$$

Based on the current filter design, the components of forces affecting momentum together with their directions are the buoyancy and Lorentz forces and are, respectively, given as follows

$$f_y^1 = g\rho\beta(T - T_w)\mathbf{j} \tag{6.3}$$

and

$$f_y^2 = -\frac{\sigma B_0^2}{\rho}\mathbf{j}. \tag{6.4}$$

The above derivations are detailed in the study by Magalakwe et al. [120]. Therefore, the

net force affecting the momentum becomes

$$\mathbf{F} = \left(g\rho\beta(T - T_w) - \frac{\sigma B_0^2}{\rho} \right)\mathbf{j}. \tag{6.5}$$

The work done by the Lorentz force yields an internal energy source or sink, which is given as

$$Q = \frac{\nu B_0^2 v^2}{\rho c_p}. \tag{6.6}$$

We refer readers to references [16, 67] for more information. The net radiative heat flux in the x and y components can be expressed in terms of temperature, T, as:

$$q_r = -\frac{16\sigma_r T_h^3}{3k_r}\left[\frac{\partial^2 T}{\partial x^2} + \frac{\partial^2 T}{\partial y^2}\right]. \tag{6.7}$$

The reader is referred to the studies of [124, 125] for a detailed derivation of the above.

The boundary conditions subject to the domain of the filter chamber are as follows:

i. At $y = 0$,

$$u(t, x, 0) = 0,\ v(t, x, 0) = v_{\text{out}} = -U_R e^{x/L}(2 - e^{-bt}),\ T(t, x, 0) = 0,\ P(t, x, 0) = 0.$$

Filter chamber's wall are stationary, hence $u = 0$. Permeate outflow is allowed at the bottom of the chamber at rate b, such that $v_{\text{out}} = -U_R e^{x/L}(2 - e^{-bt})$. The system's bottom wall permits permeates; therefore, pressure at the bottom wall is approximately the atmospheric pressure because the work done by the permeable wall is minimal. Thus, $P \approx 0$ and the bottom wall maintains the temperature, $T = 0$.

ii. At $y = 5L$,

$$u(t, x, 5L) = 0,\ v(t, x, 5L) = 0,\ T(t, x, 5L) = T_w,\ P(t, x, 5L) = P_w.$$

The top wall maintains a constant temperature T_w, which decreases the viscous property of the fluid at the wall and pushes fluid perpendicular to the wall with constant pressure P_w. There is no fluid injection/suction and the filter chamber wall movement in both the x and y directions at the top due to the no-slip condition; thus, $u = v = 0$.

iii. At $x = 0$,

$$u(t, 0, y) = U_{\text{in}} = U_R(2 - e^{-at}),\ v(t, 0, y) = 0,\ T(t, 0, y) = 0,\ \frac{\partial P}{\partial x}(t, 0, y) = 0.$$

We inject fluid into the filter chamber through the stationary permeable wall on the left at a rate a; thus, $U_{\text{in}} = U_R(2 - e^{-at})$ and $v = 0$ (no-slip condition). The left wall maintains a temperature, $T = 0$, to minimize heat transfer disturbance before and after entry. There is a pressure change at the left permeable wall.

iv. At $x = L$,

$$u(t, L, y) = 0,\ v(t, L, y) = 0,\ T(t, L, y) = T_w,\ \frac{\partial P}{\partial x}(t, L, y) = 0.$$

The right stationary wall is heated to make fluid close to the wall less viscous for smooth flow and a pressure change on the vertical right wall. The velocities on the right are zeros due to the no-slip condition.

According to the above presumption, the equations representing two-dimensional momentum and heat transfer dynamics in the vertical filter are given by

$$\left.\begin{aligned}
&\frac{\partial u}{\partial x} + \frac{\partial v}{\partial y} = 0,\\
&\frac{\partial u}{\partial t} + \frac{1}{\rho}\frac{\partial P}{\partial x} + u\frac{\partial u}{\partial x} + v\frac{\partial u}{\partial y} = \nu\left[\frac{\partial^2 u}{\partial x^2} + \frac{\partial^2 u}{\partial y^2}\right],\\
&\frac{\partial v}{\partial t} + \frac{1}{\rho}\frac{\partial P}{\partial y} + u\frac{\partial v}{\partial x} + v\frac{\partial v}{\partial y} = \nu\left[\frac{\partial^2 v}{\partial x^2} + \frac{\partial^2 v}{\partial y^2}\right] + g\beta(T - T_h) - \frac{\sigma B_0^2 v}{\rho},\\
&\frac{\partial T}{\partial t} + u\frac{\partial T}{\partial x} + v\frac{\partial T}{\partial y} = \frac{\kappa}{\rho c_p}\left[\frac{\partial^2 T}{\partial x^2} + \frac{\partial^2 T}{\partial y^2}\right] + \frac{\nu B_0^2}{\rho_r c_p}v^2 - \frac{16\sigma T_h^3}{3\rho c_p k_r}\left[\frac{\partial^2 T}{\partial x^2} + \frac{\partial^2 T}{\partial y^2}\right].
\end{aligned}\right\} \tag{6.8}$$

Where, $\bar{u}$ and $\bar{v}$ are respectively the axial and normal velocity components, T is the fluid temperature, ρ is the density, P is the pressure, ν is the kinematic viscosity of the liquid, g is the gravity, β and k are thermal diffusivity and expansion respectively, t is time, σ is the electrical conductivity of the fluid, B_0 is the magnetic induction, and c_p is the specific heat.

Subject to boundary conditions below:

$$\left.\begin{aligned}
&\text{at } y = 0,\ u(t, x, 0) = 0,\ v(t, x, 0) = v_{\text{out}} = U_R e^{x/L}(2 - e^{-bt}),\ T(t, x, 0) = 0,\\
&\text{at } y = 5L,\ u(t, x, 5L) = 0,\ v(t, x, 5L) = 0,\ T(t, x, 5L) = T_w,\\
&\text{at } x = 0,\ u(t, 0, y) = U_{\text{in}} = U_R(2 - e^{-at}),\ v(t, 0, y) = 0,\ T(t, 0, y) = 0,\\
&\text{at } x = L,\ u(t, L, y) = 0,\ v(t, L, y) = 0,\ T(t, L, y) = T_w.
\end{aligned}\right\} \tag{6.9}$$

Pressure Poisson equation is defined by applying the continuity equation and adding the derivative of momentum conservation along the axial with respect to x and the derivative of momentum conservation along the normal with respect to y, which yields:

$$\left[\frac{\partial^2 P}{\partial x^2} + \frac{\partial^2 P}{\partial y^2}\right] - 2\left[\frac{\partial u}{\partial x}\frac{\partial v}{\partial y} - \frac{\partial u}{\partial y}\frac{\partial v}{\partial x}\right] + \frac{\sigma B_0^2 L}{\rho U_R}\frac{\partial v}{\partial y} - \frac{g\beta\rho L(T_i - T_w)}{U_R^2}\frac{\partial \theta}{\partial y} = 0. \tag{6.10}$$

The dimensionless parameters below are introduced to transform the dimensional equations into non-dimensional form

$$\left.\begin{aligned}
&u^* = \frac{u}{U_R},\ v^* = \frac{v}{U_R},\ x^* = \frac{x}{L},\ y^* = \frac{y}{L},\ t^* = \frac{tU_R}{L}\ \theta = \frac{T - T_w}{T_i - T_w},\ P^* = \frac{P}{P_w U_R^2},\ R_e = \frac{LU_R}{\nu},\\
&R_i = \frac{g\beta L(T_i - T_w)}{U_R^2},\quad S_t = \frac{\sigma B_0^2 L}{\rho U_R},\quad P_r = \frac{\nu\rho c_p}{\kappa},\quad R_d = \frac{4\sigma_r T_i^3}{3\kappa_r\kappa},\quad J = \frac{\sigma B_0^2 U_R L}{(T_i - T_w)\rho c_p}.
\end{aligned}\right\} \tag{6.11}$$

The use of these variables and parameters in the conservation equations (6.8) and pressure equation (6.10) yield the following dimensionless system of equations:

$$\left.\begin{aligned}
&\frac{\partial u^*}{\partial t^*} + u^*\frac{\partial u^*}{\partial x^*} + v^*\frac{\partial u^*}{\partial y^*} + \frac{\partial P^*}{\partial x^*} - \frac{1}{R_e}\left[\frac{\partial^2 v^*}{\partial x^{*2}} + \frac{\partial^2 v^*}{\partial y^{*2}}\right] = 0,\\
&\frac{\partial v^*}{\partial t^*} + u^*\frac{\partial v^*}{\partial x^*} + v^*\frac{\partial v^*}{\partial y^*} + \frac{\partial P^*}{\partial y^*} - \frac{1}{R_e}\left[\frac{\partial^2 v^*}{\partial x^{*2}} + \frac{\partial^2 v^*}{\partial y^{*2}}\right] - R_i\theta + S_t v^* = 0,\\
&\frac{\partial^2 P^*}{\partial x^{*2}} + \frac{\partial^2 P^*}{\partial y^{*2}} - 2\left[\frac{\partial v^*}{\partial y^*}\frac{\partial u^*}{\partial x^*} - \frac{\partial v^*}{\partial x^*}\frac{\partial u^*}{\partial y^*}\right] - R_i\frac{\partial \theta}{\partial y^*} + S_t\frac{\partial v^*}{\partial y^*} = 0,\\
&\frac{\partial \theta}{\partial t^*} + u^*\frac{\partial \theta}{\partial x^*} + v^*\frac{\partial \theta}{\partial y^*} - \frac{1}{P_r R_e}\left[\frac{\partial^2 \theta}{\partial x^{*2}} + \frac{\partial^2 \theta}{\partial y^{*2}}\right] - Jv^{*2} + \frac{4R_d}{P_r R_e}\left[\frac{\partial^2 \theta}{\partial x^{*2}} + \frac{\partial^2 \theta}{\partial y^{*2}}\right] = 0.
\end{aligned}\right\} \tag{6.12}$$

The boundary conditions take the following form

$$\left.\begin{aligned}
&\text{at } y^* = 0,\ u^*(t^*, x^*, 0) = 0,\ v^*(t^*, x^*, 0) = -e^{x^*}(2 - e^{-bt^*}),\ \theta(t^*, x^*, 0) = 0,\ P^*(t^*, x^*, 0) = 0,\\
&\text{at } y^* = 5L,\ u^*(t^*, x^*, 5L) = 0,\ v^*(t^*, x^*, 5L) = 0,\ \theta(t^*, x^*, 5L) = 1,\ P^*(t^*, x^*, 5L) = 1,\\
&\text{at } x^* = 0,\ u^*(t^*, 0, y^*) = (2 - e^{-at^*}),\ v^*(t^*, 0, y^*) = 0,\ \theta(t^*, 0, y^*) = 0,\ \frac{\partial P^*}{\partial x^*}(t^*, 0, y^*) = 0,\\
&\text{at } x^* = L,\ u^*(t^*, L, y^*) = 0,\ v^*(t^*, L, y^*) = 0,\ \theta(t^*, L, y^*) = 1,\ \frac{\partial P^*}{\partial x^*}(t^*, L, y^*) = 0.
\end{aligned}\right\} \tag{6.13}$$

6.3 Numerical solution

The system of equations (6.12) is solved through a decoupled paired multivariate spectral quasilinearization method on the Chebyshev-Gauss-Lobatto (CGL) nodes. The formulation of this solution procedure has been adequately documented in the literature. The method is premised on decoupling the system, linearizing the equations using the generalization of the Newton-Raphson method proposed by Bellman and Kalaba [90], and then representing the dependent variables as a linear combination of the Lagrange polynomials on the CGL nodes. This procedure leads to a system of decoupled quasi-linear algebraic equations, which is solved iteratively after the boundary and initial conditions are imposed.

The numerical scheme for the system of equations (6.12) (asterisk dropped for brevity) is presented as follow. The system is discretized on the CGL grid which is defined as

$$\left.\begin{aligned}
\tilde{x}_i &= \cos\left(\frac{i\pi}{N_x}\right)\Bigg|_{i=0}^{N_x}, \quad \tilde{x}(x) = \frac{2}{L}\left[x - \frac{L}{2}\right], \quad x \in [0, L]\\
\tilde{y}_j &= \cos\left(\frac{j\pi}{N_y}\right)\Bigg|_{j=0}^{N_y}, \quad \tilde{y}(y) = \frac{2}{5L}\left[y - \frac{5L}{2}\right], \quad y \in [0, 5L]\\
\tilde{t}_k &= \cos\left(\frac{k\pi}{N_t}\right)\Bigg|_{k=0}^{N_t}, \quad \tilde{t}(t) = \frac{2}{T_f}\left[t - \frac{T_f}{2}\right], \quad t \in [0, T],
\end{aligned}\right\} \tag{6.14}$$

where N_x, N_y, N_t are, respectively, the numbers of collocations in x, y, t. The dependent variables are approximated as a linear combinations of a multivariate Lagrange polynomial of the forms

$$\left.\begin{aligned}
u(x,y,t) \approx U(x,y,t) &= \sum_{a=0}^{N_x}\sum_{b=0}^{N_y}\sum_{c=0}^{N_t} U(x_a,y_b,t_c)\mathcal{L}_a(x)\mathcal{L}_b(y)\mathcal{L}_c(t) \\
v(x,y,t) \approx V(x,y,t) &= \sum_{a=0}^{N_x}\sum_{b=0}^{N_y}\sum_{c=0}^{N_t} V(x_a,y_b,t_c)\mathcal{L}_a(x)\mathcal{L}_b(y)\mathcal{L}_c(t) \\
P(x,y,t) \approx P(x,y,t) &= \sum_{a=0}^{N_x}\sum_{b=0}^{N_y}\sum_{c=0}^{N_t} P(x_a,y_b,t_c)\mathcal{L}_a(x)\mathcal{L}_b(y)\mathcal{L}_c(t) \\
\theta(x,y,t) \approx \Theta(x,y,t) &= \sum_{a=0}^{N_x}\sum_{b=0}^{N_y}\sum_{c=0}^{N_t} \Theta(x_a,y_b,t_c)\mathcal{L}_a(x)\mathcal{L}_b(y)\mathcal{L}_c(t).
\end{aligned}\right\} \tag{6.15}$$

Here, the basis function is defined as

$$\mathcal{L}_a(x) = \prod_{\substack{a=0 \\ a\neq i}}^{N_x} \frac{x-x_a}{x_i-x_a}, \quad \mathcal{L}_a(x_i) = \delta_{ai} = \begin{cases} 1 & a = i \\ 0 & a \neq i. \end{cases} \tag{6.16}$$

$\mathcal{L}_b(y)$ and $\mathcal{L}_c(t)$ are defined in similar manner. The first order partial derivatives of $u(x,y,t)$ with respect to x, y, t are approximated at different collocation points $(\tilde{x}_i, \tilde{y}_j, \tilde{t}_k)$ and, respectively, defined as

$$\begin{aligned}
\frac{\partial u}{\partial x}(\tilde{x}_i,\tilde{y}_j,\tilde{t}_k) &\approx \sum_{a=0}^{N_x}\sum_{b=0}^{N_y}\sum_{c=0}^{N_t} U(x_a,y_b,t_c)\mathcal{L}'_a(\tilde{x}_i)\mathcal{L}_b(\tilde{y}_j)\mathcal{L}_c(\tilde{t}_k) = \sum_{a=0}^{N_x} U(x_a,y_j,t_k)\mathcal{L}'_a(\tilde{x}_i) \\
&= D^x U^{jk} = \frac{2}{L}\tilde{D}^x U^{jk},
\end{aligned} \tag{6.17}$$

$$\frac{\partial u}{\partial y}(\tilde{x}_i,\tilde{y}_j,\tilde{t}_k) \approx \sum_{b=0}^{N_y} U(x_i,y_b,t_k)\mathcal{L}'_b(\tilde{y}_j) = \sum_{b=0}^{N_y} D^y_{jb} U^{bk} = \sum_{b=0}^{N_y} \frac{2}{5L}\tilde{D}^y_{jb} U^{bk}, \tag{6.18}$$

$$\frac{\partial u}{\partial t}(\tilde{x}_i,\tilde{y}_j,\tilde{t}_k) \approx \sum_{b=0}^{N_y}\sum_{c=0}^{N_t} U(x_i,y_j,t_c)\mathcal{L}'_c(\tilde{t}_k) = \sum_{b=0}^{N_y}\sum_{c=0}^{N_t} D^t_{kc} U^{bc} = \sum_{b=0}^{N_y}\sum_{c=0}^{N_t} \frac{2}{T_f}\tilde{D}^t_{kc} U^{bc}. \tag{6.19}$$

$\tilde{D}^x, \tilde{D}^y, \tilde{D}^t$ in Equations (6.17) to (6.19) are first order standard Chebyshev differentiation matrices, of respective size (N_x+1)-by-(N_x+1), (N_y+1)-by-(N_y+1), (N_t+1)-by-(N_t+1), defined in Trefethen [93], and D^x, D^y, D^t are transformed versions of the matrices. U^{jk} in Equation (6.17) is the vector

$$U^{jk} = [U(x_0,y_j,t_k), U(x_1,y_j,t_k), \ldots, U(x_{N_x},y_j,t_k)]^T, \quad j = 0,1,\ldots,N_y, \quad k = 0,1,\ldots,N_t. \tag{6.20}$$

Higher order derivatives are obtained by taking matrix power of the differentiation matrices. The partial derivatives of $v(x,y,t), P(x,y,t), \theta(x,y,t)$ with respect to x, y, t approximated at the CGL points $(\tilde{x}_i, \tilde{y}_j, \tilde{t}_k)$ are defined in similar manner.

Equation (6.12) is solved by quasilinearizing its first two equations as a pair so that we have the following linear discretized system

$$\left.\begin{aligned}
&\Big[-\frac{1}{R_e}D^{xx}+\alpha_{0,r}D^{x}+\alpha_{1,r}\Big]U^{jk}_{r+1}+\sum_{b=0}^{N_y}\Big[-\frac{1}{R_e}D^{yy}_{jb}+\alpha_{2,r}D^{y}_{jb}\Big]U^{bk}_{r+1}\\
&\qquad+\sum_{b=0}^{N_y}\sum_{c=0}^{N_t}D^{t}_{kc}U^{bc}_{r+1}+\alpha_{3,r}V^{jk}_{r+1}=R_{1,r}\\
&\beta_{0,r}U^{jk}_{r+1}+\Big[-\frac{1}{R_e}D^{xx}+\beta_{1,r}D^{x}+\beta_{2,r}\Big]V^{jk}_{r+1}+\sum_{b=0}^{N_y}\Big[-\frac{1}{R_e}D^{yy}_{jb}+\beta_{3,r}D^{y}_{jb}\Big]V^{bk}_{r+1}\\
&\qquad+\sum_{b=0}^{N_y}\sum_{c=0}^{N_t}D^{t}_{kc}V^{bc}_{r+1}=R_{2,r},
\end{aligned}\right\}\tag{6.21}$$

where

$$\begin{aligned}
&\alpha_{0,r}=U_r,\quad \alpha_{1,r}=U_{x,r},\quad \alpha_{2,r}=V_r\quad \alpha_{3,r}=U_{y,r},\\
&\beta_{0,r}=V_{x,r},\quad \beta_{1,r}=U_r,\quad \beta_{2,r}=V_{y,r}+S_t\quad \beta_{3,r}=V_r,\\
&R_{1,r}=-P_{x,r}+U_{x,r}U_r+U_{y,r}V_r,\\
&R_{2,r}=-P_{y,r}+R_i\Theta_r+U_rV_{x,r}+V_rV_{y,r},
\end{aligned}$$

and $r, r+1$ are two successive iterations. Once the solutions $U(x,y,t)$ and $V(x,y,t)$ has been obtained, they are used in approximating the solutions $\Theta(x,y,t)$ and $P(x,y,t)$ by solving the last two equations in (6.12) as decoupled linear single equations, as in the following linear discrete equations

$$\left.\begin{aligned}
&\Big[\tau_{0,r}D^{xx}+\tau_{1,r}D^{x}\Big]\Theta^{jk}_{r+1}+\sum_{b=0}^{N_y}\Big[\tau_{0,r}D^{yy}_{jb}+\tau_{2,r}D^{y}_{jb}\Big]\Theta^{bk}_{r+1}+\sum_{b=0}^{N_y}\sum_{c=0}^{N_t}D^{t}_{kc}\Theta^{bc}_{r+1}=R_{3,r}\\
&D^{xx}P^{jk}_{r+1}+\sum_{b=0}^{N_y}D^{yy}_{jb}P^{bk}_{r+1}=R_{4,r},
\end{aligned}\right\}\tag{6.22}$$

where

$$\begin{aligned}
&\tau_{0,r}=-\frac{1}{P_rR_e}(1+4R_d),\quad \tau_{1,r}=U_{r+1},\quad \tau_{2,r}=V_{r+1},\quad R_{3,r}=JV^2_{r+1}\\
&R_{4,r}=2V_{y,r+1}U_{x,r+1}-2V_{x,r+1}U_{y,r+1}+R_i\Theta_{y,r+1}-S_tV_{y,r+1}.
\end{aligned}$$

When the initial and boundary conditions are imposed, the summations are adjusted to make the algebraic equations consistent.

To establish the consistency of the numerical results concerning dependency on the choice of the number of collocation nodes, we conducted a grid dependency test in which the right wall's average Nusselt number, average pressure exerted by the left wall and total

skin friction on the left wall were calculated at $t = 1$. Considering the values obtained for different grid resolutions given in Table 6.1, the results indicate that a 15×25 spatial grid resolution is sufficient to produce accurate results. The convergence of the spectral-based linearization method has been established in previous works such as Motsa and Animasaun [123], Motsa et al. [91], Motsa et al. [27].

Table 6.1: Grid independence of the overall wall drag, average heat flux at the heated walls and average pressure exerted by the left vertical wall at $t = 1$ and choosing the number of collocation points for the t-variable as 15.

$N_x \times N_y$	Average Nu_r	Average left P_{wall}	Total left C_f
15×15	6.7845	1.3606	-7.2222
15×20	7.1717	1.3670	-8.4037
20×20	7.1726	1.3671	-8.4068
15×25	7.4549	1.3684	-9.2866
20×25	7.4646	1.3684	-9.3229
25×25	7.4650	1.3684	-9.3230

6.4 Results and discussion

We analyze how specific thermophysical parameters affect the speed of the fluid, pressure and internal temperature, total wall drag of the left and top walls, average heat flux at the heated walls and average pressure exerted by the vertical walls of the filter chamber.

This section analyses the time evolution of the speed, internal pressure and temperature variation during the filtration process. The effects of injection and suction rates, Joule heating, Prandtl number, radiation parameter, Richardson number and Stuart number on the overall skin friction, Nusselt number and average wall pressure are analyzed graphically. Based on the current filter design, the flow and heat dynamics yield the following physical quantities of interest when filtering particles from contaminated fluid:

i. Permeates production speed

$$\text{speed} = |\mathbf{u}| = \sqrt{u^2 + v^2}, \tag{6.23}$$

ii. Average pressure exerted by the left and right walls of the filter chamber are, respectively, given as

$$\text{average pressure exerted by the left wall.} = \frac{1}{5L}\int_0^{5L} P(x, y, t)\Big|_{x=0}, \tag{6.24}$$

$$\text{average pressure exerted by the right wall} = \frac{1}{5L}\int_0^{5L} P(x, y, t)\Big|_{x=L}. \tag{6.25}$$

iii. Skin friction exerted by the left and the top walls of the filter chamber is given by

$$\text{skin friction} = C_f = \frac{2}{R_e}\left(\frac{\partial u}{\partial y} + \frac{\partial v}{\partial x}\right)\Bigg|_{x=0 \ \& \ y=5L}, \tag{6.26}$$

$$\tag{6.27}$$

where $x = 0$ and $y = 5L$ in the above, respectively, indicate the skin friction on the left and top walls of the filter chamber.

iv. Average heat flux (Nusselt number) on the left and the top chamber walls are, respectively, given as:

$$\text{average heat flux at the top wall} = N_{u_t} = \frac{1}{L}\int_0^L (1+4R)\frac{\partial \theta}{\partial y}\Bigg|_{y=5L}, \tag{6.28}$$

$$\text{average heat flux at the right wall} = N_{u_r} = \frac{1}{5L}\int_0^{5L} (1+4R)\frac{\partial \theta}{\partial x}\Bigg|_{x=L}. \tag{6.29}$$

Figure 6.2 shows that the internal speed increases as time evolves. The fluid moves faster on the left side and at the bottom of the chamber. This behaviour is due to the introduction of more fluid particles when injecting on the chamber's left side, which increases movement on the left. More fluid injection leads to more internal work; thus, more work is done over time, increasing internal flow speed on the left. At the same time, the system experiences the free movement of fluid particles at the bottom opening since the pressure is minimal at the bottom (atmospheric pressure). The figure also shows that as time evolves, the fluid at the top-right diagonal side starts to move faster and increases the fluid speed at the bottom since fluid injection pushes fluid particles to the right filter wall. Additionally, buoyancy effects pull fluid particles downward in the directions of the outflow velocity due to gravity.

The system's internal temperature is higher at the top-right corner of the chamber and less towards the bottom-left corner of the chamber as seen in Figure 6.3. The internal temperature maintains the s-shape profile over time. This temperature distribution is due to the fact that particles at the heated walls absorb higher heat than the ones far from the heated walls. As time evolves, there is minimal variation in the internal temperature because the heat flux along the chamber walls is not time dependent.

Figure 6.4 shows that there is an increase in the internal pressure as time evolves. Initially, at $t = 0.25$, the internal pressure near the top wall of the filter chamber is less than P_w, and as time evolves, the pressure distribution close to the top wall becomes P_w. As addition fluid particles are introduced inside the filter, and work done by fluid enhances internal pressure. The pressure distribution close to the top wall approximates the wall pressure. Further, there is an increase in pressure in the middle of the filter chamber before it decreases near the bottom wall due to atmospheric pressure. Thus, higher internal fluid mass results in higher pressure during the filtration process.

Figure 6.5 shows that the skin friction coefficient on the left wall increases and decreases with an increase in the fluid injection and permeates suction rates. The spurt in the skin

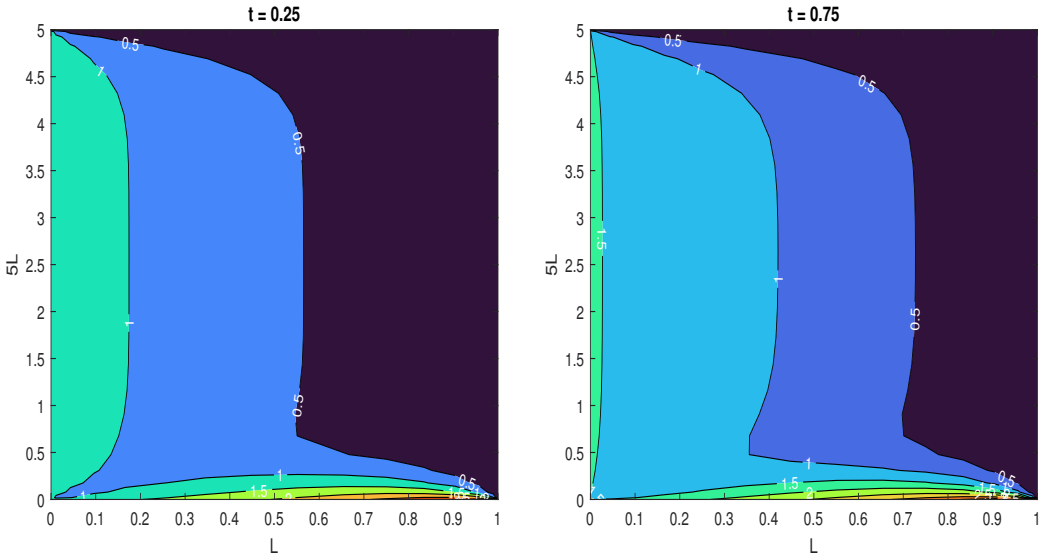

(a) $t = 0.25$ (b) $t = 0.75$

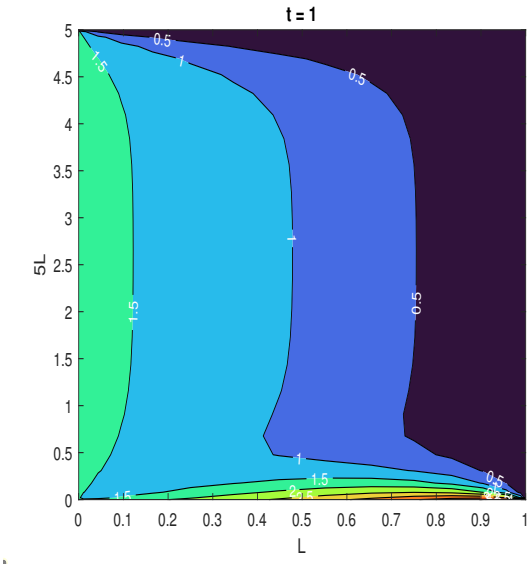

(c) $t = 1$

Figure 6.2: Time evolution of the speed of the permeates.

drag at the left wall when fluid is introduced inside the filter is due to the effect of higher fluid mass, which enhances friction. On the other hand, suction diminishes internal fluid mass and consequently decreases friction, thus, increasing fluid outflow. The figure also indicates that the skin friction coefficient on the top wall wanes with an increased fluid injection rate. When the permeates suction rate varies, the skin friction at the upper wall stays relatively the same. This behaviour at the top wall of the filter chamber is a result of the effects of heat, which become more effective with an increase in fluid mass so that on the top wall of the filter chamber, the fluid density decreases and consequently leads to a reduction of the total wall drag.

Figure 6.6 shows that the total wall drag on the left wall increases with an increase in the resistive heating parameter and a decrease in the Prandtl number. This increase

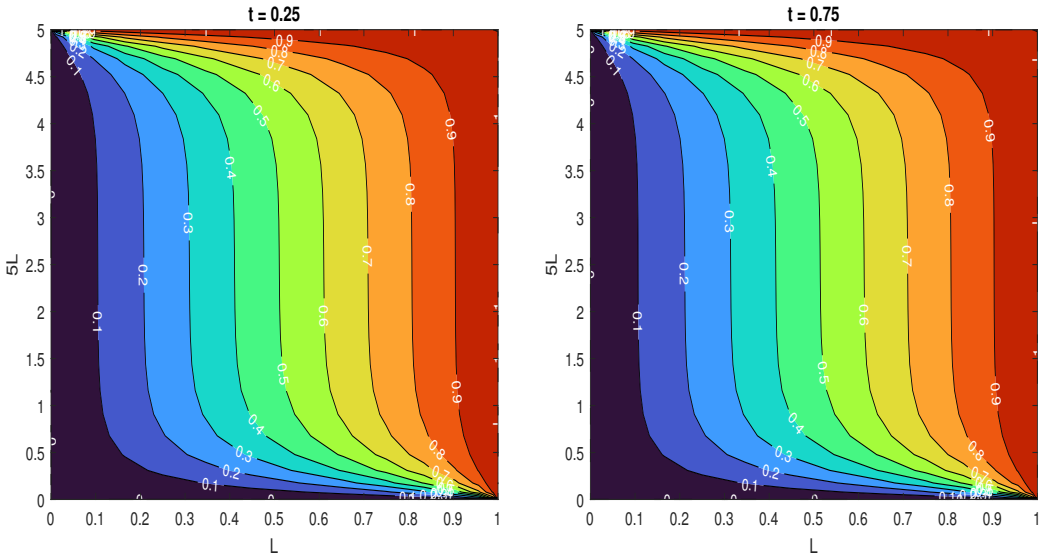

(a) $t = 0.25$ (b) $t = 0.75$

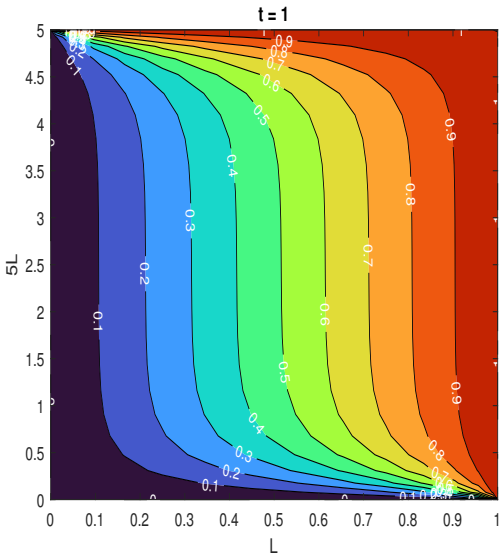

(c) $t = 1$

Figure 6.3: Time evolution of the temperature variation inside the filter chamber.

when the resistive heating parameter increases is because there is a direct proportionality between the friction and Joule heating; hence, more internal fluid particles enhance resistive heating. Additionally, the decrease in friction when the Prandtl number decreases is due to a reduction in momentum diffusivity and a decrease in fluid movement. The constant effects of the heat flux on the upper wall keep the fluid close to the wall less dense, thus leading to minimal change in the skin friction coefficient on the top wall as time evolve.

Figure 6.7 depicts enhancement in the total skin friction coefficient on the left wall of the filter chamber as both the Stuart and Richardson numbers are enhanced. These dynamics result from the frictional force created by the clustering of particles due to higher fluid injection as the Richardson number increases while increasing the Stuart number intensifies the pull of the magnetic strength on the fluid close to the left wall.

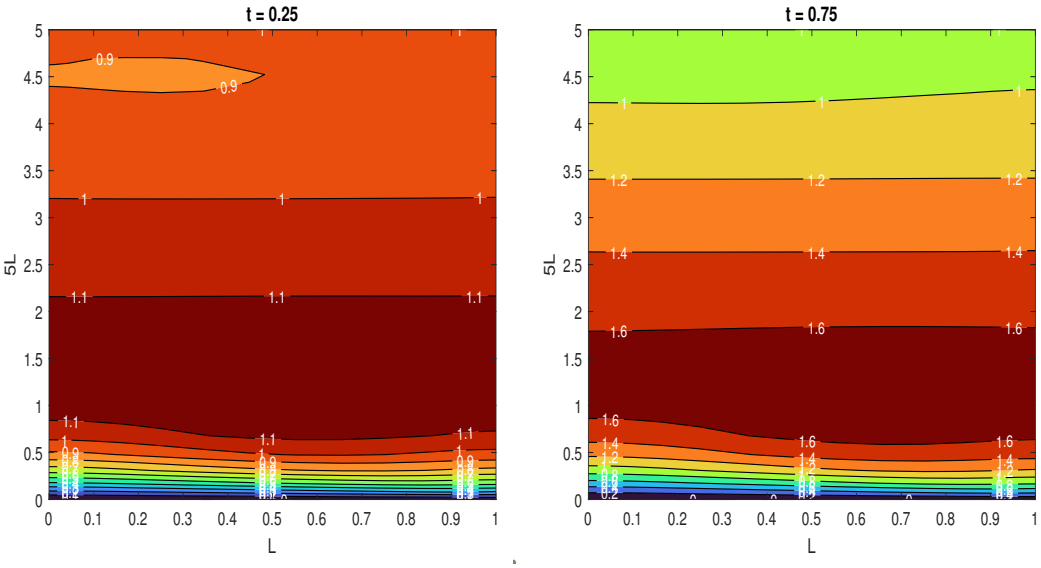

(a) $t = 0.25$ (b) $t = 0.75$

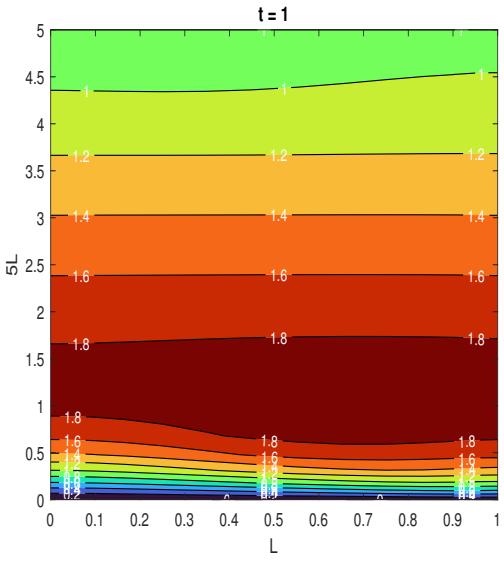

(c) $t = 1$

Figure 6.4: Time evolution of pressure distribution inside the filter chamber

We remark here that as time evolves, there is an increase in internal momentum, which reduces the overall skin friction. Additionally, except in the case where the injection rate is varied, there is minimal variation in the overall skin friction coefficient on the top wall of the filter chamber when the parametric values of suction rate, Joule heating, Prandtl, Stuart and Richardson numbers are varied. The minimal variation in the overall wall drag at the filter chamber's top wall is because of the effects of the heated wall on fluid particles near the top wall of the filter chamber. However, increasing the injection rate reduces the overall skin friction at the top wall due to the effects of the heated wall and gravity because fluid particles spend less time at the top wall before being pulled out of the filter chamber.

Figure 6.8 depicts that the average heat fluxes at the filter chamber's right and top walls reduce as the Joule heating increases. This decrease in the average Nusselt number is due

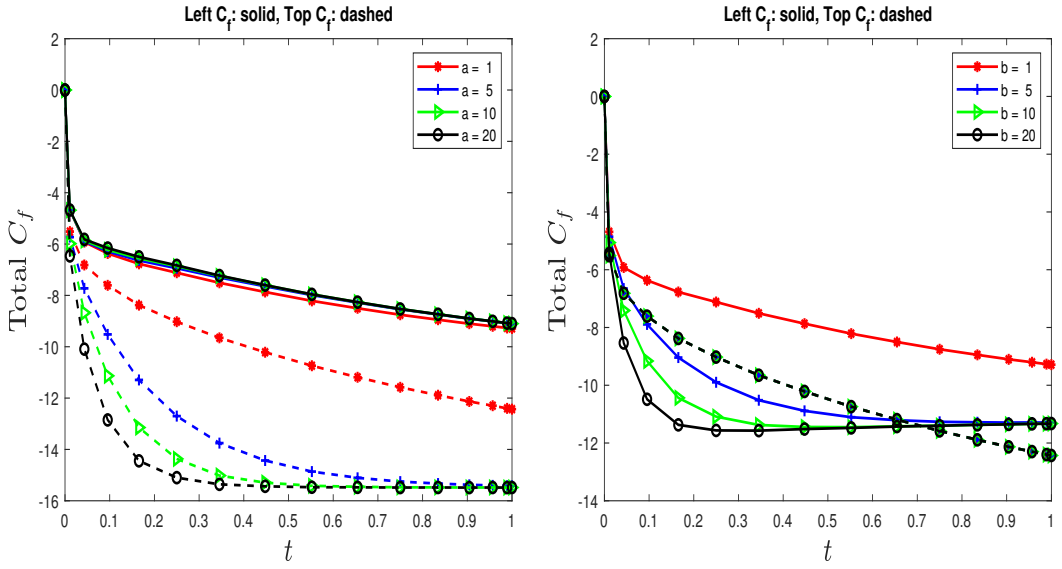

(a) (b)

Figure 6.5: Effects of injection and suction rates on skin friction as time evolves

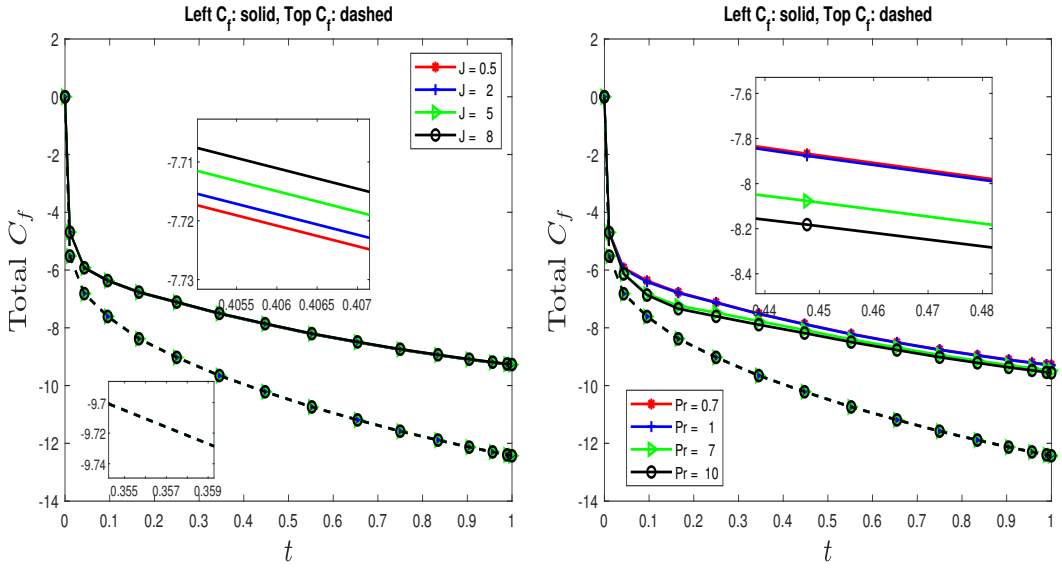

(a) (b)

Figure 6.6: Time evolution of the effects of resistive heating and Prandtl number on the total skin drag

to a rise in the energy sink. Figure 6.9 depicts an amplification in the average Nusselt number at the right vertical and top horizontal walls of the filter chamber, which is caused by the movement of warm particles when the Prandtl number increases.

Figure 6.10 indicates that the average Nusselt number at the right and top walls of the filter chamber are increasing as the thermal radiation parameter increases. The emission of radiative energy causes a rise in the average Nusselts number, which enhances internal energy and, as a result, increases the kinetic energy.

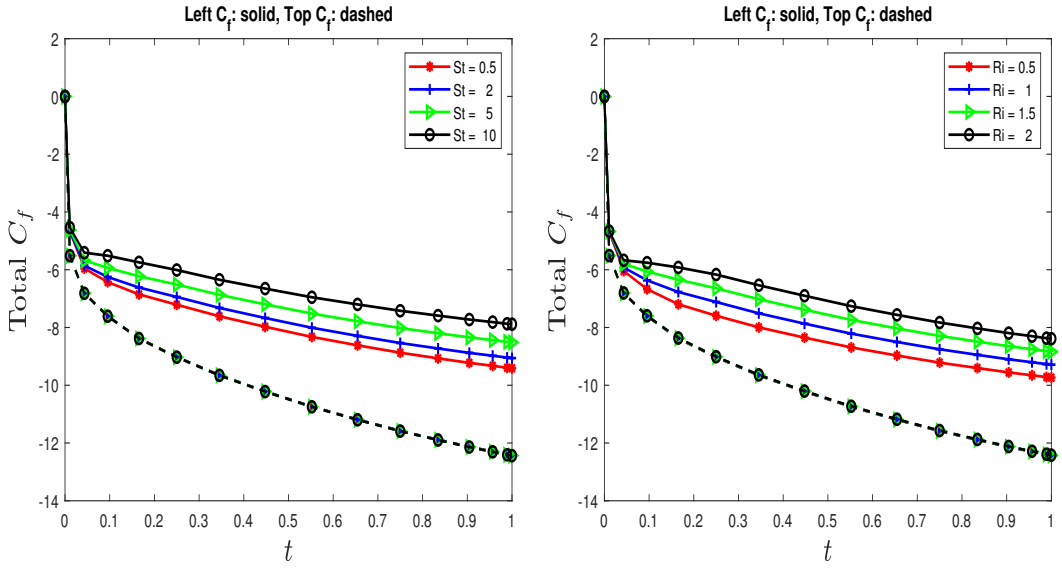

(a) (b)

Figure 6.7: Time evolution of the effects of the Stuart and Richardson numbers on the overall skin friction coefficient.

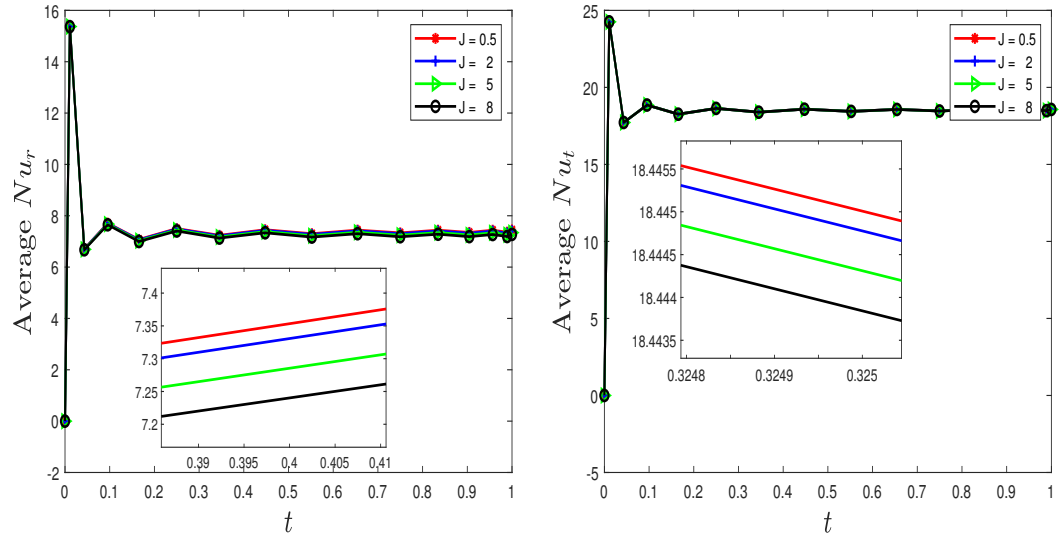

(a) (b)

Figure 6.8: Time evolution of the effects of resistive heating on the average heat fluxes at the right and top walls.

We note that the average Nusselt number initially increase when the filtration process starts. However, this initial increase in the average Nusselt number is transient because the coefficients stabilize and converge as time evolves. Further, we note that the amplitudes of the average Nusselt number on the right wall are lesser than the average Nusselt number on the top wall.

Figure 6.11 shows that an increase in both the injection and outflow rates amplifies the

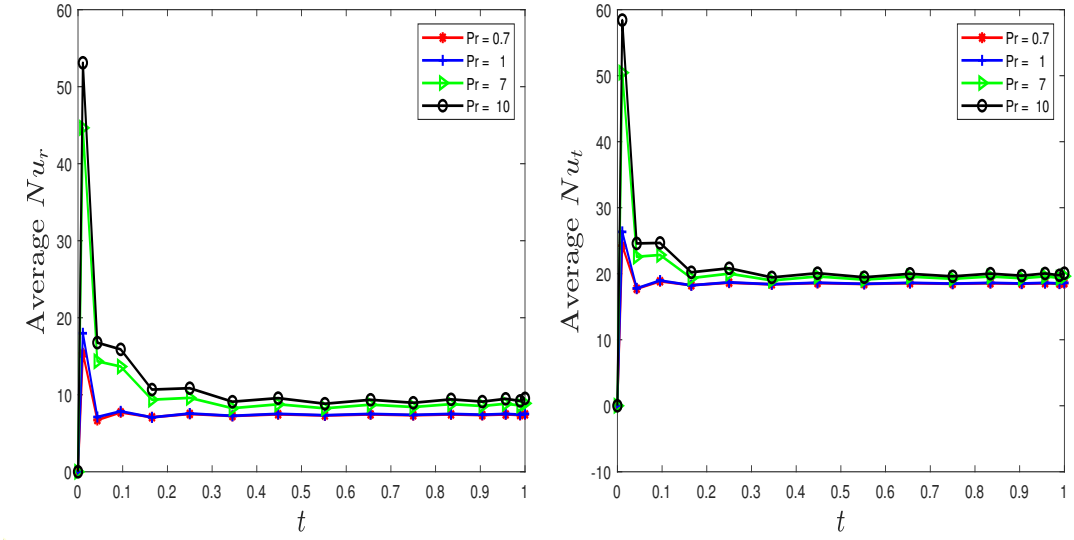

(a) (b)

Figure 6.9: Time evolution of the effects of Prandtl on the average Nusselt numbers at the right and top walls of the filter chamber.

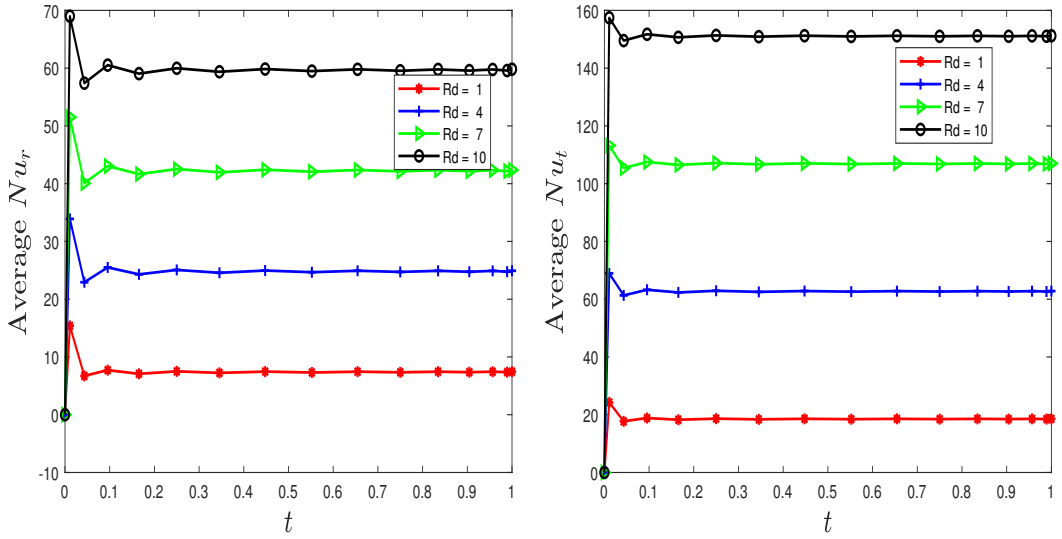

(a) (b)

Figure 6.10: Effects of thermal radiation on the average Nusselt number at the right and top walls of the filter chamber as time evolves

average pressure on the left and right walls. This increased average pressure is because injection and suction elevate the internal work done during filtration and thus increase pressure distribution inside the filter chamber and, inevitably, mean pressure at the filter walls.

Figure 6.12 portrays an increase in the mean pressure on the left and right walls as the Stuart number rise and the Richardson number drops. This rise in the wall pressure

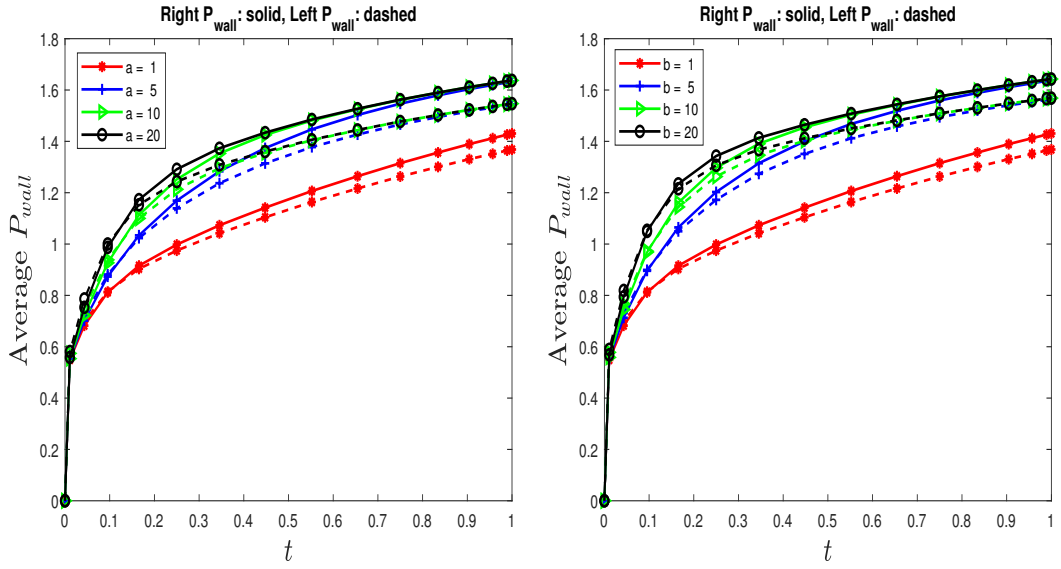

(a) (b)

Figure 6.11: Time evolution of the effects of the injection and suction rates on the average pressure at the right and left walls of the filter chamber.

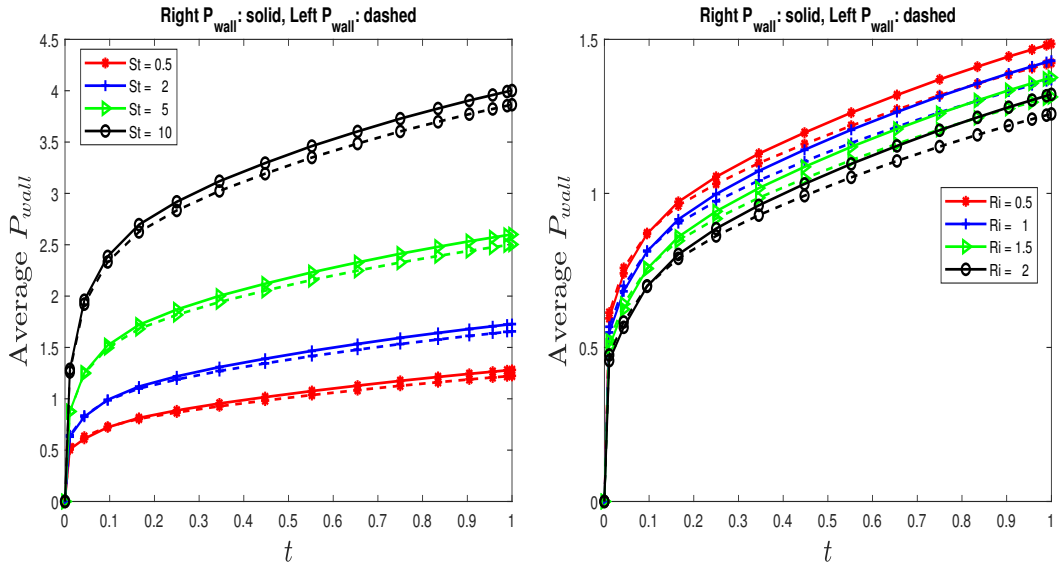

(a) (b)

Figure 6.12: Time evolution of the effects of the Stuart and Richardson numbers on the average pressure at the left and right walls of the filter chamber.

when the Stuart number is increased results from more internal work done inside the filter chamber since a strengthened magnetic field creates internal disturbances. The decreases in the average wall pressure when the Richardson number drops result from the free movement of fluid particles when the Richardson number is lower, creating minimal internal pressure because work done at the walls is minimal. In general, the average pressure at the walls increases as time evolves.

6.5 Conclusion

The work in this chapter presented the theoretical investigation into the dynamics of the time evolution of filtration inside a vertical filter chamber when fluid is injected and suctioned at different rates. A decoupled spectral-based linearization technique was used to approximate the unsteady state solutions of momentum, pressure and heat variation during filtration. To maximize the production of filtered fluid after the filtration of contaminants, the study led to the following conclusions:

i. An increase in fluid injection over time enhances internal work and pressure during the filtration process, which is vital in increasing outflow.

ii. To increase the free movement of fluid particles, high injection rate, suction rate, Richardson number, Prandtl number and Stuart number are ideal during operation to minimize the overall skin friction.

iii. To obtain effective internal temperature distribution and, invariably, decrease viscous effects, increase fluid injection, increase Prandtl number, thermal radiation, and reduce Joule heating to allow effective heat flux during filtration.

iv. The decrease in fluid suction rate increases internal temperature, which reduces the effects of viscous forces. However, this decrease in the fluid suction rate is not ideal because it reduces permeates outflow.

v. Higher injection, Joule heating, Prandtl number, Stuart number, and lower Richardson number are needed to push permeates out of the filter chamber and, consequently, increase permeate outflow.

Chapter 7

Analytical and parametric analysis on MHD mixed convection flow in a porous filter chamber with chemical reaction and heat source/sink

There are two modes of operation for industrial filtration design/equipment, namely constant rate and pressure filtration. Some industrial filter designs can operate on both constant rate and pressure filtration. Therefore, the reference point of the current filter design is to look at the filter design that operates under low differential pressure to allow the MHD fluid to flow through the filter medium embedded inside the horizontal weakly dilating channel. The current chapter analyses the physical interpretation of the internal mass and mixed convection flows under constant magnetic field strength, radiation, chemical reaction and heat source/sink. The suggested fluid dynamics model inside the filter chamber obeys the conservation equations in the form of partial differential equations, which are transformed into dimensionless ordinary differential equations by employing the Lie group analysis. The approximate analytical solutions of the study are obtained using the perturbation method. The excellent agreement of the internal fluid velocity, temperature and concentration profiles was verified with the numerical solutions obtained using the NDSolve Mathematica package. The influences of the parameters on the internal flow properties are illustrated through graphs and tables. Results reveal that enhancing chemical reaction (K_r) and Schmidt number (S_c) decreases the internal fluid concentration while amplifying the skin friction coefficient and Sherwood number. A rise in local heat transfer at the wall is observed when the buoyancy ratio (N) and Richardson number (R_i) increase; this consequently minimises the skin friction coefficient.

NOMENCLATURE

$\bar{x}, \bar{y}$ - cartesian coordinates, (m)
$\bar{t}$ - time, (s)
h - height of the chamber, (m)
$\bar{u}, \bar{v}$ - velocity components, $(m\,s^{-1})$
g - gravitation, $(m\,s^{-2})$
$\bar{P}$ - pressure, (Pa)
T - temperature, (K)
c - concentration, $(mol\,m^{-3})$
ρc_p - heat capacitance, $(J\,m^{-3}\,K^{-1})$
ρ - density, $(kg\,m^{-3})$
ν - kinematic viscosity, $(m^2\,s^{-1})$
$\bar{\kappa}$ - heat conductivity, $(W\,m^{-1}\,K^{-1})$
σ - electrical conductivity, $(\Omega^{-1}\,m^{-1})$
B_0 - magnetic field strength, $(\Omega^{1/2}\,m^{-1}\,s^{-1/2}\,kg^{1/2})$
σ_r - Stefan Boltzmann constant, $(W\,m^{-2}\,K^{-4})$
k_r - mean absorption coefficient, (m^{-1})
q_r - radiative heat flux, $(kg\,s^{-3})$
D - molecular diffusivity, $(m^2\,s^{-1})$
$K_r{}^*$ - chemical reaction term, (s^{-1})
Q_o - heat source/sink, $(kg\,K\,m^{-1}\,s^{-3})$
k - medium permeability, $(H\,m^{-1})$
β - heat expansion, (K^{-1})
β - solutal expansion, $((mol\,m^3)^{-1})$
ϕ - porosity
α - wall dilation parameter
G_r - Grashoff number
M - magnetic parameter
R_e - Reynolds number
K - Porosity parameter
R_i - Richardson number
N - buoyancy ratio
P_r - Prandtl number
R - radiation parameter
λ - internal heat source/sink parameter
J - Joule or resistive heating parameter
S_c - Schmidt number
K_r - chemical reaction parameter
C_f - skin friction coefficient
N_{uL} - local Nusselt number
Sh - local Sherwood number

Abbreviations

MHD - Magnetohydrodynamics
PDE - Partial Differential Equation
ODE - Ordinary Differential Equation
PM - Perturbation Method

Subscripts

w - chamber wall
h - chamber height

7.1 Introduction

When designing a fluid filtration system, factors such as the nature of the contaminants, the flow rate of the fluid process, fluid flow characteristics and filtration efficiency should be considered for best, if not perfect, filtration system operations. Fluid filtration removes contaminants, impurities and solids suspended in a fluid stream. Various filters are such that the contaminated fluid flows through a porous filter medium with tiny pores that allow only filtrates to pass through, leaving contaminants/unwanted solids on the other side of the filter medium. One of the most important industrial applications which use filter mediums is fluid purification [5, 126], where particles are removed from the water. Improving oil recovery Munirasu et al. [127], processing fruit juice Bhattacharjee et al. [128] and recycling of microorganisms Monte et al. [129] are few other applications of the filter medium. Through filtration operation, the fluid encounters flow resistance when it passes through the filter medium and the maturity of the so-called filter cake. Magnetic filters can be included to minimise the maturity of the filter cake and improve the quality of filtrates and production. The filter will, therefore, capture weak magnetic iron contaminants (such as iron filling and rust) and other small ferromagnetic impurities before entering or blocking the filter pores. Modern studies have put more effort into understanding the interaction between the magnetic field and fluid flow characteristics in the survey of electrically-conducting fluid flows. Matebese et al. [130] investigated the impact of a variable magnetic field on a two-dimensional flow in a deformable channel with a porous medium. They found that a rise in the variable magnetic strength enhances the self-axial velocity. Sheikholeslami et al. [131] performed an analytical investigation of MHD nano-fluid flow inside a semi-porous channel. They observed that due to the retarding effects of the Lorenz force, increasing the Hartmann number, the momentum boundary layer thickness decreases by about 66.59%. Das and Mohammed [132] reported the impact of heat radiation on mass and heat transfer characteristics of an incompressible electrically conducting fluid in the presence of the magnetic field. Results indicate that increasing magnetic field strength is desirable since the fluid's drag force and rate of heat transfer decrease. It is also vitally important to control heat transfer in various energy systems because of the energy cost increase. Sheikholeslami et al. [133] studied how radiation affects nano-fluid natural convection heat transfer with the presence of the magnetic field. The study showed that increasing the Lorenz forces decreases the heat transfer rate. Studies of single and multi-phase models for the condensation of nano-fluid film flow and heat transfer have been done by Turkyilmazoglu [134]. The author observed more heat transfer enhancement as diffusion parameters rose in the multi-phase model. Talebi et al. [135] made a numerical investigation of mixed convection laminar flow past a copper-water nano-fluid in a lid-driven cavity. They found that enhancing the Rayleigh number increases buoyancy's effect and the flow's intensity, yet forced convection dominance was observed. Al-Saif and Harfash [136] analysed heat and mass transfer in the unsteady squeezing flow between parallel plates. Authors found that molecular diffusivity diminishes with the enhancement of values S_c. It is also reported that increasing the chemical reaction minimises the internal fluid concentration.

Mustafa et al. [137] considered the chemical reaction and viscous dissipation effects on mass and heat transfer in the squeezing flow between parallel plates. They declared that the concentration field becomes a decreasing function for destructive chemical reaction, that is, $\gamma > 0$, increasing the local Sherwood number magnitude. The study by Mat Noor et al. [138] explored the new entry for better protection systems in nuclear power plants and energy optimisation by studying a hydromagnetic squeezing flow of nano-fluid in a porous channel with a heat source/sink. It was observed that the fluid temperature elevates in the heat generation case and decreases in the heat absorption case. More studies on mass and heat transfer flow inside expanding/contracting channels are reported in articles [139–147].

The mathematical models in the literature are described by boundary value problems related to different types of partial differential equations or systems. Perturbation methods [148, 149] are widely used for obtaining approximate solutions to these equations involving a small physical parameter. The technique relies on a non-dimensional parameter that is relatively small and is effective for the analysis of weakly non-linear problems. Most researchers have employed these perturbation methods in fluid mechanics. Sobamowo [150] made a comparative study of two approximate analytical methods for a two-dimensional transient flow of nano-fluid through a deformable porous channel wall with huge injection or suction under the effects of the magnetic field. The author verified the two analytical methods, differential transformation and perturbation. It was observed that differential transformation shows more remarkable accuracy than the method of matched asymptotic expansion. Perturbation solution to transient flow in a porous channel with expanding or contracting walls in the presence of a transverse magnetic field was found in the study by Si et al. [151]. The authors showed that enhancement of skin friction is observed when the Reynold number drops or the Hartmann number rise. A laminar flow pushed by fluid injection through a porous surface for which fluid inside the filtration chamber is incompressible was investigated by Magalakwe et al. [16]. The authors employed double perturbation to find semi-analytical solutions. They discovered that reverse flow is experienced away from the chamber's centre when the magnetic parameter increases, leading to a decrease in the outflow.

One of the most difficult problems that designers, engineers, and scientists face is controlling mass and heat transfer to avoid structural malfunctioning of filter chamber designs. Studies on MHD mixed convection heat and mass transfer in an expanding or contracting channel have been conducted, as evidenced by the preceding literature review. Motivated by the literature above, the current chapter builds up on the flow investigated by Magalakwe et al. [16] to unfold some additional thermal and solute parameters which play a vital role in controlling mass and heat transfer. The inclusion of heat source/sink, radiation, chemical reaction and fluid concentration are considered to simulate the flow inside the filter chamber. The idea is to examine how concentrated filter walls affect the internal permeate temperature and concentration when there is a chemical reaction happening, and the walls conduct radiatively with the addition of an internal heat source/sink. The perturbation method is employed as a solution tool to portray the flow properties behaviour of this chapter, which aims to provide useful physical information for designers who plan to

use/design a system which does not need sedimentation or clarification before the filtration stage. A sufficient number of graphs, streamlines, and tables are provided to supplement the results.

7.2 Model Formulation

This section considers the mass and heat transfer by mixed convection in a laminar boundary layer flow of an incompressible viscous fluid inside a horizontal filter channel. The walls are maintained at a constant temperature T_w, which is higher than the temperature T_h of the internal fluid and the concentration c_w is greater than the concentration c_h. The fluid properties are assumed to be constant. The mathematical model describing the filtration process heat and mass transfer distribution inside the filter channel is given by

$$\frac{\partial \bar{u}}{\partial \bar{x}} + \frac{\partial \bar{v}}{\partial \bar{y}} = 0, \tag{7.1}$$

$$\frac{\partial \bar{u}}{\partial \bar{t}} + \bar{u}\frac{\partial \bar{u}}{\partial \bar{x}} + \bar{v}\frac{\partial \bar{u}}{\partial \bar{y}} = -\frac{1}{\rho}\frac{\partial \bar{P}}{\partial \bar{x}} + \nu\left[\frac{\partial^2 \bar{u}}{\partial \bar{x}^2} + \frac{\partial^2 \bar{u}}{\partial \bar{y}^2}\right] - \frac{\nu\phi}{k}\bar{u} - \frac{\sigma B_0^2}{\rho}\bar{u}, \tag{7.2}$$

$$\frac{\partial \bar{v}}{\partial \bar{t}} + \bar{u}\frac{\partial \bar{v}}{\partial \bar{x}} + \bar{v}\frac{\partial \bar{v}}{\partial \bar{y}} = -\frac{1}{\rho}\frac{\partial \bar{P}}{\partial \bar{y}} + \nu\left[\frac{\partial^2 \bar{v}}{\partial \bar{x}^2} + \frac{\partial^2 \bar{v}}{\partial \bar{y}^2}\right] - \frac{\nu\phi}{k}\bar{v}$$
$$+g\beta(T - T_h) + g\beta^*(c - c_h), \tag{7.3}$$

$$\frac{\partial T}{\partial \bar{t}} + \bar{u}\frac{\partial T}{\partial \bar{x}} + \bar{v}\frac{\partial T}{\partial \bar{y}} = \frac{\bar{k}}{\rho c_p}\left[\frac{\partial^2 T}{\partial \bar{x}^2} + \frac{\partial^2 T}{\partial \bar{y}^2}\right] - \frac{1}{\rho c_p}\frac{\partial q_r}{\partial \bar{y}} + \frac{Q_o}{\rho c_p}(T - T_h) + \frac{\sigma B_0^2}{\rho c_p}\bar{u}^2, \tag{7.4}$$

$$\frac{\partial c}{\partial \bar{t}} + \bar{u}\frac{\partial c}{\partial \bar{x}} + \bar{v}\frac{\partial c}{\partial \bar{y}} = D\left[\frac{\partial^2 c}{\partial \bar{x}^2} + \frac{\partial^2 c}{\partial \bar{y}^2}\right] - K_r^*(c - c_h), \tag{7.5}$$

where $\bar{u}$, $\bar{v}$ are the components of velocity along the $\bar{x}$, $\bar{y}$ directions respectively, ν is kinematic viscosity, ρ is fluid density, $\bar{t}$ is time, $\bar{P}$ is dimensional pressure, T and c are fluid temperature and concentration respectively, q_r is radiative heat flux, g is the gravity, β and β^* are heat and solutal expansions, B_0 is magnetic strength, ϕ is the dimensional porosity parameter, k is medium permeability, $\bar{k}$ heat conductivity, c_p specific thermal capacity, Q_o internal thermal source/sink, K_r^* chemical reaction term and D mass diffusivity.

The boundary conditions for velocity, temperature and concentration fields are

$$\begin{aligned}
&\text{(i)} && \bar{u} = 0, \quad \bar{v} = -V_w, \quad T = T_w, \quad c = c_w \quad \text{at } \bar{y} = h,\\
&\text{(ii)} && \bar{u}_{\bar{y}} = 0, \quad \bar{v} = 0, \quad T_{\bar{y}} = 0, \quad c_{\bar{y}} = 0 \quad \text{at } \bar{y} = 0,\\
&\text{(iii)} && \bar{u} = 0 \quad \text{at } \bar{x} = 0.
\end{aligned} \tag{7.6}$$

Using the dimensionless variables below in the system (7.1)-(7.5)

$$\begin{aligned}
&u = \frac{\bar{u}}{V_w}, \quad v = \frac{\bar{u}}{V_w}, \quad x = \frac{\bar{x}}{h(t)}, \quad y = \frac{\bar{y}}{h(t)}, \quad \Psi = \frac{\bar{\Psi}}{hV_w}, \quad P = \frac{\bar{P}}{\rho V_w^2},\\
&t = \frac{\bar{t}h}{V_w}, \quad \alpha = \frac{h\dot{h}}{\nu}, \quad \theta = \frac{T - T_h}{T_w - T_h}, \quad \Phi = \frac{c - c_h}{c_w - c_h},
\end{aligned} \tag{7.7}$$

yield the following dimensionless system:

$$\Psi_{y\bar{t}} + \Psi_y\Psi_{xy} - \Psi_x\Psi_{yy} + P_x - \frac{1}{R_e}[\alpha\Psi_y + \alpha y\Psi_{yy} + \Psi_{xxy} + \Psi_{yyy}] + \frac{1}{K}\Psi_y + M\Psi_y = 0, \tag{7.8}$$

$$\Psi_{x\bar{t}} + \Psi_y\Psi_{xx} - \Psi_x\Psi_{xy} - P_y - \frac{1}{R_e}[\alpha y\Psi_{xy} + \Psi_{xyy} + \Psi_{xxx}] + \frac{1}{K}\Psi_x + R_i\big[\theta + N\Phi\big] = 0, \tag{7.9}$$

$$\theta_{\bar{t}} + \Psi_y\theta_x - \Psi_x\theta_y - \frac{1}{P_rR_e}\Big[\theta_{xx} + (1+4R)\theta_{yy}\Big] - \lambda\theta - J\Psi_y^2 = 0, \tag{7.10}$$

$$\frac{\partial\Phi}{\partial\bar{t}} + \Psi_y\frac{\partial\Phi}{\partial\bar{x}} - \Psi_x\frac{\partial\Phi}{\partial y} = \frac{1}{S_cR_e}\left[\frac{\partial^2\Phi}{\partial x^2} + \frac{\partial^2\Phi}{\partial y^2}\right] - K_r\Phi, \tag{7.11}$$

where $\alpha = \dfrac{h\dot{h}}{\nu}$ is the wall dilation rate, $R_e = \dfrac{hV_w}{\nu}$ is the Reynolds number ($R_e > 0$ injection and $R_e < 0$ suction), $M = \frac{\sigma\nu hB_0^2}{\rho V_w}$ is the magnetic parameter, $K = \dfrac{kV_w}{\nu\phi h}$ is the porosity parameter, $R_i = \dfrac{G_r}{R_e^2}$ is the Richardson number, $N = \frac{\beta^*(c_w - c_h)}{\beta(T_w - T_h)}$ buoyancy ratio, $G_r = \frac{hg\beta(T_w - T_h)}{\nu^2}$ and $G_c = \frac{hg\beta(C_w - C_h)}{\nu^2}$ are the thermal and solutal Grashoff number, $P_r = \frac{\rho C_p\nu}{k}$ is the Prandtl number, $R = \frac{4\sigma_r T_h^3}{3k_rk}$ is the radiation parameter ($R < 0$ absorption and $R > 0$ emission), $\lambda = \frac{Q_oh}{V_w\rho c_P}$ is heat source/sink parameter ($\lambda > 0$ source and $\lambda < 0$ sink), $J = \frac{\sigma B_0^2hV_w}{\rho c_p(T_w - T_h)}$ is the Joule/resistive heating parameter, $S_c = \frac{\nu}{D}$ is the Schmidt number, $K_r = \dfrac{K_r^*h}{V_w}$ is the chemical reaction parameter.

Similarly, the boundary conditions change to:

$$\begin{aligned}
&\text{(i)} && \Psi_y = 0, \quad \Psi_x = 1, \quad \theta = 1, \quad \Phi = 1, \quad \text{at } y = 1,\\
&\text{(ii)} && \Psi_{yy} = 0, \quad \Psi_x = 0, \quad \theta_y = 0, \quad \Phi_y = 0, \quad \text{at } y = 0,\\
&\text{(iii)} && \Psi_y = 0 \quad \text{at } x = 0.
\end{aligned} \tag{7.12}$$

7.3 Solution methodology

We use Lie group analysis [19, 120, 125, 152–155] to transform (7.8) -(7.11) to system of ordinary differential equations. After that, double perturbation is employed to find semi-analytical solutions for the problem under investigation.

7.3.1 Lie group analysis

With the help of Maple, the dimensionless system (7.8)-(7.11) admits the following six symmetries:

$$X_1 = \frac{\partial}{\partial t}, \quad X_2 = \frac{\partial}{\partial x}, \quad X_3 = z_1(t)\frac{\partial}{\partial\Psi}, \quad X_4 = z_2(t)\frac{\partial}{\partial P},$$
$$X_5 = e^{\lambda t}\Big(yR_i\frac{\partial}{\partial P} - \frac{\partial}{\partial\theta}\Big), \quad X_6 = e^{K_rt}\Big(yNR_i\frac{\partial}{\partial P} - \frac{\partial}{\partial\Phi}\Big).$$

Thus the general invariant solutions are given by

$$\Psi = h(y)H(x,y), \ P = \Gamma(x,y), \ \theta = \tau(x,y), \ \Phi = \xi(x,y). \tag{7.13}$$

Where $h(y)$ is a function of y and H, Γ, τ, ξ are functions of both x and y. Substituting equation (7.13) into equation (7.8) and applying similar manipulations as in Magalakwe et al. [16], we obtain the dimensionless stream function to be

$$\Psi = xU(y), \tag{7.14}$$

where $U(y)$ is a function of y. Substituting the above stream function to revert back to axial and normal velocities yields

$$\frac{u}{x} = \frac{dU}{dy}, \qquad v = -U(y). \tag{7.15}$$

The above velocity components confirm that normal flow is injected into the filter chamber and axial velocity changes along the normal direction per length of the chamber. This information confirms the parabolic flow field inside the chamber.

Differentiating equation obtained from substituting equation (7.14) in equation (7.9) with respect to x, yields

$$P_{xy} = R_i\big[\theta_x + N\Phi_x\big]. \tag{7.16}$$

Similarly by substituting equation (7.14) into equation (7.8) and invoking (7.16) yields

$$\begin{aligned}\bigg[\frac{d^4U}{dy^4} + \alpha\bigg(y\frac{d^3U}{dy^3} + 2\frac{d^2U}{dy^2}\bigg) + R_eU\frac{d^3U}{dy^3} - \frac{R_e}{K}\frac{d^2U}{dy^2} - Re\frac{d^2U}{dy^2}M \\ -R_e\frac{dU}{dy}\frac{d^2U}{dy^2}\bigg]x - R_i\big[\theta_x + N\Phi_x\big] = 0.\end{aligned} \tag{7.17}$$

Differentiating the above equation (7.17) twice with respect to x, yields

$$R_i\big[\theta_{xxx} + N\Phi_{xxx}\big] = 0, \tag{7.18}$$

since, we consider mixed convection flow, the importance of natural convection relative to the forced is very crucial in the study; thus, R_i cannot be zero from equation (7.18), hence

$$\theta_{xxx} + N\Phi_{xxx} = 0, \tag{7.19}$$

comparing powers of N yields

$$\left.\begin{aligned}N^0 : \theta_{xxx} = 0, \\ N : \Phi_{xxx} = 0.\end{aligned}\right\} \tag{7.20}$$

Integrating the equations in system (7.20) twice with respect to x, we get

$$\left.\begin{aligned}\theta_x = A(y)x + B(y), \\ \Phi_x = C(y)x + D(y),\end{aligned}\right\} \tag{7.21}$$

where A, B, C and D are functions of integration. Substituting equation (7.21) into equation (7.17) and comparing the powers of x, we obtain the following equations

$$\begin{aligned}x : \bigg[\frac{d^4U}{dy^4} + \alpha\bigg(y\frac{d^3U}{dy^3} + 2\frac{d^2U}{dy^2}\bigg) + R_eU\frac{d^3U}{dy^3} - \frac{R_e}{K}\frac{d^2U}{dy^2} - Re\frac{d^2U}{dy^2}M \\ -R_e\frac{dU}{dy}\frac{d^2U}{dy^2}\bigg] - R_i\big[A(y) + NC(y)\big] = 0,\end{aligned} \tag{7.22}$$

$$x^0 : R_i\big[B(y) + ND(y)\big] = 0. \tag{7.23}$$

Solving equation (7.23), we get that

$$B(y) = D(y) = 0.$$

Since other parameters are non-zero constants. Thus, the ordinary differential equation representing the stream velocity variation becomes

$$\left[\frac{d^4U}{dy^4} + \alpha\left(y\frac{d^3U}{dy^3} + 2\frac{d^2U}{dy^2}\right) + R_eU\frac{d^3U}{dy^3} - \frac{R_e}{K}\frac{d^2U}{dy^2} - Re\frac{d^2U}{dy^2}M - R_e\frac{dU}{dy}\frac{d^2U}{dy^2}\right] - R_i\big[A(y) + NC(y)\big] = 0. \tag{7.24}$$

Using equation (7.14), $\theta = \tau(x, y)$ and $\Phi = \xi(x, y)$ from (7.13) in (7.10) and (7.11) respectively, we obtain

$$x\frac{\partial\tau}{\partial x}\frac{dU}{dy} - \frac{\partial\tau}{\partial y}U - \frac{1}{P_rR_e}\left[\frac{\partial^2\tau}{\partial x^2} + (1+4R)\frac{\partial^2\tau}{\partial y^2}\right] - \lambda\tau - Jx^2\left(\frac{dU}{dy}\right)^2 = 0, \tag{7.25}$$

$$x\frac{\partial\xi}{\partial x}\frac{dU}{dy} - \frac{\partial\xi}{\partial y}U - \frac{1}{ScR_e}\left[\frac{\partial^2\xi}{\partial x^2} + \frac{\partial^2\xi}{\partial y^2}\right] - K_r\xi = 0, \tag{7.26}$$

since $B(y) = D(y) = 0$, equation (7.21) becomes

$$\left.\begin{aligned}\theta_x &= A(y)x,\\ \Phi_x &= C(y)x.\end{aligned}\right\} \tag{7.27}$$

Integrating (7.27) with respect to x yields

$$\left.\begin{aligned}\theta &= A(y)\frac{x^2}{2} + E(y),\\ \Phi &= C(y)\frac{x^2}{2} + F(y)\end{aligned}\right\} \tag{7.28}$$

where $E(y) = F(y) = 0$ after using border constraints at $x = 0$, making the temperature and concentration to become

$$\theta = A(y)\frac{x^2}{2}, \tag{7.29}$$

$$\Phi = C(y)\frac{x^2}{2} \tag{7.30}$$

which confirms the parabolic nature of both temperature and concentration. Using the above results, the temperature and concentration becomes

$$2A(y)\frac{dU}{dy} - \frac{dA}{dy}U(y) - \frac{(1+4R)}{P_rR_e}\frac{d^2A}{dy^2} - \lambda A(y) - 2J\left(\frac{dU}{dy}\right)^2 = 0, \tag{7.31}$$

$$2C(y)\frac{dU}{dy} - \frac{dC}{dy}U(y) - \frac{1}{S_cR_e}\frac{d^2C}{dy^2} - K_rC(y) = 0. \tag{7.32}$$

Thus, the system of ordinary differential equations representing the momentum stream,

energy and concentration for a steady state filtration operation becomes

$$\frac{d^4U}{dy^4}+\alpha\left(y\frac{d^3U}{dy^3}+2\frac{d^2U}{dy^2}\right)+R_eU\frac{d^3U}{dy^3}-\frac{R_e}{K}\frac{d^2U}{dy^2}-Re\frac{d^2U}{dy^2}M$$
$$-R_e\frac{dU}{dy}\frac{d^2U}{dy^2}-R_i\big[A(y)+NC(y)\big]=0, \tag{7.33}$$

$$2A(y)\frac{dU}{dy}-\frac{dA}{dy}U(y)-\frac{(1+4R)}{P_rR_e}\frac{d^2A}{dy^2}-\lambda A(y)-2J\left(\frac{dU}{dy}\right)^2=0, \tag{7.34}$$

$$2C(y)\frac{dU}{dy}-\frac{dC}{dy}U(y)-\frac{1}{S_cR_e}\frac{d^2C}{dy^2}-K_rC(y)=0, \tag{7.35}$$

subject to the following border constraints

$$\text{(i)}\qquad \frac{dU(y)}{dy}=0,\quad U(y)=1,\quad A(y)=1,\quad C(y)=1,\quad \text{at } y=1,$$
$$\text{(ii)}\qquad \frac{d^2U(y)}{dy^2}=0,\quad U(y)=0,\quad \frac{dA(y)}{dy}=0,\quad \frac{dC(y)}{dy}=0,\quad \text{at } y=0. \tag{7.36}$$

7.4 Method of solution using regular perturbation method

In this section, we apply a relatively simple and accurate method to approximate analytical solutions, the perturbation method. The method is based on the fact that the equation(s) describing the phenomena or process under investigation contain(s) a small parameter (or several small parameters), explicitly or implicitly. For minimising turbulence behaviour, the current design is such that permeation of the fluid into the filter chamber through the chamber walls is weak, and the walls dilate slowly at a constant rate. Thus, we choose small parameters to be R_e and α.

In solving the system of the ordinary differential equation describing the phenomena under investigation, we expand the momentum stream, temperature and concentration as

$$\left.\begin{aligned} U(y)&=U_0(y)+R_eU_1(y)+\cdots,\\ A(y)&=A_0(y)+R_eA_1(y)+\cdots,\\ C(y)&=C_0(y)+R_eC_1(y)+\cdots,\\ \text{where}&\\ U_0(y)&=U_{00}(y)+\alpha U_{01}(y)+\cdots,\\ U_1(y)&=U_{10}(y)+\alpha U_{11}(y)+\cdots. \end{aligned}\right\} \tag{7.37}$$

Substituting equation (7.37) into system (7.33)-(7.35), and solving the resulting equations, yield the leading order term solutions U_0, A_0 and C_0 as

$$A_0(y)=1, \tag{7.38}$$
$$C_0(y)=1, \tag{7.39}$$
$$U_0(y)=\frac{y}{2880}\Big[72\left(3(\alpha+20)+3\alpha y^4-2(3\alpha+10)y^2\right)$$
$$-(N+1)(y-1)^2R_i\big(-3(\alpha+20)$$
$$+16\alpha y^3+5\alpha y^2-6(\alpha+20)y\big)\Big] \tag{7.40}$$

and the first-order term solutions for U_1, A_1 and C_1 as

$$
\begin{aligned}
A_1(y) = \frac{P_r}{3193344000(4R+1)}\Big[&144(N+1)(y-1)R_i\big[3J\big(-413\alpha^2-14850\alpha\\
&+3360\alpha^2y^{10}-2415\alpha^2y^9-175\alpha(49\alpha+264)y^8+50\alpha(109\alpha+561)y^7\\
&+10(721\alpha^2+11605+17600)y^6-2\left(1554\alpha^2+32835\alpha+50600\right)y^5\\
&-2\left(1554\alpha^2+42075\alpha+235400\right)y^4+\left(742\alpha^2+31350\alpha+299200\right)y^3\\
&+\left(742\alpha^2+31350\alpha+299200\right)y^2-(413\alpha^2+14850\alpha+162800)y-162800\big)\\
&-1100(y-1)^2\big(-3(\alpha+42)+32\alpha y^4+33\alpha y^3+3(\alpha-112)y^2-9(\alpha+42)y\big)\big]\\
&-J(N+1)^2(y-1)R_i^2\big(1361\alpha^2+49390+53760\alpha^2y^{11}-127680\alpha^2y^{10}\\
&+35\alpha(807\alpha-22528)y^9+35\alpha(3271\alpha+48752)y^8-10\big(4144\alpha^2+29843\alpha\\
&-316800\big)y^7-10\left(5200\alpha^2+124883\alpha+633600\right)y^6+2\big(7033\alpha^2+165605\alpha\\
&+574200\big)y^5+2(7033\alpha^2+221045\alpha+1683000)y^4-2(1052\alpha^2+44605\alpha\\
&+396000)y^3-2(1052\alpha^2+44605\alpha+396000)y^2+(1361\alpha^2+49390\alpha+594000)y\\
&+594000\big)-57024\left(y^2-1\right)\big(J\big(151\alpha^2+4890\alpha+175\alpha^2y^8-250\alpha(2\alpha+9)y^6\\
&+\left(466\alpha^2+6990\alpha+8400\right)y^4-2\big(82\alpha^2+3855\alpha+16800\big)y^2+92400\big)\\
&-1400\left(\alpha-20\lambda+\alpha y^4-2(\alpha+5)y^2+50\right)\big)\Big],
\end{aligned}
\tag{7.41}
$$

$$
\begin{aligned}
C_1(y) = -\frac{S_c}{20160}\Big[&-10080\left(y^2-1\right)K_c+(N+1)(y-1)^3R_i\big(-3(\alpha+42)\\
&+32\alpha y^4+33\alpha y^3+3(\alpha-112)y^2-9(\alpha+42)y\big)-504\left(y^2-1\right)\\
&\big(\alpha+\alpha y^4-2(\alpha+5)y^2+50\big)\Big],
\end{aligned}
\tag{7.42}
$$

$$
\begin{aligned}
U_1(y) = \frac{y}{6974263296000(4RK+K)}\Big[&JK(N+1)^2(y-1)^2\big[110080\alpha y^{11}-282160\alpha y^{10}\\
&-50(1203\alpha+11648)y^9+20(27749\alpha+72800)y^8+(4946\alpha+251160)y^7\\
&-16(39073\alpha+159705)y^6+28(12011\alpha+1560)y^5+8(162223\alpha+330330)y^4\\
&-20(289439\alpha+158340)y^3-16(168346\alpha+561015)y^2+6(816033\alpha+6544720)y\\
&+3(816033\alpha+6544720)\big]P_rR_i^3-1092K(N+1)(y-1)^2\Big(2\big[5\big(416\alpha y^8-620\alpha y^7\\
&-8(207\alpha+440)y^6+8(274\alpha+605)y^5+40(151\alpha+330)y^4-8(1767\alpha+1925)y^3\\
&-125(53\alpha+352)y^2+(4846\alpha+93720)y+2423\alpha+46860\big)+2J\big(920\alpha y^{10}-410\alpha y^9\\
&-300(21\alpha+16)y^8+6(733\alpha+380)y^7+48(342\alpha+745)y^6-12(1343\alpha+2480)y^5\\
&-24(2027\alpha+3970)y^4+300(473\alpha+388)y^3+12(6251\alpha+27340)y^2-6(20921\alpha\\
&+154240)y-62763\alpha-462720\big)\big]P_r+5(4R+1)\big[(N+1)\big(3232\alpha y^8-4360\alpha y^7\\
&+2(459\alpha-8800)y^6-8(133\alpha-3025)y^5-2(1127\alpha+2640)y^4-4(399\alpha-550)y^3\\
&+(1471\alpha+9680)y^2+2(2269\alpha+8580)y+2269\alpha+8580\big)+2N\big(416\alpha y^8-620\alpha y^7\\
&-8(207\alpha+440)y^6+8(274\alpha+605)y^5+40(151\alpha+330)y^4-8(1767\alpha+1925)y^3\\
&-125(53\alpha+352)y^2+(4846\alpha+93720)y+2423\alpha+46860\big)S_c\big]\Big)R_i^2\\
&-26208\Big(55(4R+1)(y-1)^2\Big[(N+1)\big[24\big(50\alpha y^5-20\alpha y^4-10(9\alpha+28)y^3\\
&+(70-27\alpha)y^2+12(3\alpha+35)y+6(3\alpha+35)\big)+K\big(-328\alpha y^7+124\alpha y^6\\
&-36(59\alpha-50)y^5-4(601\alpha+180)y^4+(6840-2180\alpha)y^3+75(11\alpha+192)y^2\\
&+10(383\alpha+2196)y+5(383\alpha+2196)+24M\big(50\alpha y^5-20\alpha y^4-10(9\alpha+28)y^3\\
&+(70-27\alpha)y^2+12(3\alpha+35)y+6(3\alpha+35)\big)\big)\big]-2KN\big[44\alpha y^7+88\alpha y^6\\
&-24(44\alpha+15)y^5-40(55\alpha+18)y^4+40(349\alpha+225)y^3+3(1787\alpha+6240)y^2\\
&-2(2879\alpha+48780)y-2879\alpha-60\big(6\alpha y^5+12\alpha y^4-2(47\alpha+28)y^3\\
&-16(2\alpha+7)y^2+6(5\alpha+112)y+15\alpha+336\big)K_c-48780\big]S_c\Big]\\
&-2K\big[3J\big(250\alpha y^{11}-44(73\alpha+30)y^9+990(37\alpha+20)y^7-9240(47\alpha+30)y^5\\
&+591624\alpha y^4+990(163\alpha+3080)y^3-11(41339\alpha+358560)y^2+102347\alpha\\
&+1153680\big)+55\big(44\alpha y^9+36(10\lambda\alpha-33\alpha-10)y^7-168(40\lambda\alpha-103\alpha\\
&+20\lambda-60)y^5+63\alpha(160\lambda-393)y^4-2520(\alpha-20\lambda+50)y^3-6(770\lambda\alpha\\
&-2333\alpha+11200\lambda-27510)y^2-2879\alpha+900\alpha\lambda+20160\lambda-48780\big)\big]P_r\Big)R_i\\
&-69189120(4R+1)(y^2-1)^2\big(-480\alpha y^2+552\alpha+K\big(65\alpha y^4\\
&+(454\alpha-360)y^2+681\alpha+M\left(\left(552-480y^2\right)\alpha+2520\right)-720\big)+2520\big)\Big]. \quad (7.43)
\end{aligned}
$$

Using the above results into (7.37), we obtain temperature, concentration and stream velocity as

$$
\begin{aligned}
A(y) &= 1+\frac{P_rR_e}{3193344000(4R+1)}\Big[144(N+1)(y-1)R_i\big[3J\big(-413\alpha^2-14850\alpha\\
&+3360\alpha^2y^{10}-2415\alpha^2y^9-175\alpha(49\alpha+264)y^8+50\alpha(109\alpha+561)y^7\\
&+10\left(721\alpha^2+11605\alpha+17600\right)y^6-2\left(1554\alpha^2+32835\alpha+50600\right)y^5\\
&-2\left(1554\alpha^2+42075\alpha+235400\right)y^4+\left(742\alpha^2+31350\alpha+299200\right)y^3\\
&+\left(742\alpha^2+31350\alpha+299200\right)y^2-\left(413\alpha^2+14850\alpha+162800\right)y\\
&-162800\big)-1100(y-1)^2\big(-3(\alpha+42)+32\alpha y^4+33\alpha y^3+3(\alpha-112)y^2\\
&-9(\alpha+42)y\big)\big]-J(N+1)^2(y-1)R_i^2\big(1361\alpha^2+49390\alpha+53760\alpha^2y^{11}\\
&-127680\alpha^2y^{10}+35\alpha(807\alpha-22528)y^9+35\alpha(3271\alpha+48752)y^8\\
&-10\big(4144\alpha^2+29843\alpha-316800\big)y^7-10\left(5200\alpha^2+124883\alpha+633600\right)y^6\\
&+2\big(7033\alpha^2+165605\alpha+574200\big)y^5+2\left(7033\alpha^2+221045\alpha+1683000\right)y^4\\
&-2\left(1052\alpha^2+44605\alpha+396000\right)y^3-2\left(1052\alpha^2+44605\alpha+396000\right)y^2\\
&+\left(1361\alpha^2+49390\alpha+594000\right)y+594000\big)-57024\left(y^2-1\right)\big(J\big(151\alpha^2\\
&+4890\alpha+175\alpha^2y^8-250\alpha(2\alpha+9)y^6+\left(466\alpha^2+6990\alpha+8400\right)y^4\\
&-2\left(82\alpha^2+3855\alpha+16800\right)y^2+92400\big)-1400\big(\alpha-20\lambda+\alpha y^4\\
&-2(\alpha+5)y^2+50\big)\big)\Big], \qquad (7.44)
\end{aligned}
$$

$$
\begin{aligned}
C(y) &= 1-\frac{S_cR_e}{20160}\Big[-10080\left(y^2-1\right)K_c+(N+1)(y-1)^3R_i\big(-3(\alpha+42)\\
&+32\alpha y^4+33\alpha y^3+3(\alpha-112)y^2-9(\alpha+42)y\big)-504\left(y^2-1\right)\\
&\left(\alpha+\alpha y^4-2(\alpha+5)y^2+50\right)\Big], \qquad (7.45)
\end{aligned}
$$

$$
\begin{aligned}
U(y) \;=\;& \frac{1}{48}\big[2Ny^4R_i - 3Ny^3R_i + NyR_i + 2y^4R_i - 3y^3R_i + yR_i - 24y^3 + 72y\big] \\
&+\frac{\alpha}{2880}\big[-16Ny^6R_i + 27Ny^5R_i - 14Ny^3R_i + 3NyR_i - 16y^6R_i + 27y^5R_i \\
&-14y^3R_i + 3yR_i + 216y^5 - 432y^3 + 216y\big] + \frac{yR_e}{6974263296000(4RK+K)} \\
&\Big[JK(N+1)^2(y-1)^2\big[110080\alpha y^{11} - 282160\alpha y^{10} - 50(1203\alpha + 11648)y^9 \\
&+20(27749\alpha + 72800)y^8 + (4946\alpha + 251160)y^7 - 16(39073\alpha + 159705)y^6 \\
&+28(12011\alpha + 1560)y^5 + 8(162223\alpha + 330330)y^4 - 20(289439\alpha + 158340)y^3 \\
&-16(168346\alpha + 561015)y^2 + 6(816033\alpha + 6544720)y + 3(816033\alpha + 6544720)\big] \\
&P_rR_i^3 - 1092K(N+1)(y-1)^2\Big(2\big[5\big(416\alpha y^8 - 620\alpha y^7 - 8(207\alpha + 440)y^6 \\
&+8(274\alpha + 605)y^5 + 40(151\alpha + 330)y^4 - 8(1767\alpha + 1925)y^3 - 125(53\alpha + 352)y^2 \\
&+(4846\alpha + 93720)y + 2423\alpha + 46860\big) + 2J\big(920\alpha y^{10} - 410\alpha y^9 - 300(21\alpha + 16)y^8 \\
&+6(733\alpha + 380)y^7 + 48(342\alpha + 745)y^6 - 12(1343\alpha + 2480)y^5 - 24(2027\alpha + 3970)y^4 \\
&+300(473\alpha + 388)y^3 + 12(6251\alpha + 27340)y^2 - 6(20921\alpha + 154240)y \\
&-62763\alpha - 462720\big)\big]P_r + 5(4R+1)\big[(N+1)\big(3232\alpha y^8 - 4360\alpha y^7 + 2(459\alpha - 8800)y^6 \\
&-8(133\alpha - 3025)y^5 - 2(1127\alpha + 2640)y^4 - 4(399\alpha - 550)y^3 + (1471\alpha + 9680)y^2 \\
&+2(2269\alpha + 8580)y + 2269\alpha + 8580\big) + 2N\big(416\alpha y^8 - 620\alpha y^7 - 8(207\alpha + 440)y^6 \\
&+8(274\alpha + 605)y^5 + 40(151\alpha + 330)y^4 - 8(1767\alpha + 1925)y^3 - 125(53\alpha + 352)y^2 \\
&+(4846\alpha + 93720)y + 2423\alpha + 46860\big)S_c\big]\Big)R_i^2 \\
&-26208\Big(55(4R+1)(y-1)^2\Big[(N+1)\big[24\big(50\alpha y^5 - 20\alpha y^4 - 10(9\alpha + 28)y^3 \\
&+(70 - 27\alpha)y^2 + 12(3\alpha + 35)y + 6(3\alpha + 35)\big) + K\big(-328\alpha y^7 + 124\alpha y^6 \\
&-36(59\alpha - 50)y^5 - 4(601\alpha + 180)y^4 + (6840 - 2180\alpha)y^3 + 75(11\alpha + 192)y^2 \\
&+10(383\alpha + 2196)y + 5(383\alpha + 2196) + 24M\big(50\alpha y^5 - 20\alpha y^4 - 10(9\alpha + 28)y^3 \\
&+(70 - 27\alpha)y^2 + 12(3\alpha + 35)y + 6(3\alpha + 35)\big)\big)\big] - 2KN\big[44\alpha y^7 + 88\alpha y^6 \\
&-24(44\alpha + 15)y^5 - 40(55\alpha + 18)y^4 + 40(349\alpha + 225)y^3 + 3(1787\alpha + 6240)y^2 \\
&-2(2879\alpha + 48780)y - 2879\alpha - 60\big(6\alpha y^5 + 12\alpha y^4 - 2(47\alpha + 28)y^3 \\
&-16(2\alpha + 7)y^2 + 6(5\alpha + 112)y + 15\alpha + 336\big)K_c - 48780\big]S_c\Big] \\
&-2K\big[3J\big(250\alpha y^{11} - 44(73\alpha + 30)y^9 + 990(37\alpha + 20)y^7 - 9240(47\alpha + 30)y^5 \\
&+591624\alpha y^4 + 990(163\alpha + 3080)y^3 - 11(41339\alpha + 358560)y^2 + 102347\alpha \\
&+1153680\big) + 55\big(44\alpha y^9 + 36(10\lambda\alpha - 33\alpha - 10)y^7 - 168(40\lambda\alpha - 103\alpha + 20\lambda \\
&-60)y^5 + 63\alpha(160\lambda - 393)y^4 - 2520(\alpha - 20\lambda + 50)y^3 - 6(770\lambda\alpha - 2333\alpha \\
&+11200\lambda - 27510)y^2 - 2879\alpha + 900\alpha\lambda + 20160\lambda - 48780\big)\big]P_r\Big)R_i \\
&-69189120(4R+1)(y^2-1)^2\big(-480\alpha y^2 + 552\alpha + K\big(65\alpha y^4 \\
&+(454\alpha - 360)y^2 + 681\alpha + M\left(\left(552 - 480y^2\right)\alpha + 2520\right) - 720\big) + 2520\big)\Big]. \qquad (7.46)
\end{aligned}
$$

The shear stress on the body's surface due to fluid motion is known as the skin friction coefficient. For the quantity of heat exchange between the body and the fluid, at the boundary, the heat exchanged between the fluid and the body is due to conduction and radiation; the local Nusselt number and Sherwood number are used to analyse heat flux and radiation, respectively. These parameters of physical importance are defined as skin friction coefficient C_f, the local Nusselt number N_{uL} and Sherwood number Sh below:

$$C_f = \frac{2\tau_w}{\rho V_w^2}, \quad N_{uL} = \frac{\bar{x}q_w}{k(T_w - T_h)}, \quad Sh = \frac{\bar{x}J_w}{D(C_w - C_h)} \tag{7.47}$$

where τ_w is the shear stress along the permeable wall, q_w is the wall heat flux and J_w is the wall mass flux, respectively defined as

$$\tau_w = -\mu\left(\frac{\partial \bar{u}}{\partial \bar{y}}\right)_{\bar{y}=1}, \quad q_w = -k\left(\frac{\partial T}{\partial \bar{y}} + \frac{16\sigma_r T_h^3}{3k_r k}\frac{\partial T}{\partial \bar{y}}\right)_{\bar{y}=1}, \quad J_w = -D\left(\frac{\partial C}{\partial y}\right)_{\bar{y}=1}. \tag{7.48}$$

The dimensionless skin friction coefficient, local heat transfer rate and Sherwood at the permeable top wall are defined as

$$\left.\begin{aligned} C_f &= \frac{-2}{R_e}U''(1), \\ N_{uL} &= -x(1+4R)A'(1), \\ Sh &= -xC'(1). \end{aligned}\right\} \tag{7.49}$$

The negative sign above indicates the work done on the system by these parameter.

7.5 Results and discussion

In this section, we analyse the axial permeate velocity, coefficient skin friction, local Nusselt number, local Sherwood, temperature and concentration distribution under the influence of physical parameters. Also, the verification of the approximate analytical solutions to numerical methods and stream flow patterns are represented graphically. The choice values of a physical parameter used in the current chapter are picked based on the design of the filter chamber. The following values are used to analyse the parameters of the flow properties. Our preference for $x = 1$ is to study the behaviour at the outlet of the filter chamber, where fully developed fluid is stable. $R_e = 1$ to show minimal constant fluid injection, which minimises turbulence. The values $-1 \leq \alpha \leq 1$ were chosen to examine how chamber space affects flow properties. The positive α indicates the expansion of the filter space, while negative values show contraction. For the effectiveness of the porous medium, $K = 3$ was picked since smaller values of K indicate big pores and more significant values of small pores of the medium. The values were chosen to investigate how magnetic field strength affects flow properties. The choice of $M = 2$ was preferred since magnetic strength must be high to restrict magnetic impurities from entering the filter chamber. Since the flow is mixed convection, for analysis, we picked $0.1 \leq R_i \leq 10$, to neutralise natural/forced convection dominance in the system. The choice of $N > 0$ was to learn how the proportionality between thermal and solutes Grashof number affects the flow properties. The values $-1 \leq R \leq 1$ were preferred to investigate how emission ($R > 0$),

absorption ($R < 0$), and no radiation affects fluid flow properties. The P_r values to study how momentum diffusivity ($P_r < 1$) and thermal diffusivity ($P_r > 1$) dominance behaves in the system. Still, for analysing, we picked $P_r < 1$ since the idea is to maximise the permeates outflow. The source ($\lambda > 0$)/sink ($\lambda < 0$) were picked to analyse which one of these two contributes positively to the internal dynamics of the filter system. Since high resistance (electrically conducting fluid acting as a resistor) produces higher heat, the Joule/resistive heating parameter was chosen to be $J \geq 0$. Momentum diffusivity is crucial to maximising permeates outflow; hence Schmidt was preferred for $S_c > 0$. Finally, the values of chemical reaction were chosen to be $K_r > 0$ to examine how it affects flow properties.

Table 7.1 shows the effects of thermal and mass coefficients, dimensionless parameters affecting the internal flow field. The table shows that the fluid velocity is zero at the upper wall due to the no-slip condition, and it is maximum at the centre of the filter chamber. This behaviour happens for every varying dimensionless parameter. The rise in Schmidt number, according to sub-table b, increases the fluid viscosity and makes fluid particles struggle to move, decreasing the fluid velocity. The increase in fluid chemical reaction parameter decreases the fluid velocity since higher values of the chemical reaction results in less chemical molecular diffusivity, thus less diffusion as portrayed in sub-table c. It can also be observed from sub-table d that for a small buoyancy ratio, the fluid velocity is maximum towards the centre. This happens since a small buoyancy ratio leads to small temperature differences, thus decreasing shear forces and resulting in effortless fluid flow inside the filter chamber. The increase in velocity towards the centre as the Richardson number decreases due to both natural and forced convection (since $0.10 < R_i < 10$) taking place, thus making the buoyancy forces more dominant and minimizing shear forces as shown in sub-table e.

Figure 7.1 shows the numerical and semi-analytical solutions for flow, temperature, concentration profiles and stream flow. It can be observed from the figures that both numerical and semi-analytical solutions display similar flow, temperature and concentration dynamics. Also, the numerical and semi-analytical solutions agree regarding the profiles. The deviation is caused by chopping higher perturbation series terms for the momentum, temperature and concentration during the solution process. The streamlines in Figure 7.1d show the internal flow is towards the centre and opening on the right side of the chamber due to injection and the work done by the surface wall on the left.

Figure 7.2 represents the changes in the internal temperature and concentration profiles due to the effects of deformation rate α. It is observed in Figure 7.2a that when the filter chamber walls contract ($\alpha < 0$), internal fluid temperature diminishes since filter chamber space decreases, leading to less kinetic energy. On the other hand, when filter chamber walls expand ($\alpha > 0$), it enhances the temperature since kinetic energy increases as a result of the free movement of fluid when the chamber space increase. The contraction of the filter chamber walls leads to the internal fluid being highly concentrated compared to expansion; hence the concentration is higher towards the centre since the mass diffusion

Table 7.1: Values of internal filtrates velocity for various parameters.

y	S_c	K_r	N	R_i	$U'(y)$
0	0.2	0.5	0.5	5.05	1.62895
0.2					1.52917
0.4					1.26735
0.6					0.894582
0.8					0.456904
1					0

(a) Impacts of filter height

y	S_c	K_r	N	R_i	$U'(y)$
0.5	0.2	0.5	0.5	5.05	1.62895
	1.5				1.47167
	3				1.26697
	3.5				1.00936
	4				0.600976
	5				0

(b) Impacts of Schmidt Number

y	S_c	K_r	N	R_i	$U'(y)$
0.5	0.2	0.5	0.5	5.05	1.62895
		1.5			1.52622
		2.5			1.26728
		3.5			0.901502
		4.5			0.47078
		5			0

(c) Impacts of chemical reaction

y	S_c	K_r	N	R_i	$U'(y)$
0.5	0.2	0.5	0.5	5.05	1.62895
			0.8		1.54096
			1		1.26868
			1.5		0.865493
			1.8		0.410503
			2		0

(d) Impacts of buoyancy ratio

y	S_c	K_r	N	R_i	$U'(y)$
0.5	0.2	0.5	0.5	0.10	1.50673
				1	1.46107
				2	1.26489
				3	0.920771
				4	0.472829
				5.05	0

(e) Impacts of Richardson number

Table 7.2: Values of skin friction coefficient, local Nusselt number and Sherwood number for different values of the physical parameters

x	R_e	α	K	M	R_i	N	R	P_r	λ	J	S_c	K_r	C_f	N_{uL}	Sh
0	1	1	3	2	5.05	0.5	1	0.72	1	1	0.2	0.5	0	0	0
0.5													2.25139	0.589533	−0.25000
1													4.50277	1.17907	−0.5000
1	−1	1	3	2	5.05	0.5	1	0.72	1	1	0.2	0.5	−1.56223	−1.17907	0.5000
	1												4.50277	1.17907	−0.5000
	2												2.98652	2.35813	−0.5000
1	1	−1	3	2	5.05	0.5	1	0.72	1	1	0.2	0.5	6.25594	1.05074	−0.5000
		0											5.37936	1.1112	−0.5000
		1											4.50277	1.17907	−0.5000
1	1	1	1	2	5.05	0.5	1	0.72	1	1	0.2	0.5	4.81583		
			2										4.58104		
			3										4.50227		
1	1	1	3	0	5.05	0.5	1	0.72	1	1	0.2	0.5	3.56358		
				1									4.03318		
				2									4.50277		
1	1	1	3	2	0.1	0.5	1	0.72	1	1	0.2	0.5	5.75383	1.06275	−0.5000
					5.05								4.50277	1.17907	−0.5000
					10								3.24152	1.32065	−0.5000
1	1	1	3	2	5.05	0.5	1	0.72	1	1	0.2	0.5	4.50277	1.17907	−0.5000
						1							4.19126	1.22438	−0.5000
						2							3.57677	1.32377	−0.5000
1	1	1	3	2	5.05	0.5	−1	0.72	1	1	0.2	0.5	4.79930	1.17907	
							0						4.05797	1.17907	
							1						4.50277	1.17907	
1	1	1	3	2	5.05	0.5	1	0.72	1	1	0.2	0.5	4.50277	1.17907	
								1					4.45953	1.63759	
								2.72					4.19388	4.45425	
1	1	1	3	2	5.05	0.5	1	0.72	−1	1	0.2	0.5	4.61488	−0.260935	
									0				4.55883	0.459065	
									1				4.50277	1.17907	
1	1	1	3	2	5.05	0.5	1	0.72	1	0	0.2	0.5	4.69581	−0.7200	
										1			4.50277	1.17907	
										5			3.73063	8.77533	
1	1	1	3	2	5.05	0.5	1	0.72	1	1	0.2	0.5	4.50277		−0.50000
											3		6.11587		−7.50000
											6		7.84419		−15.0000
1	1	1	3	2	0.1	0.2	1	0.72	1	0.1	0.1	0.5	4.50277		−0.5000
												2	4.56116		−0.80000
												5	4.67794		−1.40000

rate is lower for small internal space Figure 7.2b.

The effects of the buoyancy ratio on the internal fluid temperature and concentration are depicted in Figure 7.3. A rise in the internal temperature is observed for higher values of the buoyancy ratio effects, as shown in Figure 7.3a. The physical interpretation of this behaviour is due to the temperature difference becoming very small when the buoyancy ratio

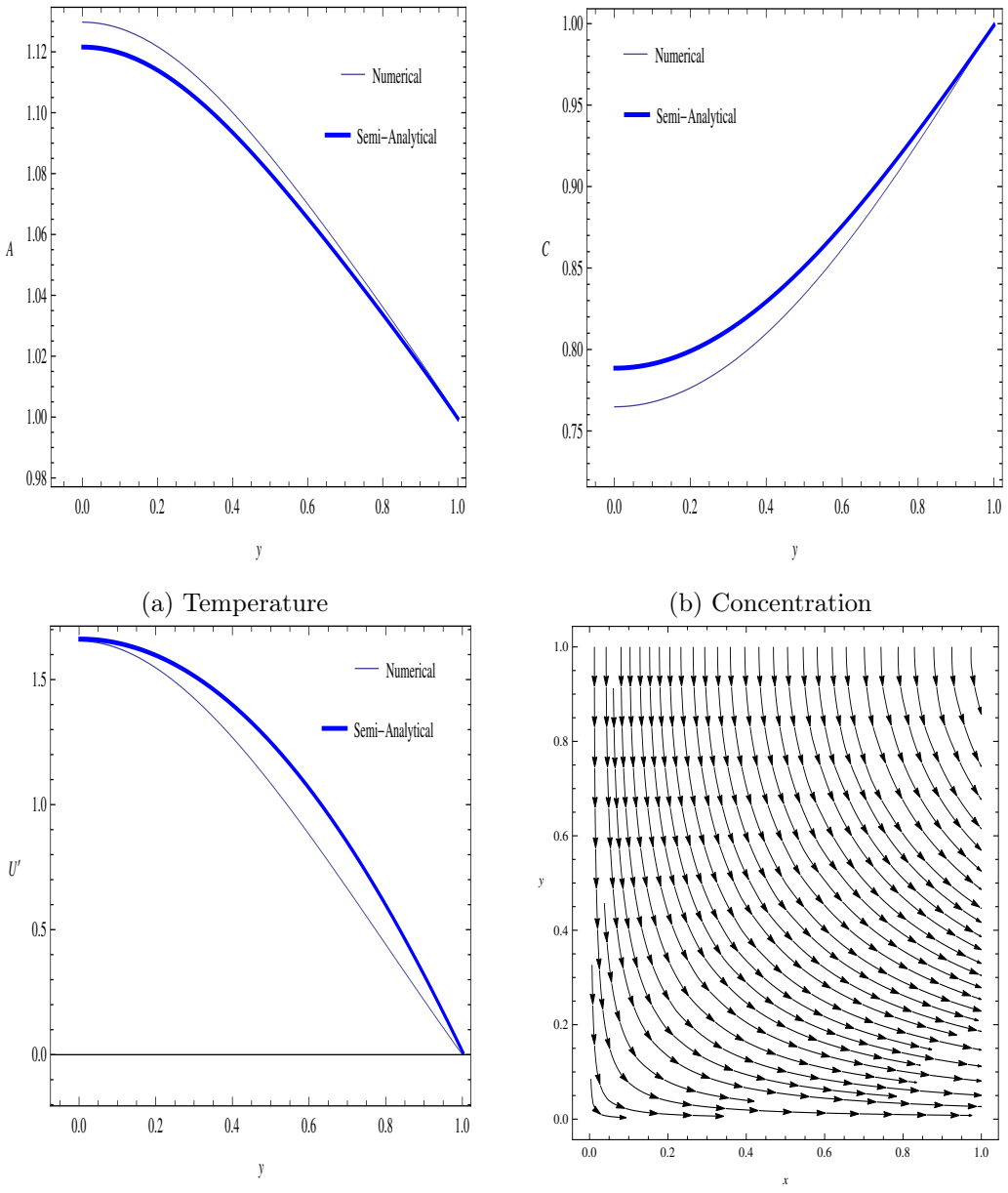

(a) Temperature

(b) Concentration

(c) Velocity.

(d) Streamlines.

Figure 7.1: Verification of temperature, concentration and velocity dynamics during operation.

increases. A distinction is noticed in the fluid concentration as portrayed in Figure 7.3b since higher values of the buoyancy ratio lead to high concentration difference; hence fluid has less concentration towards the centre of the filter chamber.

Figure 7.4 reveals the impact of the Reynolds number on the internal fluid temperature and concentration, respectively. The internal fluid temperature in Figure 7.4a drops for fluid suction ($R_e < 0$) and rise for fluid injection ($R_e > 0$). This performance of the internal temperature dropping is due to the withdrawal of internal particles that possess energy. On the other side, introducing fluid particles increases momentum variation, increasing kinetic energy; hence, internal fluid temperature increases. Figure 7.4b display the enhancement of the internal fluid concentration when fluid suction occurs compared to when fluid is in-

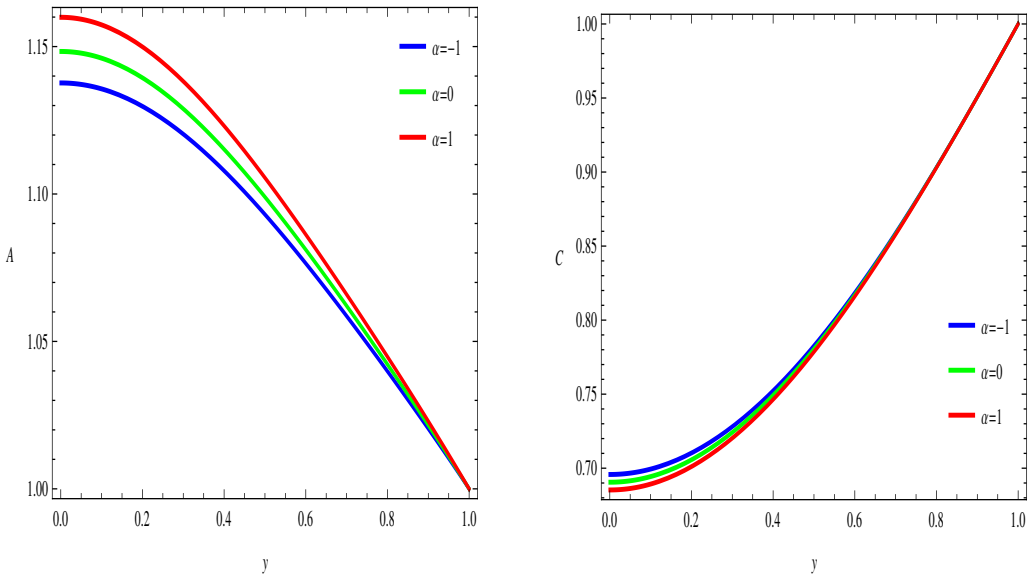

(a) Temperature (b) Concentration

Figure 7.2: Wall dilation effects.

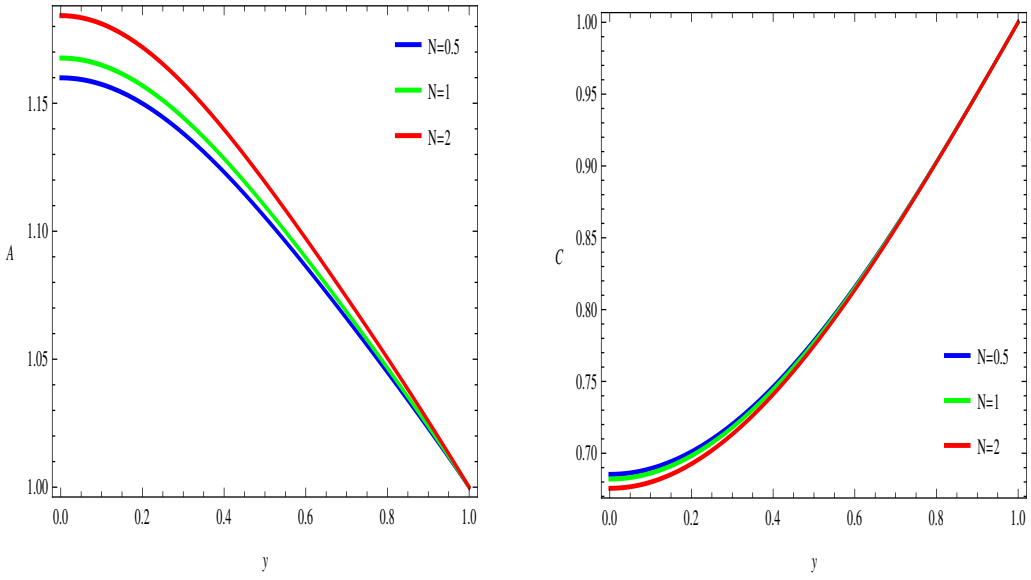

(a) Temperature (b) Concentration

Figure 7.3: Buoyancy ratio effects.

jected into the filter chamber. The fluid addition reduces fluid concentration since internal concentrated fluid diffuses into an unconcentrated fluid.

The influence of the R_i on the internal fluid temperature and concentration distribution is displayed in Figure 7.5. Figure 7.5a illustrates internal temperature enhancement as the Richardson number grows, owing to forced convection becoming dominant as R_i increases. This behaviour leads to higher kinetic energy because energy transfer is due to forced convection. Increasing the Richardson number increases the temperature difference, resulting in minimal natural convection. As the Richardson number increases, the internal fluid

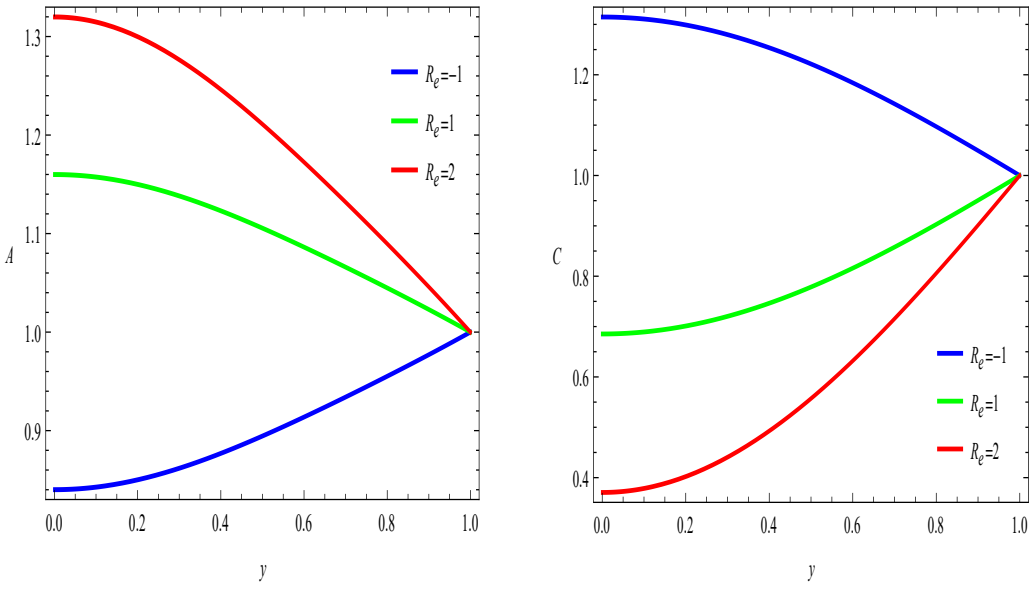

(a) Temperature (b) Concentration

Figure 7.4: Reynolds number effects.

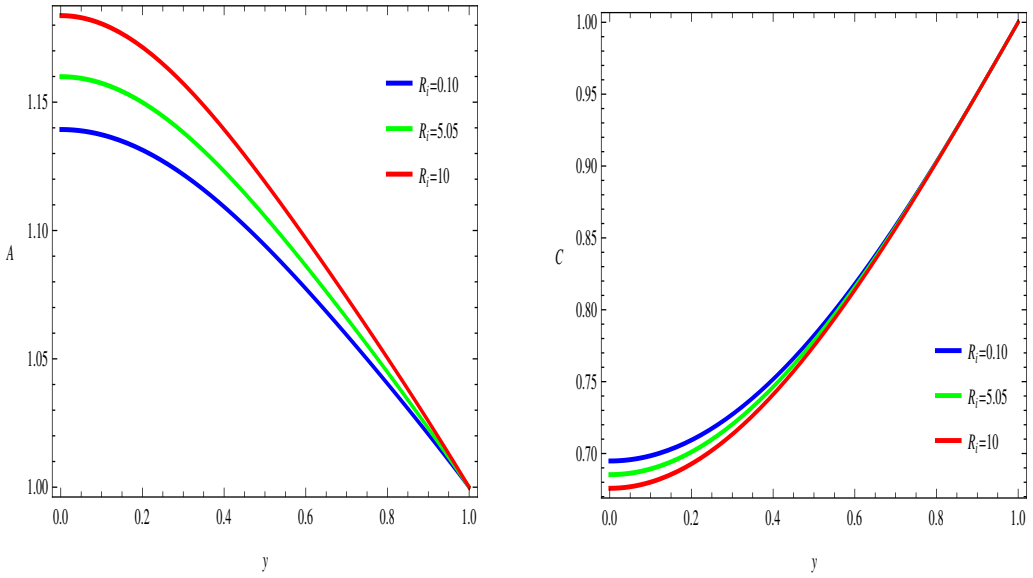

(a) Temperature (b) Concentration

Figure 7.5: Richardson number effects.

concentration reduction towards the filter chamber's centre is observed in Figure 7.5b. As natural convection's strength becomes less than forced convection's, the concentrated fluid diffuses faster due to forced convection, making fluid lose concentration.

Figure 7.6 outlines the impact of the Prandtl number and heat source/sink parameter on the internal fluid temperature. It can be observed that the internal fluid temperature increases with the rise in the Prandtl number and source/sink parameter. The swelling of internal fluid temperature when the Prandtl number increases are due to momentum diffusivity dominating within the system, creating lower kinetic energy as shown in Figure 7.6a.

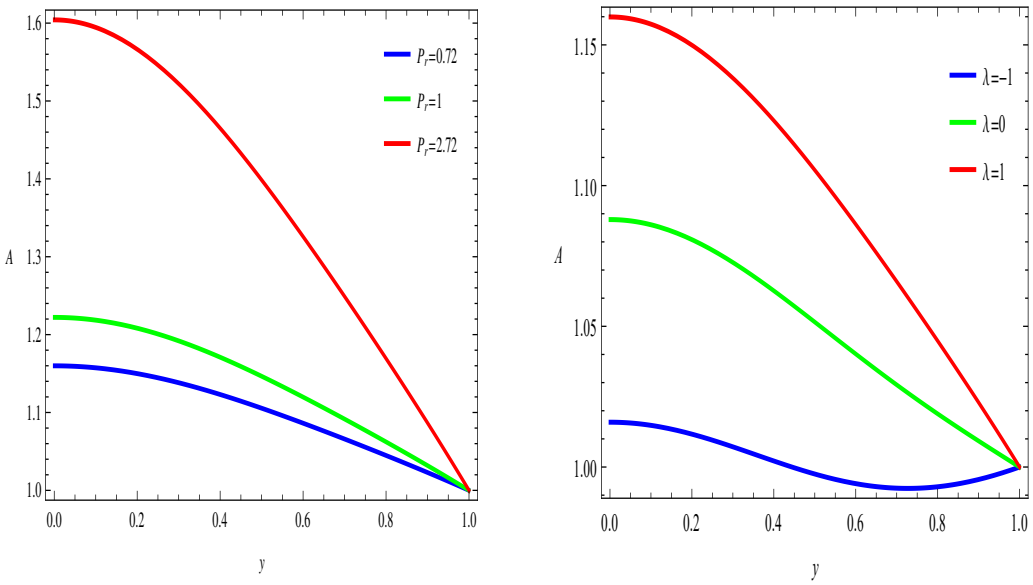

(a) Prandtl number effects. (b) heat source/sink effects.

Figure 7.6: Effects of Prandtl number and source/since parameter on fluid temperature.

Figure 7.6b reveals that when the source/sink parameter acts as the sink ($\lambda < 0$,), the internal fluid experiences a lower temperature. In contrast, the internal fluid temperature is higher when the parameter operates as the source ($\lambda > 0$). It is clear that when increasing the value of $\lambda > 0$, the energy is emitted/released, which leads to internal fluid temperature rising, while decreasing the value of $\lambda < 0$, the energy is absorbed, and this causes the internal fluid temperature to drop. Mat Noor et al. [138] noticed similar behaviour for both parameters.

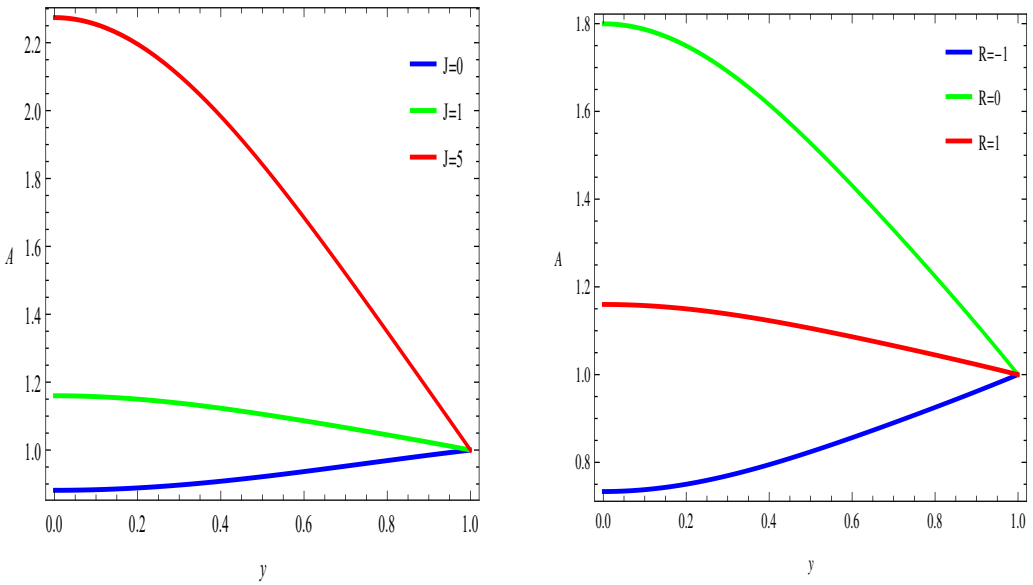

(a) Joule effects. (b) Radiation effects.

Figure 7.7: Effects of Joule and radiation on fluid temperature.

The effects of Joule/resistive heating and radiation parameters are plotted in Figure 7.7.

From Figure 7.7a, it is evident that the internal fluid temperature increases towards the centre of the filter chamber with the rise in the Joule heating parameter. This rise in resistive heating parameter makes the fluid behave as a higher electrical resistor generating higher internal heat; hence temperature increases remarkably. Consequently, the internal fluid temperature drops from a less resistive heating parameter since low resistance generates less internal energy. Figure 7.7b anticipates that when the radiation term is zero ($R = 0$), the internal fluid temperature is higher since there is no radiative heat transfer. It is also evident that increasing the radiation parameter ($R > 0$) increases internal fluid temperature since energy is emitted to the fluid. On the other hand, the energy is absorbed when the radiation parameter ($R < 0$); hence the internal fluid temperature decreases. The same result of internal temperature influenced by radiation was noticed in Mat Noor et al. [138]

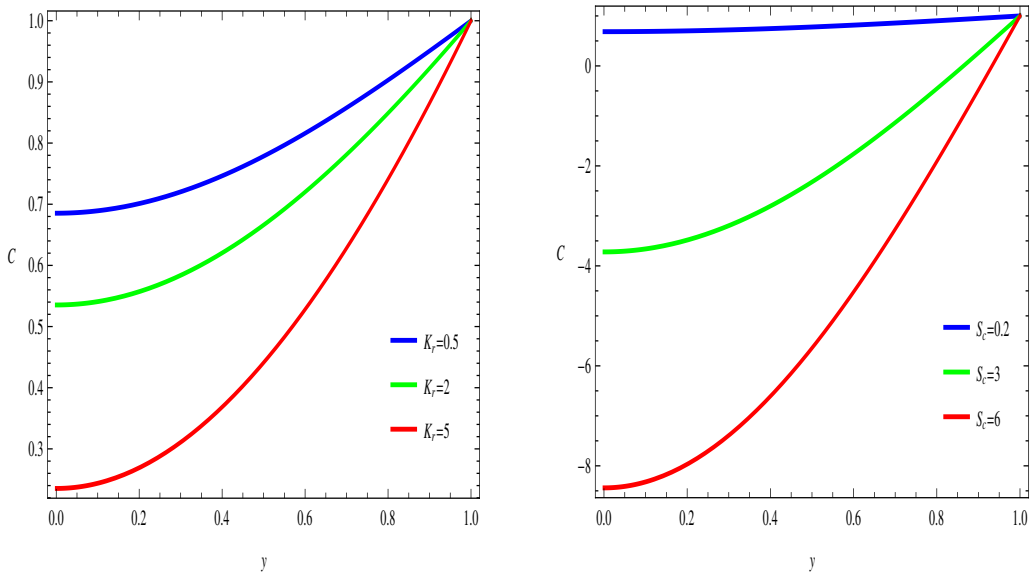

(a) Chemical reaction effects.

(b) Schmidt number effects

Figure 7.8: Effects of chemical reaction and Schimdt number on concentration.

Figure 7.8 is plotted to perceive the effects of the chemical reaction parameter and Schmidt number on the internal fluid concentration. Increasing the chemical reaction parameter decreases the internal fluid concentration towards the centre of the filter chamber, as depicted in Figure 7.8a. The physical clarification of this behaviour is due to higher values of chemical reaction parameters leading to a drop in molecular diffusivity. From Figure 7.8b, it is clear that by increasing the Schmidt number, the internal fluid concentration diminishes since high values of the Schmidt number lead to a high viscous diffusion rate and less molecular diffusion rate. Al-Saif and Harfash [136] support these results.

7.6 Conclusion

A steady-state flow inside a rectangular filter chamber with a porous medium has been theoretically scrutinised. In addition, thermal radiation, chemical reaction and mixed convection are incorporated. The evolving dimensionless ODEs are solved analytically

by employing a perturbation procedure. Furthermore, NDSolver was used to verify the semi-analytical solution's velocity, temperature and concentration profiles. Based on the obtained results, the following remarks can be concluded from this chapter:

- Small values of buoyancy ratio and Richardson number lead to highly concentrated fluid with lower temperature, maximising fluid velocity while increasing skin friction coefficient.
- A highly concentrated permeate outflow with maximum velocity and the minimum skin friction coefficient is ideal for lowering the chemical reaction parameter and Schmidt number.
- High Joule/resistive heating parameter values are ideal for generating more internal heat and increasing the internal temperature to minimise skin friction coefficient.
- For less internal friction and a high heat transfer rate, it is essential to consider the heat source parameter rather than the heat sink parameter.

Chapter 8

Closed-form solutions of injection driven flow and heat transfer inside an inclined horizontal filter chamber using Lie group method

The closed-form solutions of models provide operators and designers with a better understanding of how the systems perform practically, thus improving critical industrial production operations. Due to this importance, this chapter seeks to find closed-form solutions to the internal momentum and temperature variation during filtration to advance fluid purification. Lie group analysis is used to transform a system of equations representing the flow and heat transfer into a solvable system without changing the dynamics of the case study. The transformed solvable system is then integrated to find closed-form solutions of the internal velocity (momentum) and temperature variation. The obtained closed-form solutions are then used to analyse the effects of physical parameters arising from the process dynamics to find combinations of parameters that yield maximum permeates outflow. Graphical representations of the unsteady and steady-state regime of the internal velocity and temperature are presented and analysed. The analysis conveys that the internal fluid velocity increases when enhancing the permeation parameter and minimising the Reynolds number, wave speed parameter and chamber height.

NOMENCLATURE

t - time

x - axial coordinate

y - normal coordinate

u - axial velocity

v - normal velocity

T - temperature of the fluid

l - chamber length

h - chamber height

$\bar{t}$ - non-dimensional time

$\bar{x}$ - non-dimensional axial coordinate

$\bar{y}$ - non-dimensional normal coordinate

$\bar{u}$ - non-dimensional axial velocity

$\bar{v}$ - non-dimensional normal velocity

L - characteristic length

H - characteristic height

T_w - temperature at wall

U_w - velocity at wall

ν - mass diffusivity

c_p - specific heat

g - acceleration due to gravity

R_e - Reynolds number

G_r - Grashoff number

K - permeation parameter

P_r - Prandtl number

Q - heat generation parameter

C_f - skin friction coefficient

N_u - Nusselt number

Greek symbols

β - thermal expansion

θ - non-dimensional temperature

λ - heat diffusion

ρ - fluid density

α - angle of inclination

ψ - stream function

Subscripts

w - filter wall

h - filter height

8.1 Introduction

The quest to refine industrial fluids to have clean lubricants within the industrial space has been an active topic of fluid dynamics in the past and recently. The contaminations and components in many industrial fluids vary in boiling temperatures, weight, and size. For example, crude oil comprises short and long hydrocarbons with different diameters and boiling temperatures. During the manufacturing process of such lubricants, the crucial task is to separate these components from the fluid to achieve optimal performance, which leads to the most desirable distillate fluids that meet standard requirements for a specific fluid quality while ensuring the lowest possible cost and energy use.

As a result, it is ideal for developing mathematical models that provide better knowledge of the system's dynamics to improve production. Such models give designers insight into how the system performs practically and what to expect from the system. The solutions to such models are critical to the industry. Engineers and designers require a theoretical foundation (models) to construct realistic and optimum filter systems (the current case study) and understand experimental data. As a result, research has been conducted to understand better the impacts of flow dynamics and heat transfer factors on the number of parallel flows, such as Poiseuille and Couette-type flows, which have applications in the movement of industrial fluids in various channels. Poiseuille and Couette flows are essential when industries clean fluid during fluid purification and filtering.

To learn more about flow and heat transfer in various channels, Shah and London [156] reported heat transfer through Poiseuille laminar flow in parallel plates with stationary plates for Newtonian fluids, and Irine and Karni [157] for both non-Newtonian and Newtonian fluids. The works of [158–161] studied the steady flow regime of heat transfer in a Poiseuille-Couette laminar flow inside parallel plates with simultaneous pressure gradient and axial movement of one of the plates. Lin [162] demonstrated an analytical technique for determining heat development in a non-Newtonian Couette flow with a pressure gradient. The author used an implicit finite difference approach to simulate the general heat transfer model to investigate the impact of thermophysical parameters on temperature distribution. The study discovered that rapid thermal growth leads to a smaller temperature gradient, which may primarily cause a lower Nusselt number.

The impact of continuous suction and sinusoidal injection on the three-dimensional Couette flow of an electrically conducting viscous fluid through a porous material between two infinite flat permeable plates in the presence of a transverse magnetic field was investigated by Das [163]. The analysis of the study shows that the magnetic strength creates a force called Lorentz force acting on the flow field, which retards the central velocity at all flow points while accelerating the cross velocity. Attia and Kotb [164] studied an MHD flow confined by two parallel plates with heat transfer. The authors solved the governing nonlinear ordinary differential equations numerically. The study compared the velocity and temperature distributions for variable and constant viscosity instances. In Seth et al. [165], an examination of an unsteady MHD Couette flow of a viscous incompressible electrically

conducting fluid in the presence of a transverse magnetic field between two parallel porous plates was made. The authors used the Laplace transform approach to derive the velocity field solution. Their research revealed that suction has a retarding effect on fluid velocity while injection accelerates.

Baoku et al. [166] analysed high fluid viscosity through a porous channel in the presence of a uniform transverse magnetic field and heat radiation to investigate a hydromagnetic Couette flow. The impact of the channel's permeability was also considered. The authors found that the permeability of the porous media and heat radiation had minimal effects on the steady hydromagnetic Couette fluid flow. The investigation of hydromagnetic steady flow between two parallel porous plates and heat transfer in the presence of a high magnetic field applied transverse to the direction of flow was examined by Boniface et al. [167]. The study's governing equations describing the flow and heat transfer were solved using the finite difference technique. It was discovered that increasing the Grashoff number and magnetic field parameter leads to an increase in velocity, whereas increasing the Prandtl number and suction leads to a velocity decrease. The work of Makinde and Mhone [168] examines the heat transfer to MHD oscillatory flow in a channel filled with a porous material. In their study, they found solutions for the velocity and temperature analytically. The authors discovered that raising the strength of the magnetic field decreases wall shear stress while increasing the radiation parameter through heat absorption increases the magnitude of wall shear stress.

The Lie group technique of infinitesimal transformations is a traditional method for determining similarity reduction of non-linear differential equations. Many researchers and applied mathematicians [11–17] have concentrated their efforts on demonstrating and explaining the advantages of using the Lie group technique to reduce the mathematical model and transform the governing equations to those that can be solved easily, particularly in the field of fluid mechanics. The works of [67, 96] used the Lie group method and the spectral method to find numerical solutions that give an insight into the filtration process.

Inspired by the works above, this chapter aims to advance the filtration process. The numerical approach by [67, 96] to study the steady filtration process drove the motivation behind this investigation. The literature above shows that none of these studies has found closed-form solutions to better understand the unsteady filtration process. Hence, the present case study uses the Lie group method to analyse the unsteady state filtration regime. This chapter aims to address the knowledge gap in the literature by using the Lie group method to transform the system of equations representing flow and heat transfer during filtration into more manageable and solvable equations that can be solved analytically. The obtained closed-form solutions of the flow velocity and heat transfer will give insight into the impact of flow and thermophysical parameters arising from the current case study. The study in this chapter also looks to understand parameters that increase outflow, thus increasing permeates production.

8.2 Mathematical representation of the case study

Figure 8.1 illustrates the schematic view of the filter design under investigation. The filter design is such that it filters injected contaminated incompressible fluid using the top permeable wall and porous medium embedded inside the filter chamber. The permeable cold adiabatic top wall moves at constant velocity U_w to ensure no filter cake is formed. In contrast, the impermeable bottom wall is fixed and exposed to constant heat T_w. The current chapter considers an incompressible flow and has density variation due to temperature differences. According to Boussinesq approximation, [84], the fluid density is constant except in the gravitational term, which results in buoyancy effects. The system is such that fluid injection into the chamber happens when $t > 0$ and creates internal flow variation along the horizontal due to the work done by the left surface wall closing the left chamber side and the opening on the right. The work done by the bottom wall and the constant injection yields no momentum variation along the y.

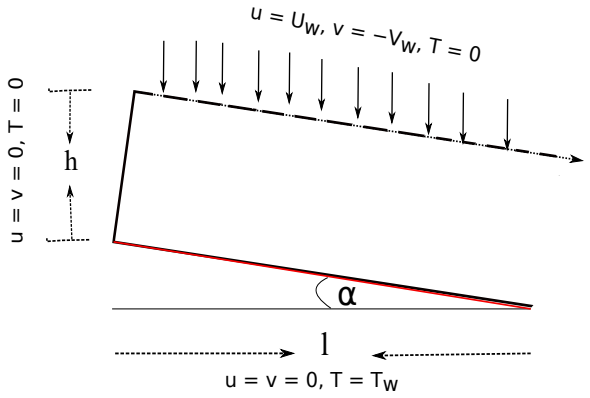

Figure 8.1: Schematic view of the filter design.

The governing equations that represent mass, momentum and energy variation during unsteady inside the filter chamber are as follows [169]

$$\left.\begin{aligned} &\frac{\partial u}{\partial x}+\frac{\partial v}{\partial y}=0,\\ &\frac{\partial u}{\partial t}+u\frac{\partial u}{\partial x}+v\frac{\partial u}{\partial y}=\nu\frac{\partial^2 u}{\partial y^2}+g\beta(T-T_h)\cos\alpha-\frac{\nu\phi}{\kappa}u,\\ &\frac{\partial T}{\partial t}+u\frac{\partial T}{\partial x}+v\frac{\partial T}{\partial y}=\frac{\lambda}{\rho c_p}\frac{\partial^2 T}{\partial y^2}+\frac{q_0}{\rho c_p}(T-T_h). \end{aligned}\right\} \tag{8.1}$$

Here u is axial velocity, v is normal velocity, t is time, x and y are chamber space variables, T is temperature, T_h is cold adiabatic temperature, ρ is density, ν is kinematic viscosity, g is gravitational acceleration, β is thermal expansion, λ is thermal diffusivity, ϕ is porosity parameter, k is permeability of porous medium, α is chamber's angle of inclination, q_0 is heat generation and c_p is specific heat.

The appropriate boundary conditions according to the filter design (Figure 8.1) are as follows:

$$\begin{aligned} &\text{(i)} \quad u=v=0, \quad T=T_w, \quad \text{at } y=0, \\ &\text{(ii)} \quad u=U_w, \quad v=V_w=-U_w, \quad T=0 \quad \text{at } y=h. \end{aligned} \tag{8.2}$$

8.3 Solution method

In this section, we reduce the system of governing equations (8.1) and boundary conditions (8.2) into a non-dimensional form and transform the resulting set of dimensionless equations into a solvable system of equations using the Lie group transformation. Lastly, we integrate the solvable system of equations to obtain closed-form solutions of the internal momentum and temperature variation.

8.3.1 Dimensional analysis

This subsection represents the system of equations of the current case study in dimensionless form.
The non-dimensional variables are [169]

$$\bar{t} = \frac{tU_w}{L},\ \bar{x} = \frac{x}{L},\ \bar{y} = \frac{y}{L},\ \bar{u} = \frac{u}{U_w},\ \bar{v} = \frac{v}{U_w},\ \theta = \frac{T - T_h}{T_w - T_h}, \tag{8.3}$$

where $\bar{u}$ and $\bar{v}$ are the dimensionless velocity components, $\bar{t}$ is dimensionless time, $\bar{x}$ and $\bar{y}$ are the dimensionless space coordinates, L is the characteristic length, U_w is the upper wall velocity, T_w is the bottom wall temperature and θ is the dimensionless temperature. Substituting dimensionless variables (8.3) into (8.1)-(8.2) and dropping the bars for simplicity, yields the following dimensionless system:

$$\left.\begin{aligned} &\frac{\partial u}{\partial x} + \frac{\partial v}{\partial y} = 0, \\ &\frac{\partial u}{\partial t} + u\frac{\partial u}{\partial x} + v\frac{\partial u}{\partial y} = \frac{1}{R_e}\frac{\partial^2 u}{\partial y^2} + Gr\theta\cos\alpha - \frac{1}{K}u, \\ &\frac{\partial \theta}{\partial t} + u\frac{\partial \theta}{\partial x} + v\frac{\partial \theta}{\partial y} = \frac{1}{PrR_e}\frac{\partial^2 \theta}{\partial y^2} + Q\theta, \end{aligned}\right\} \tag{8.4}$$

where $Pr = \frac{\nu\rho c_p}{\lambda}$ is a Prandtl number, $Q = \frac{q_0 L}{\rho c_p U_w}$ is heat generation parameter, $K = \frac{kU_w}{\nu\phi L}$ is the porosity parameter, $R_e = \frac{LU_w}{\nu}$ is Reynolds number and $Gr = \frac{g\beta(T_w - T_h)L^3}{\nu^2}$ is Grashoff number.

The boundary conditions takes the following dimensionless form

$$\begin{aligned} &\text{(i)} \quad u = v = 0, \quad \theta = 1, \quad \text{at } y = 0, \\ &\text{(ii)} \quad u = 1, \quad v = -1 \quad \theta = 0 \quad \text{at } y = \frac{h}{l} = H. \end{aligned} \tag{8.5}$$

We now express the axial and normal velocity in terms of the stream function ψ. From the continuity equation, there exists a dimensionless stream velocity $\psi(t, x, y)$ such that

$$u = \frac{\partial \psi}{\partial y}, \qquad v = -\frac{\partial \psi}{\partial x}, \tag{8.6}$$

which satisfies continuity equation from system (8.4) identically. Thus, we get the following dimensionless system of equations

$$\left.\begin{aligned}\frac{\partial^2\psi}{\partial ty}+\frac{\partial\psi}{\partial y}\frac{\partial^2\psi}{\partial xy}-\frac{\partial\psi}{\partial x}\frac{\partial^2\psi}{\partial y^2}&=\frac{1}{R_e}\frac{\partial^3\psi}{\partial y^3}+Gr\theta\cos\alpha-\frac{1}{K}\frac{\partial\psi}{\partial y},\\ \frac{\partial\theta}{\partial t}+\frac{\partial\psi}{\partial y}\frac{\partial\theta}{\partial x}-\frac{\partial\psi}{\partial x}\frac{\partial\theta}{\partial y}&=\frac{1}{PrR_e}\frac{\partial^2\theta}{\partial y^2}+Q\theta.\end{aligned}\right\} \tag{8.7}$$

The boundary conditions take the following dimensionless form

$$\begin{aligned}&\text{(i)} \quad \psi(t,x,y)=0, \quad \theta=1, \quad \text{at } y=0,\\ &\text{(ii)} \quad \psi(t,x,y)=y-x+1, \quad \theta=0, \quad \text{at } y=h.\end{aligned} \tag{8.8}$$

The above ψ satisfy the positive stream flow according to the flow velocity and the filter chamber in the region $x, y > 0$, when $y - x + 1 > 0$.

8.3.2 Symmetry reduction

This subsection aims to establish Lie similarity groups of transformation and use them to transform equations representing the momentum variation and heat transfer during the filtration process into solvable equations.

We consider the one-parameter group of infinitesimal transformations in t, x, y, ψ, θ which leaves the dynamics of the phenomenon represented by system (8.7) and boundary conditions (8.8) unchanged, to be given by

$$\begin{aligned}t^* &= t+\varepsilon\tau(t,x,y,\psi,\theta)+0(\varepsilon^2),\\ x^* &= x+\varepsilon\xi(t,x,y,\psi,\theta)+0(\varepsilon^2),\\ y^* &= y+\varepsilon\zeta(t,x,y,\psi,\theta)+0(\varepsilon^2),\\ \psi^* &= \psi+\varepsilon\eta(t,x,y,\psi,\theta)+0(\varepsilon^2),\\ \theta^* &= \theta+\varepsilon\phi(t,x,y,\psi,\theta)+0(\varepsilon^2),\end{aligned} \tag{8.9}$$

where ε is the small group parameter. The symmetry group of system (8.7) is generated using the generator of the form

$$X=\tau\frac{\partial}{\partial t}+\xi\frac{\partial}{\partial x}+\zeta\frac{\partial}{\partial y}+\eta\frac{\partial}{\partial\psi}+\phi\frac{\partial}{\partial\theta}, \tag{8.10}$$

where τ, ξ, ζ, η and ϕ are functions of t, x, y, ψ and θ.

The solutions $\psi = \psi(t, x, y)$ and $\theta = \theta(t, x, y)$ leave the dynamics of the flow and heat distribution invariant under the transformation (8.10) if and only if

$$\begin{aligned}\Phi_\psi &= X\big(\psi-\psi(t,x,y)\big)=0,\\ \Phi_\theta &= X\big(\theta-\theta(t,x,y)\big)=0,\end{aligned} \tag{8.11}$$

where Φ is the transformation which leaves the dynamics of the flow and heat distribution unchanged.

Letting

$$\begin{aligned}\Delta_1 &= \frac{\partial^2\psi}{\partial ty}+\frac{\partial\psi}{\partial y}\frac{\partial^2\psi}{\partial xy}-\frac{\partial\psi}{\partial x}\frac{\partial^2\psi}{\partial y^2}-\frac{1}{R_e}\frac{\partial^3\psi}{\partial y^3}-Gr\theta\cos\alpha+\frac{1}{K}\frac{\partial\psi}{\partial y},\\ \Delta_2 &= \frac{\partial\theta}{\partial t}+\frac{\partial\psi}{\partial y}\frac{\partial\theta}{\partial x}-\frac{\partial\psi}{\partial x}\frac{\partial\theta}{\partial y}-\frac{1}{PrR_e}\frac{\partial^2\theta}{\partial y^2}-Q\theta,\end{aligned}$$

a vector generator X is said to be a symmetry generator of system (8.7) if and only if

$$X^{[3]}(\Delta_j)\Big|_{\Delta_j=0} = 0, \quad j = 1, 2, \tag{8.12}$$

where

$$\begin{aligned} X^{[3]} &= \tau\frac{\partial}{\partial t} + \xi\frac{\partial}{\partial x} + \zeta\frac{\partial}{\partial y} + \eta\frac{\partial}{\partial \psi} + \phi\frac{\partial}{\partial \theta} + \eta^x\frac{\partial}{\partial \psi_x} + \eta^y\frac{\partial}{\partial \psi_y} + \phi^t\frac{\partial}{\partial \theta_t} + \phi^x\frac{\partial}{\partial \theta_x} \\ &+\phi^y\frac{\partial}{\partial \theta_y} + \eta^{tx}\frac{\partial}{\partial \psi_{tx}} + \eta^{ty}\frac{\partial}{\partial \psi_{ty}} + \eta^{xy}\frac{\partial}{\partial \psi_{xy}} + \eta^{xx}\frac{\partial}{\partial \psi_{xx}} + \eta^{yy}\frac{\partial}{\partial \psi_{yy}} + \psi^{xx}\frac{\partial}{\partial \theta_{xx}} \\ &+\psi^{yy}\frac{\partial}{\partial \theta_{yy}} + \eta^{xxy}\frac{\partial}{\partial \psi_{xxy}} + \eta^{xyy}\frac{\partial}{\partial \psi_{xyy}} + \eta^{xxx}\frac{\partial}{\partial \psi_{xxx}} + \eta^{yyy}\frac{\partial}{\partial \psi_{yyy}} \end{aligned} \tag{8.13}$$

is called the third prolongation of X.

Introducing the total derivatives by differentiating the dependent variables from (8.9) with respect to time and space variables, yields

$$\begin{aligned} D_x &= \partial_x + \psi_x\partial_\psi + \theta_x\partial_\theta + \psi_{xx}\partial_{\psi_x} + \theta_{xx}\partial_{\theta_x} + \psi_{xy}\partial_{\psi_y} + \theta_{xy}\partial_{\theta_y} + \cdots, \\ D_y &= \partial_y + \psi_y\partial_\psi + \theta_y\partial_\theta + \psi_{yy}\partial_{\psi_y} + \theta_{yy}\partial_{\theta_y} + \psi_{xy}\partial_{\psi_x} + \theta_{xy}\partial_{\theta_x} + \cdots, \\ D_t &= \partial_t + \psi_t\partial_\psi + \theta_t\partial_\theta + \psi_{tt}\partial_{\psi_t} + \theta_{tt}\partial_{\theta_t} + \psi_{xt}\partial_{\psi_x} + \theta_{xt}\partial_{\theta_x} + \cdots. \end{aligned} \tag{8.14}$$

Since τ, ξ, ζ, η, and ϕ depend only on t, x, y, ψ and θ by treating the variables t, x, y, ψ, θ and the derivatives of ψ and θ as independent variables, we obtain the determining equations by separating the resulting equations from (8.12) on derivatives of ψ and θ. Solving the resulting determining equations from (8.12) with the help of Maple, yields the following seven Lie point symmetries admitted by the dimensionless system (8.7) as:

$$\begin{aligned} &X_1 = \frac{\partial}{\partial t}, \quad X_2 = \frac{\partial}{\partial x}, \quad X_3 = F(x,t)\frac{\partial}{\partial y}, \quad X_4 = G(x,t)\frac{\partial}{\partial \psi}, \\ &X_5 = Ke^{-\frac{t}{K}}\frac{\partial}{\partial x} - ye^{-\frac{t}{K}}\frac{\partial}{\partial \psi}, \quad X_6 = x\frac{\partial}{\partial x} + \psi\frac{\partial}{\partial \psi} + \theta\frac{\partial}{\partial \theta}, \\ &X_7 = K\cos(\alpha)G_re^{Qt}\frac{\partial}{\partial x} + y\cos(\alpha)G_rQKe^{Qt}\frac{\partial}{\partial \psi} + (Ke^{Qt}Q^2 + Qe^{Qt})\frac{\partial}{\partial \theta}. \end{aligned} \tag{8.15}$$

For unsteady behaviour, we firstly consider the linear combination of X_1 and X_2, which gives $\frac{\partial}{\partial t} + c\frac{\partial}{\partial x}$, where c is the permeates travelling wave speed. The resulting characteristic equations yields the following invariants:

$$\psi = w(s,y), \quad \theta = h(s,y), \quad s = x - ct \quad \text{and} \quad y = y. \tag{8.16}$$

Using the above invariants while treating w and h as velocity and temperature, s and y as new parameters that affect flow and heat dynamics during filtration process, system (8.7) becomes

$$\left.\begin{aligned} &\cos(\alpha)G_rh(y,s) + cw_{ys} + \frac{w_{yyy}}{R_e} - \frac{w_y}{K} - w_yw_{ys} + w_sw_{yy} = 0, \\ &Qh(y,s) + ch_s + \frac{h_{yy}}{R_eP_r} + h_yw_s - h_sw_y = 0. \end{aligned}\right\} \tag{8.17}$$

Similarly, the above system (8.17) admits the following three Lie symmetry generators

$$X_1 = \frac{\partial}{\partial s}, \quad X_2 = \frac{\partial}{\partial y}, \quad X_3 = \frac{H(s)}{c+1}\left(\frac{\partial}{\partial y} + c\frac{\partial}{\partial \psi}\right). \tag{8.18}$$

Thus, the linear combination $X_1 + X_2 = \dfrac{\partial}{\partial s} + \dfrac{\partial}{\partial y}$, yields the following invariants:

$$w = f(p), \quad h = z(p) \quad \text{and} \quad p = y - s, \tag{8.19}$$

which further reduces system (8.7) into the following system of ODE:

$$cf''(p) - \frac{f'''(p)}{R_e} - \cos(\alpha) G_r z(p) + \frac{f'(p)}{K} = 0, \tag{8.20}$$

$$cz'(p) - \frac{z''(p)}{R_e P_r} - Qz(p) = 0. \tag{8.21}$$

Here $f(p)$ is velocity, $z(p)$ is the temperature, and p is the combination of space and time variables which affect internal flow and heat dynamics during the filtration process.

8.3.3 Closed-form solutions

This subsection aims to establish closed-form solutions to study momentum variation and heat transfer during the filtration process.

Integrating equation (8.21) yields internal temperature as

$$z(p) = e^{\frac{1}{2}(A_2 z - A_1 z)} \left(k_3 e^{A_1 z} + k_4 \right), \tag{8.22}$$

where k_1 and k_2 are constants of integration. Please refer to Appendix A for the values of A_1 and A_2.

Substituting the internal temperature $z(p)$ above into momentum equation (8.20), yields

$$\cos(\alpha) \left(-e^{\frac{1}{2}(A_2 - A_1)p} \right) G_r \left(k_2 e^{A_1 z} + k_1 \right) + cf''(p) - \frac{f'''(p)}{R_e} + \frac{f'(p)}{k} = 0. \tag{8.23}$$

Similarly integrating equation (8.23) with the help of Maple, yields momentum variation as

$$f(p) = \quad 2\sqrt{k} \left(\frac{k_3 e^{A_3 p}}{T_{13}} + \frac{k_4}{A_4} \right) e^{\frac{1}{2} c p R_e - \frac{A_3 p}{2}} - \frac{k \cos(\alpha) e^{\frac{1}{2}(A_2 p - A_1 p)} G_r \left(k_2 T_{11} e^{A_1 p} + k_1 T_{10} \right)}{2 q T_2 \sqrt{R_e} P_r} + k_5,$$

where k_3, k_4 and k_5 are constants of integration. See Appendix for the values of $A_1, \ldots, A_4$ and $T_2, T_{10}, T_{11}, \text{and}, T_{13}$.

Thus, the general solutions of axial velocity, normal velocity and temperature are given by

$$u(t,x,y) = \frac{1}{2qT_2\sqrt{R_e}P_r}\Bigg\{ - A_1kk_2T_{11}\cos(\alpha)G_re^{\frac{1}{2}p(A_1+A_2)} + \frac{2k_3\sqrt{c^2kR_e+4}e^{A_3\left(\frac{p}{2}\right)+\frac{1}{2}cpR_e}}{T_{12}} + \sqrt{k}\left(cR_e - A_3\right)e^{-\frac{1}{2}p(A_3-cR_e)}\left(\frac{k_3e^{A_3p}}{T_{13}} + \frac{k_4}{A_4}\right) + \frac{1}{2}\left(A_1 - A_2\right)k\cos(\alpha)e^{\frac{1}{2}(A_2-A_1)p}G_r \left(k_2T_{11}e^{A_1p} + k_1T_{10}\right)\Bigg\}, \tag{8.24}$$

$$v(t,x,y) = \frac{1}{2qT_2\sqrt{R_e}P_r}\Bigg\{ - A_1kk_2T_{11}\cos(\alpha)G_re^{\frac{1}{2}p(A_1+A_2)} + \frac{2k_3\sqrt{c^2kR_e+4}e^{A_3\left(\frac{p}{2}\right)+\frac{1}{2}cpR_e}}{T_{12}} - \sqrt{k}\left(A_3 - cR_e\right)e^{-\frac{1}{2}p(A_3-cR_e)}\left(\frac{k_3e^{A_3p}}{T_{13}} + \frac{k_4}{A_4}\right) + \frac{1}{2}\left(A_1 - A_2\right)k\cos(\alpha)e^{\frac{1}{2}(A_2-A_1)p}G_r \left(k_2T_{11}e^{A_1p} + k_1T_{10}\right)\Bigg\} \tag{8.25}$$

and

$$\theta(t,x,y) = e^{\frac{1}{2}(A_2-A_1)p}\left(k_2e^{A_1p} + k_1\right), \tag{8.26}$$

where $p = ct - x + y$ and for T_{12} see Appendix B.

Using the following boundary conditions which arise from the current filter design

$$\begin{aligned} &u(1,L,0) = 0, \quad u(1,L,H) = 1, \quad \theta(1,L,0) = 1, \quad \theta(1,L,H) = 0 \quad \text{and} \\ &\psi(1,L,H) = H - L + 1, \end{aligned} \tag{8.27}$$

yield particular values of constants of integration as

$$k_1 = \frac{e^{\frac{1}{2}[A_1(3c+2H-3L)+A_2(L-c)]}}{e^{A_1(c+H-L)} - e^{A_1(c-L)}}, \quad k_2 = \frac{e^{-\frac{1}{2}(A_2-A_1)(c-L)}}{e^{A_1(c-L)} - e^{A_1(c+H-L)}}, \tag{8.28}$$

$$\begin{aligned} k_3 = {} & \frac{\sqrt{K}qT_1^2\sqrt{R_e}P_r\left(cR_e - A_3\right)e^{\frac{1}{2}(A_3H - cR_e(2c+H-2L))}}{A_4T_2\left(e^{A_1H}-1\right)\left(e^{A_3H}-1\right)}\Bigg(\frac{2e^{\frac{1}{2}(c-L)(cR_e-A_3)}}{T_1\sqrt{-P_r}} \\ & \Bigg[KP_r\Bigg(Kq^2\left(-e^{A_1H}\right)\left(-P_r\right)^{3/2} + 2q\left(e^{A_1H}-1\right)\sqrt{-P_r} - cT_3\left(P_r-1\right)e^{\frac{1}{2}(HA_1+HA_2)} \\ & + T_5\left(P_r - \left(P_r-1\right)e^{H\sqrt{R_e}\sqrt{-P_r}\sqrt{4q-c^2R_eP_r}}\right) + Kq^2\left(-P_r\right)^{3/2} - T_5\Bigg) + \left(e^{A_1H}-1\right)\sqrt{-P_r}\Bigg] \\ & + \frac{1}{T_4}\Bigg\{K\cos(\alpha)G_re^{\frac{1}{2}(c+H-L)(cR_e-A_3)}\Bigg[A_1cK\left(P_r-1\right)\left(e^{HA_1}+1\right) - \left(e^{A_1H}-1\right)T_6\Bigg]\Bigg\}\Bigg), \end{aligned} \tag{8.29}$$

$$\begin{aligned} k_4 = {} & \frac{q\sqrt{R_e}P_r}{\left(e^{A_1H}-1\right)\left(e^{A_3H}-1\right)}e^{\frac{1}{2}(c+H-L)\left[A_3-cR_e\right]} \\ & \Bigg(\left(e^{A_1H}-1\right)\left(2T_1 - KT_7\cos(\alpha)G_re^{\frac{1}{2}H(A_3+cR_e)}\right) - A_1cK^2\cos(\alpha)G_r\left(P_r-1\right) \\ & \Bigg[e^{\left(\frac{1}{2}HA_3+HA_1+\frac{1}{2}HR_ec\right)} - 2e^{\frac{1}{2}(HA_1+HA_2)} + e^{\frac{HA_3}{2}+\frac{1}{2}cHR_e}\Bigg]\Bigg), \end{aligned} \tag{8.30}$$

$$
\begin{aligned}
k_5 \;=\; & 1+H-L-\frac{1}{\left(-1+e^{HA_1}\right)qP_r\sqrt{R_e}T_2}\Bigg\{e^{\frac{1}{2}H(A_1+A_2)}T_9+\frac{1}{\left(-1+e^{HA_3}\right)A_4}\Bigg[e^{\frac{1}{2}(c+H-L)(cR_e-A_3)} \\
& \left(\frac{1}{\left(c\sqrt{K}R_e+\sqrt{KR_ec^2+4}\sqrt{R_e}\right)T_2}\Bigg\{e^{\left[\frac{(2c+3H-2L)A_3}{2}-\frac{cR_e(2c+H-2L)A_3}{2}\right]}\sqrt{K}\left(cR_e-A_3\right)\right. \\
& \left(\frac{1}{T_4}\Bigg\{e^{\frac{1}{2}(c+H-L)(cR_e-A_3)}K\cos(\alpha)G_r\Big(c\left(1+e^{HA_1}\right)KA_1\left(P_r-1\right)-\left(-1+e^{HA_1}\right)T_6\Big)\Bigg\}\right. \\
& +\frac{1}{\sqrt{-P_r}T_1}\Bigg[2e^{\frac{1}{2}(c-L)(cR_e-A_3)}\Big(K\Big(\left(-1+e^{HA_1}\right)K\sqrt{-P_r}q^2-ce^{\frac{1}{2}(A_2H+A_1H)}T_3 \\
& +\left(1-e^{HA_1}\right)T_5\Big)P_r^2+K\Bigg\{2\left(-1+e^{HA_1}\right)\sqrt{-P_r}\,q+ce^{\frac{1}{2}(A_2H+A_1H)}T_3+\left(-1+e^{HA_1}\right)T_5\Bigg\}P_r \\
& \left.+\left(-1+e^{HA_1}\right)\sqrt{-P_r}\Big)\Bigg]\Big)T_1^2\Bigg\}+e^{-\frac{1}{2}(c+H-L)(cR_e-A_3)}\Big[K\cos(\alpha)G_r\Big(-c\Big\{e^{\frac{1}{2}cR_eH+\frac{A_3}{2}} \\
& +e^{\frac{1}{2}H(R_ec+A_3+2A_1)}-2e^{\frac{1}{2}(A_2H+A_1H)}\Big\}KA_1\left(P_r-1\right)-e^{\frac{1}{2}H(A_3+cR_e)}\left(-1+e^{HA_1}\right)T_7\Big) \\
& \left.+2\left(-1+e^{HA_1}\right)T_1\Big]\Big)T_8\Bigg]\Bigg\}. \qquad (8.31)
\end{aligned}
$$

See the Appendix A and B for the values of exponents $A_i(i=1,\cdots,4)$ and the terms $T_j(j=1,\cdots,9)$ found in the constants of integration above.

Finally, the closed-form solutions that represent momentum variation and temperature distribution during the filtration process are given by equations (8.24), (8.25) and (8.26), and the constants of integration (8.28), (8.29), (8.30) and (8.31).

The above obtained results were validated by substituting the closed-form solutions back into system of equations (8.4) and found to satisfy both the continuity, momentum and energy equations.

The Heat transfer coefficient h_c and the skin shear stress τ_w on the wall are the relevant physical quantities of interest, which are defined as

$$
h_c(T_w-T_h)=-k\Big(\frac{\partial T}{\partial y}\Big) \quad \text{and} \quad \tau_w=-\mu\Big(\frac{\partial u}{\partial y}\Big), \qquad (8.32)
$$

and the dimensionless Nusselt number and skin friction coefficient at the top wall are obtained as

$$
Nu=\frac{h_ch}{k}=-\theta_y(t,x,y=1) \quad \text{and} \quad C_f=\frac{2\tau_w}{\rho U_w^2}=\frac{-2}{R_e}u_y(t,x,y=1). \qquad (8.33)
$$

8.4 Results and discussion

This section provides a graphical representation and the analysis of the effect of various parameters which affect the flow, temperature, skin friction coefficient and heat transfer rate.

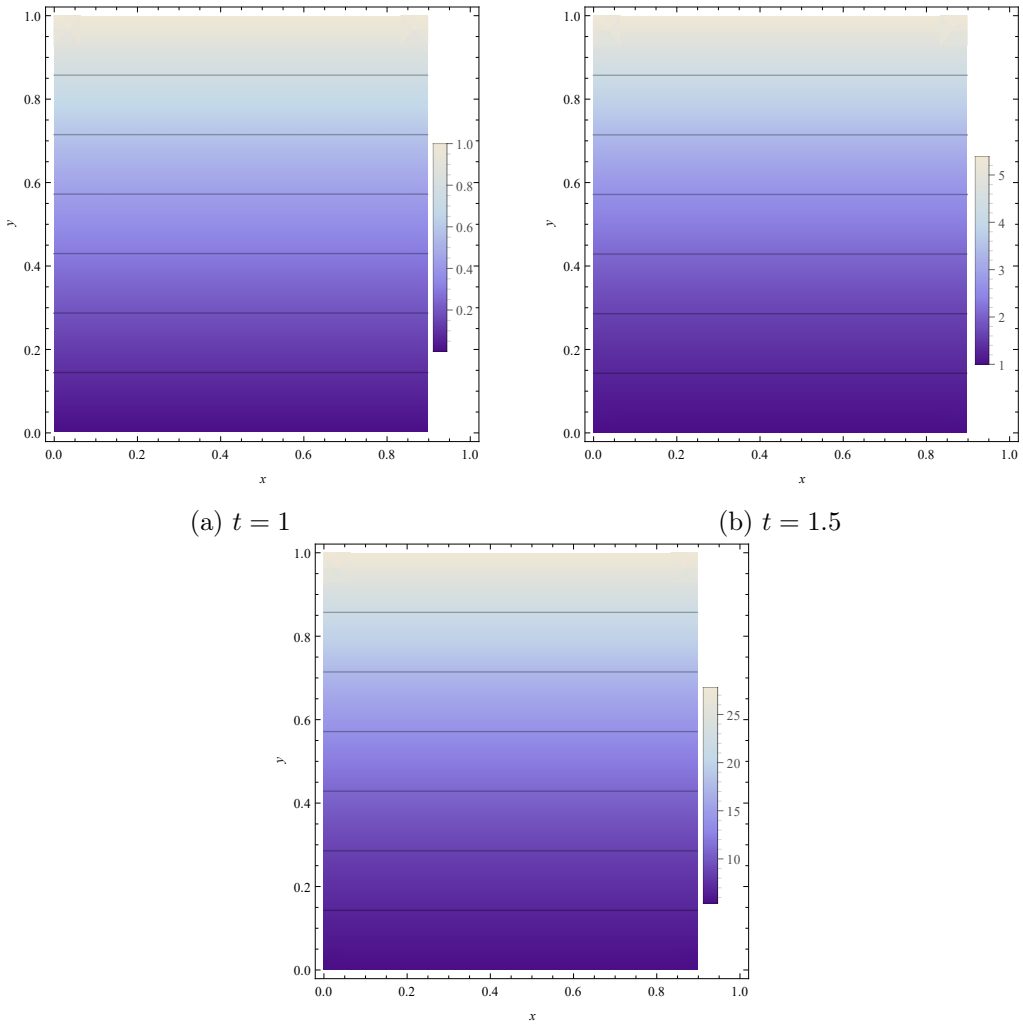

(a) $t = 1$ (b) $t = 1.5$

(c) $t = 2$

Figure 8.2: Time evolution of the permeates velocity.

8.4.1 Time evolution of internal fluid velocity

From Figure 8.2, we found that as time evolves, the internal velocity increases during the filtration operation since, over time, more fluid particles are introduced. It can also be noted that more movement is happening at the top due to the moving wall and constant fluid injection. This injection pushes fluid particles to the bottom wall leading to minimal movement at the bottom due to no-slip effects compared to the top. As time evolves, more movement is also experienced throughout the chamber; when more fluid particles are introduced, the no-slip condition is not respected as time increases during unsteady operation.

8.4.2 Time evolution of internal fluid temperature

Figure 8.3 illustrates the internal fluid temperature on an unsteady state regime as time increases. According to the plots, it can be seen that the internal fluid temperature drops as time evolves. The internal fluid experiences higher temperature at the bottom due to the heated wall and cold at the top because the cold wall and cooler introduced fluid. As

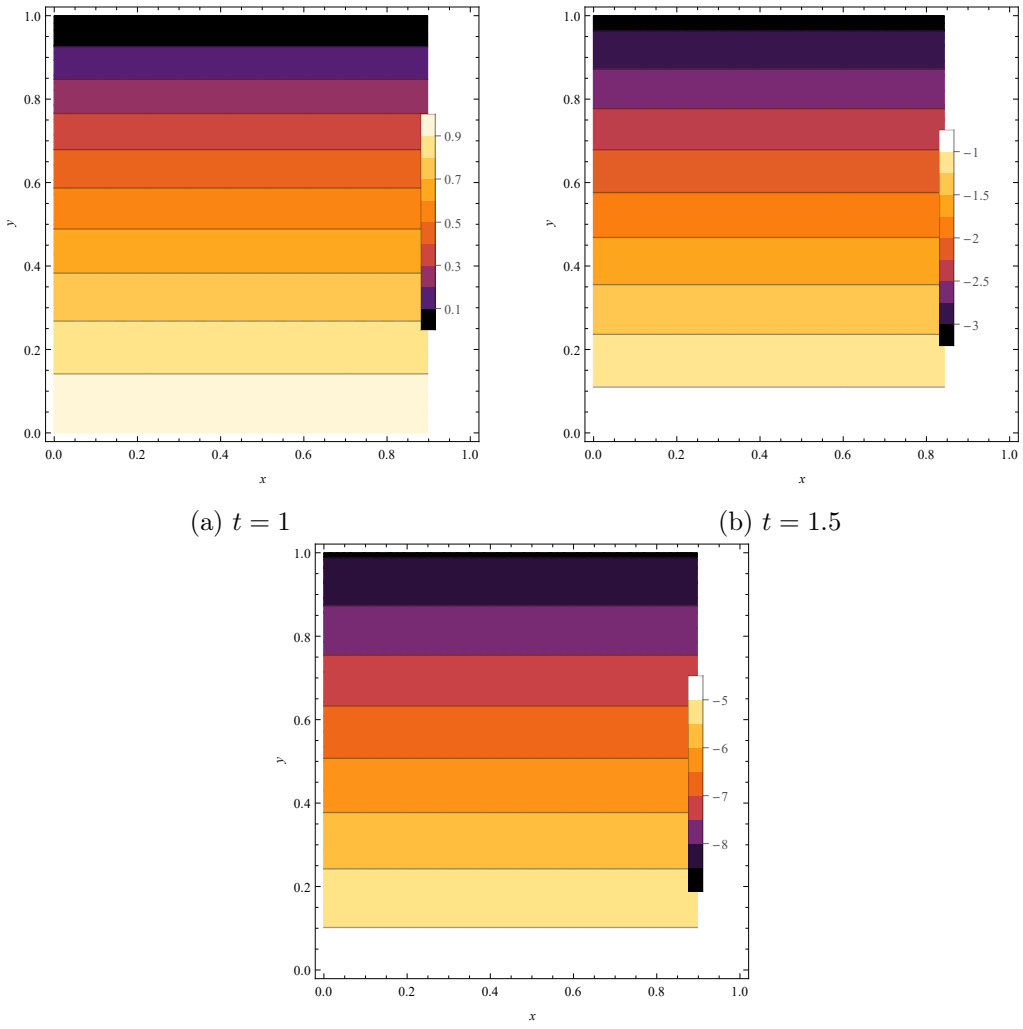

(a) $t = 1$

(b) $t = 1.5$

(c) $t = 2$

Figure 8.3: Time evolution of the internal fluid temperature.

time increases, more dense fluid particles sink to the bottom, absorbing heat from the less dense particles, leading to a temperature decrease at the bottom.

Remark: The velocity and temperature are sketched against filter chamber length and height for different time values t with other parameters fixed to study how velocity and temperature evolve during an unstable regime.

Figure 8.4 illustrates the effect of Reynolds number (injection) on the internal velocity and fluid temperature. The internal velocity diminishes as the R_e increases due to enhancement of fluid bulk mass, making internal fluid heavier, resulting in a decrease in velocity as shown in Figure 8.4a. An increase in internal fluid temperature is experienced when the Reynolds number increases, as depicted in Figure 8.4b; this happens because the increase in mass density enhances contact between the heated wall and particles, thus increasing heat transfer.

Figure 8.5 exhibits how fluid wave speed parameter variation influences the internal fluid velocity and temperature distribution. The internal fluid velocity in Figure 8.5a drops for

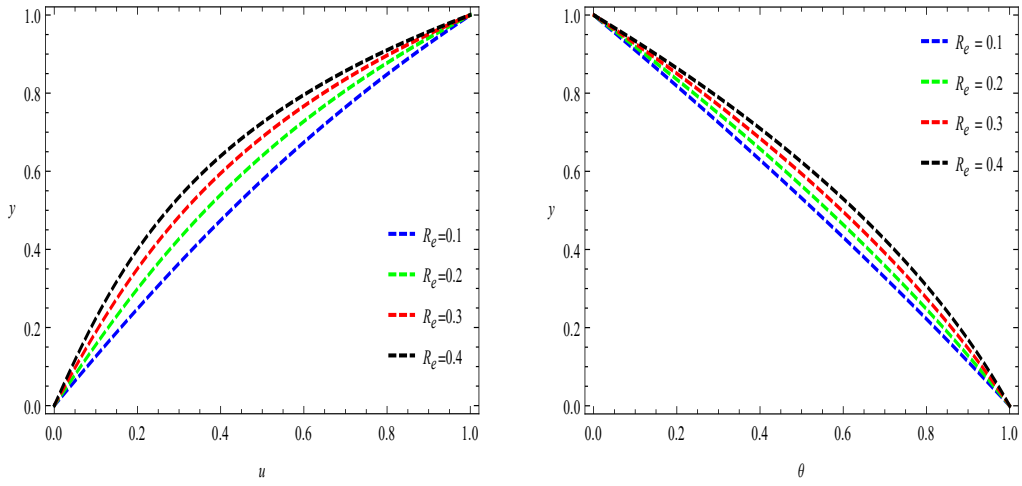

(a) (b)

Figure 8.4: Effects of Reynolds number on internal fluid velocity and temperature.

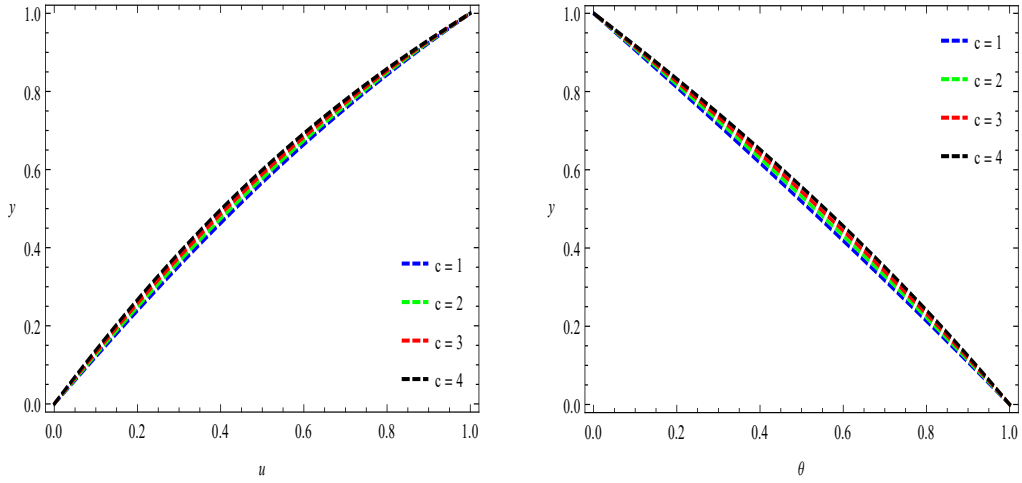

(a) (b)

Figure 8.5: Effects of fluid wave speed parameter on velocity and temperature.

enhancement of fluid wave speed parameter due to fluid particles moving towards the walls decreasing the horizontal movement and thus less fluid velocity. Figure 8.5b discloses that internal temperature distribution increases when the fluid wave speed parameter increases. This increase in temperature is caused by the slower permeate flow allowing particles to absorb temperature for a longer time, hence the increase in internal temperature when particles delay exiting the filter chamber.

The impact of medium permeability on the internal fluid velocity and temperature is displayed in Figure 8.6. An increasing trend in the internal fluid velocity is shown in Figure 8.6a for growing values of medium permeability. The resistance created by the porous medium becomes weak as the permeability increases, allowing the free movement of fluid particles. It can be noted from Figure 8.6b that the impact of medium permeability does not affect the internal fluid temperature distribution.

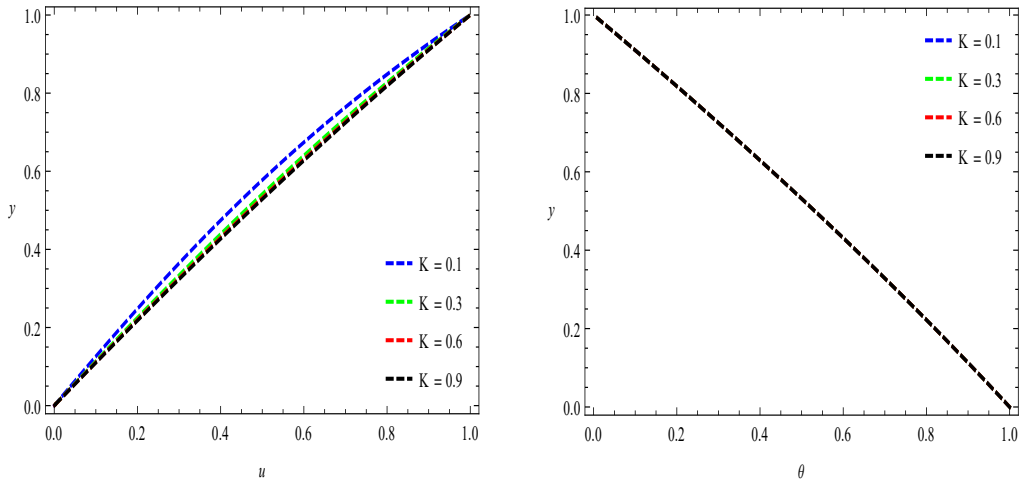

(a) (b)

Figure 8.6: Effects of medium permeability on fluid velocity and temperature distribution.

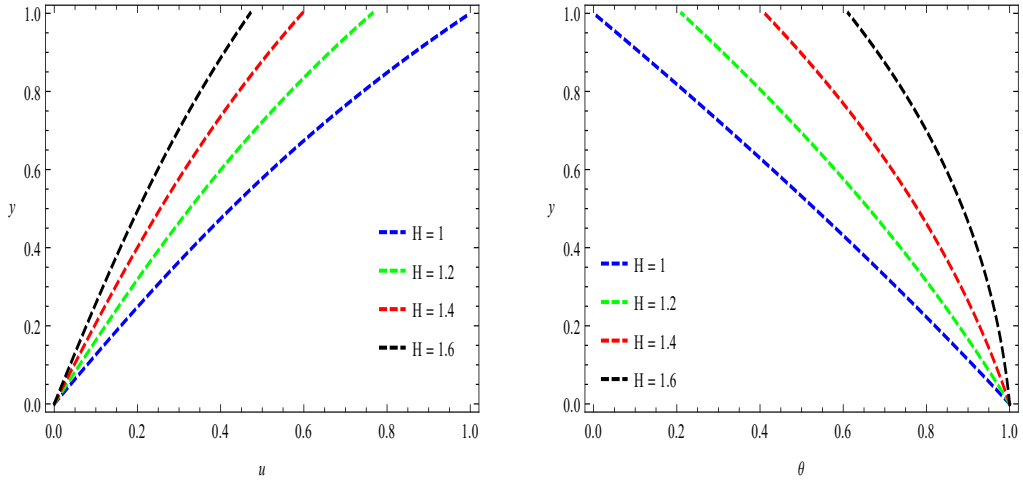

(a) (b)

Figure 8.7: Effects of chamber height on fluid velocity and temperature.

Figure 8.7 shows that the increase in filter chamber height decreases the internal fluid velocity and increases the fluid temperature. This decrease in velocity when chamber height increases, as shown in 8.7a, is caused by more fluid particles moving towards the chamber walls to occupy additional space, thus decreasing the outflow velocity. It can be observed from Figure 8.7b that increasing filter chamber space increases the internal fluid temperature. This happens since slower-moving fluid particles absorb more temperature compared to faster-moving ones.

Figure 8.8 show the influence of the angle of inclination and Grashof number on the internal fluid velocity. It can be noted from Figure 8.8a that increasing the angle of inclination increases the internal fluid velocity since pulling effects of gravity in the direction of the outflow become more effective as inclination increases. Also, Figure 8.8b discloses that increasing the Grashof number enhances the internal fluid velocity. Since the buoyancy force is more dominant for higher values of Grashof number, making the fluid less dense,

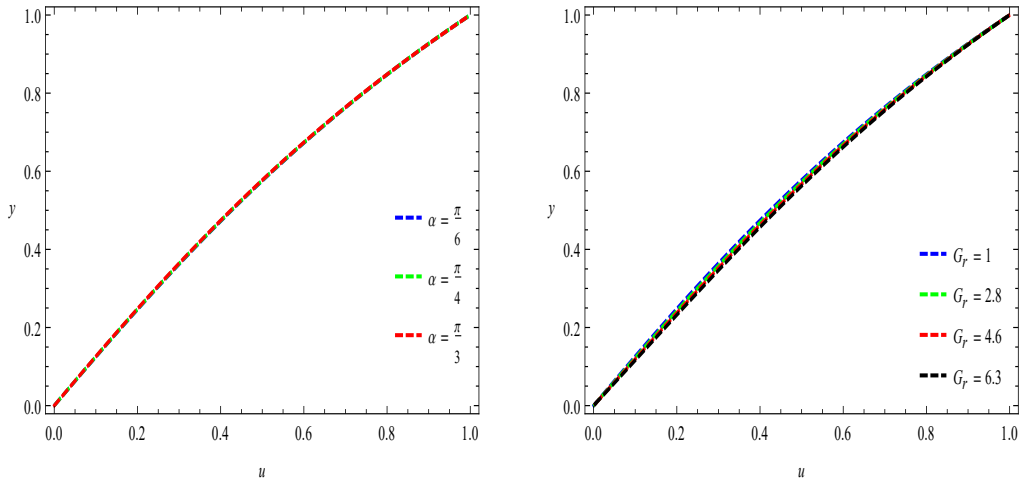

(a) (b)

Figure 8.8: Effects of angle of inclination and Grashof number on the internal fluid velocity.

thus allowing easy flow of the fluid particles inside the filter chamber.

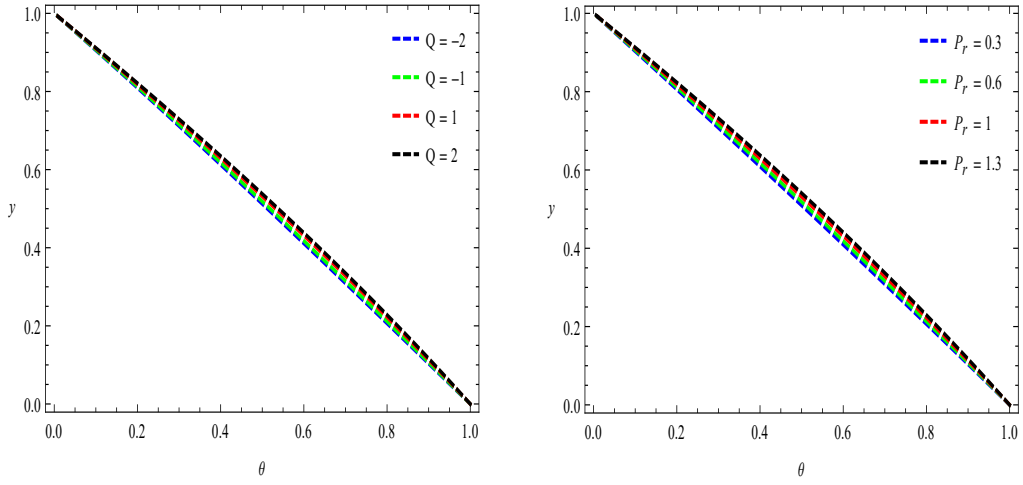

(a) (b)

Figure 8.9: Effects of source/sink parameter and Prandtl number on fluid temperature.

The effects of the source/sink parameter and Prandtl number on the internal fluid temperature distribution are shown in Figure 8.9. It can be observed that increasing the heat source/sink parameter gives rise to the internal temperature as portrayed in Figure 8.9a since the energy is emitted/released leading to internal fluid temperature rising. Also, when the value of q ($q < 0$,) decreases, the energy is absorbed, and this causes the internal fluid temperature to drop. Figure 8.9b illustrates that higher values of the Prandtl number enhance the internal fluid temperature because dominant thermal diffusivity allows fluid to absorb more energy caused by heat conduction.

Figure 8.10 portrays the impact of different parameters on the skin friction coefficient at the upper wall for various injection values. It can be noted that more drag is experienced

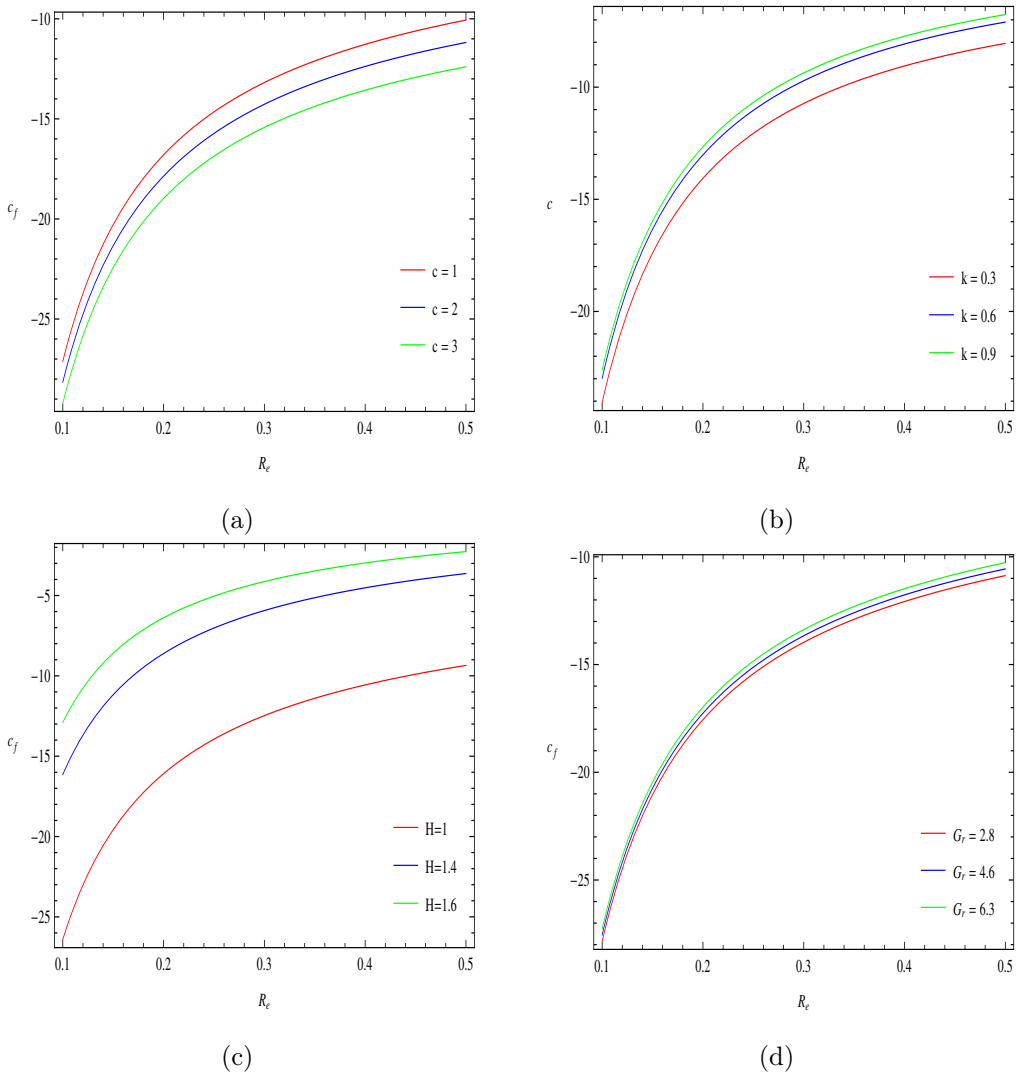

Figure 8.10: Effects of fluid wave speed parameter, medium permeability, filter height and Grashof number on the skin drag coefficient for various values injection.

when less fluid is injected into the filter compared to when more is injected, and this maximises drag at the wall. The rise in fluid wave speed pushes more particles to the filter walls; hence higher drag is observed in Figure 8.10a. More resistance is observed for small medium permeation as shown Figure 8.10b hence more drag. Figure 8.10c demonstrate that increasing the chamber space minimises the drag due to the free movement of particles in a wider space. Higher values of the Grashof number decrease the drag coefficient due to fluid becoming less dense when buoyancy force is more dominant in the system, as depicted in Figure 8.10d.

Figure 8.11 delineates the influence of fluid wave speed parameter, Prandtl number, filter height and heat source/sink parameter on Nusselt number at the upper wall of the filter chamber for various values of Reynolds number. It can be seen that as the Reynolds number increases for all parameters, the local heat transfer rate elevates. From Figure 8.11a, it is found that a higher fluid wave speed parameter increases the heat transfer rate at the top wall. Similarly, increasing the Prandtl number gives rise to the local Nusselt number as

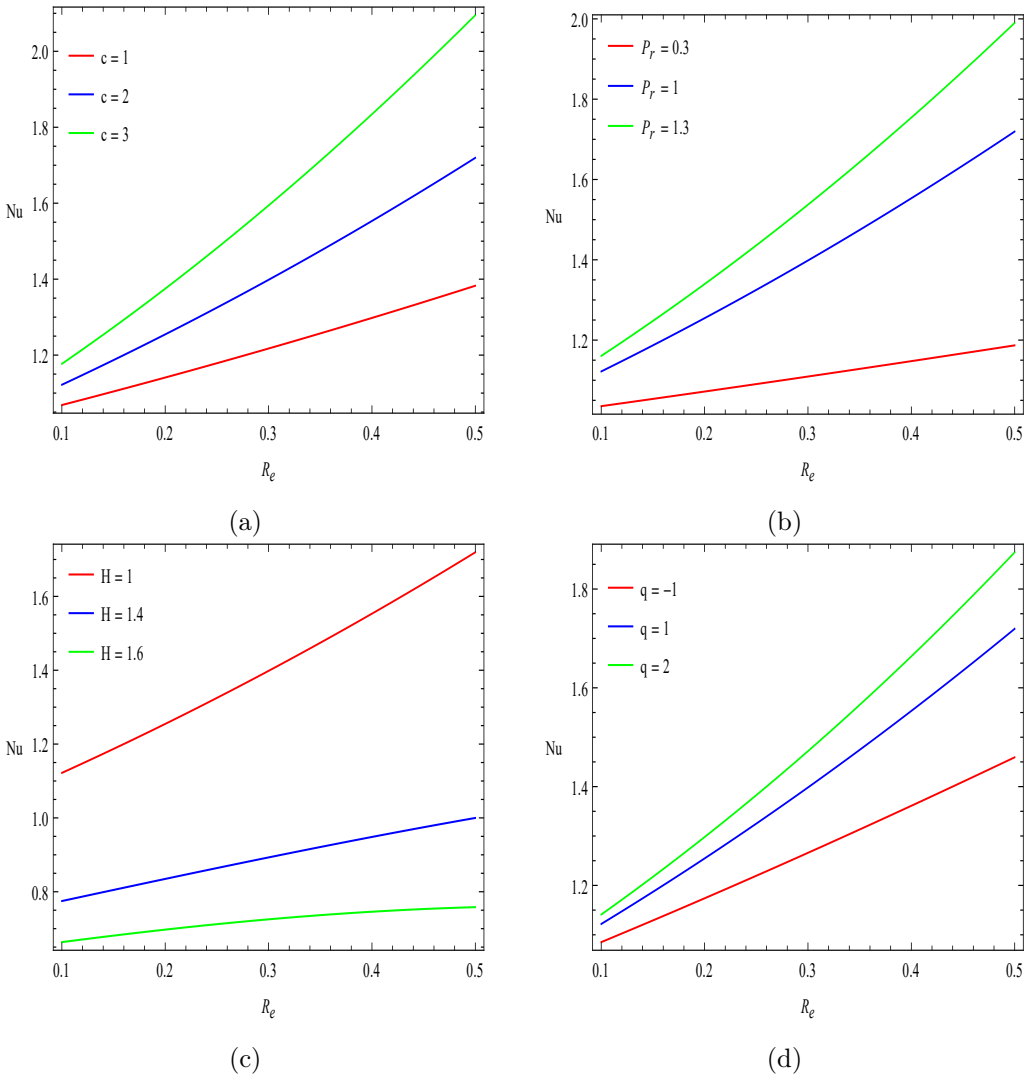

Figure 8.11: Effects of fluid wave speed parameter, Prandtl number, filter height and heat source/sink parameter on the local heat transfer rate for various values injection.

portrayed in Figure 8.11b. The heat transfer rate decreases as the chamber space increase due to the rise in temperature difference between two walls, as shown in Figure 8.11c. Figure 8.11d shows that the heat source brings an additional heat transfer rate while the heat sink withdraws the system's heat transfer rate.

8.5 Conclusion

This chapter presented the theoretical investigation into the dynamics of unsteady and steady state filtration operation inside an inclined horizontal filter chamber influenced by a constant injection of contaminated fluid perpendicular to the upper porous wall. A Lie point symmetry method was used transform the model into solvable equations which were directly integrated to obtain momentum and temperature variation solutions. For maximum outflow velocity while reducing viscous shear during filtration operation, the study led to the following conclusions:

i. To increase permeates outflow velocity during an unsteady regime, it is ideal to leave the filter system to operate for some time to allow an increase in internal particles, which increases the internal work done.

ii. During operation, it is not ideal for increasing the Grashof number since it adds less fluid energy while increasing particles' vertical movement. Thus decreasing permeate outflow velocity.

iii. It is ideal for increasing the permeation parameter for a porous medium to restrict contaminants while increasing permeate outflow velocity.

iv. Increasing the heat source/sink parameter is essential to increase the internal fluid temperature and heat transfer.

v. Increasing the inclination angle is ideal for increasing permeate outflow velocity.

vi. To minimize internal drag at the top more chamber, minimum wave speed, more Grashof number, and permeation are ideal.

vii. More injection, wave speed, Prandtl number, heat source/sink, and less filter chamber space are ideal for increasing heat transfer inside the system.

Chapter 9

Comparison and concluding remarks

This research objective was to solve various mathematical models of the internal flows, heat and mass transfer in different filter designs and theoretically investigate those models. Firstly the project reviewed key definitions and results from Lie group theory, which were later used in the thesis. Each filter design studied in this research project can perform optimally depending on the filter operation requirements and the choice of physical parameters used according to that particular design. For a filter to act as a clarifier that removes tiny amounts of solid particles from the fluid before purification. The magnetic force acting on the system and pore size which restrict particles can be weakened to allow permeates to have certain particles flow through the filter such that the permeates contain particle which are small enough to pass through the filter chamber while filtering a particular shape and size of particles. While on the other hand, this two parameters can be enhanced to allow only fluid to pass through the medium, thus separating particles from the fluid. Therefore, filter operators can use each filter design according to output requirements.

Heating fluid can change the quality/state of the fluid, and depending on the fluid used, heat transfer can be used as a classifier. For example, heating crude oil to different boiling points can give different types of petroleum. Therefore finding the right balance of heat transfer parameters is essential depending on the output requirements. Similarly, the optimal concentration parameter is ideal depending on the type of concentrated fluid needed for the operation.

Here we highlight combination of parameters that lead maximum permeate velocity, and a desirable heat distribution according to each filter design studied in this research project. In chapter 3, the best permeate velocity is observed when more fluid is injected into the filter with increased medium pore size as shown in Figure 3.7a . This also brings better heat transfer distribution, reducing the fluid density to allow effortless fluid flow in the filter. Even though this parametric selection is the better combination for optimal permeate outflow in chapter 3, it has some disadvantages since increasing pore size allows some unwanted tiny particles/contamination to flow out of the filter chamber. This filter

chamber can be advantageous if used in the clarification stage before the pure filtration process.

In chapter 4, less fluid injection gives maximum outflow velocity as shown in Figure 4.5a. From all combinations of parameters, it is found that at the entry length region, reverse flow is observed except for less injection, which gives positive outflow velocity in the direction of the outflow. The cause of this outflow behaviour is because of less internal viscous shears experienced at the walls due to less fluid injection. These parameters can be advantageous during the operation of this filter since it maintains the laminar flow attained with fewer shear stresses.

The filter design considered in chapter 5 gives maximum outflow velocity when there is no work done by the walls as shown in Figure 5.3a. The significance of no work done by the walls plays a vital role in making the permeate outflow velocity field symmetric; this makes the filter operate in a well-balanced flow nature. This filter design does not use lot of energy to produce permeates when there is no work done by the wall and this might be advantageous for energy saving.

The vertical filter design in chapter 6 operates in a transient regime which produce permeates with maximum speed as time evolves see Figure 6.2. Therefore with time, the fluid flow in the filter design becomes fully developed and production speeds up. According to this design the particles close the heat walls (top and right walls) absorbs more temperature and maintains a constant s-shape temperature distribution over time. The fluid injection needs to be slow to decrease clustering of particles on left and bottom cold walls which is not ideal since at a lower injection rate the amount of fluid going through the chamber becomes less. The effects from the heat walls enhance movement of permeates outflow.

In chapter 7, it is observed that the system produce maximum permeates velocity when parameters affecting the flow according to this design are low. On the other hand when these parameters are low the internal temperature decreases since more temperature is removed out of the chamber when permeates moves fast. This is ideal since low Richardson number implies that the system allows more particles into the chamber since Richardson number is inversely propositional to injection, thus more inflow of fluid more fluid goes through filtration process.

In chapter 8, maximum permeate velocity is observed when the filter design volume is decreased as depicted in Figure 8.7a. From physics point of view small filter chamber space holds small amount of permeates this is a disadvantage for production of more permeates since small amount of fluid goes through filtration process. Therefore this filter design produces less permeates at the higher speed when filter chamber volume is small.

From the above conclusion below are critical things to point out

1. High temperature is need to decrease viscous effect.

2. More permeates outflow consume internal energy.

3. When the system conserve energy it produce less permeates.

4. During unsteady regime the outflow of permeates increases as time evolves.

5. Injecting more fluid inside the chamber increase internal mass however it leads to less outflow when small pore size are used to restrict particles. On the other hand increasing the pore size is not ideal since it allows contaminants to pass through the chamber. Thus the best operation is when free movement of particles is enhanced by injecting fewer particles into the chamber with small pore size.

Bibliography

[1] G. Bolton, D. LaCasse, and R. Kuriyel, "Combined models of membrane fouling: Development and application to microfiltration and ultrafiltration of biological fluids," *Journal of Membrane Science*, vol. 277, no. 1-2, pp. 75–84, 2006.

[2] R. Van der Sman, H. Vollebregt, A. Mepschen, and T. Noordman, "Review of hypotheses for fouling during beer clarification using membranes," *Journal of Membrane Science*, vol. 396, pp. 22–31, 2012.

[3] A. Brown, P. Levison, N. Titchener-Hooker, and G. Lye, "Membrane pleating effects in 0.2 μm rated microfiltration cartridges," *Journal of Membrane Science*, vol. 341, no. 1-2, pp. 76–83, 2009.

[4] R. C. Daniel, J. M. Billing, R. L. Russell, R. W. Shimskey, H. D. Smith, and R. A. Peterson, "Integrated pore blockage-cake filtration model for crossflow filtration," *Chemical Engineering Research and Design*, vol. 89, no. 7, pp. 1094–1103, 2011.

[5] E. Iritani, "A review on modeling of pore-blocking behaviors of membranes during pressurized membrane filtration," *Drying technology*, vol. 31, no. 2, pp. 146–162, 2013.

[6] H. Fallah, H. B. Fathi, and H. Mohammadi, "The mathematical model for particle suspension flow through porous medium," *Geomaterials*, vol. 2, no. 3, pp. 57–62, 2012.

[7] S. Chellam and M. R. Wiesner, "Slip flow through porous media with permeable boundaries: implications for the dimensional scaling of packed beds," *Water environment research*, vol. 65, no. 6, pp. 744–749, 1993.

[8] Z. Zuo-jin, "On the filtration of non-newtonian fluid in porous media with a multiple parameter model," *Journal of Hydrodynamics, Ser. B*, vol. 1, pp. 39–46, 2001.

[9] S. Uchida and H. Aoki, "Unsteady flows in a semi-infinite contracting or expanding pipe," *Journal of Fluid Mechanics*, vol. 82, no. 2, pp. 371–387, 1977.

[10] C. Zhou and J. Majdalani, "Large injection and suction driven channel flows with expanding and contracting walls," in *15th AIAA Computational Fluid Dynamics Conference*, 2001, p. 2713.

[11] H. A. Nabwey, S. El-Kabeir, and A. Rashad, "Lie group analysis of effects of radiation and chemical reaction on heat and mass transfer by unsteady slip flow from a non-isothermal stretching sheet immersed in a porous medium," *Journal of Computational and Theoretical Nanoscience*, vol. 12, no. 11, pp. 4056–4062, 2015.

[12] H. A. Nabwey and H. A. El-Mky, "Lie group analysis of thermophoresis on a vertical surface in a porous medium," *Journal of King Saud University-Science*, vol. 31, no. 4, pp. 1048–1055, 2019.

[13] M. Uddin, M. Ferdows, and O. A. Bég, "Group analysis and numerical computation of magneto-convective non-newtonian nanofluid slip flow from a permeable stretching sheet," *Applied Nanoscience*, vol. 4, no. 7, pp. 897–910, 2014.

[14] M. Rashidi, E. Momoniat, M. Ferdows, and A. Basiriparsa, "Lie group solution for free convective flow of a nanofluid past a chemically reacting horizontal plate in a porous media," *Mathematical Problems in Engineering*, vol. 2014, 2014.

[15] M. Rashidi, N. Rahimzadeh, M. Ferdows, M. J. Uddin, and O. A. Bég, "Group theory and differential transform analysis of mixed convective heat and mass transfer from a horizontal surface with chemical reaction effects," *Chemical Engineering Communications*, vol. 199, no. 8, pp. 1012–1043, 2012.

[16] G. Magalakwe, M. Lekoko, K. Modise, and C. M. Khalique, "Lie group analysis for mhd squeezing flow of viscous fluid saturated in porous media," *Alexandria Engineering Journal*, vol. 58, no. 3, pp. 1001–1010, 2019.

[17] S. Javaid and A. Aziz, "Group invariant solutions for flow and heat transfer of power-law nanofluid in a porous medium," *Mathematical Problems in Engineering*, vol. 2021, 2021.

[18] G. W. Bluman and J. D. Cole, *Similarity methods for differential equations*. Springer Science & Business Media, 2012, vol. 13.

[19] G. W. Bluman and S. Kumei, *Symmetries and differential equations*. Springer Science & Business Media, 2013, vol. 81.

[20] C. Chevalley, *Theory of Lie groups*. Courier Dover Publications, 2018.

[21] T. L. Chow, "Systems of partial differential equations and group methods," 1996.

[22] N. H. Ibragimov, *CRC handbook of Lie group analysis of differential equations*. CRC press, 1995, vol. 3.

[23] N. H. Ibragimov and N. K. Ibragimov, *Elementary Lie group analysis and ordinary differential equations*.

[24] S. D. Oloniiju, S. P. Goqo, and P. Sibanda, "Heat and mass transfer in an unsteady second grade nanofluid with viscous heating dissipation," *International Journal of Computational Methods*, vol. 17, no. 05, p. 1940005, 2020.

[25] S. P. Goqo, H. Mondal, P. Sibanda, and S. S. Motsa, "A multivariate spectral quasi-linearisation method for entropy generation in a square cavity filled with porous medium saturated by nanofluid," *Case Studies in Thermal Engineering*, vol. 14, p. 100415, 2019.

[26] S. Goqo, S. Oloniiju, H. Mondal, P. Sibanda, and S. Motsa, "Entropy generation in mhd radiative viscous nanofluid flow over a porous wedge using the bivariate spectral quasi-linearization method," *Case studies in thermal engineering*, vol. 12, pp. 774–788, 2018.

[27] S. Motsa, V. Magagula, and P. Sibanda, "A bivariate chebyshev spectral collocation quasilinearization method for nonlinear evolution parabolic equations," *The Scientific World Journal*, vol. 2014, 2014.

[28] M. Iqbal, A. Ghaffari, and I. Mustafa, "Investigation into thermophoresis and brownian motion effects of nanoparticles on radiative heat transfer in hiemenz flow using spectral method," *Scientia Iranica*, vol. 26, no. 6, pp. 3905–3916, 2019.

[29] K. Modise and G. Magalakwe, "An internal flow and heat transfer inside a solid rocket motor combustion chamber; a lie symmetry approach," *Thermal Science and Engineering Progress*, p. 101237, 2022.

[30] H. Stephani, *Differential equations: their solution using symmetries*. Cambridge University Press, 1989.

[31] L. V. Ovsiannikov, *Group analysis of differential equations*. Academic press, 2014.

[32] P. J. Olver, *Applications of Lie groups to differential equations*. Springer Science & Business Media, 1993, vol. 107.

[33] E. C. Dauenhauer and J. Majdalani, "Exact self-similarity solution of the navier–stokes equations for a porous channel with orthogonally moving walls," *Physics of Fluids*, vol. 15, no. 6, pp. 1485–1495, 2003.

[34] T. A. Jankowski and J. Majdalani, "Laminar flow in a porous channel with large wall suction and a weakly oscillatory pressure," *Physics of Fluids*, vol. 14, no. 3, pp. 1101–1110, 2002.

[35] C. Zhou and J. Majdalani, "Improved mean-flow solution for slab rocket motors with regressing walls," *Journal of Propulsion and Power*, vol. 18, no. 3, pp. 703–711, 2002.

[36] J. Majdalani and C. Zhou, "Moderate-to-large injection and suction driven channel flows with expanding or contracting walls," *ZAMM-Journal of Applied Mathematics and Mechanics/Zeitschrift für Angewandte Mathematik und Mechanik: Applied Mathematics and Mechanics*, vol. 83, no. 3, pp. 181–196, 2003.

[37] A. Ali, Y. Ali, P. Kumam, K. Babar, A. Ahmed, and Z. Shah, "Flow of a nanofluid and heat transfer in channel with contracting/expanding walls," *IEEE Access*, vol. 7, pp. 102 427–102 436, 2019.

[38] A. T. Akinshilo, "Flow and heat transfer of nanofluid with injection through an expanding or contracting porous channel under magnetic force field," *Engineering Science and Technology, an International Journal*, vol. 21, no. 3, pp. 486–494, 2018.

[39] W. Robinson, "The existence of multiple solutions for the laminar flow in a uniformly porous channel with suction at both walls," *Journal of Engineering Mathematics*, vol. 10, no. 1, pp. 23–40, 1976.

[40] M. Zaturska, P. Drazin, and W. Banks, "On the flow of a viscous fluid driven along a channel by suction at porous walls," *Fluid Dynamics Research*, vol. 4, no. 3, p. 151, 1988.

[41] X. Si, L. Zheng, X. Zhang, and Y. Chao, "Existence of multiple solutions for the laminar flow in a porous channel with suction at both slowly expanding and contracting walls," *International Journal of Minerals, Metallurgy, and Materials*, vol. 18, no. 4, pp. 494–501, 2011.

[42] X. Si, L. Zheng, X. Zhang, M. Li, J. Yang, and Y. Chao, "Multiple solutions for the laminar flow in a porous pipe with suction at slowly expanding or contracting wall," *Applied Mathematics and Computation*, vol. 218, no. 7, pp. 3515–3521, 2011.

[43] J. Majdalani, C. Zhou, and C. A. Dawson, "Two-dimensional viscous flow between slowly expanding or contracting walls with weak permeability," *Journal of Biomechanics*, vol. 35, no. 10, pp. 1399–1403, 2002.

[44] K. S. Mekheimer and R. Abo-Elkhair, "Lie point symmetries for biological magneto-jeffrey fluid flow in expanding or contracting permeable walls: a blood vessel model," *Journal of Taibah University for Science*, vol. 12, no. 6, pp. 738–747, 2018.

[45] S. Dinarvand, A. Doosthoseini, E. Doosthoseini, and M. M. Rashidi, "Comparison of HAM and HPM methods for Berman's model of two-dimensional viscous flow in porous channel with wall suction or injection," *Advances in Theoretical and Applied Mechanics*, vol. 1, no. 7, pp. 337–347, 2008.

[46] M. Sobamowo, "Thermal analysis of longitudinal fin with temperature-dependent properties and internal heat generation using Galerkin's method of weighted residual," *Applied Thermal Engineering*, vol. 99, pp. 1316–1330, 2016.

[47] A. Majeed, T. Javed, A. Ghaffari, and M. Rashidi, "Analysis of heat transfer due to stretching cylinder with partial slip and prescribed heat flux: A chebyshev spectral newton iterative scheme," *Alexandria Engineering Journal*, vol. 54, no. 4, pp. 1029–1036, 2015.

[48] A. Mahmood, B. Chen, and A. Ghaffari, "Hydromagnetic hiemenz flow of micropolar fluid over a nonlinearly stretching/shrinking sheet: Dual solutions by using chebyshev spectral newton iterative scheme," *Journal of Magnetism and Magnetic Materials*, vol. 416, pp. 329–334, 2016.

[49] A. Ghaffari, I. Mustafa, and T. Javed, "Time dependent convective non-orthogonal hiemenz flow of viscoelastic walter's b fluid towards a non-uniformly heated vertical surface: Using spectral method," *Nihon Reoroji Gakkaishi*, vol. 46, no. 4, pp. 155–164, 2018.

[50] J. Tenreiro Machado, N. Özdemir, and D. Baleanu, "Mathematical modelling and optimization of engineering problems: vol 30," 2020.

[51] R. Bellman and R. E. Kalaba, *Quasilinearization and nonlinear boundary-value problems*. New York: American Elsevier, 1965, vol. 3.

[52] L. N. Trefethen, *Spectral methods in MATLAB*. SIAM, 2000.

[53] S. Aleksandrova, S. Molokov, and C. Reed, "Modeling of liquid metal duct and free-surface flows using CFX," Argonne National Lab., IL (US), Tech. Rep., 2002.

[54] J. Lig̀ere, "Analytical solutions of magnetohydrodynamical problems on a flow of conducting fluid in the entrance region of channels in a strong magnetic field," Ph.D. dissertation, Riga Technical University, 2014.

[55] L. Fan, C. Hwang, P. Knieper, and U. Hwang, "Heat transfer on magnetohydrodynamic flow in the entrance region of a flat duct," *Zeitschrift für angewandte Mathematik und Physik ZAMP*, vol. 18, no. 6, pp. 826–844, 1967.

[56] H. Yang and C. Yu, "Combined forced and free convection MHD channel flow in entrance region," *International Journal of Heat and Mass Transfer*, vol. 17, no. 6, pp. 681–691, 1974.

[57] J. Shercliff, "Entry of conducting and non-conducting fluids in pipes," in *Mathematical Proceedings of the Cambridge Philosophical Society*, vol. 52, no. 3. Cambridge University Press, 1956, pp. 573–583.

[58] S. Nigam and S. Singh, "Heat transfer by laminar flow between parallel plates under the action of transverse magnetic field," *The Quarterly Journal of Mechanics and Applied Mathematics*, vol. 13, no. 1, pp. 85–97, 1960.

[59] R. Alpher, "Heat transfer in magnetohydrodynamic flow between parallel plates," *International Journal of Heat and Mass Transfer*, vol. 3, no. 2, pp. 108–112, 1961.

[60] L. Back, "Laminar heat transfer in electrically conducting fluids flowing in parallel plate channels," *International Journal of Heat and Mass Transfer*, vol. 11, no. 11, pp. 1621–1636, 1968.

[61] A. H. Eraslan and N. F. Eraslan, "Heat transfer in magnetohydrodynamic channel flow," *The Physics of Fluids*, vol. 12, no. 1, pp. 120–128, 1969.

[62] A. Bhat and M. Mittal, "Heat transfer in a MHD channel with uniform wall heat flux–effects of Hall and ion slip currents," *International Journal of Heat and Mass Transfer*, vol. 23, no. 7, pp. 919–926, 1980.

[63] V. Javeri, "Magnetohydrodynamic channel flow heat transfer for temperature boundary condition of the third kind," *International Journal of Heat and Mass Transfer*, vol. 20, no. 5, pp. 543–547, 1977.

[64] O. Otegbeye and S. Motsa, "A paired quasilinearization method for solving boundary layer flow problems," in *AIP Conference Proceedings*, vol. 1975, no. 1. AIP Publishing LLC, 2018, p. 030020.

[65] M. S. Ansari, O. Otegbeye, M. Trivedi, and S. Goqo, "Magnetohydrodynamic bioconvective Casson nanofluid flow: A numerical simulation by paired quasilinearisation," *Journal of Applied and Computational Mechanics*, 2020.

[66] O. Otegbeye, "On paired decoupled quasi-linearization methods for solving nonlinear systems of differential equations that model boundary layer fluid flow problems." Ph.D. dissertation, 2018.

[67] M. L. Lekoko, S. D. Oloniiju, and G. Magalakwe, "Analysis of pressure and heat distribution in a dilating or contracting filter chamber with two outlets using multivariate spectral quasilinearization method," *Heat Transfer*, vol. 51, no. 2, pp. 1543–1567, 2022.

[68] J.-Y. Sa and D. Kwak, *A numerical method for incompressible flow with heat transfer*. National Aeronautics and Space Administration, Ames Research Center, 1997.

[69] M. Hossain, S. Asghar, and R. S. R. Gorla, "Buoyancy-driven flow of a viscous incompressible fluid in an open-ended rectangular cavity with permeable horizontal surfaces," *International Journal of Numerical Methods for Heat & Fluid Flow*, 2010.

[70] S. Zeraati Dizjeh and J. Brinkerhoff, "Stability of buoyancy-driven flow in a vertical channel with one heated wall," *Physics of Fluids*, vol. 33, no. 8, p. 084103, 2021.

[71] C. Hermes, M. Marques, C. Melo, and C. Negrao, "A cfd model for buoyancy driven flows inside refrigerated cabinets and freezers," 2002.

[72] A. A. Rejeesh, S. Udhayakumar, T. Sekhar, R. Sivakumar *et al.*, "Mixed convection and heat transfer studies in non-uniformly heated buoyancy driven cavity flow," *Open Journal of Fluid Dynamics*, vol. 7, no. 02, p. 231, 2017.

[73] M. Moallemi and K. Jang, "Prandtl number effects on laminar mixed convection heat transfer in a lid-driven cavity," *International Journal of Heat and Mass Transfer*, vol. 35, no. 8, pp. 1881–1892, 1992.

[74] T. Basak, S. Roy, P. K. Sharma, and I. Pop, "Analysis of mixed convection flows within a square cavity with uniform and non-uniform heating of bottom wall," *International Journal of Thermal Sciences*, vol. 48, no. 5, pp. 891–912, 2009.

[75] M. Cánovas, I. Alhama, G. García, E. Trigueros, and F. Alhama, "Numerical simulation of density-driven flow and heat transport processes in porous media using the network method," *Energies*, vol. 10, no. 9, p. 1359, 2017.

[76] M. Sathiyamoorthy, T. Basak, S. Roy, and I. Pop, "Steady natural convection flows in a square cavity with linearly heated side wall (s)," *International Journal of Heat and Mass Transfer*, vol. 50, no. 3-4, pp. 766–775, 2007.

[77] E. Chen and F. Xu, "Transient thermocapillary convection flows in a rectangular cavity with an evenly heated lateral wall," *Physics of Fluids*, vol. 33, no. 1, p. 013602, 2021.

[78] F. Pan and A. Acrivos, "Steady flows in rectangular cavities," *Journal of Fluid Mechanics*, vol. 28, no. 4, pp. 643–655, 1967.

[79] K. Torrance, R. Davis, K. Eike, P. Gill, D. Gutman, A. Hsui, S. Lyons, and H. Zien, "Cavity flows driven by buoyancy and shear," *Journal of Fluid Mechanics*, vol. 51, no. 2, pp. 221–231, 1972.

[80] J. Patterson and J. Imberger, "Unsteady natural convection in a rectangular cavity," *Journal of Fluid Mechanics*, vol. 100, no. 1, pp. 65–86, 1980.

[81] H. Celik, M. Mobedi, O. Manca, and B. Buonomo, "Enhancement of heat transfer in partially heated vertical channel under mixed convection by using al2o3 nanoparticles," *Heat Transfer Engineering*, vol. 39, no. 3, pp. 229–240, 2018.

[82] J. N. Momanyi, J. K. Sigey, J. A. Okelo, and J. M. Okwoyo, "Effects of forced convection on temperature distribution and velocity profiles in a room."

[83] N. Acharya, "Spectral simulation to investigate the effects of active passive controls of nanoparticles on the radiative nanofluidic transport over a spinning disk," *Journal of Thermal Science and Engineering Applications*, vol. 13, no. 3, 2021.

[84] I. G. Currie, *Fundamental mechanics of fluids*. CRC press, 2016.

[85] S. Whitaker, *Fundamental principles of heat transfer*. Elsevier, 2013.

[86] M. Schatzmann and A. Policastro, "Effects of the boussinesq approximation on the results of strongly-buoyant plume calculations," *Journal of Applied Meteorology and Climatology*, vol. 23, no. 1, pp. 117–123, 1984.

[87] H. G. Lee and J. Kim, "A comparison study of the boussinesq and the variable density models on buoyancy-driven flows," *Journal of Engineering Mathematics*, vol. 75, no. 1, pp. 15–27, 2012.

[88] C. Bardos, F. Golse, and B. Perthame, "The rosseland approximation for a simplified model of the radiative transfer equations," *Comptes Rendus des Seances de l'Academie des Sciences. Serie 1*, vol. 301, no. 12, pp. 627–630, 1985.

[89] A. A. Al-Rashed, A. Shahsavar, M. Akbari, D. Toghraie, M. Akbari, and M. Afrand, "Finite volume simulation of mixed convection in an inclined lid-driven cavity filled with nanofluids: effects of a hot elliptical centric cylinder, cavity angle and volume fraction of nanoparticles," *Physica A: Statistical Mechanics and its Applications*, vol. 527, p. 121122, 2019.

[90] R. Bellman and R. E. Kalaba, "Quasilinearization and nonlinear boundary-value problems," *New York: American Elsevier*, vol. 3, 1965.

[91] S. Motsa, P. Dlamini, and M. Khumalo, "Spectral relaxation method and spectral quasilinearization method for solving unsteady boundary layer flow problems," *Advances in Mathematical Physics*, vol. 2014, 2014.

[92] N. Acharya, "Spectral simulation to investigate the effects of nanoparticle diameter and nanolayer on the ferrofluid flow over a slippery rotating disk in the presence of low oscillating magnetic field," *Heat Transfer*, vol. 50, no. 6, pp. 5951–5981, 2021.

[93] L. N. Trefethen, "Spectral methods in MATLAB," 2000.

[94] A. S. Bded, S. M. Talib, and F. L. Rashid, "Thermal analysis of vertical flow of steam through a porous media," *Journal of Mechanical Engineering Research and Developments*, vol. 43, no. 5, pp. 494–503, 2020.

[95] H. K. Miyagawa, I. V. Curcino, F. A. Pontes, E. N. Macêdo, P. C. Pontes, and J. N. Quaresma, "Hybrid solution for the analysis of mhd micropolar fluid flow in a vertical porous parallel-plates duct," *Journal of Applied and Computational Mechanics*, vol. 6, no. Special Issue, pp. 1107–1124, 2020.

[96] M. L. Lekoko, S. D. Oloniiju, and G. Magalakwe, "Injection driven flow in a dilating or contracting filter chamber with parabolic left inlet velocity," *International Journal of Non-Linear Mechanics*, vol. 142, p. 103986, 2022.

[97] H. F. Oztop and K. Al-Salem, "A review on entropy generation in natural and mixed convection heat transfer for energy systems," *Renewable and Sustainable Energy Reviews*, vol. 16, no. 1, pp. 911–920, 2012.

[98] R. Sehgal and Y. Jaluria, "Horizontal recirculation in water bodies due to thermal discharge," *Energy*, vol. 7, no. 5, pp. 419–428, 1982.

[99] A. T. Kirkpatrick and D. D. Hill, "Mixed convection heat transfer in a passive solar building," *Solar energy*, vol. 40, no. 1, pp. 25–34, 1988.

[100] C. Afonso and A. Oliveira, "Solar chimneys: simulation and experiment," *Energy and buildings*, vol. 32, no. 1, pp. 71–79, 2000.

[101] J. Bosbach, J. Pennecot, C. Wagner, M. Raffel, T. Lerche, and S. Repp, "Experimental and numerical simulations of turbulent ventilation in aircraft cabins," *Energy*, vol. 31, no. 5, pp. 694–705, 2006.

[102] A. Ali, N. Kechiche, and H. B. Aissia, "Prandtl-number effects on vertical buoyant jets in forced and mixed convection regimes," *Energy conversion and management*, vol. 48, no. 5, pp. 1435–1449, 2007.

[103] M. H. Elnaggar, M. Abdullah, and M. A. Mujeebu, "Experimental analysis and fem simulation of finned u-shape multi heat pipe for desktop pc cooling," *Energy Conversion and Management*, vol. 52, no. 8-9, pp. 2937–2944, 2011.

[104] A. K. Satapathy, "Thermodynamic optimization of a coiled tube heat exchanger under constant wall heat flux condition," *Energy*, vol. 34, no. 9, pp. 1122–1126, 2009.

[105] İ. Kurtbaş, N. Celik, and İ. Dinçer, "Exergy transfer in a porous rectangular channel," *Energy*, vol. 35, no. 1, pp. 451–460, 2010.

[106] M. Mossolly, K. Ghali, and N. Ghaddar, "Optimal control strategy for a multi-zone air conditioning system using a genetic algorithm," *Energy*, vol. 34, no. 1, pp. 58–66, 2009.

[107] J. Xamán, A. Ortiz, G. Álvarez, and Y. Chávez, "Effect of a contaminant source (co2) on the air quality in a ventilated room," *Energy*, vol. 36, no. 5, pp. 3302–3318, 2011.

[108] J. Clark and A. Novoselac, "Flow and mixed convection heat transfer in buoyant jets from floor registers," *Energy and buildings*, vol. 61, pp. 140–145, 2013.

[109] S. Jaisankar, T. Radhakrishnan, and K. Sheeba, "Studies on heat transfer and friction factor characteristics of thermosyphon solar water heating system with helical twisted tapes," *Energy*, vol. 34, no. 9, pp. 1054–1064, 2009.

[110] W. Sun, J. Ji, and W. He, "Influence of channel depth on the performance of solar air heaters," *Energy*, vol. 35, no. 10, pp. 4201–4207, 2010.

[111] D. A. Granados, F. Chejne, J. M. Mejía, C. A. Gómez, A. Berrío, and W. J. Jurado, "Effect of flue gas recirculation during oxy-fuel combustion in a rotary cement kiln," *Energy*, vol. 64, pp. 615–625, 2014.

[112] O. O. Onyejekwe, "Combined effects of shear and buoyancy for mixed convection in an enclosure," *Advances in Engineering Software*, vol. 47, no. 1, pp. 188–193, 2012.

[113] C. Cha and Y. Jaluria, "Recirculating mixed convection flow for energy extraction," *International Journal of Heat and Mass Transfer*, vol. 27, no. 10, pp. 1801–1812, 1984.

[114] Y. Jaluria and C. Cha, "Heat rejection to the surface layer of a solar pond," 1985.

[115] B. K. Jha, B. Aina, and A. Ajiya, "Role of suction/injection on mhd natural convection flow in a vertical microchannel," *Int. J. Energy Technol*, vol. 7, no. 2, pp. 30–39, 2015.

[116] J. Garandet, T. Alboussiere, and R. Moreau, "Buoyancy driven convection in a rectangular enclosure with a transverse magnetic field," *International journal of heat and mass transfer*, vol. 35, no. 4, pp. 741–748, 1992.

[117] C.-K. Chen and H. C. Weng, "Natural convection in a vertical microchannel," 2005.

[118] B. K. Jha, B. Aina, and S. B. Joseph, "Natural convection flow in a vertical microchannel with suction/injection," *Proceedings of the Institution of Mechanical Engineers, Part E: Journal of Process Mechanical Engineering*, vol. 228, no. 3, pp. 171–180, 2014.

[119] M. Sheikholeslami, M. Gorji-Bandpy, D. Ganji, and S. Soleimani, "Natural convection heat transfer in a nanofluid filled inclined l-shaped enclosure," *Iranian Journal of Science and Technology. Transactions of Mechanical Engineering*, vol. 38, no. M1+, p. 217, 2014.

[120] G. Magalakwe, M. Lekoko, K. Modise, and C. M. Khalique, "Lie group method solution for two-dimensional heat and viscous flow driven by injection through a deformable rectangular channel with porous walls," in *Mathematical Modelling and Optimization of Engineering Problems*. Springer, 2020, pp. 89–114.

[121] S. Oloniiju, S. Goqo, and P. Sibanda, "A chebyshev spectral method for heat and mass transfer in mhd nanofluid flow with space fractional constitutive model," *Frontiers in Heat and Mass Transfer (FHMT)*, vol. 13, 2019.

[122] S. D. Oloniiju, S. P. Goqo, and P. Sibanda, "A geometrically convergent pseudo–spectral method for multi–dimensional two–sided space fractional partial differential equations," *Journal of Applied Analysis & Computation*, vol. 11, no. 4, pp. 1699–1717, 2021.

[123] S. S. Motsa and I. L. Animashaun, "A new numerical investigation of some thermo-physical properties on unsteady MHD non-Darcian flow past an impulsively started vertical surface," *Thermal Science*, vol. 19(1), pp. 249–258, 2015.

[124] M. F. Modest and S. Mazumder, *Radiative heat transfer*. Academic press, 2021.

[125] J. Lee, P. Kandaswamy, M. Bhuvaneswari, and S. Sivasankaran, "Lie group analysis of radiation natural convection heat transfer past an inclined porous surface," *Journal of mechanical science and technology*, vol. 22, no. 9, pp. 1779–1784, 2008.

[126] C. R. O'Melia, "Particles, pretreatment, and performance in water filtration," *Journal of Environmental Engineering*, vol. 111, no. 6, pp. 874–890, 1985.

[127] S. Munirasu, M. A. Haija, and F. Banat, "Use of membrane technology for oil field and refinery produced water treatment—a review," *Process safety and environmental protection*, vol. 100, pp. 183–202, 2016.

[128] C. Bhattacharjee, V. Saxena, and S. Dutta, "Fruit juice processing using membrane technology: A review," *Innovative Food Science & Emerging Technologies*, vol. 43, pp. 136–153, 2017.

[129] J. Monte, M. Sá, C. Parreira, J. Galante, A. R. Serra, C. F. Galinha, L. Costa, V. J. Pereira, C. Brazinha, and J. G. Crespo, "Recycling of dunaliella salina cultivation medium by integrated membrane filtration and advanced oxidation," *Algal Research*, vol. 39, p. 101460, 2019.

[130] B. Matebese, A. Adem, C. Khalique, and T. Hayat, "Two-dimensional flow in a deformable channel with porous medium and variable magnetic field," *Mathematical and Computational applications*, vol. 15, no. 4, pp. 674–684, 2010.

[131] M. Sheikholeslami, M. Hatami, and D. Ganji, "Analytical investigation of mhd nanofluid flow in a semi-porous channel," *Powder Technology*, vol. 246, pp. 327–336, 2013.

[132] K. Das and U. Mohammed, "Radiation effects on an unsteady squeezing flow in the presence of a magnetic field," 2016.

[133] M. Sheikholeslami, T. Hayat, and A. Alsaedi, "Mhd free convection of al2o3–water nanofluid considering thermal radiation: a numerical study," *International Journal of Heat and Mass Transfer*, vol. 96, pp. 513–524, 2016.

[134] M. Turkyilmazoglu, "Analytical solutions of single and multi-phase models for the condensation of nanofluid film flow and heat transfer," *European Journal of Mechanics-B/Fluids*, vol. 53, pp. 272–277, 2015.

[135] F. Talebi, A. H. Mahmoudi, and M. Shahi, "Numerical study of mixed convection flows in a square lid-driven cavity utilizing nanofluid," *International Communications in Heat and Mass Transfer*, vol. 37, no. 1, pp. 79–90, 2010.

[136] A.-S. Al-Saif and A. Harfash, "Perturbation-iteration algorithm for solving heat and mass transfer in the unsteady squeezing flow between parallel plates," *Journal of Applied and Computational Mechanics*, vol. 5, no. 4, pp. 804–815, 2019.

[137] M. Mustafa, T. Hayat, and S. Obaidat, "On heat and mass transfer in the unsteady squeezing flow between parallel plates," *Meccanica*, vol. 47, no. 7, pp. 1581–1589, 2012.

[138] N. A. Mat Noor, S. Shafie, and M. A. Admon, "Heat and mass transfer on mhd squeezing flow of jeffrey nanofluid in horizontal channel through permeable medium," *Plos one*, vol. 16, no. 5, p. e0250402, 2021.

[139] N. Naduvinamani and U. Shankar, "Radiative squeezing flow of unsteady magneto-hydrodynamic casson fluid between two parallel plates," *Journal of Central South University*, vol. 26, no. 5, pp. 1184–1204, 2019.

[140] M. Hatami, D. Jing, D. Song, M. Sheikholeslami, and D. Ganji, "Heat transfer and flow analysis of nanofluid flow between parallel plates in presence of variable magnetic field using hpm," *Journal of Magnetism and Magnetic Materials*, vol. 396, pp. 275–282, 2015.

[141] N. Naduvinamani and U. Shankar, "Thermal-diffusion and diffusion-thermo effects on squeezing flow of unsteady magneto-hydrodynamic casson fluid between two parallel plates with thermal radiation," *Sādhanā*, vol. 44, no. 8, pp. 1–16, 2019.

[142] B. Bin-Mohsin, N. Ahmed, U. Khan, S. Tauseef Mohyud-Din *et al.*, "A bioconvection model for a squeezing flow of nanofluid between parallel plates in the presence of gyrotactic microorganisms," *The European Physical Journal Plus*, vol. 132, no. 4, pp. 1–12, 2017.

[143] M. Sobamowo and A. Akinshilo, "On the analysis of squeezing flow of nanofluid between two parallel plates under the influence of magnetic field," *Alexandria Engineering Journal*, vol. 57, no. 3, pp. 1413–1423, 2018.

[144] A. M. Obalalu, "Heat and mass transfer in an unsteady squeezed casson fluid flow with novel thermophysical properties: Analytical and numerical solution," *Heat Transfer*, vol. 50, no. 8, pp. 7988–8011, 2021.

[145] T. Hayat, A. Yousaf, M. Mustafa, and S. Asghar, "Influence of heat transfer in the squeezing flow between parallel disks," *Chemical Engineering Communications*, vol. 199, no. 8, pp. 1044–1062, 2012.

[146] U. Khan, S. I. Khan, N. Ahmed, S. Bano, and S. T. Mohyud-Din, "Heat transfer analysis for squeezing flow of a casson fluid between parallel plates," *Ain Shams Engineering Journal*, vol. 7, no. 1, pp. 497–504, 2016.

[147] M. S. Kumar, N. Sandeep, B. R. Kumar, and S. Saleem, "Effect of aligned magnetic field on mhd squeezing flow of casson fluid between parallel plates," in *Defect and Diffusion Forum*, vol. 384. Trans Tech Publ, 2018, pp. 1–11.

[148] R. H. Rand and D. Armbruster, *Perturbation methods, bifurcation theory and computer algebra*. Springer Science & Business Media, 2012, vol. 65.

[149] A. H. Nayfeh, *Introduction to perturbation techniques*. John Wiley & Sons, 2011.

[150] M. Sobamowo, "Singular perturbation and differential transform methods to two-dimensional flow of nanofluid in a porous channel with expanding/contracting walls subjected to a uniform transverse magnetic field," *Thermal Science and Engineering Progress*, vol. 4, pp. 71–84, 2017.

[151] X.-h. Si, L.-c. Zheng, X.-x. Zhang, and Y. Chao, "Perturbation solution to unsteady flow in a porous channel with expanding or contracting walls in the presence of a transverse magnetic field," *Applied Mathematics and Mechanics*, vol. 31, no. 2, pp. 151–158, 2010.

[152] G. Magalakwe, B. Muatjetjeja, and C. Khalique, "Generalized double sinh-gordon equation: Symmetry reductions, exact solutions and conservation laws," 2015.

[153] M. L. Lekoko, S. D. Oloniiju, and G. Magalakwe, "Analysis of pressure and heat distribution in a dilating or contracting filter chamber with two outlets using multivariate spectral quasilinearization method," *Heat Transfer*.

[154] A. Shafiq and C. M. Khalique, "Lie group analysis of upper convected maxwell fluid flow along stretching surface," *Alexandria Engineering Journal*, vol. 59, no. 4, pp. 2533–2541, 2020.

[155] M. M. Bhatti, S. Jun, C. M. Khalique, A. Shahid, L. Fasheng, and M. S. Mohamed, "Lie group analysis and robust computational approach to examine mass transport process using jeffrey fluid model," *Applied Mathematics and Computation*, vol. 421, p. 126936, 2022.

[156] R. Shah and A. London, *Laminar flow forced convection in ducts.* Elsevier, 1978, vol. 1.

[157] J. P. Hartnett and M. Kostic, "Heat transfer to newtonian and non-newtonian fluids in rectangular ducts," in *Advances in heat transfer.* Elsevier, 1989, vol. 19, pp. 247–356.

[158] J. Hudson and S. Bankoff, "Heat transfer to a steady couette flow with pressure gradient," *Chemical Engineering Science*, vol. 20, no. 5, pp. 415–423, 1965.

[159] J. Ŝesták and F. Rieger, "Laminar heat transfer to a steady couette flow between parallel plates," *International Journal of Heat and Mass Transfer*, vol. 12, no. 1, pp. 71–80, 1969.

[160] S. Bruin, "Temperature distributions in couette flow with and without additional pressure," *International Journal of Heat and Mass Transfer*, vol. 15, no. 2, pp. 341–349, 1972.

[161] E. J. Davis, "Exact solutions for a class of heat and mass transfer problems," *The Canadian Journal of Chemical Engineering*, vol. 51, no. 5, pp. 562–572, 1973.

[162] S. Lin, "Heat transfer to plane non-newtonian couette flow," *International Journal of Heat and Mass Transfer*, vol. 22, no. 7, pp. 1117–1123, 1979.

[163] S. Das, "Effect of constant suction and injection on mhd three dimensional couette flow and heat transfer through a porous medium," *Journal of Naval Architecture and Marine Engineering*, vol. 6, pp. 41–51, 03 2010.

[164] H. A. Attia and N. A. Kotb, "Mhd flow between two parallel plates with heat transfer," *Acta Mechanica*, vol. 117, pp. 215–220, 1996.

[165] G. S. Seth, M. S. Ansari, and R. Nandkeolyar, "Unsteady hydromagnetic couette flow within a porous channel," *Journal of Applied Science and Engineering*, vol. 14, pp. 7–14, March 2011.

[166] I. Baoku, C. israel cookey, and B. olajuwon, "I. g. baoku, c. israel-cookey, b. i. olajuwon," *Surveys in Mathematics and its Applications*, vol. 5, pp. 215 – 228, 01 2010.

[167] K. Boniface, K. Jackson, and O. Thomas, "Investigation of hydro magnetic steady flow between two infinite parallel vertical porous plates," *American Journal of Applied Mathematics*, vol. 2, pp. 170–178, 2014.

[168] O. Makinde and P. Mhone, "Heat transfer to mhd oscillatory flow in a channel filled with porous medium," *Romanian Journal of physics*, vol. 50, no. 9/10, p. 931, 2005.

[169] M. Bhuvaneswari, S. Sivasankaran, and Y. J. Kim, "Lie group analysis of radiation natural convection flow over an inclined surface in a porous medium with internal heat generation," *Journal of porous media*, vol. 15, no. 12, 2012.

Appendix A

An Appendix Chapter

Appendix A1. Exponents

$$
\begin{aligned}
A_1 &= \sqrt{R_e}\sqrt{-P_r}\sqrt{4q - c^2 R_e P_r}, \quad A_2 = cR_eP_r, \quad A_3 = \frac{\sqrt{R_e}\sqrt{c^2 k R_e + 4}}{\sqrt{k}}, \\
A_4 &= c\sqrt{k}R_e - \sqrt{R_e}\sqrt{c^2 k R_e + 4}.
\end{aligned}
$$

Appendix A2. Terms

$$
\begin{aligned}
T_1 &= kP_r^2\left(kq^2 - c^2R_e(kq+1)\right) + kP_r\left(c^2R_e(kq+1) + 2q\right) + 1, \\
T_2 &= c^2kR_e(kq+1)\left(P_r - 1\right)P_r - \left(kqP_r + 1\right)^2, \quad T_3 = k\cos(\alpha)\sqrt{R_e}G_r\sqrt{4q - c^2R_eP_r}, \\
T_4 &= kP_r^2\left(c^2R_e(kq+1) - kq^2\right) - kP_r\left(c^2R_e(kq+1) + 2q\right) - 1, \quad T_5 = c^2R_e(kq+1)\sqrt{-P_r}, \\
T_6 &= kP_r\left(2q - c^2R_e\left(P_r - 1\right)\right) + 2, \quad T_7 = -kP_r\left(c^2R_e + 2q\right) + c^2kR_eP_r^2 - 2, \quad T_8 = \sqrt{k}q\sqrt{R_e}P_r, \\
T_9 &= k\cos(\alpha)G_r\sqrt{-P_r}\sqrt{4q - c^2R_eP_r}\left(-kP_r\left(c^2R_e + q\right) + c^2kR_eP_r^2 - 1\right), \\
T_{10} &= \sqrt{-P_r}\sqrt{4q - c^2R_eP_r} + P_r\Big\{c^3(-k)R_e^{3/2}\left(P_r - 1\right)P_r - c^2kR_e\left(P_r - 1\right)\sqrt{-P_r}\sqrt{4q - c^2R_eP_r} \\
&\quad + kq\sqrt{-P_r}\sqrt{4q - c^2R_eP_r} + c\sqrt{R_e}\left(3kqP_r - 2kq + 1\right)\Big\}, \\
T_{11} &= P_r\Big\{c^3(-k)R_e^{3/2}\left(P_r - 1\right)P_r + c^2kR_e\left(P_r - 1\right)\sqrt{-P_r}\sqrt{4q - c^2R_eP_r} - kq\sqrt{-P_r}\sqrt{4q - c^2R_eP_r} \\
&\quad + c\sqrt{R_e}\left(3kqP_r - 2kq + 1\right)\Big\} - \sqrt{-P_r}\sqrt{4q - c^2R_eP_r}, \\
T_{12} &= \sqrt{c^2kR_e + 4} + c\sqrt{k}\sqrt{R_e}, \\
T_{13} &= \sqrt{R_e}\sqrt{c^2kR_e + 4} + c\sqrt{k}R_e
\end{aligned}
$$